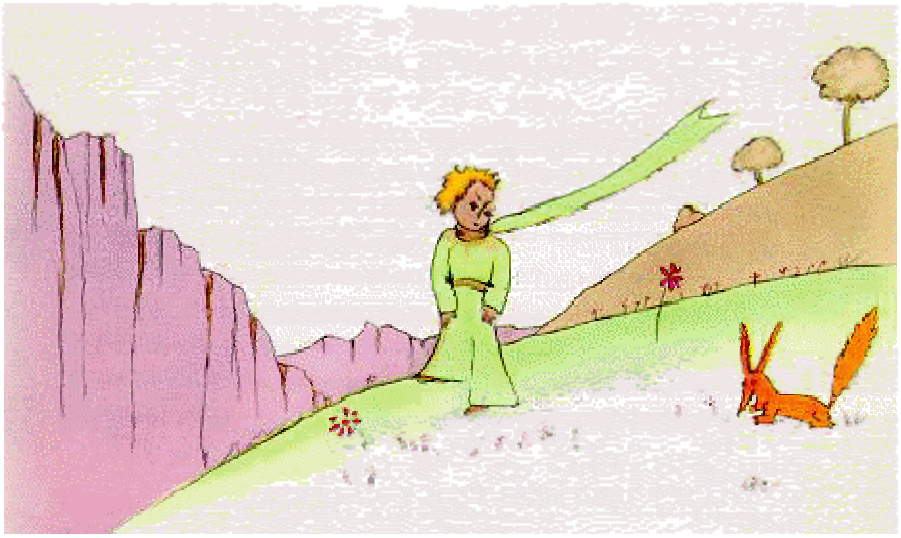

-Adiós -dijo el zorro-. He aquí mi secreto, que no puede ser más simple: ***Sólo con el corazón se puede ver bien. Lo esencial es invisible para los ojos.***

*-**Lo esencial es invisible para los ojos** -repitió el principito para acordarse.*

-Lo que hace más importante a tu rosa, es el tiempo que tú has perdido con ella.

-Es el tiempo que yo he perdido con ella... -repitió el principito para recordarlo.

-Los hombres han olvidado esta verdad -dijo el zorro-, pero tú no debes olvidarla. Eres responsable para siempre de lo que has domesticado. Tú eres responsable de tu rosa...

-Yo soy responsable de mi rosa... -repitió el principito a fin de recordarlo

Saint Exupery

A mi padre que me enseñó a emprender todos mis proyectos sin tener miedo a esa parte del éxito que es el fracaso.

Gracias a mi madre por su ejemplo y por su dedicación, a mi hermano Gerardo por su paciencia ante las dificultades y a mi hermana por su valentía.

Gracias Merce, porque me has comprendido.

Gracias Susana por la dedicación con la que has dirigido esta tesis. He aprendido mucho contigo a nivel científico y personal.

Gracias Lourdes por todo el trabajo con los pacientes con lentes intraoculares. Bien se que el trabajo presentado en esta tesis no hubiese sido posible sin tu ayuda.

Gracias Sergio (Ortiz) por implementar el sistema de fijación en el montaje para la detección de las imágenes de Purkinje. Gracias por tu apoyo durante estos meses en los que he estado escribiendo la tesis, sin tu ayuda hoy no estaría presentando esta tesis.

Gracias Sergio (Barbero), porque contigo di mis primeros pasos en la investigación, por enseñarme a manejar Zemax, por tus sugerencias en los artículos y por haberme transmitido tu ilusión por la investigación.

Gracias Carlos, todo tu trabajo en la programación para el trazado de rayos ha sido de gran ayuda para la programación del control del sistema de imágenes de Purkinje, gracias también por esos comics tan didácticos y por esas páginas webs tan interesantes.

Gracias Jose por tus sugerencias en las reuniones de laboratorio, por todo lo que he aprendido de ti en tus charlas y por esas conversaciones tan interesantes durante las comidas.

Gracias Helena, por tu acogida cuando llegué a Madrid, por enseñarme a manejarme en el laboratorio, a recibir pedidos y a encontrar tornillos de métricas difíciles que sólo tú conocías.

Gracias Dani, tu modo de trabajar tan detallista ha sido un ejemplo que he ntentado seguir en el trabajo de la tesis.

Gracias Lucie por tus sugerencias y tu trabajo con la Pentacam, por tu alegría y optimismo, por tu continua sonrisa y porque nunca abandonaste la "dificil" tarea de avisarme para tomar un café a media mañana.

Gracias Alberto por todo el trabajo de comparación de medidas de inclinación y descentramiento con la Pentacam y las imágenes de Purkinje y por todos los comentarios y sugerencias con los que me has ayudado a mejorar.

Gracias Alfonso, compañero de despacho durante los últimos meses de tesis, por haberme escuchado con tanta paciencia y también por tu ayuda en los programas con la Pentacam.

Gracias Enrique, porque siempre has sabido sacarme una sonrisa cuando he coincidido contigo. A ti también te agradezco tu paciencia y tu comprensión en estos últimos meses de tesis.

Bueno, Carlos, tú también has sido mi compañero de despacho en estos últimos meses. Gracias por haberme ayudado a concentrarme cuando comencé a escribir la tesis, por tu ayuda cuando tuve que enviar el borrador y por tu disponibilidad continua para ayudar siempre que hiciese falta.

Gracias también a ti, Gemma, aunque coincidimos sólo durante unos meses, fuiste de gran ayuda con toda la organización del laboratorio.

Gracias Ester Moreno por tu trabajo con el trazado de rayos y por tus publicaciones que tanto me han ayudado para escribir la introducción.

Rafa, ¿Creías que me iba a olvidar de ti? Vamos, vamos. Imposible que olvide tus clases de música, las conversaciones sobre filosofía y, por supuesto, imposible olvidar tu actitud tolerante y tu mente abierta para aceptar las diferencias.

Tampoco me olvido de ti Sylvain, es imposible que te recuerde sin que deje de sonreir. Por tus ocurrencias, por las excursiones a la montaña y por tu valentía para ser tú mismo.

Ainara, Sara, Noemí…gracias porque siempre habéis estado ahí y porque me habéis animado en momentos difíciles.

Eloy, Encarnita y Chary, ¿Cómo podré agradecer toda vuestra dedicación con el papeleo con el que siempre me pierdo y me despisto? Bien se que me habéis librado de mas de una.

Encarnita y Sole, muchas gracias por haberme dado la primera sonrisa de la mañana. Mº Paz, muchas gracias por haberme dado la última sonrisa de la tarde al salir de trabajar. Esa sonrisa, aún en vuestros momentos difíciles, ha sido un acicate para afrontar la tarea diaria.

Benito, tú has sido la "pieza" clave de esta tesis, sin tu inestimable ayuda no hubiese podido montar el sistema de imágenes de Purkinje. Gracias porque siempre he tenido las piezas del montaje preparadas cuando las he necesitado a pesar de todo el trabajo que tenías.

Mº Luisa, gracias por haberme facilitado el trabajo manteniendo con tanto cariño el despacho siempre tan limpio y ordenado.

Paquita, gracias porque siempre has estado pendiente de todo el mundo y por tu entereza en tus malos momentos.

Gracias Armando, siempre he podido contar contigo ante cualquier problema con el ordenador, gracias por haberme introducido en el mundo de la fotografía y por todas las conversaciones contigo en las que he aprendido tanto.

Gracias a tanta gente con la que he coincidido estos años y que de un modo u otro me habéis ayudado: Amelia , Oscar, Raúl, Ana, Laura, Víctor, Vincenzo, Hector, Dani, David, Jeremie, Andrés, Jesús, Marcial, Jan, José Olivares, Soto…

Durante las estancias en otros laboratorios he tenido la oportunidad de coincidir con gente de gran talla científica y humana, como Rob van der Heijde, Michiel Dubbelman (Vrije University Medical Center, Ámsterdam) y Adrian Glasser (Optometry School, Houston Tx). Estas estancias han significado mucho para mí para madurar científica y humanamente, también gracias a la ayuda de los que fueron mis compañeros de laboratorio durante esas estancias: Nanouk, Erik, Arni, Mark Wendt…

Saro, gracias a ti me embarqué en este proyecto en el que he madurado y aprendido tantas cosas. Gracias por tu continuo interés, porque siempre me has animado y porque siempre has estado cerca cuando te he necesitado.

Sara, me has ayudado mucho, ha sido una gran suerte haber coincidido contigo en esta etapa de "mi viaje". He aprendido mucho contigo y no se expresar mi agradecimiento por tu ayuda en algunos momentos verdaderamente difíciles por los que he pasado.

Bueno, y jamás de los jamases podría olvidar yo a mis amigos del grupo de montaña: Ana, Juan y Mº José. ¡Cuánto me habéis ayudado! Me habéis sabido dar buenos consejos, me habéis apoyado, y habéis creído en mí más que yo misma.

Por último, pero no por eso sois los menos importantes, gracias a todos los compañeros del CIDA, especialmente a Yolanda, Charo y Mónica, porque me habéis animado tanto durante la escritura de la tesis.

Y por último, muchas gracias a Beethoveen y a la banda U2… ellos saben por qué.

Agradecimientos a las fuentes de financiación:

Ministerio de Educacion y Ciencia
BFM2002-02638. Role of ocular aberrations in the development and compensation of refractive errors. PI: Susana Marcos. 2002-2005

FIS2005-04382 "Optical Properties of the anterior segment of the eye. Application to the correction of refractive errors and presbyopia. PI: Susana Marcos. 2005-2008

Comunidad Autonoma de Madrid
CAM08.7/004.1/2003 "Optical and visual quality in patients after cataract surgery: study of new aspheric and multifocal IOL designs. PI. Susana Marcos 2003-2004

GR/SAL/0387/2004 "Development and application of new technologies to the evaluation of cataract surgery. PI. Susana Marcos. 2005

Contratos de investigación de Alcon Research Laboratories, Fort Worth, Tx

Y la beca FPI del MEC Referencia de la ayuda: BES-2003-1901
Referencia del proyecto: BFM2002-02638

También agradezco el haber podido disponer de las instalaciones y recursos del Instituto de Optica (Consejo Superior de Investigaciones Científicas) y de las instalaciones de la Fundación Jiménez-Díaz donde se hicieron todas las cirugías de cataratas que forman parte del estudio de esta tesis, al cirujano Ignacio Jiménez-Alfaro y a los pacientes que aceptaron participar en los estudios.

TABLE OF CONTENTS

Introduction 1

1. MOTIVATION OF THE STUDY

The optical system of the eye is formed by the cornea and the crystalline lens, which project the images of the outside world on the retina. A scheme of the eye is depicted in Figure 1.1. In the last few years there has been an increased interest in the assessment of the optical quality of the normal eye (Castejon-Mochon, Lopez-Gil, Benito & Artal, 2002, Marcos, Burns, Prieto, Navarro & Baraibar, 2001), as well as the changes of optical quality with certain conditions such as aging (Mclellan, Marcos & Burns, 2001), accommodation (He, Burns & Marcos, 2000) and refractive errors (Llorente, Barbero, Cano, Dorronsoro & Marcos, 2004), and particularly how the optical aberrations are modified after certain interventions such as refractive surgery (Moreno-Barriuso, Merayo-Lloves, Marcos, Navarro, Llorente & Barbero, 2001), intraocular surgery (Barbero, Marcos & Jimenez-Alfaro, 2003) and contact lenses (Dorronsoro, Barbero, Llorente & Marcos, 2003). While there is a good description of the ocular aberrations of the eye, driven by the development of reliable aberrometers (Marcos, Burns, Moreno-Barriuso & Navarro, 1999), the sources of the aberrations in individual eyes and their changes associated with different conditions are not well understood. The anterior cornea is the most powerful refractive surface in the eye (due in part to the change in the refractive index between air and corneal surface). Measurements of the corneal elevation maps allow estimation of the contribution of anterior corneal aberrations to the ocular aberrations. However, the contribution of the crystalline lens to the overall optical quality of the eye is not well understood. First, the crystalline lens is not that easily accessible in vivo as the corneal surface, as it needs to be imaged through different ocular surfaces which produce optical distortions. Second, the geometry of the lens changes dynamically with accommodation (Dubbelman, van der Heijde & Weeber, 2005, Fincham, 1925, Kirschkamp, Dunne & Barry, 2004, Koretz, Cook & Kaufman, 2002, Koretz, Handelman & Brown, 1984, Strenk, Strenk, Semmlow & DeMarco, 2004). Third, the index of refraction of the lens is not homogenous, as it shows a gradient index distribution (Atchison & Smith, 1995, Dick, 1994, Dubbelman & van der Heijde, 2001, Garner & Smith, 1997, Mutti, Zadnik, Fusaro, Friedman, Sholtz & Adams, 1998, Pierscionek, 1997, Smith & Atchison, 2001). And forth, the crystalline lens grows throughout life and its shape and structure experiences important changes with age (Brown, 1974, Dubbelman & van der Heijde, 2001, Dubbelman, van der Heijde & Weeber, 2001, Garner, Ooi & Smith, 1998, Glasser & Campbell, 1998,

Hemenger, Garner & Ooi, 1995, Kasthurirangan, Markwell, Atchison, Pope & Smith, 2007, Koretz, Cook & Kaufman, 1997, Koretz, Cook & Kaufman, 2001, Smith, Atchison & Pierscionek, 1992, Strenk et al., 2004).

Apart from the optical properties of the "isolated" optical components, the interactions between cornea and crystalline lens, and their relative positioning, are critical to understand the overall quality in the eye. Measurements of total and corneal aberrations have demonstrated that in the normal young eye the aberrations of the crystalline lens partially balance those of the cornea. A better understanding of the structural properties of the crystalline lens will help to better understand how this is achieved. While there have been attempts to relate the presence of asymmetric aberrations such as coma to the tilt of the optical axis (Marcos et al., 2001), the lack of precise measurements of geometry and positioning (tilt and decentration) of the crystalline lens in the past have prevented full understanding the contributions of internal optics to the ocular aberrations. In particular, there is an open debate on the active (Kelly, Mihashi & Howland, 2004) or passive (Artal, Benito & Tabenero, 2006) nature of this compensation mechanism on which accurate measurements of individual structural properties in eyes will shed light.

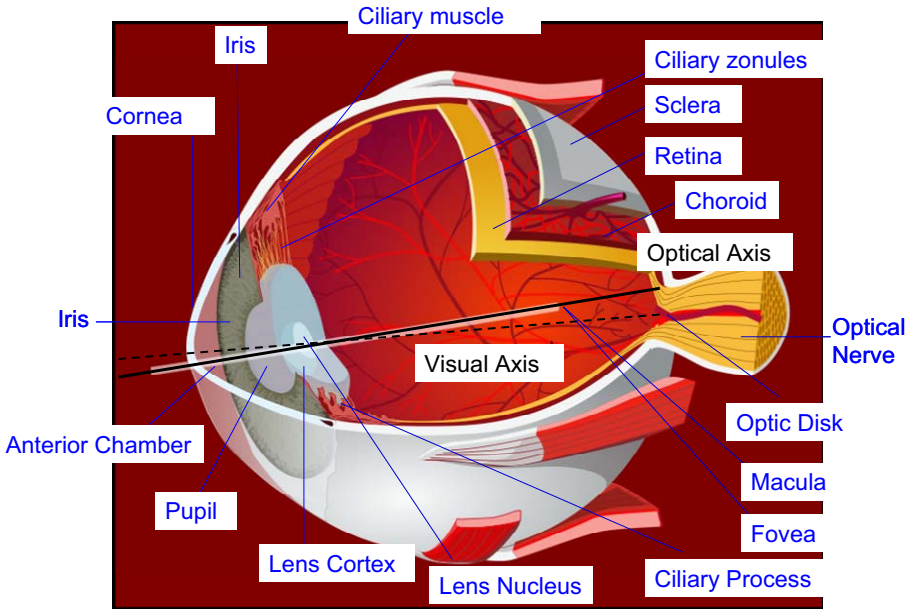

Figure 1.1. Scheme of the human eye's anatomy.

One of the most extraordinary capabilities of the human eye is the ability to focus near and far objects. This accommodation capacity is progressively lost with age affecting performance in near tasks (presbyopia). While this condition affects 100% of the population beyond 45 years, the mechanism that leads to presbyopia is not well understood (Glasser & Campbell, 1999, Glasser, Croft & Kaufman, 2001, Koretz et al., 1997, Lewis, 1983, Spierer & Shalev, 2003, Strenk, Strenk & Koretz, 2005). While it is well known that the crystalline lens changes its shape to accommodate, the data regarding the change of the lens shape with accommodation in literature are controversial, with discrepancies arising from differences between in vivo and in vitro accommodative states and potentially the use of imaging techniques not fully correcting for distortion. An accurate knowledge of the changes in shape with accommodation is critical to assess the relative contribution of surface power and gradient index distribution (not covered in this thesis) to the accommodative amplitude, and to understanding the optical aberrations of the crystalline lens. In addition, the change in tilt and decentration of the crystalline lens with accommodation has never been addressed in depth. To our knowledge there is only one study of changes in tilt and decentration of the crystalline lens with accommodation using the Purkinje imaging technique (Kirschkamp et al., 2004). Fully characterizing the accommodative mechanism is essential to understanding the progression of presbyopia, and to aid in strategies to correct presbyopia, i.e., for the design of accommodative intraocular lenses (Küchle, Seitz, Langenbucher & et al, 2004, Stachs, Schneider, Stave & Guthoff, 2005), lens refilling (Koopmans, Terwee, Glasser, Wendt, Vilupuru, van Kooten & et al, 2006, Norrby, Koopmans & Terwee, 2006), chemical laser treatment of the lens (Krueger, Seiler, Gruchman, Mrochen & Berlin, 2001, Myers & Krueger, 1998), and other surgical procedures (Qazi, Pepose & Shuster, 2002).

When the crystalline lens becomes opaque with aging, it is generally surgically removed and replaced by an intraocular lens. Cataract surgery has benefited from technical advances that allow smaller corneal incisions (leading to less incision-induced corneal aberrations) and cotinuous improvements of intraocular lens design (Marcos et al., 2005). However, customization of cataract surgery will be ultimately limited by the IOL design and IOL positioning. The study of the contributions to optical quality of corneal aberrations, intraocular lens design, intraocular lens tilt and decentration, particularly in combination with measurements of ocular aberrations, are very valuable to evaluate the actual performance of a given IOL design and to guide new designs.

In brief, this thesis addresses novel and validated in vivo measurements on eyes with intact crystalline lenses and pseudophakic eyes with intraocular lenses, which will contribute to the understanding of the image forming capabilities of the eye (particularly the lens), the optical changes in the crystalline lens with accommodation and optical performance after cataract surgery.

2. THE CRYSTALLINE LENS AND THE ACCOMMODATIVE SYSTEM

2.1 Human and primate crystalline lens

2.1.1. Human crystalline lens

The crystalline lens is a unique transparent, biconvex intraocular structure that lies in the anterior segment of the eye, suspended radially at its equator by the zonular fibers and ciliary body between the iris and the vitreous body. Enclosed in an elastic capsule, the lens has no innervation or blood supply after fetal development. Its nourishment must be obtained from the surrounding aqueous and vitreous that is thought to provide support and stabilization for the posterior surface of the lens, and the same media must also remove metabolic waste products. The aqueous humor continuously flows from the ciliary body to the anterior chamber, bathing the anterior surface of the lens. The lateral border of the lens is the equator, formed from the joining of the anterior and posterior capsules, and is the site of insertion of the zonules.

The anterior and posterior lens surface curvatures are usually described as aspherical in shape. Some authors report a steeper curvature located centrally near the optical axis with the surfaces becoming progressively flatter toward the midperiphery and then steeper toward the equatorial edges (Dubbelman & van der Heijde, 2001). This aspherical anterior and posterior lens surface tends to minimize spherical aberration. The magnitude of lens curvature, and particularly the change of curvature with accommodation and aging has been a matter of long debate in the literature. These measurements will be addressed in Chapters 4 and 6. The most recent measurements of lens asphericity in vivo by Dubbelman (Dubbelman et al., 2005) show large intersubject variability.

The crystalline lens is composed of multiple layers of long, fiber cells that originate from the equator and stretch toward the poles of the lens. At the point where the cells meet, they form suture patterns. In the human, the embryonic lens has “Y” sutures, but

as it ages, the suture patterns in the new layers become increasingly more complex, resulting in a lens whose suture patterns have a starlike appearance (Koretz, Cook & Kuszak, 1994).

The lens consists of three components: capsule, epithelium, and lens substance. The lens substance is a product of the continuous growth of the epithelium and consists of the cortex and nucleus. The transition between the cortex and nucleus is gradual. There is no a concise line of demarcation when observed in histological sections. The lines of demarcation are often better visualized by slit-lamp microscopy.

The lens capsule is a basement membrane formed of the lens epithelium anteriorly and by superficial fibers posteriorly. With light microscopy, the lens capsule appears as a structureless, elastic membrane that completely surrounds the lens. The capsule functions as a metabolic barrier and may play a role in lens shaping during accommodation. The lens capsule is of variable thickness being much thicker in the anterior than the posterior capsule.

The lens epithelium is confined to the anterior surface and the equatorial lens bow. It consists of a single row of cuboidal-cylindrical cells, which can biologically be divided into two different zones with two different types of cells: *A-cells*, located in the central zone of the anterior lens capsule, with minimal mitotic activity and rarely migrating; *E-cells*, located in the second zone as a continuation of the anterior lens epithelial cells around the equator and responsible for the continuous formation of all cortical fibers, in early life, nuclear fibers, and therefore accounting for the continuous growth in size and weight of the lens throughout life. During lens enlargement, the location of older fibers becomes relatively more central as new fibers are formed at the periphery.

The lens cortex and nucleus consists of the lens fibers themselves. On cross-section, these cells are hexagonal and bound together by ground substance. After formation, the cellular nuclei of the lens fibers are present only temporarily. Subsequently, they disappear, leaving the lens center devoid of cell nuclei. The most peripherally located fibers, which underlie the lens capsule, form the lens cortex once the nucleus is completed. The designation of cortex is actually an arbitrary term signifying a peripheral location within the lens, rather than specific fibers.

Figure 1.2 shows images of the crystalline lens in vitro, in a postmortem phakic human eye (A), and the anatomical relationship of the human crystalline lens, ciliary body, and zonules, viewed at higher magnification (B), from a study by Pandey (Pandey, Wilson & Trivedi, 2001). The human ciliary body extends from the base of the

iris to become continuous with the choroid at the ora serrata. Histologically, the human ciliary body consists of seven layers, one of which is the ciliary muscle. In accommodation, contraction of the ciliary muscle releases zonular tension on the crystalline lens, which allows the lens to assume a more spherical shape, thereby increasing the power of the eye.

The ciliary zonules consist essentially of a series of fibers passing from the ciliary body to the lens. They hold the lens in position and enable the ciliary muscle to act on the lens during accommodation. The lens and zonules form a diaphragm, which divide the eye into a smaller anterior portion and a larger posterior portion. The zonule forms a ring, which is roughly triangular in a meridional section. The base of the triangle is concave and faces the equatorial edge of the lens.

Figure 1.2. Parasagittal section of a phakic human eye obtained postmortem. Note the crystalline lens suspended by the ciliary zonules. **A.** Crystalline lens and zonules. **B.** Higher magnification of crystalline lens, ciliary body, and zonules from another case. **C.** Higher magnification of ciliary body and zonules from another case, posterior view. Image adapted from Pandey (Glasser, Wendt & Ostrin, 2006, Pandey, Thakur, Werner, Wilson, Werner, Izak & Apple, 2002)

2.1.2.Primate Crystalline lens

Several studies have shown the similarity of the ocular anatomy and accommodative mechanism of the rhesus monkey and human. For example, the study by Kaufman on 108 monkey eyes after total iridectomy show that this is an appropriate model of human accommodation and presbyopia (Kaufman & Lütjen-Drecoll, 1975). Figure 1.3 shows images of isolated crystalline lenses obtained by shadowphotography (Augusteyn et al., 2006) on human eyes and rhesus monkeys, where typical dimensions can be compared. To make ages comparable in the human and rhesus monkey ages the following expression must be taken into account: human_years = 1.3846*monkey_years + 10.385 (Vilupuru & Glasser, 2002).

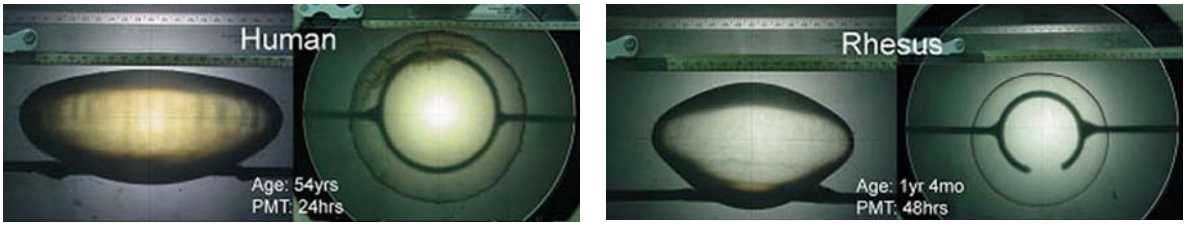

Figure 1. 3. Coronal and sagittal shadow photographs of a 54 years old human eye and a 1 and four months year old Rhesus Monkey. The lenses are shown with their anterior sides up and are magnified 20x relative to the ruler in the photograph. Images obtained by Augusteyn (Augusteyn, Rosen, Borja, Ziebarth & Parel, 2006).

Using a distortion-corrected Scheimpflug camera, LaPuerta & Schein (Lapuerta & Schein, 1995) measured the intraocular distances, and curvatures of the anterior and posterior cornea and lens of eight eyes of four monkey eyes (Macaca fascicularis). Table 1 compares biometric values of a human schematic eye (Le Grand full schematic eye (Le Grand & El Hage, 1980) Table 1.a) with the monkey schematic eye developed by Lapuerta and Schein (Table 1.b).

Table 1.a. Le Grand schematic human eye.

Medium		Refractive Index n	Radius of curvature R (mm)	Intraocular distances d (mm)
Air		1.0000		
Cornea	Anterior Cornea	1.3771	7.80	0.55
	Posterior Cornea		6.50	
Aqueous		1.3374		3.05
Lens	Anterior Lens	1.4200	10.20	4.00
	Posterior Lens		-6.00	
Vitreous		1.3360		16.59

Table 1.b. La Puerta schematic model eye.

Medium		n	R (mm)	d (mm)
Air		1.0000		
Cornea	Anterior Cornea	1.3771	5.75	0.55
	Posterior Cornea		5.12	
Aqueous		1.336		3.05
Lens	Anterior Lens	1.4200	10.34	4.00
	Posterior Lens		-6.390	
Vitreous		1.3360		10.32

There are several studies of the similarity of the accommodative mechanism (Crawford, Kaufman & Bito, 1990, Glasser & Kaufman, 1999, McWhae & Reimer, 2000, Vilupuru & Glasser, 2002, Vilupuru & Glasser, 2003) and age dependent loss of accommodative amplitude in rhesus monkeys (Koretz, Bertasso, Neider & Kaufman PL, 1988, Koretz, Bertasso, Neider, True-Galbelt & Kaufman, 1987a, Koretz, Neider, Kaufman, Bertasso, DeRousseau & Bito, 1987c, Neider, Crawford, Kaufman & Bito, 1990). According to those studies, rhesus monkeys and humans exhibit a similar accommodative mechanism and lens growth throughout life and develop presbyopia with a similar relative age course, although differences between monkeys and human accommodation can be found in the extent to which presbyopia affects the various intraocular accommodative structures (Croft, Glasser & Kaufman, 2001).

2.2 The Accommodative Mechanism

Accommodation is an increase in the dioptric power of the eye that enables the image of near objects to be focused on the retina. The act of focusing the eye on objects at different distances includes far-to-near (accommodation) and near-to-far (disaccommodation) focus.

2.2.1 Different accommodative mechanism theories

According to the classic Helmholtz mechanism of accommodation theory (Von Helmholtz, 1855), during distant vision (when the lens is unaccommodated, Figure 1.4.A) the ciliary muscle is relaxed, the zonular fibers are under tension and the lens is pulled flat. During accommodation (Figure 1.4.B), the ciliary muscle contracts, releasing tension on the zonular fibers at the lens equator, allowing the lens equatorial diameter to decrease, the lens thickness to increase, and the lens surfaces to become more steeply curved.

Schachar (Schachar, Cudmore & Black, 1993) based on Thscherning's theory (Tscherning, 1904) postulated that with accommodation, ciliary muscle contraction causes a relaxation of the anterior and posterior zonular fibres, but an increased tension in the equatorial zonular fibres (Schachar, 1994), which cause the peripheral part of the lens to flatten, whereas the central part of the lens becomes more convex (increasing lens power). This theory erroneously relies on an increase of the equatorial lens diameter during accommodation, while it has been demonstrated that the equatorial diameter decreases with accommodation (Glasser et al., 2006) .

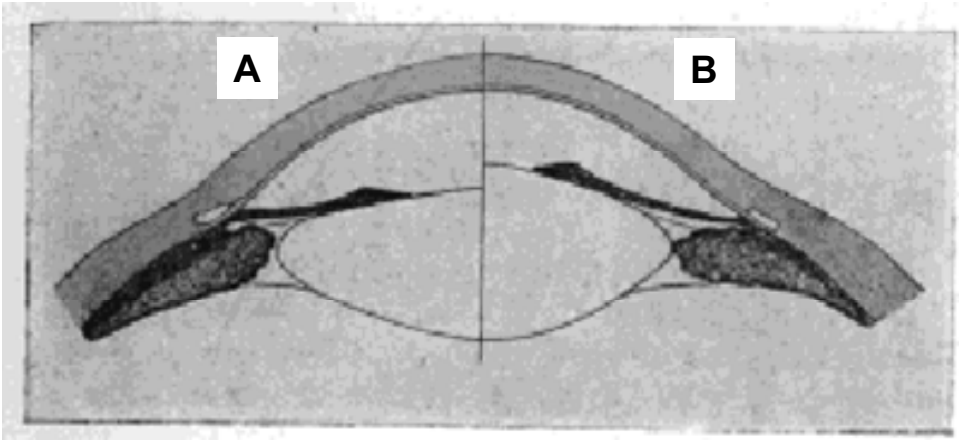

Figure 1.4. Helmholtz theory of accommodation. **A.** is a representation of the unaccommodated state of the lens, **B.** represents the accommodated state, where the ciliary muscle is contracted, so the tension of the zonular fibres is relaxed and the lens becomes more convex by virtue of its own elasticity (image adapted from http://www.iblindness.org/books/bates/ch3.html)

2.2.2 Biometric changes during accommodation

The study of biometric changes of the crystalline lens and ciliary body during dynamic accommodation is essential to understanding the mechanism of accommodation and age-related changes leading to presbyopia. The lenticular accommodative biometric data most widely available refer to axial changes in the anterior segment. Anterior movement of the anterior crystalline lens surface and an increase in lens thickness has been demonstrated in several studies, in both humans (Beers & van der Heijde, 1994a, Bolz, Prinz, Drexler & Findl, 2007, Dubbelman et al., 2005, Garner & Yap, 1997, Ostrin, Kasthurirangan, Win-Hall & Glasser, 2006, Zadnik, Mutti & Adams, 1992) and rhesus monkeys either drug stimulated (Koretz, Bertasso, Neider, True-Galbelt & Kaufman, 1987b) or centrally stimulated (Vilupuru & Glasser, 2005). Accommodative movement of the posterior lens surface has only recently become clear. Corrected Scheimpflug images show a posterior accommodative movement of the posterior lens surface (Dubbelman et al., 2005). Two recent studies in humans related measurements of anterior chamber depth, lens thickness and anterior segment length using A-scan ultrasonography or partial coherence interferometry with refraction measured simultaneously either in the same eye or in the contralateral eye (Bolz et al., 2007, Ostrin et al., 2006). These studies show an accommodative movement of the posterior lens surface. Similar results occur with centrally stimulated accommodation in rhesus monkeys (Vilupuru & Glasser, 2005). Changes in anterior and/or posterior lens curvature with accommodation in humans have been reported by several authors (Garner, 1983, Garner & Smith, 1997, Garner & Yap, 1997, Kirschkamp et al., 2004, Brown, 1973, Dubbelman et al., 2005, Koretz et al., 1987b, Koretz et al., 1984). The change in lens radii of curvature with accommodation will be discussed in depth in Chapter 4 and 6, and new data will be reported in this thesis, both in humans and iridectomized monkeys.

The use of iridectomized monkeys (Kaufman & Lütjen-Drecoll, 1975) has allowed measurements to be performed on lenticular regions generally not accessible with optical techniques in eyes with intact irides. For example, a decrease in lens equatorial diameter with increased accommodation (Glasser et al., 2006), as well as centripetal ciliary processes and lens edge movements have been demonstrated dynamically using slit-lamp goniovideography (Croft, Glasser, Heatley, McDonald, Ebbert, Nadkarni & Kaufman, 2006, Ostrin & Glasser, 2007). While axial changes in

lens position, and centripetal movements of the crystalline lens have been studied in detail, to our knowledge, only one human study has looked at possible changes in crystalline lens tilt and decentration (in the horizontal direction) for unaccommodated and accommodated eyes (Kirschkamp et al., 2004). The change in crystalline lens shape and alignment has implications for the accommodative mechanism and for accommodative optical performance. This thesis will present measurements of phakometry, tilt and decentration of the crystalline lens in the unaccommodated state (Chapters 2, 6, 9 and 10) and phakometry as function of accommodation (Chapter 5) in humans and phakometry and lens tilt and decentration as function of accommodation in rhesus monkeys (Chapter 7). Figures 1.5 shows biometric changes with accommodation in the human lens using Scheimpflug camera, and Figure 1.6 shows the tendencies in lens surface with accommodation obtained from Vilupuru and Glasser (Vilupuru & Glasser, 2003) and Glasser (Glasser et al., 2006) in rhesus monkeys.

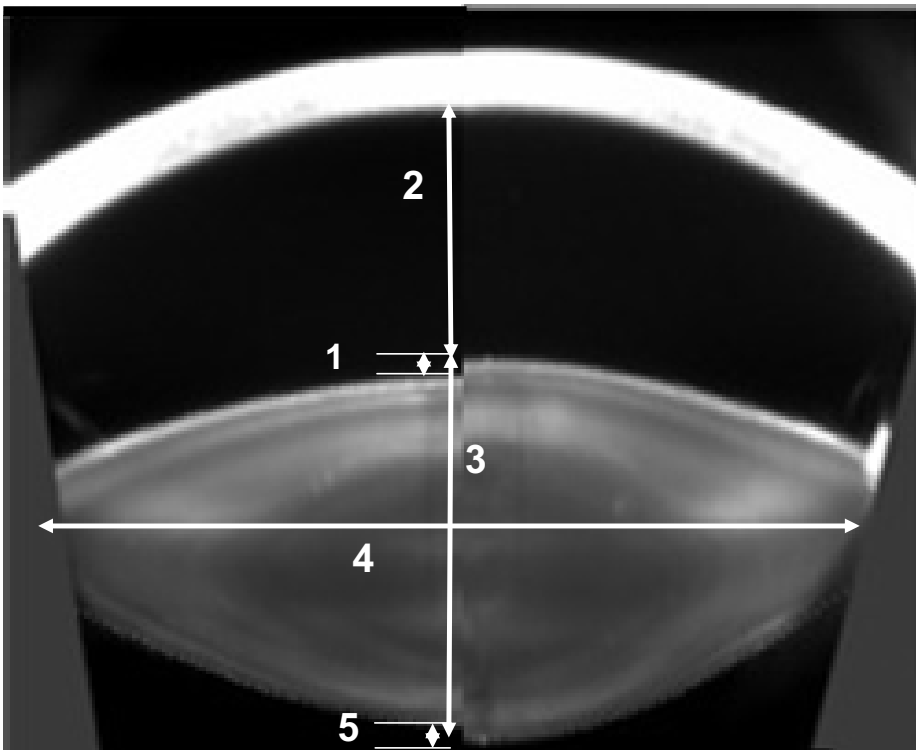

Figure 1.5. Illustration of the biometric changes with accommodation. The left half of the image corresponds to the unaccommodated state and the right half to the accommodated state. The changes indicated in the image include: 1. Forward movement of the anterior lens surface; 2. Decrease in anterior chamber depth. 3.Increase in lens thickness. 4. A. Decrease in lens equatorial diameter with increased accommodation and B. Centripetal ciliary processes (not indicated in the image).5. Accommodative backward movement of the posterior lens surface. Courtesy of Rob van der Heijde and Michiel Dubbelman.

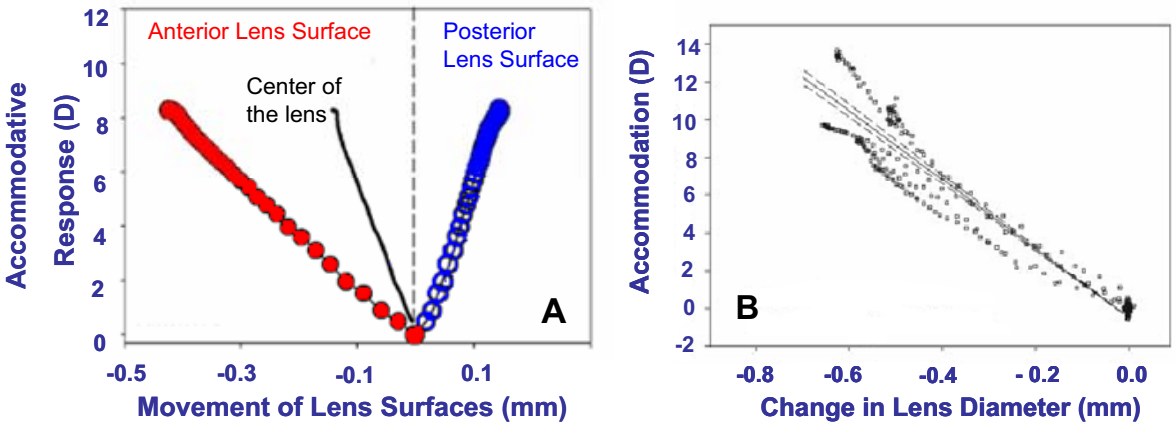

Figure 1.6. Crystalline lens biometric changes with accommodation. **A.** Represents the forward movement of the anterior lens and the backward movement of the posterior lens surface as the accommodative response increases. **B.** Represents the decrease in lens diameter with accommodation**.** The plots have been adapted from Vilupuru & Glasser (Vilupuru & Glasser, 2005).

2.3 The aging of the crystalline lens: presbyopia and cataracts

With increasing age, there are important optical and physical changes in the human crystalline lens. These changes are continuous through life, although their effects are more evident after the age of 40 years. The effect from which the eye losses its ability to accommodate affecting performance in near tasks is called presbyopia. The causes of presbyopia have been studied from physiological (Dubbelman et al., 2005, Glasser & Campbell, 1998, Glasser & Campbell, 1999, Kasthurirangan et al., 2007, Koretz et al., 2001, Koretz et al., 2002, Koretz et al., 1984, Koretz, Kaufman, Neider & Goeckner, 1989, Moffat, Atchison & Pope, 2002a, Strenk et al., 2004), anatomical (Croft et al., 2001, Glasser et al., 2001), biomechanical (Burd, Judge & Flavell, 1999, Hermans, Dubbelman, van der Heijde & Heethaar, 2006, Judge & Burd, 2002, Weeber & van der Heijde 2007), and biochemical approaches (McGinty & Truscott, 2006, Y Bron, Vrensen, Koretz, Maraini & Harding, 2000) although complete understanding is difficult due to the complexity of the process.

2.3.1 The aging lens

Several physical, biometric, optical and morphophysiological changes associated with aging of the human crystalline lens include (Agarwal, 2002, Croft et al., 2001, Glasser et al., 2001, Marcos, Barbero, McLellan & Burns, 2003):

Increased mass. Lens weight increases linearly from approximately 1100 mg at the end of the first year after birth to 200 mg at the age of 80 years, as has been shown from in vitro measurements of the excised lens (Smith, 1883, Willekens, Kappelhof & Vrensen, 1987).

Increased lens thickness. The crystalline lens thickness increases steadily with age after the age of 10 years (Zadnik, Mutti, Fusaro & Adams, 1995). Using in vivo Scheimpflug imaging, it has been shown that with age, the anterior lens surface moves toward the cornea, which results in a decrease of the anterior chamber depth of about 10 μm/year (Dubbelman & van der Heijde, 2001, Koretz et al., 1989) and increase in lens thickness at a rate about of 24 μm/year (Dubbelman et al., 2001) or 13 μm/year (Koretz et al., 1989), depending upon whether the distortion correction applied to the Scheimpflug images or not.

*Increased anterior and posterior surface curvatures***.** In vivo Scheimpflug measurements of unaccommodated eyes suggest that the lens anterior and posterior surface curvature increase with increasing age, although corrected Scheimpflug imaging (Dubbelman & van der Heijde, 2001) showed less extent in the increased lens curvatures that uncorrected ones (Brown, 1974, Koretz et al., 2001). These results have led to what has been described as the "lens paradox" (Koretz & Handelman, 1986b, Koretz & Handelman, 1988), since the curvature of the human eye lens increases (steepens) with age, yet most human eyes do not become more powerful as they get older (Moffat, Atchison & Pope, 2002b), changes in the index of refraction with age has been postulated.

Increasing lens curvatures should produce an optically more powerful lens and an eye focused for near vision. This thesis will provide validated measurements of anterior and posterior surface curvatures in human (Chaper 2, 6) and monkey eyes (Chapter 7).

Change in gradient refractive index. As an explanation of the "lens paradox", it has been postulated that the lens gradient refractive index changes with increasing age to compensate for the increased surface curvatures. Empirical studies using calculations from population data suggest that the refractive index gradient does change to become relatively flatter in the nucleus of older lenses and that this could give a decrease in power of approximately 2D which matches the increased power due to increased thickness and surface curvatures (Hemenger et al., 1995, Ooi & Grosvenor, 1995). Other empirical studies have not been able to measure age-related changes of the index of refraction (Glasser & Campbell, 1999, Pierscionek, 1997). However, recent

measurements (Moffat et al., 2002a) of the gradient refractive index of excised lenses using magnetic resonance microimaging provides evidence for a change in the refractive index distribution as a function of age, which offsets the changes in lens curvature.

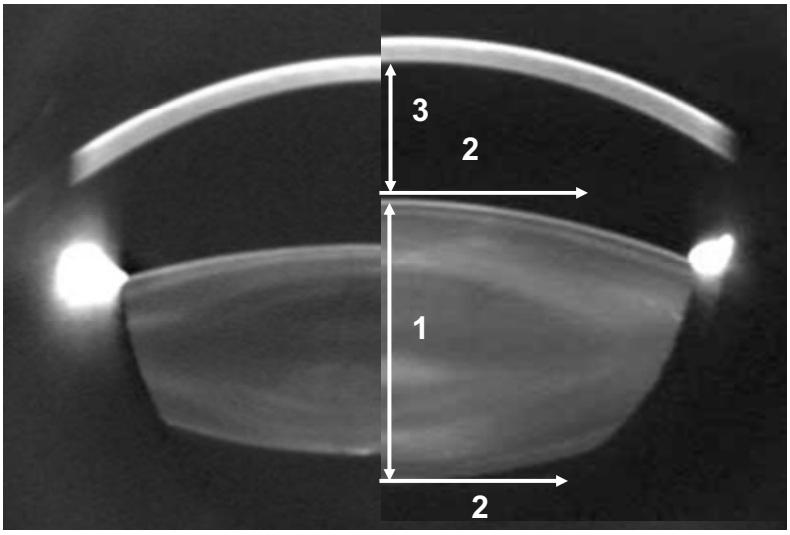

Figure 1.7. Illustration (using images from Scheimpflug photography) of the biometric changes with age in the crystalline lens. The left half of the image corresponds to a 16 years old crystalline lens, and right part of the image corresponds to a 54 years old crystalline lens. The changes indicated in the image include: 1 Increase lens thickness. Increase in refractive index. 2. Increase in anterior and posterior surfaces curvatures. 3. Anterior lens surface movement. Images provided by Dubbelman and van Der Heijde (Vrije University, Medical Center, Amsterdam).

Changes in the spherical aberration with age. Several methods have been used to measure the spherical aberration of the crystalline lens: 1) in vitro measurements of spherical aberration (along one meridian) of donor lenses, using a scanning laser apparatus (Sivak & Kreuzer, 1983), 2) neutralization of the cornea and measurement of the aberrations of the eye (Artal, Guirao, Berrio & Williams, 2001, Millodot & Sivak, 1979) and 3) measurement of total and anterior corneal aberrations and computation of the internal aberrations by subtraction of the two measurements (Artal & Guirao, 1998, El Hage & Berny, 1973). Glasser and Campbell (Glasser & Campbell, 1999) used the first method to assess the spherical aberration of the crystalline lens and found dramatic changes in the spherical aberration going from negative to positive with aging. Parallel beams were used in the experimental ray tracing rather than converging rays used in the other studies (for most distances, the cornea converges light from a target onto the lens), which prevents the measurements to be fully comparable. Artal (Artal, Berrio, Guirao &

Piers, 2002) used a subtraction method to estimate the aberrations of the crystalline lens as a function of age. They found an increase in the RMS of the aberrations of the crystalline lens with aging. Smith (Smith, Cox, Calver & Garner, 2001) measured the total and corneal spherical aberration and the crystalline lens by subtraction, in two group of young and old adults, and found lens spherical aberration to be less negative in the older group. The increase of spherical aberration with age found in the study by McLellan (Mclellan et al., 2001) is also suggestive of an absolute increase of the spherical aberration of the crystalline lens. A more detailed review of optical aberrations will be addressed in Section 4 of this Chapter.

Morphophysiological changes with age. Several morphophysiological factors have been associated with the aging of the human crystalline lens, ciliary body, and zonular apparatus: 1) The capsule becomes thicker and less extensible with increasing age (Krag, Olsen & Andreassen, 1997). 2) Lens hardening (nuclear sclerosis), traditionally associated with decreased water content of the lens. Although the extent to which lens hardening occurs is debated, evidence has unequivocally demonstrated increased hardness of the lens with age (Fisher, 1971, Fisher, 1977, Glasser & Campbell, 1999).3) Aging of the ciliary muscle and zonules (Strenk, Semmlow & Strenk, 1999, Tamm, Tamm & Rohe, 1992). The zonular attachments are narrow, especially in the first two decades of life. The zonule-free zone of the anterior capsule reduces from 8 mm at age 20 years to 6.5 mm (or even as low as 5.5 mm) at about 80 years of age.

Figure 1.7 shows the changes with age in human crystalline lenses. The left side represents the young crystalline lens of a 16 years old woman, and the right side represents the eldest crystalline lens of her 54 years old mother. Figure 1.8 shows the tendencies with age for the anterior and posterior lens radius of curvature and anterior and posterior lens positions.

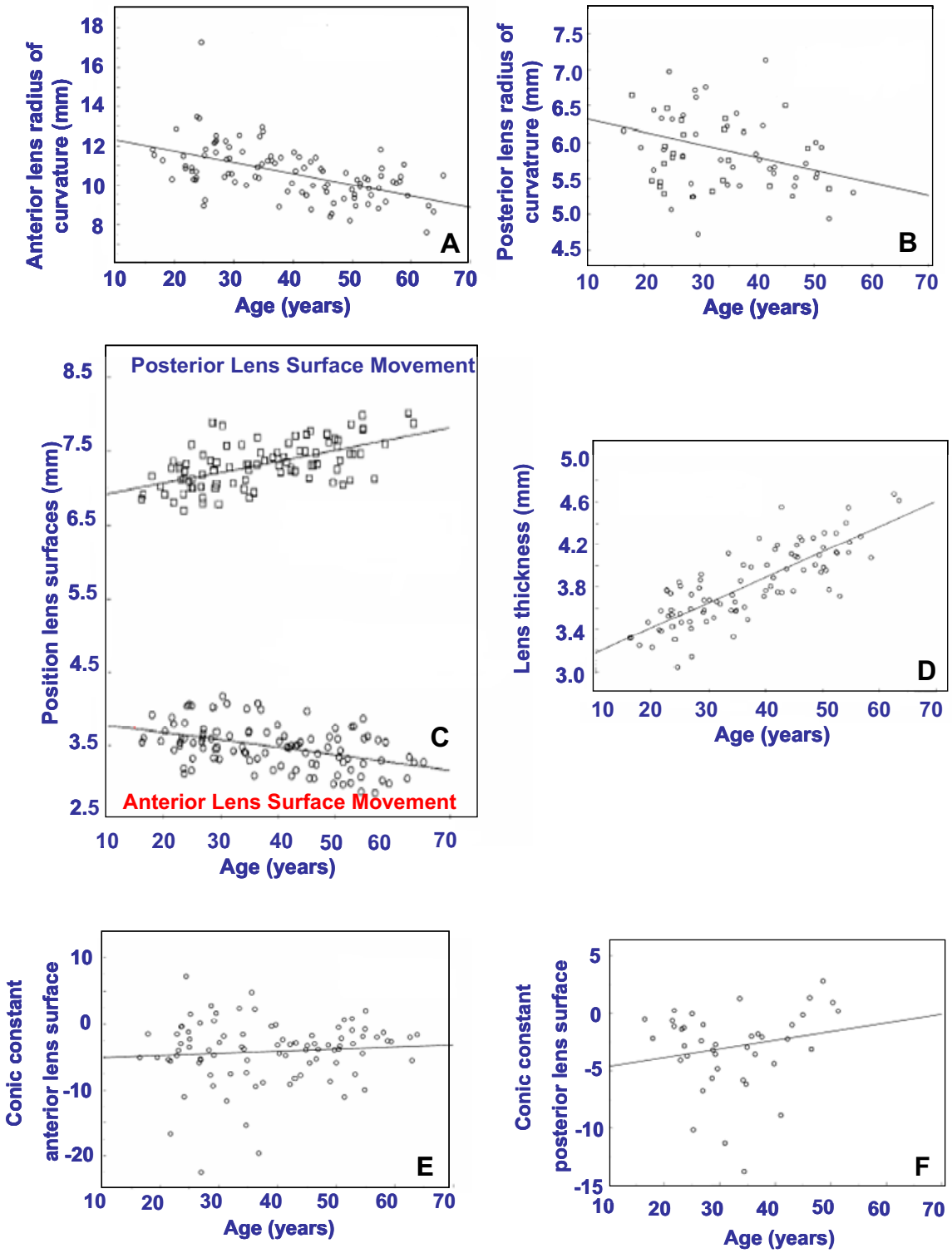

Figure 1.8. Crystalline lens biometric changes changes with age. **A.** and **B.** represent the changes in anterior and posterior lens radius of curvature with accommodation. **C.** represents the forward and backward movement of the anterior and posterior lens surfaces with accommodation. **D.** reflects the increase in lens thickness with accommodation. **E.** and **F.** plot the changes in anterior and posterior lens asphericity. Plots have been adapted from Dubbelman & van der Heijde (Dubbelman & van der Heijde, 2001).

3. IMAGING TECHNIQUES OF THE ANTERIOR SEGMENT OF THE EYE: AN OVERVIEW

The biometry and structural properties of the anterior segment of the eye (intraocular distances and shapes of the ocular components) can be assessed by various techniques. In this thesis we made use of several techniques to measure ocular biometry and structural properties of the cornea and crystalline lens, and implemented techniques for phakometry and measurement of lens misalignment. In this section we revise briefly the different techniques available, with a focus on a historical perspective. The techniques implemented in this thesis will be described in more detail in Chapters 2 and 3.

3.1. Techniques based on specular reflections from the ocular components.

3.1.1. Corneal videokeratoscopy

Corneal videokeratoscopy has been extensively used to obtain information of the shape of the anterior cornea (Campbell, 1997, Reynolds, 1980, Sicam & van der Heijde, 2006). The first corneal topograph can be dated to 1880, when the Portuguese ophthalmologist Antonio Placido viewed a painted disk (Placido's disk) of alternating black and white rings reflected in the cornea. The rings showed as contour lines projected on the corneal epithelium. In 1896, Allvar Gullstrand incorporated the disk in his ophthalmoscope, examining photographs of the cornea via a microscope and was able to manually calculate the curvature by means of a numerical algorithm. Gullstrand recognized the potential of the technique and commented it could "give a resultant accuracy that previously could not be obtained in any other way" (Gullstrand, 1909). The flat field of Placido's disk reduced the accuracy close to the corneal periphery and in the 1950s the Wesley-Jessen company made use of a curved bowl to reduce the field defects. The curvature of the cornea could be determined from comparison of photographs of the rings against standardized images.

In the 1980's, photographs of the projected images became hand-digitized and then analysed by computer. Automation of the process soon followed with the image captured by a digital camera and passed directly to a computer (Busin, Wilmanns & Spitznas, 1989). In the 1990s, systems became commercially available from a number of suppliers. In the corneal topographer used in this thesis (Humphrey-Zeiss MasterVue Atlas Model 990) the anterior corneal elevation was obtained using a Placido disk videokeratoscope which uses an arc step reconstruction algorithm. This system uses the

tear film as a convex mirror to view the first Purkinje image. The reflected image of the placido rings is captured on video camera and digitized. The computer analyses the position of each of the 15-38 circular mires along 256-360 semi-meridians, theoretically providing about 6,000 to 11,000 data points. Algorithms then compute the curvature at each point. The accuracy of measurements is about 0.15 D in the central zone of a normal cornea, but is commonly less in other situations due to the assumptions and approximations made by the algorithms. Corneal elevation maps are used in this thesis to generate computer eye models (Chapter 8), to compute corneal aberrations (Chapter 8 and 9). An extensive analysis of the accuracy of this corneal topography system and corneal aberrations estimation had been already performed in the Visual Optics and Biophotonics Lab at the Instituto de Optica, CSIC (Barbero, 2003, Barbero, Marcos, Merayo-Lloves & Moreno-Barriuso, 2002a, Barbero et al., 2002b).

3.1.2. Keratometry

A simpler method to obtain the anterior corneal radius of curvature is keratometry. A keratometer uses the first Purkinje image, PI, that is a reflection of a light source from the anterior cornea. The relationship between object size (O), generally multiple LED sources separated by a fixed distance; image size (PI), generally available on a camera; the distance between the reflective surface and the object (d), and the radius of curvature of the reflective surface (R) is given by the formula: $R = 2dPI/O$**.** In keratometry two meridians are measured, the steepest and the flattest. These measurements provide the anterior corneal radius of curvature, focusing power (assuming a particular refractive index for the cornea) and the amount of corneal astigmatism.

In this thesis, a keratometer to measure the apical corneal radius of curvature, was implemented to process phakometry data in a Rhesus Monkey model (Chapter 7).

3.1.3. Purkinje imaging phakometry

Purkinje images PIII and PIV are formed by reflections in the anterior and posterior crystalline surfaces and can be used to estimate the radii of curvature of the crystalline lens.

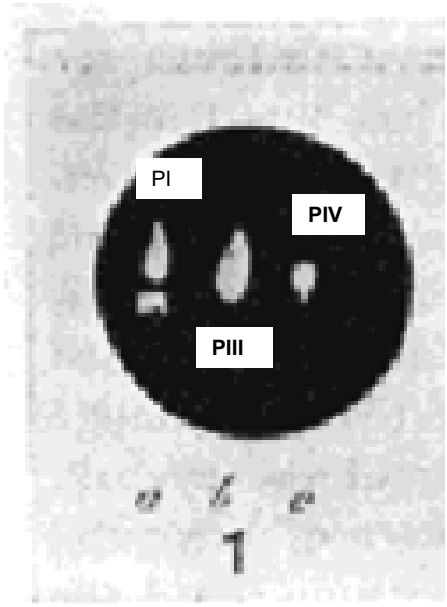

Figure 1.9. Original Purkinje images obtained by Purkinje. These are formed by reflections of a candle light by the different ocular surfaces. First Purkinje image comes from the anterior cornea, the third Purkinje image comes from the anterior lens surface and fourth Purkinje image comes from reflection of the posterior lens surface.

Since their description by Purkinje in 1832 (Figure 1.9) Purkinje images have been widely used to obtain the power of the crystalline lens, or the change of crystalline lens radii with accommodation. Several algorithms have been proposed to obtain anterior and posterior crystalline lens radii of curvature from Purkinje images. Smith and Garner (Smith & Garner, 1996) developed the so-called Equivalent Theorem Mirror method, based on the replacement of the different ocular surfaces by a single mirror. Garner (Garner, 1997) proposed the alternative recursive method called the merit function to obtain radii of curvature of the lens surfaces. This method was implemented experimentally by Barry and Dunne (Barry, Dunne & Kirschkamp, 2001) with physical model eyes and has been used to study the change of equivalent and gradient refractive index of the crystalline lens with accommodation (Garner & Smith, 1997), the changes in ocular dimensions and refraction with accommodation (Garner & Yap, 1997), and the refractive index of the crystalline lens in young and aged eyes (Garner et al., 1998). In this thesis we have developed a Purkinje-imaging based method to measure phakometry and tilt and decentration of the crystalline lens or intraocular lenses. A detailed description can be found in Chapter 2, and applications of it are given in Chapters 5, 6, 7, 9 and 10.

3.2. Ultrasound-based techniques

A widespread technique to measure intraocular distances (most commonly axial length, but also corneal thickness, anterior chamber depth and lens thickness) is ultrasound biometry (A-scan). The technique has also been developed to produce 3-D images of the anterior segment of the eye (ultrasound biomicroscopy). These are contact techniques, which are routinely performed under topic anesthesia.

3.2.1. A-scan Biometry

A-scan ultrasound biometry (Mundt & Hughes, 1956) relies on the generation of extremely high frequency sound waves that penetrate the eye and give a measurement of distances between the probe and specific structures. The sound wave is produced by a probe vibrating at a frequency of 10 MHz. The A-scan biometer pulses an electrical current to the tip of its probe, inducing a crystal to vibrate and emit the sound beam. The parallel sound beam travels from the point of contact (anterior surface of the cornea) through the eye. Several microseconds later, the A-scan pulse stops in order to detect echoes received from the reflection of the sound beam. These echoes are then converted to characteristic spikes and visualized on the biometer's display system. An echo bounces back to the probe tip whenever the beam encounters a media interface with different densities.

More recently, A-scan ultrasonography has been adapted to perform biometric changes dynamically. The so-called Continuous Ultrasound Biometry (CUB) (Beers & van der Heijde, 1994a, Vilupuru & Glasser, 2005), developed by van der Heijde and colleagues allows high-resolution A-scan biometric measurements at 100 Hz, using a 10-MHz transducer. The transducer contacts the cornea through ultrasound transmission gel to generate sharp A-scan peaks representing the anterior and posterior cornea surfaces, anterior and posterior lens surfaces, and the retina. The CUB measures the time between peaks associated with the intraocular surfaces. This method has proven to be a reliable and precise method to measure small, to about 1 μm, sagittal intraocular movements. This method has been used to measure microfluctuation in the lens and axial length during steady state accommodation (van der Heijde, Beers & Dubbelman, 1996), to model the dynamic behavior of the accommodation system (Beers & van der Heijde, 1994a, Beers & van der Heijde, 1994b, Niessen, De Jong & van der Heijde, 1992), to measure thickening and translation of the aging lens (van der Heijde,

Dubbelman & Beers, 1999), and it has been also extensively used in dynamic accommodation in monkeys (Vilupuru & Glasser, 2002, Vilupuru & Glasser, 2005). CUB is able to measure changes in the intraocular distances with a precision of 1 μm. This high precision should not be confused with the accuracy, which is limited by the wavelength of the ultrasonic pulse, i.e. approximately 0.15 mm. In this thesis, this technology has been used to assess dynamic changes of anterior chamber depth and lens thickness in monkeys and to process dynamic phakometry data in Chapter 6.

3.2.2 Ultrasound biomicroscopy

While in A-scan ultrasonography, a thin, parallel sound beam is emitted, which passes through the eye and images one small axis of tissue; the echoes of which are represented as spikes arising from the baseline, in B-scan ultrasonography an oscillating sound beam is emitted, passing through the eye and imaging a slice of tissue; the echoes of which are represented as a multitude of A-scan which can be combined to generate an image.

Three-dimensional (3-D) ultrasound is the natural extension of two-dimensional B-scan imaging (Coleman, Woods, Rondeau & Silverman, 1992, Downey, Nicolle, Levin & Fenster, 1996, Jensen & Hansen, 1991, Jezzi, Rosen & Tello, 1996, Silverman, Rondeau, Lizzi & Coleman, 1995). The 3-D image is constructed from ultrasound data acquired in a series of ordered B-scan planes that are either parallel to each other or separated by regular angular increments. The 3-D ultrasound allows evaluation of hidden ocular structures and measurement and monitoring of the shape and volume of normal and pathologic ocular structures. Ultrasonography performed at standard frequencies (10 MHz), providing a resolution of approximately 150 μm, is insufficient to resolve fine details of ocular structures, or assess complex surface shapes. The use of improved transducer technology (Pavlin, Harasiewicz, Sherar & Foster, 1991, Pavlin, Sherar & Foster, 1990) allowed very high ophthalmic ultrasound scanning frequencies (VHF) in the 30- to 80 MHz range in a commercial instrument, the Ultrasound Biomicroscope (Humphrey Instruments, San Leandro, CA). These higher frequencies, although limited in application to the anterior segment, provide a resolution of approximately 35 μm. Commercial ultrasound scanning systems using intermediate frequency ranges (15-30 MHz) or interchangeable transducers permitting scanning at various frequency ranges have also been introduced (Cusumano, Coleman, Silverman, Reinstein, Rondeau, Ursea, Daly & Lloyd, 1998). The system incorporates two

computer-controlled linear motion stages mounted at right angles to each other. By moving the transducer in a series of parallel planes, a sequence of VHF ultrasound images suitable for 3-D reconstruction of the anterior segment can be acquired. Recent developments involve digitization of radio frequency (RF) ultrasound data, rather than the processed envelope of the data (which discards phase information with consequent reduction in measurement accuracy). From ultrasonic RF data, spectrum analysis can be performed using frequency-domain signal processing techniques (Allemann, Silverman, Reinstein & Coleman, 1993, Reinstein, Silverman, Trokel & Coleman, 1994, Silverman et al., 1995). Spectrum analysis can provide quantitative information on the structure of tissue inhomogeneities smaller than those directly resolvable on conventional B-scan images.

3.3. Techniques based on low coherence interferometry

3.3.1. Partial coherence interferometry

In general, A-scan biometry is easy to perform and gives accurate results in the majority of patients. However, the most commonly performed type of ultrasound A-scan (applanation biometry) requires contact with the cornea, and the force applied on the cornea does decrease the measured axial length by a fraction of a millimeter. Advances in partial coherence interferometry now allow a non–contact way of measuring interocular distances. This technique relies on optical interferometry rather than ultrasound. A superluminescent diode in a Michelson interferometer emits a 780 nm infrared light with short coherence length light to determine the distance from the cornea to the retinal pigment epithelium. Drexler et al. were the first to describe the partial coherence interferometry (Drexler, Baumgartner, Findl, Hitzenberger, Sattmann & Fercher, 1997, Drexler, Findl, Menapace, Rainer, Vass, Hitzenberger & Fercher, 1998), and also suggested, a special heterodyne detection technique, called laser Doppler interferometry (Drexler, Hitzenberger, Sattmann & Fercher, 1995, Hitzenberger, 1991) to obtain short measurement times. This technique has been used for anterior chamber depth (Kriechbaum, Findl, Kiss, Sacu, Petternel & Drexler, 2003, Kriechbaum, Findl, Preussner, Koppl, Wahl & Drexler, 2003), corneal thickness (Rainer, Petternel, Findl, Schmetterer, Skorpik, Luksch & Drexler, 2002) and axial length measurements, and subsequently used to calculate more accurately intraocular

lens power (Findl, Drexler, Menapace, Heinzl, Hitzenberger & Fercher, 2001, Rajan, Keilhorn & Bell, 2002) .

In this thesis we used a commercially available apparatus (IOL Master, Zeiss Humphrey), based on partial coherence interferometry to obtain biometric measurements for phakometry/IOL tilt and decentration measurements in Chapters 2, 5, 8 and 9. The disadvantage of the commercial instrument is that only axial length measurements are based on interferometry, while anterior chamber depth measurements are based on slit-lamp imaging. In addition it does not allow continuous optical biometric measurements during accommodation.

3.3.2 Optical Coherence Tomography (OCT)

First devised in 1991 by Huang (Huang, Swanson, Lin, Schuman, Stinson, Chang, Hee, Flotte, Gregory & Pulifito, 1991, Li, Shekhar & Huang, 2006) and Fercher (Fercher, Hitzenberger, Drexler, Kamp & Sattmann, 1993) in 1993 and later improved by Izatt (Izatt, Hee, Swanson, Lin, Huang, Schuman, Puliafito & Fujimoto, 1994) in 1994 for anterior chamber imaging, optical coherence tomography (OCT) with micrometer resolution and cross-sectional imaging capabilities, has become a prominent biomedical tissue imaging technique. With this technique it is possible to perform non-invasive cross-sectional imaging of internal structures in biological tissues by measuring their optical reflections.

Optical Coherence Tomography (OCT) (Huang, Swanson, Lin, Schuman, Stinson, Chang, Hee, Flotte, Gegory, Puliafito & Fujimoto, 1991) has found widespread applications for cross sectional imaging of tissue *in situ* with micron scale resolution. Earlier OCT systems were based on time domain detection where echo time delays of light were detected by measuring the interference signal as a function of time, while scanning the optical path length of the reference arm (Drexler, Morgner, Kartner, Pitris, Boppart, Li, Ippen & Fujimoto, 1999, Swanson, Huang, Hee, Fujimoto, Lin & Puliafito, 1992). Recently, OCT techniques based on Fourier domain detection have become an active area of research (Fercher, Hitzenberger, Kamp & Elzaiat, 1995, Park, Pierce, Cense, Yun, Mujat, Tearney, Bouma & de Boer, 2005). OCT with Fourier domain detection uses either a spectrograph (Fercher et al., 1995, Häusler & Lindner, 1998) or a frequency swept laser source (Chinn, Swanson & Fujimoto, 1997, Choma, Hsu & Izatt, 2005, Fercher et al., 1995, Yun, Tearney, De Boer, Iftimia & Bourna, 2003) to measure echo time delays of light by spectrally resolving the interference signal. The magnitude

and time delay of the backscattered light is reconstructed by Fourier transformation of the fringe signal versus frequency. Recent studies have shown that Fourier domain detection using spectrometers or frequency swept lasers can dramatically improve the detection sensitivity and enable significantly higher scan speeds than standard time domain detection techniques (Choma, Sarunic, Yang & Izatt, 2003, de Boer, Cense, Park, Pierce, Tearney & Bouma, 2003). Time domain OCT imaging using two-dimensional zone focusing and image fusion or focus tracking to increase the depth of view has been demonstrated, but suffers from slow data acquisition speeds (Cobb, Liu & Li, 2005, Drexler et al., 1999, Lexer, Hitzenberger, Drexler, Molebny, Sattmann, Sticker & Fercher, 1999). Full, three-dimensional data sets with enhanced depth of field can be acquired within several seconds by acquiring and fusing multiple three dimensional data sets with different focus depths. This overcomes depth of field limitations which are normally associated with the small focused spot sizes required for high transverse resolution.

Anterior segment OCT systems are less common that retinal systems. Commercial systems have been recently introduced, but these tend to provide more qualitative than quantitative information of geometrical parameters. Izatt (Goldsmith, Li, Chalita, Westphal, Patil, Rollins, Izatt & Huang, 2005) in 2005 proposed a novel high-speed (4000 axial scans/second) OCT prototype anterior segment scanning that used a long wavelength (1310 nm) for deeper angle penetration, rectangular scanning for undistorted imaging, and short image acquisition time (0.125 seconds) to reduce motion error to obtain three horizontal cross-sectional OCT images (15.5 mm wide and 6 mm deep) of the anterior segment .

3.4. Magnetic Resonance Imaging (MRI)

Magnetic resonance imaging (MRI) is an imaging technique used primarily in medical settings to produce high quality images of the inside of the human body. MRI is based on the principles of nuclear magnetic resonance (NMR), a spectroscopic technique used by scientists to obtain microscopic chemical and physical information about molecules. MRI started out as a tomographic imaging technique and has advanced to a volume imaging technique. This technique is capable of producing undistorted images of the whole eye in vivo and has been used to study the anterior segment of the aging eye by Strenk (Strenk et al., 2005, Strenk et al., 2004, Strenk et al., 1999, Strenk & Strenk, 2006). However, up until now, the disadvantage of this method is the poor

resolution of the images of ±0.2 mm. Therefore, the method is not appropriate to measure small changes and the asphericity of the surfaces.

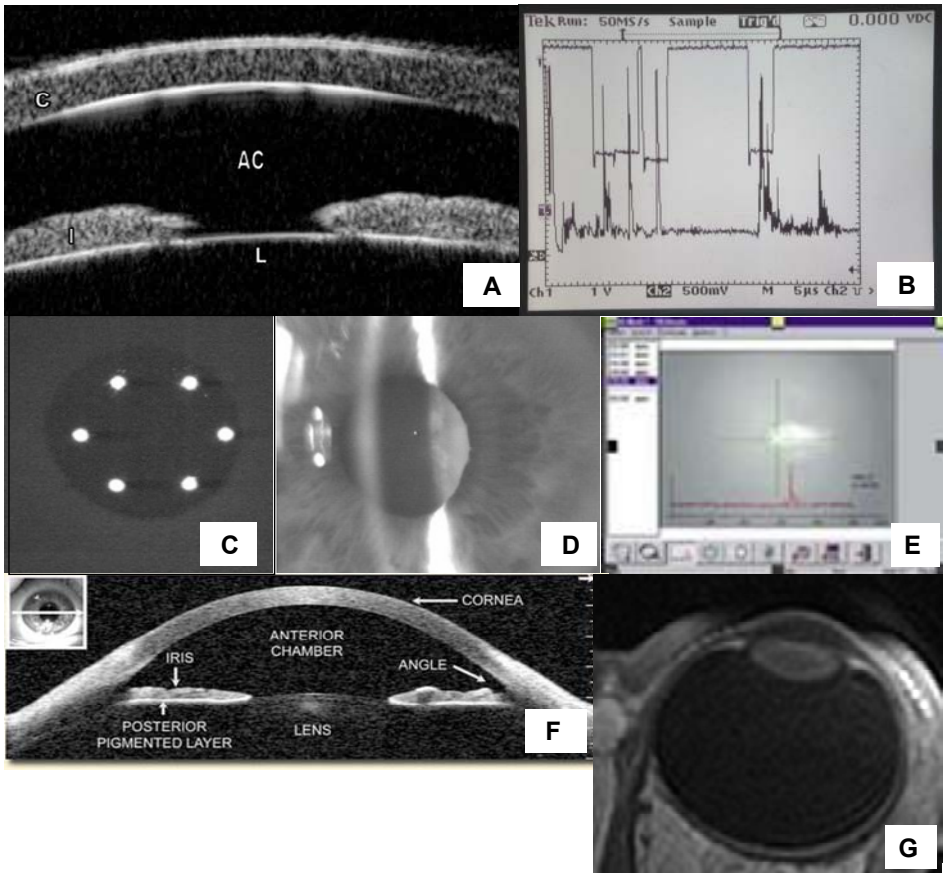

Figure 1.10. Illustration of image outputs from several anterior segment imaging/ocular biometry techniques: **A.** Ultrasound biomicroscopy (adapted from de Guzman et al. 2005)(de Guzman, Thiagalingam, Ong & Goldberg, 2005); **B.** A-Scan from Continuous Ultrasound Biometry (Courtesy of Rob van der Heijde). **C.** Keratometry **D.** Anterior chamber depth from slit lamp imaging **E.** Partial coherence interferometry for axial length measurements (c) with the IOLMaster (Zeiss)**. F.** Anterior chamber imaging obtained with Optical Coherence Tomography (Courtesy of the New York Eye Enfermery) **G.** Image of the eye globe obtained by Magnetic Resonance Imaging (Adapted from Strenk et al. 2004)

3.5. Slit lamp biomicroscopy

In this system, invented by Alvar Gullstrand in 1911, a narrow "slit" beam of very bright light produced by a lamp is focused on to the eye which is then viewed under magnification with a microscope (Gullstrand, 1911). The illumination system is composed by a light source and condensing lenses which allow uniform illumination of a slit aperture (with generally variable width, length and orientation). Magnification of the observing microscope ranges from about x 10 to about x 50. While this technique is extremely useful for clinical examinations, it is limited to provide quantitative information of ocular component dimensions by small depth of focus, that prevents

obtaining a sharp image of the cornea and the lens simultaneously**.** Figure 1.11 shows the principle of Slit-Lamp photography.

3.5.1 Scanning slit corneal topography

The basis of the method is to photograph a series of slit-beam sections through the eye at varying angles to the optic axis (generally using a scanning optical slit device), to obtain an image of the profile of the anterior and posterior cornea (and in principle, also the lens, at least the anterior surface). Because of the refraction of the previous ocular surfaces, the shapes of the inner surfaces of the anterior segment imaged are distorted. Several studies have tested the validity of measurements of posterior corneal surface with the commercially available slit scanner, Orbscan (Maldonado, Nieto, Díez-Cuenca & Piñero, 2006, Quisling, Sjoberg, Zimmerman, Goins & Sutphin, 2006), but because a correction of optical distortion has not been reported, the accuracy of those measurements, is still unclear (Wilson, 2000).

3.5.2. Scheimpflug imaging

To obtain complete anterior segment images, the Scheimpflug imaging improves the slit lamp geometry, by using the Scheimpflug's principle. Normally, the lens and image (film or sensor) planes of a camera are parallel, and the plane of focus is parallel to the lens and image planes. If a planar subject (such as the side of a building) is also parallel to the image plane, it can coincide with the plane of focus, and the entire subject can be rendered sharply. If the subject plane is not parallel to the image plane, it will be in focus only along a line where it intersects the plane of focus, as illustrated in Figure 1.11 A. When an oblique tangent is extended from the image plane, and another is extended from the lens plane, they meet at a point through which the plane of focus also passes, as illustrated in Figure 1.11 B. With this condition, a planar subject that is not parallel to the image plane can be completely in focus.

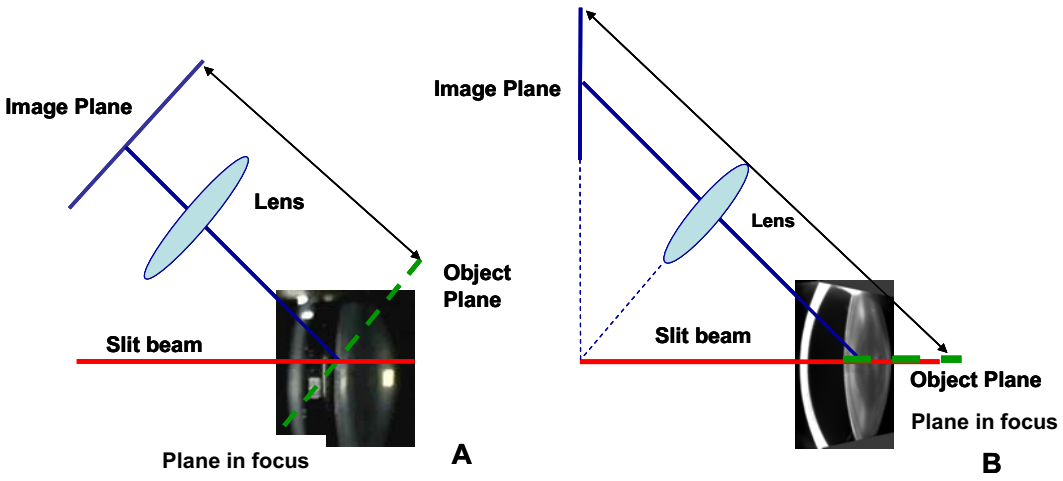

Figure 1.11. A. Principle of Slit lamp imaging. A slit beam is focused on the eye which is viewed with a microscope. The Plane image and Object image are parallel to each other. **B.** Principle of Scheimpflug imaging, where the image and objects planes are tilted with respect to each other in such way that they intersect in one point.

The special geometry of the Scheimpflug configuration allows imaging the anterior segment with large depth of focus, but it introduces a geometrical distortion, because the magnification is not constant over the image. Additionally, because of the refraction from the different ocular surfaces, the Scheimpflug camera also introduces an optical distortion, due to the fact that each of the ocular surfaces is seen trhough the previous one (i.e., the anterior lens is seen through the posterior and anterior cornea). In order to obtain reliable information from those images, those distortions must be corrected. The methods for correction of these distortions are further explained in Chapter 3. In this thesis two different Scheimpflug instruments have been used and evaluated.
A modified Topcon SL-45 corrected system (Chapter 4) for phakometry.
A Pentacam (Oculus) system in Chapter 5 for intraocular lens tilt and decentration measurements.

4. THE OPTICAL QUALITY OF THE NORMAL HUMAN EYE

The eye is an optical instrument that projects scenes of the visual world onto the retina. It has been known for many years that the eye is far from being a perfect optical system, in particular for large pupil diameters. Refractive anomalies (defocus or astigmatism) occur frequently in the eye.

However the eye suffers also from other optical imperfections (called high order aberrations). Like defocus, optical aberrations blur the retinal image, reducing image

contrast and limiting the range of spatial frequencies available to further stages of the visual processing. With the development of rapid and reliable aberrometers, ocular aberrations can be easily measured. The contribution of the cornea to the overall aberrations of the eye can be also be computed from corneal topography. The contribution of the internal optics to the ocular aberration of the eye is typically estimated by subtracting corneal from total aberrations. However, the sources of optical aberrations in the crystalline lens, and misalignments of the optical components are not well understood. This thesis will shed light into the contributions of lens shapes and misalignments to the optical degradation in the normal eye, and most completely the pseudophakic eye.

4.1 Optical aberrations.

The wave aberration, $W(x, y)$, defines how the phase of light is affected as it passes through the optical system. The wavefront is a line that joins every point on a wave that has the same phase, i.e it is a surface that joins the leading edges of all rays at some instant. The wave aberration is defined as the deviation of this wavefront from a reference surface that is usually defined as a surface of curvature near the wavefront whose origin is located at the Gaussian image point (where the light would be focused if the eye were perfect) (Figure 1.12). If the Gaussian image is at infinity, then it follows that the reference surface is a plane. For the human eye, the natural choices for the reference would be a sphere whose center of curvature is at the fovea for line-of sight (Applegate, Thibos, Bradley, Marcos, Roorda, Salmon & Atchison, 2000) measurements, or at infinity for light emerging from the eye.

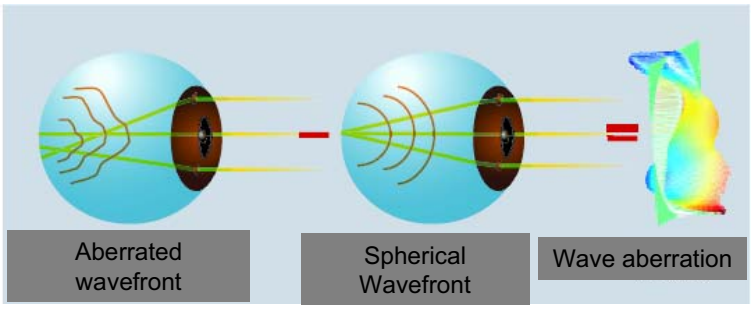

Figure 1.12. Schematic diagram of the concept of ocular wavefront aberration **A.** The wave front takes a spherical shape for a diffraction-limited optical system **B.** The wave front of an aberrated optical system is irregular, wave front aberration WA is defined as the deviation of the wave front from a reference wave front. Figure adapted from Marcos (Marcos, 2005)

The wave aberration is often defined mathematically by a series of polynomials, such as the Seidel polynomials, but these can define only a limited range of aberrations. Howland (Howland & Howland, 1977) proposed a Taylor expansion to describe the wave aberration function in terms of pupil coordinates. The most popular polynomials are Zernike polynomials, first introduced by Frits Zernike in interferometric contrast phase microscopy (Zernike, 1934). The main advantage of the set of Zernike polynomials is that they are orthonormal in a unit circle. As pupil coordinates are usually normalized for a unit circle, any continuous wave aberration function can be expressed in terms of a Zernike expansion. Each Zernike term is formed by the product of a radial, an angular function and a normalization factor, specified by radial indexes. The Optical Society of America has established a set of recommendations (Thibos et al., 2000) about sign, normalization (Noll's normalization) and ordering, that has been followed in this thesis. Figure 1.13 shows the representation of the Zernike polynomial terms from 2nd to 4th order polynomials.

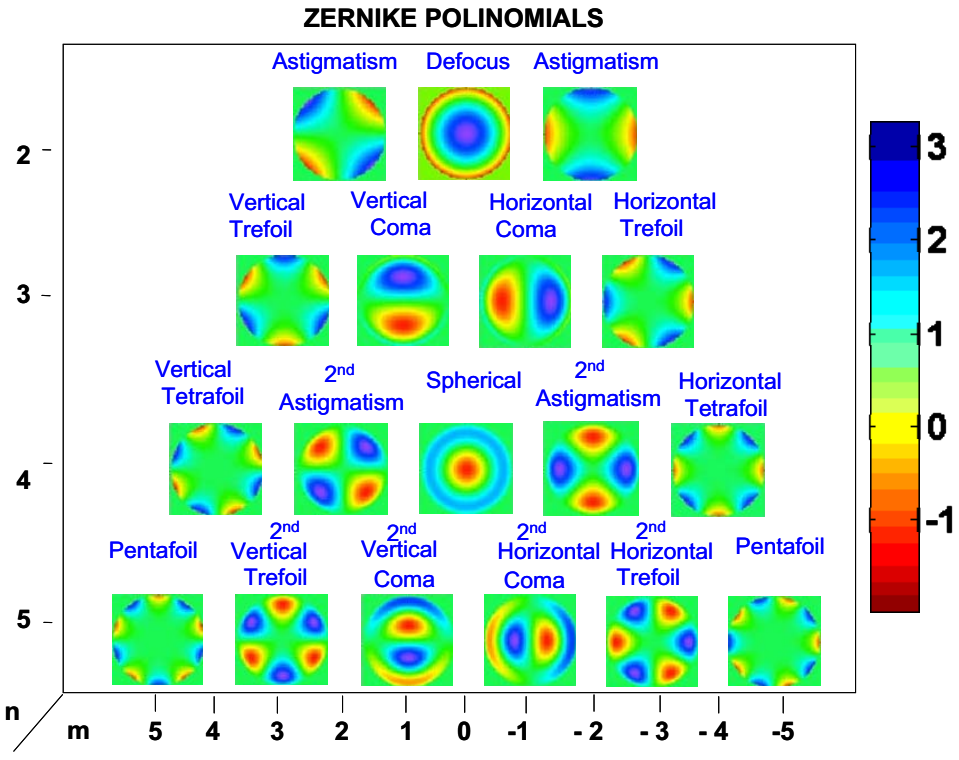

Figure 1.13. Representation of the Zernike polynomial terms from 2nd to 4th order polynomials, according to the Optical Society of America nomenclature (Thibos, Applegate, Schwiegerling, Webb & Members, 2000) . The scale is in microns.

4.2 Aberrometry

Many scientists throughout the history of physiological optics have attempted to measure the optical aberrations of the human eye. Scheiner in 1619 (Scheiner, 1619) published the work "Oculus, sive fundamentum opticum" where he announced the invention of a disc with a centered and a peripheral pinhole that was placed before the eyes of a subject to view a distant light source. If the subject saw a single spot he was an emmetrope, if he saw two inverted spots, he was a myope; and if he saw two upright spots, a hyperope. This device was the first qualitative refractor and became known as Scheiner's disc. After Scheiner, many scientists attempted to construct more precise refractors. Tscherning (Tscherning, 1894) in 1894 used a four-dimensional spherical lens with a grid pattern on its surface to project a regular pattern on the retina. He would then ask the patient to sketch drawings of the pattern. Depending on the pattern's distortion, Tscherning was able to obtain a semiquantitative measurement of the patient's aberrations. One of the earliest quantitative aberrometers was devised by Howland (Howland, 1960, Howland & Howland, 1976, Howland & Howland, 1977). The aberroscope consisted of a nearly square grid mounted between the plane surfaces of +5 and -5 D plano-cylindrical lenses, with the cylindrical axes mutually perpendicular and at 45 deg to the vertical. The grid is distorted slightly so that it projects squares onto the entrance pupil of the eye. A shadow of the grid is formed on a subject’s retina. The initial version of this technique was subjective. Howland and Howland analyzed sketchs of grid shadows drawn by their subjects to obtain wave-aberration polynomials and optical transfer functions. Walsh (Walsh, Charman & Howland, 1984) and Walsh and Charman (Walsh & Charman, 1985) made the technique objective by inserting a beam splitter between the aberroscope and the eye, so that the retinal grid shadow could be photographed.

Another subjective technique first introduced by Smirnov (Smirnov, 1961) for testing the human eye by spatially examining the refractive performance of light rays point by point across the entire pupil was not widely adopted in the study of aberrations of the eye because it was time consuming. A faster implementation of Smirnov’s technique was developed by Webb (Webb, Penney & Thompson, 1992), and called the spatially resolved refractometer (SRR). A new version of the SRR was developed by He (He, Marcos, Webb & Burns, 1998) that allows rapid estimates of both the overall wave-front aberration and individual aberrations. An objective version of the SRR, the

Laser Ray Tracing (LRT) technique was developed by Navarro and Moreno-Barriuso (Navarro & Moreno-Barriuso, 1999). The method consists of delivering narrow pencils of light (rays) sequentially through the optical system and measuring the position (centroid) of the image spot on the detector (image) plane. It is possible to scan the pupil plane by sequentially delivering rays through different pupil positions. A new generation of a much more compact LRT system was developed, with significant improvements over the first generation (Llorente et al., 2004). This system is used in the current thesis in Chapters 8 and 9, and will be briefly described in Chapter 8.

Figure 1.14 shows the laser ray tracing set up used to measure the ocular aberrations reported in this thesis. Briefly, the light source is either a green (532 nm) or infrared (786 nm) laser diode. An x-y scanner deflects the rays. The light reflected back from the retina is captured by high-resolution camera CCD_2 conjugate to the retina. Another camera (CCD_1) conjugate to the pupil and coaxial with the system captures images of the pupil simultaneously and is used for continuous alignment.

One of the most popular aberrometric techniques is the so-called Hartmann-Shack wavefront sensor. Liang (Liang, Grimm, Goelz & Bille, 1994) applied to the human eye an idea originally applied to general optical instruments such as astronomical telescopes since the 1950s (Babcock, 1953). The sensor used to measure the aberrations was first developed by Hartmann in 1900 (Hartmann, 1900) and later improved by Shack in 1971 (Shack & Platt, 1971). This sensor became known as the Hartmann-Shack sensor, abbreviated HS sensor, which consists of a mono-lithic array of small circular apertures (microlenses) to sample the wave front in a reference sphere at the exit pupil, as opposed to the LRT which uses a single Gaussian beam as a ray whose coordinates (for both the point object and the entrance-pupil position) can be specified as in standard ray-tracing software. Studies at the Visual Optics and Biophotonics laboratory have shown the equivalency of LRT, HS and SRR on human eyes (Llorente, Diaz-Santana, Lara-Saucedo & Marcos, 2003, Marcos, Díaz-Santana, Llorente & C., 2002, Moreno-Barriuso, Marcos, Navarro & Burns, 2001).

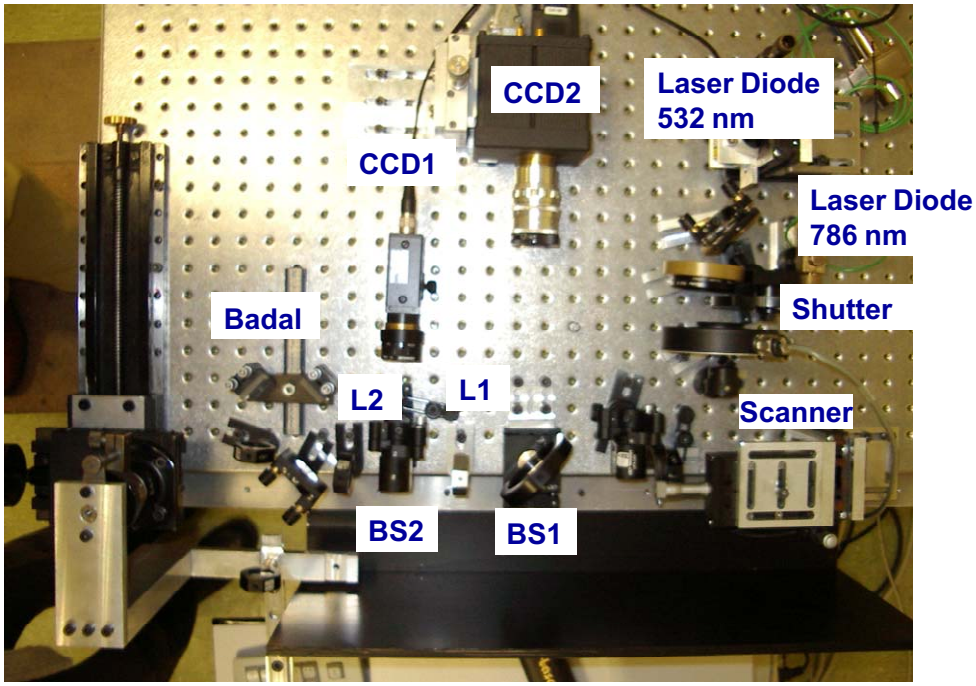

Figure 1.14. Photograph of the Laser Ray Tracing set up at the Visual Optics and Biophotonics Lab (Instituto de Optica). A detailed description of the principle and technical specifications of the system appear in the text. This system, developed previous to this thesis, has been used to measure the ocular aberrations reported in this thesis.

The principle for wave front measurements can be summarized as follows.

Considering a mathematical expression of the wave aberrations in terms of Zernike polynomials:

$$W(x,y) \approx \sum_{m=1}^{37} Z_m P_m(x,y) \qquad [1.1]$$

with Z_m being the coefficients of the expansion, in microns, and P_m the Zernike polynomials.

The eye's pupil is sampled at a set of points (X_i, Y_i) $i = 1,...,n$ according to a sampling pattern. Normalizing the pupil coordinates, given by $\overline{X} = \frac{X}{R_p}$ and $\overline{Y} = \frac{Y}{R_p}$, (with R_p being the pupil radius), the ray aberrations $\left[\Delta x'(X_i, Y_i), \Delta y'(X_i, Y_i)\right]$

corresponding to the pupil locations can be obtained from the partial derivates of the Wave Aberration (W):

$$\Delta x' = \frac{1}{R_p}\frac{\partial W(\bar{X},\bar{Y})}{\partial \bar{X}}; \quad \Delta y' = \frac{1}{R_p}\frac{\partial W(\bar{X},\bar{Y})}{\partial \bar{Y}} \qquad [1.2]$$

The partial derivates can be obtained from Equation [1.1], and the wave aberration can be obtained by least squares fitting of the ray aberration to the partial derivates of the Zernike polynomials for each pupil location sampled.

4.3 Total aberrations

The amount and distribution of aberrations vary greatly among the population. Several population studies show a wide distribution of the aberrations in human eyes. Typically all high order terms average to zero. Smirnov (Smirnov, 1961) was the first to study the intersubject variability in the eye's wave aberration for a population of ten subjects. Howland and Howland (Howland & Howland, 1977) studied the monochromatic aberrations by using the aberroscopic technique and found that the wave aberration differs greatly across subjects. In particular, Porter (Porter, Guirao , Cox & Williams, 2001), Thibos (Thibos, Hong, Bradley & Cheng, 2002), Castejon Mochon (Castejon-Mochon et al., 2002) found that most of the total RMS were in the first two and three orders. They found a relative symmetry between aberration pattern between right and left eyes, although previous studies by Marcos & Burns (Marcos & Burns, 2000) and Castejon-Mochon reported some symmetry, but to a lesser extent.

Porter found that spherical aberration was the only mode to have a mean that is significantly different from zero, with a mean value of 0.138 ±0.13 μm for a 5.7 mm pupil. They found that even though there appears to be a random variation in the eye's aberrations from subject to subject, many aberrations in the left eye were found to be significantly correlated with their counterparts in the right eye. Other studies reported a negative mean significant value for oblique trefoil (Cheng, Barnett, Vilupuru, Marsack, Kasthurirangan, Applegate & Roorda, 2004, Thibos et al., 2002, Wang & Koch, 2003).

A recent review by Salmon (Salmon & van de Pol, 2006) combining Hartmann-Shack aberrometry data from multiple sites (a total of 2560 eyes from 1433 subjects) found that the most prominent modes were Z_3^{-3} (horizontal trefoil), Z_3^{-1} (vertical

coma), and Z_4^0 (spherical aberration), with mean absolute values of 0.11 μm, 0.14 μm, and 0.13 μm and average total higher-order RMS values (from the third to sixth order) of 0.33 μm for a 6 mm pupil.

4.4 Corneal Aberrations

Basic data regarding corneal wavefront aberrations, such as the distribution in the population and changes with aging, are essential to understanding the contribution of the cornea to the overall optical degradation. In young eyes the anterior cornea is typically steeper in the vertical than in the horizontal meridian, which results in corneal astigmatism. Interestingly this asymmetry tends to reverse with increasing age (Hayashi, Hayashi & Hayashi, 1995 i.e, corneal astigmatism changes from "with-the-rule" to "against-the-rule" with age). In general, the cornea becomes steeper with age.

Oshika (Oshika, Klyce, Applegate & Howland, 1999) estimated corneal aberrations from corneal elevation maps, finding that for a 7.0 mm pupil, total wavefront aberrations and coma-like aberrations of the cornea correlated with age, whereas spherical-like aberrations did not vary significantly with age. Because comalike aberrations consist of tilt and/or asymmetry, these results imply that the corneas become less symmetric with aging.

Guirao (Guirao, Redondo & Artal, 2000), using similar technique, reported that despite a large intersubject variability, the average amount of aberration of the human cornea tends to increase moderately with age, finding that spherical aberration was significantly larger in the middle aged (40-50 years old) and older corneas (60-70 years old).

Wang Li (Wang, Dai, Koch & Nathoo, 2003), studied corneal high order aberrations from the central 6.0 mm zone of the corneal topographic of mean age 50 years and found a wide individual variability in aberrations, with ranges of individual Zernike terms from -0.579 to +0.572 μm. The mean coefficient of the fourth order spherical aberration (Z_{40}) was 0.280 ± 0.086 μm and positive in all corneas. The mean root-mean-square (RMS) values were 0.479 ± 0.124 μm for high order aberrations, 0.281 ± 0.086 μm for spherical aberration (Z_{40} and Z_{60}), and 0.248 ± 0.135 μm for coma (Z_{3_1}, Z_{31}, Z_{5_1}, and Z_{51}). Moderate correlations were found between right and left eyes for high order aberration, spherical aberration, and coma. This study also reported an increase in high

order aberrations and coma with age, but spherical aberration did not show any dependence with age.

Using a distortion-corrected Scheimpflug camera, it has been found, that the posterior corneal surface compensates for 31% of the anterior corneal surface astigmatism, which is larger than could be expected based on the astigmatism of the anterior surface alone (Dubbelman, Sicam & van der Heijde, 2006). Scheimpflug studies also show that the spherical aberration of the posterior corneal surface (Sicam, Dubbelman & van der Heijde 2006) is negative at a young age and becomes positive at an older age, with the ratio (posterior spherical aberration)/(anterior spherical aberration) therefore shifting to compensate the postive spherical aberration of the cornea (-10%) in young subjects to add up aberration (26%) in old subjects. As for coma, these studies show the posterior corneal surface compensates approximately 3.5% the anterior surface coma, this compensation being larger for young subjects (6%) than for older subjects (0%). It can be therefore concluded that the posterior cornea has in general a small effect on high order aberrations of the eye, and that the slight compensation found in young eyes is lost with age (Dubbelman, Sicam & van der Heijde, 2007).

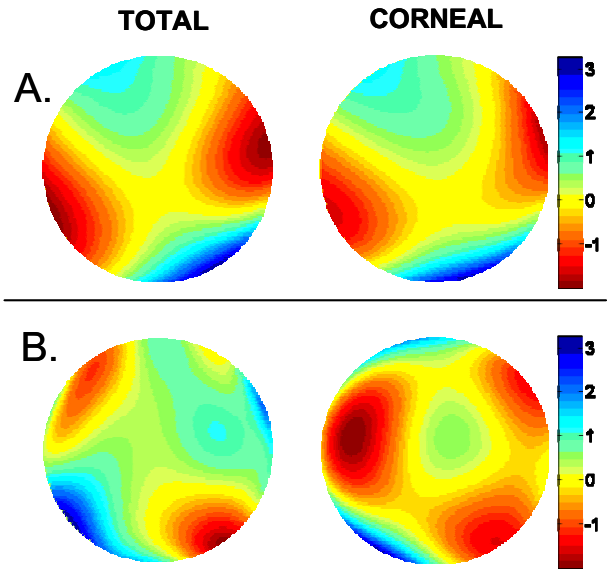

Figure 1.15. Total and corneal wave aberrations of both eyes of an unilateral aphakic 30-old patient. **A.** Aphakic eye (with no crystalline lens) and **B.** Normal contralateral eye. Note the similarity of corneal and total aberrations in the aphakic eye, and the compensation of corneal spherical aberration by the internal optics in the normal eye. Pupil diameter=6.5 mm. Figure adapted from Barbero (Barbero, Marcos & Merayo-Lloves, 2002b).

4.5 Interaction between Total and Corneal Aberrations:

The relative contribution of the cornea and crystalline lens to the overall ocular wave aberration is a relevant question in both the basic study of human eye optical quality and clinical ophthalmic applications. Although the magnitude and distribution of ocular aberrations differ substantially across subjects, a balance of corneal aberrations by internal optics, resulting in smaller ocular aberrations than those of the individual ocular components appears to be a common trend in young eyes.

The first reports of a compensation of corneal spherical aberration by the crystalline lens date back to the 70's, (El Hage & Berny, 1973, Millodot & Sivak, 1979). In a different study, Tomlinson (Tomlinson, Hemenger & Garriott, 1993) measured the contrast sensitivity of the eye for a small and large pupil size and using a knowledge of the expected aberration contribution from the cornea, predicted the aberration of the lens, finding positive values for the spherical aberration of the cornea, in the range 0-0.83 D, and negative spherical aberration of the crystalline lens, in the range 0 to -0.81 D. Similar findings were reported by Smith (Smith et al., 2001) who, as previously suggested by El Hage, measured the aberration of the whole eye, estimated the corneal aberration from the corneal shape, and from their difference reported a negative value of the spherical aberration of the lens approximately the same level as the positive value of the anterior corneal surface. Smith also studied the age effects on the spherical aberration and found that the older eye had much more total aberration than the younger eye while the aberration of the anterior corneal surface did not seem to be different between younger and older eye. In a recent study, Barbero (Barbero et al., 2002b) showed much higher spherical aberration in the aphakic eye of an unilateral aphakic young patient that in the normal eye, where corneal spherical aberration was reduced by the crystalline lens.

More recent studies have confirmed previous results on the balance of corneal and internal spherical aberration and also showed a reduction of corneal third-order coma by internal optics in young eyes. Artal (Artal & Guirao, 1998, Artal et al., 2001) found a significant coupling of individual aberration terms between the cornea and the internal ocular optics. Astigmatism for the cornea and internal optics (Zernike terms 3 and 5) had opposite signs, confirming the well-known fact in clinical practice that the internal optics tend to compensate for the corneal astigmatism. However, he found that this compensation also takes place for higher order aberrations. Third- and fourth-order

aberrations were also partially compensated. A large fraction of the spherical aberration of the cornea is cancelled by the internal optics. The magnitude of comalike aberrations of the cornea was also significantly reduced by the internal optics. Artal then opened the question whether this compensation was an active or passive process. In a later work, they showed that this compensation is larger in the less optically centered eyes (primarily hyperopic eyes), concluding that there was an auto-compensation mechanism that preserve the optical quality of the eye despite large variation in the ocular shape and geometry (Artal et al., 2006). Kelly (Kelly et al., 2004) in a study on 30 young subjects with relaxed accommodation, found strong evidence for compensation of horizontal/vertical astigmatism, lateral coma (for which they attributed an active compensation mechanism) and spherical aberration (which would occur passively). The active or passive nature of the compensation mechanism will be further addressed in this thesis in Chapter 9. This corneal/internal balance of spherical aberration and coma has been shown to be disrupted in older eyes (Artal et al., 2002), presumably because of structural changes in the crystalline lens, producing the reported increase of aberrations with age (Artal, 1993, Guirao, Gonzalez, Redondo, Geraghty, Norrby & Artal, 1999).

4.6 Misalignment of the ocular components

The eye is not a centered optical system. The fovea does not lie on the optical axis of the eye, and in fact, the optical axis of the ocular components cannot be defined. These commonly defined axes in the eye (Atchison & Smith, 2000b), which will be used in these thesis:

The *optical axis* is the line passing through the centers of curvature of the different surfaces of a centered system. Because the different surfaces of the eye are not centered to each other, this axis does not exist in the eye, although it has sometimes defined as the axis linking the center of curvature of the anterior corneal surface and that of the posterior lens surface.

The *line of sight* is the line joining the fixation point and the center of the entrance pupil. The position at which the line of sight intercepts the cornea is called the *corneal sighting center* (Mandell, 1995) or *visual center of the cornea* (Cline, Hofstetter & Griffin, 1989). Total aberrations measured (or simulated) in this thesis (Chapters 8 and 9) are referred to the line of sight.

The *visual axis* is defined by the line that joins the fixation target and the fovea position passing trough the nodal points. It is sometimes referred to as the foveal achromatic axis, since it can be located by searching the pupil location that produces minimun transverse chromatic aberration for foveal fixation. The angle between the optical axis and the visual axis is the *angle alpha*.

Pupillary axis is defined by the line that passes through the center of the entrance pupil, which is normal to the cornea. The angle between the pupillary axis and the line of sight is defined as *angle lambda*. The angle between the pupillary axis and the visual axis is the *angle kappa*. In practical terms, angles kappa and lambda are the same. Lens tilt and decentration measurements reported in this thesis are referred to this axis (Chapters 2, 5, 8, and 9), except when the pupil was not available (iridectomized monkey eyes of Chapter 6).

The Videokeratoscopic axis is the axis of a keratometer or videokeratographic instrument, and it contains the center of curvature of the anterior cornea. In the standard operation of a corneal topographic instrument, the axis intercepts the line of sight at the fixation target Corneal aberrations reported in this thesis are referred to the videkeratoscopic axis (Chapter 7) or the line of sight (Chapter 8).

4.7 Sources of optical aberrations in the normal eye: state of the art

The cornea and the crystalline lens are the major refractive components in the eye, and aberrations of the individual components are expected to contribute to overall image quality. Few studies address the sources of ocular aberrations from geometrical and optical structure of the individual components. Van Meeteren (van Meeteren & Dunnewold, 1983a) predicted, using schematic eye models, that tilt and misalignment of optical surfaces or a larger displacement of the fovea from the optical axis could give rise to both an increase in monochromatic aberrations (particularly astigmatism and coma) and an increase in optical transverse chromatic aberration (van Meeteren, 1974, van Meeteren & Dunnewold, 1983b). Marcos (Marcos et al., 2001) attempted to correlate the amount of misalignment of ocular surfaces and corneal shape with the amount of high order monochromatic aberrations of the eye (also tranverse chromatic aberrations) in a group of 15 eyes, and concluded that simple relationships were not present. These are potential sources of optical aberrations that have been identified:

4.7.1. Ocular surface misalignments.

Early models in the literature Bennet and Rabbets (Bennett & Rabbetts, 1984) and van Meeteren (van Meeteren & Dunnewold, 1983a)) predicted that larger amounts of coma (van Meeteren & Dunnewold, 1983b) and TCA (Simonet & Campbell, 1990, Thibos, Bradley, Still, Zhang & Howarth, 1990) apppear associated to large angle alpha. While those predictions were based on assumed average values, Marcos (Marcos et al, 2001) found that on an individual basis, the amount of coma (and TCA) was uncorrelated with the magnitude of angle alpha. This could be explained by a compensation of corneal horizontal coma by the internal optics, as demonstrated by Artal (Artal et al., 2006).

4.7.2. Pupil Centration.

Simple models show that pupil decentration causes an increase in the monochromatic aberrations (van Meeteren & Dunnewold, 1983b, Walsh & Charman, 1988) and in transverse chromatic aberration (Artal, Marcos, Iglesias & Green, 1996, Bradley, Thibos, Zhang & Ye, 1991, Thibos, 1987, Thibos et al., 1990), which produce a degradation in the retinal image (Artal et al., 1996, van Meeteren & Dunnewold, 1983b). Eye models proposed by Atchison and Smith, based on on-axis, rotationally symmetric components, predict that coma will be produced if the pupil is decentered (Atchison & Smith, 2000a). However, although it is clear that a systematic pupil decentration will increase retinal image degradation, and this has been experimentally demonstrated (Artal et al., 1996), typical pupil decentration occurring in normal eyes does not appear to be a major contributor to coma. Marcos (Marcos et al., 2001) did not find any correlation between pupil decentration and coma or TCA. Also, pupil shifts with pupil dilation have been reported to be small (Yabo, Thompson & Burns, 2002).

4.7.3. Corneal shape, corneal irregularities and refractive index

The effect of anterior corneal shape and irregularities on corneal aberrations has been discussed in section 4.4. The contribution of the corneal posterior surface to the overall aberrations has been shown to be limited in the normal eye (as discussed in section 4.4.), and to play a moderate compensatory role, particularly on astigmatism, spherical aberration and coma terms (as discussed in section 4.5) (Dubbelman et al., 2007, Dubbelman et al., 2006, Sicam et al., 2006)

Recent studies address the potential role on the refractive power of the cornea of the differences in refractive index of the different corneal layers and tear film (including a gradient index structure in the stroma) (Barbero, 2006). The effect of using a multilayer cornea (rather than an average refractive index) on high order aberrations has not been addressed but it is likely to be small.

4.7.4. Crystalline lens shape, structure and refractive index.

As it has been reported in sections 2.4.1, spherical aberration of the young crystalline lens is negative (Artal & Guirao, 1998, Artal et al., 2001, El Hage & Berny, 1973, Kelly et al., 2004, Sivak & Kreuzer, 1983, Smith et al., 2001, Tomlinson et al., 1993). Lens radius of curvature, asphericity and gradient index contribute to the final value of the spherical aberration (Artal et al., 2002). As has been presented in 2.4, all these factors are age dependent although there are controversial data in the literature on the magnitude and rate of these changes. The influence of the changes of lens radii of curvature with age on refraction (particularly in relationship with the lens paradox) have been studied (Dubbelman & van der Heijde, 2001, Koretz & Handelman, 1986a). However, the impact of individual lens geometry and structure on high order aberration has not been addressed, in part because of the lack of knowledge on the gradient index structure.

Another potential source of lens irregulaties are the crystalline lens sutures. Some scatter and refractive changes occur at the suture points, especially along the optical axis of the lens, as it has been demonstrated by Kuszak (Kuszak, 2004, Kuszak, Peterson, Sivak & Herbert, 1994) in primate lenses. This study found that focal variability was least when the beam was passed through uniformly hexagonal fibers aligned along the optical axis, and greatest when the beam passed through irregularly-sized and shaped fibers ends arranged as suture branches within growth shell and suture planes aligned along the optical axis. Significant amount of total trefoil measured in vivo has often been attributed to the lens sutures both in humans (Thibos et al., 2000) and monkeys (Ramamirtham, Kee, Hung, Qiao-Grider, Roorda & Smith, 2006), and have been shown to play an impact on retinal image quality (Navarro & Losada, 1997).

5. THE OPTICAL QUALITY OF THE PSEUDOPHAKIC EYE

5.1 Cataract surgery

Metabolic changes of the crystalline lens fibers over time lead to the development of a loss of transparency producing an opacification, is called cataract. Cataract surgery consists of the removal of the lens that has developed this opacification. There are different types of surgery, the most used methods, are phacoemulsification and extracapsular cataract extraction**:** *1) Phacoemulsification***.** It involves the use of a machine with an ultrasonic handpiece with a titanium or steel tip. The tip vibrates at ultrasonic frequency (40.000 Hz) and the lens material is emulsified. Fragmentation into smaller pieces makes emulsification easier, as well as the aspiration of cortical material (soft part of the lens around the nucleus). After phacoemulsification of the lens nucleus and cortical material is completed, a dual irrigation-aspiration (I-A) probe or a bimanual I-A system is used to aspirate out the remaining peripheral cortical material. All cataract surgeries reported in this thesis were performed using this technique. *2) Extracapsular cataract extraction (ECCE)*: It involves manual extraction of the lens through a large (usually 10-12 mm) incision made in the cornea or sclera. Although it requires a larger incision and the use of stitches, the conventional method may be indicated for patients with very hard cataracts or other situations in which phacoemulsification is problematic. None of the cataract surgeries reported in this thesis were performed using ECCE, but some of the literature results presented for comparison were. After cataract extraction, a foldable intraocular lens is introduced through the incision; once inside the eye, the lens unfolds to take position inside the capsule.
Figure 1.16 shows a scheme of a typical procedure for cataract surgery.

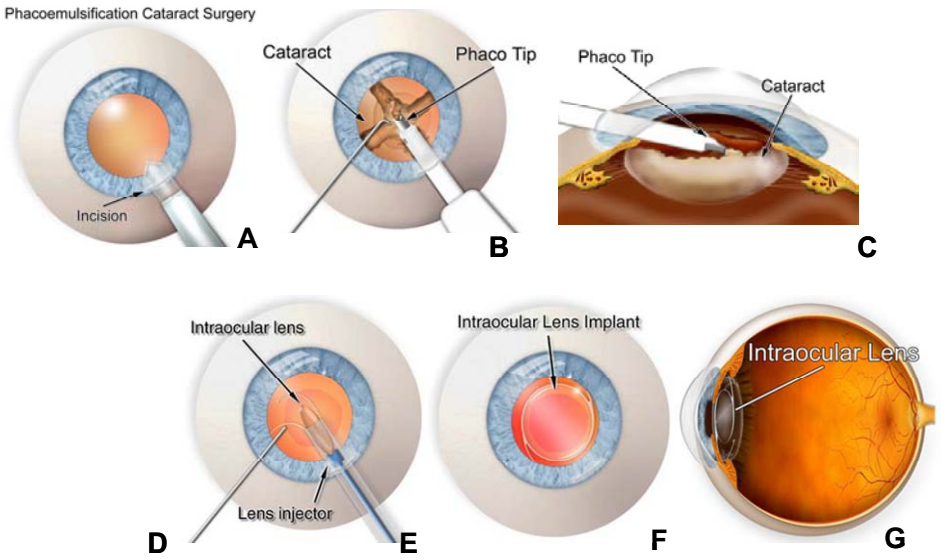

Figure 1.16. Illustration of the cataract surgery procedure. **A.** Incision. All the surgeries reported in this tesis used 3.2-mm superior incisions. **B.** Capsulorhexis: The surgeon creates an opening in the capsule. **C.** Phacoemulsification. Ultrasonic vibrations are used to break the cataract into smaller fragments that are then aspirated from the eye using the same instrumentation. **D.** Creation of grooves in the cataract. **E.** Once the denser central nucleus of the cataract has been removed, the softer peripheral cortex of the cataract is removed using an irrigation/aspiration handpiece. The posterior or back side of the lens capsule is left intact to help support the intraocular lens implant. **F.** Injection of the intraocular lens. **G.** Intraocular lens implanted.

5.2 New designs of intraocular lenses.

Since 1949, when Ridley first introduced an artificial intraocular lens (IOL), the design and material used to make the IOL has been in a continuous evolution to find the ideal IOL design to minimize decentration, dislocation, optical aberrations and the most biocompatible material (Doan, Olson & Mamalis, 2002). The original IOL that Ridley implanted was made of rigid polymethyl methacrylate (PMMA), inserted through an extracapsular route with a relatively large wound inducing postoperative astigmatism, with a long healing process and slow recovery despite the proven biocompatibility. Since then, significant advances have been made in materials that reduce the risk of posterior capsule opacification (i.e. hydrophobic acrylic and some silicone materials (Hayashi, Hayashi & Nakao, 1998)) can be easily folded, and allow thinner optics and therefore smaller wound size due to their higher indices of refraction. Efforts have also been directed to better haptic designs, and multiple designs are available either as single piece or three piece-IOLs. The design of the haptics is critical to prevent forces that may cause capsular bag contraction, leading to movement, rotation, tilt and decentration

(Faucher & Rootman, 2001, Petersen, Bluth & Campion, 2000). Another important aspect of the design affects the IOL edge. For example, it is well known that squared edges create a capsular bend that stops the posterior capsular opacification (Nishi, Nishi & Akura, 2001, Schmack & Gerstmeyer, 2000), but allow for reflection of light internally producing higher rate of glare (Ellis, 2001, Farbowitz, Zabriskie & Crandall, 2000). Newer designs have a frosted edged or rounded anterior edge to prevent the formation of those images. Finally, the most critical design parameter affecting retinal image quality is the shape of the IOL surfaces (radii of curvature, asphericities and shape factor for monofocal lenses (Barbero & Marcos, 2007, Tabenero, Piers & Artal, 2007), and more complex relationships in multifocal or pseudo-acomodative IOLs. A major goal in current cataract refractive surgery is to achieve ametropia (with monofocal designs), or extended range of focus in multifocal or pseudo-accommodative designs. In this regard, accurate ocular biometry and reliable methods to determine the required IOL power are essential. A good control of high order aberrations with IOLs will allow to improve those primary goals and optimise retinal image quality.

5.2.1 Monofocal Intraocular lenses: spherical and aspheric surfaces

Monofocal IOLs attempt to produce optimal retinal image quality at a single plane of focus (generally infinity). Until recently, most common designs exhibited spherical anterior and posterior surfaces. Spherical IOLs show inherent spherical aberration, which generally adds up to the spherical aberration of the cornea, which as described in 4.4 is typically positive. Still, an appropriate choice of design parameters of spherical IOLs can optimise retinal image quality (spherical aberration in combination with defocus) (Barbero & Marcos, 2007). The advantages of having a finite amount of residual positive spherical aberration are known to include: an increased depth of focus (Marcos et al., 2005) , which in certain circumstances may partially compensate for loss of accommodation in a presbyopic eye; positive spherical aberration may help patients with hyperopic postoperative refraction; and modest amounts of positive spherical aberration may mitigate the adverse effects of chromatic aberration and higher order monochromatic aberrations (McLellan, Marcos, Prieto & Burns, 2002) .

Examples of spherical IOLs used in this thesis are Acrysof SA60AT (Alcon) or Ceeon 912 (Pharmacia).

Aspheric IOLs have a controlled amount of inherent negative spherical aberration and mimics that of a healthy natural crystalline lens in a relaxed state.

Examples of the aspheric intraocular lenses used in this thesis are the Tecnis Z9000 (AMO) IOL (Altmann, 2005), made of silicone, refractive index of 1.458, with an anterior aspheric surface, and Acrysof IQ (Alcon) with a posterior aspheric surface. Figure 1.17 shows aberrations patterns in eyes after implantation of spherical and aspheric intraocular lenses.

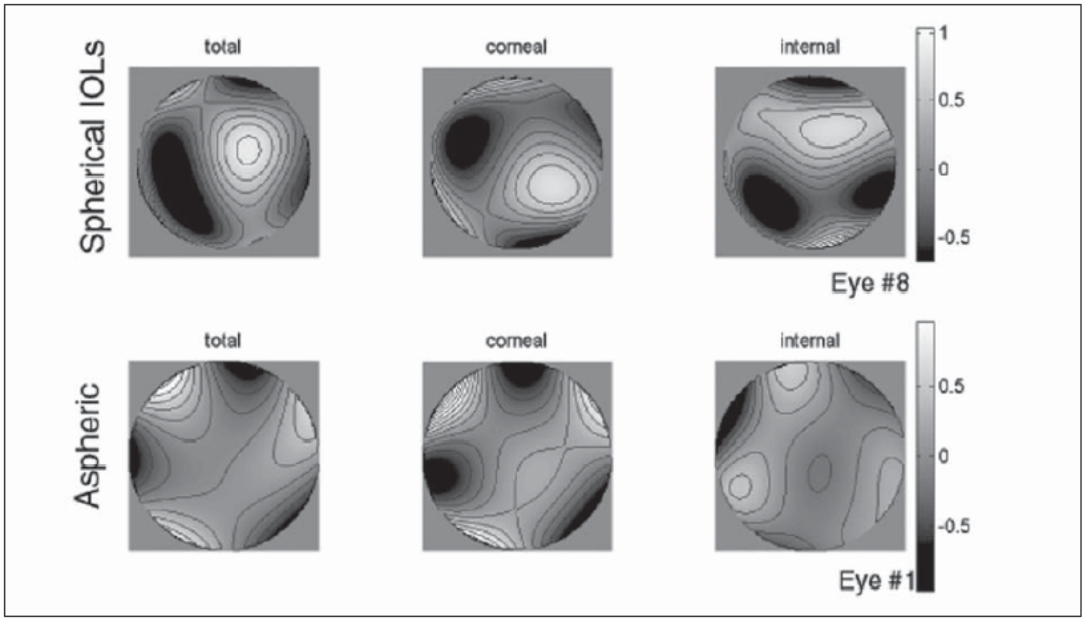

Figure 1.17. Example of corneal, internal and total aberration patterns (referred to the pupil center) in eyes after implantation of spherical and aspheric intraocular lenses adapted from Marcos (Marcos, Barbero & Jiménez-Alfaro, 2005). Pupil diameter: 4.5 mm).

5.2.2. Multifocal Intraocular Lenses

As opposed to monofocal IOLs, multifocal IOLs (McDonald, 2003) attempt to provide usable vision at various focal planes (far, intermediate, or near). In general, they are based on two possible different approaches: *1) Refractive multifocal IOLs* show different refractive concentric zones, some of which focus light from near objects, some from intermediate objects and some from distance objects that distributes light over the optical zones to provide near, intermediate, and distance vision. *2) Diffractive Multifocal IOL* (Lee & Simpson, 1997) are diffractive optic elements that produce typically two foci, one for near and the other one for far vision (with light intensity distribution dependent on the design). Other designs (Altmann, Nichamin, Lane & Pepose, 2005) combine a diffractive design with central and peripheral refractive areas.

None of the experiments presented in this thesis involves patients with multifocal IOLs, but some of the techniques developed (i.e. IOL tilt and decentration measurements with Purkinje imaging) could be applied to this case (of particular relevance to refractive multifocal IOLs with multiple bands, which rely on an accurate centration).

5.2.3.Accommodative lenses

Accommodating intraocular lens (IOL) assemblies have been developed that comprise an IOL that moves in response to ciliary muscular contraction and relaxation, thereby to simulate the movement of the natural lens in the eye, and, inter alia, help provide patients with better focusing ability (Israel, 2003).

There are several types of accommodative intraocular lenses, including: 1) *Single-optic accommodative lens designs* The mechanism of action is based on the concept of relaxation of zonular fibers with contraction of the ciliary body, leading to relaxation of the capsular bag and forward movement of the intraocular lens at the hinged haptics (Helmholtz theory); 2) *Two-optic accommodative lens design (Peng, Yang & Zhang, 2005)* with two lenses that move relative to each other along the optical axis of the lens system in reaction to movement of the ciliary muscle.

None of the experiments presented in this thesis involves patients with accommodative IOLs, but some of the techniques developed (i.e. IOL tilt and decentration measurements with Purkinje imaging) could be applied to this case (of particular relevance due to the moving nature of these lenses). Also, the customized computer model eyes developed in these thesis could be used to accurately predict their optical performance.

5.2.4 Other innovative pseudophakic IOL designs

Multiple IOL approaches are still under investigation or clinical trials. Based on the innovation and potential, we highlight *1) Light Adjustable IOLs:* The LAL is a photosensitive silicone intraocular lens whose power can be adjusted noninvasively and cured after implantation using a low-power light source. It is primarily devised as a monofocal implant, and other than focus, higher order aberrations could be optimised (i.e. correcting post-operatively corneal aberrations). The technology developed in this thesis is well suited for the in vivo characterization of this devices. 2) Hydrophobic acrylic gel polymer (Ho, Erickson, Manns & Parel, 2006), as a method to restore

accommodation using a thermodynamic material sensible to the changes of temperature that would replace the crystalline lens material and could be dynamically reshaped by the capsule, as in a young crystalline lens. The phakometry techniques developed in this thesis are ideal to fully characterize the changes in lens curvature with this implanted material in vivo.

5.2.5. Phakic lenses

Typically designed to correct high myopia in young patients, phakic IOLs (Tran & van Noy, 2003), unlike in clear lens extraction, are implanted without removal of the crystalline lens of the eye. Patients undergoing this procedure can retain any pre-existing focusing ability. In the phakic IOL procedure, a lens, made of plastic or silicone, is placed inside the eye. There are three designs under development (IOLs placed in front of the iris, iris claw lens, attached on the front of the iris and so-called Implantable Contact Lens, or ICL placed between the iris and crystalline lens). We have not included this type of implant in this thesis, but the technology developed could be equally applied to these cases.

5.3 Optical quality of eyes after cataract surgery.

The advances produced in cataract surgery, particularly foldable intraocular lenses that allow implantation through small incisions, or more sophisticated optical surfaces will definitely have an impact on the optical outcomes. To evaluate optical quality of eyes after cataract surgery is important to study the efficiency of those new designs.

Double-pass retinal image quality was first used to evaluate objectively optical quality after cataract surgery (Artal, Marcos, Navarro, Miranda & Ferro, 1995, Hayashi, Hayashi, Nakao & Hayashi, 2000, Guirao et al., 2002). This technique was used to compare optical performance and depth-of-field between multi- and monofocal IOLs (Artal et al., 1995). Also, a comparison of the double pass retinal quality of patients after cataract surgery with an age matched control group, and with healthy young subjects, showed that pseudophakic eyes' optical quality was worse than of healthy younger subjects. This suggests that factors associated to the implantation, the design of the lens, and the lack of aberration coupling in eyes with IOLs (as opposed to young crystalline lenses) contributed to optical image degradation.

Barbero (Barbero et al., 2003) measured for the first time in vivo corneal, total and internal aberrations of patients after cataract surgery. Measurements of the aberrations of the individual optical components allowed better identify sources of optical aberrations. This study showed (as later reported in more eyes in a study by Guirao (Guirao, Tejedor & Artal, 2004) and another study presented in Chapter 7 of this thesis) a slight increase in corneal aberrations due to the incision.

More recently, studies on ocular aberrations and visual performance with newer IOL designs have been presented. Marcos (Marcos et al., 2005) in a comparative study of patients wih spherical and aspherical IOLs implanted (Holladay, Piers, Koranyi, van der Mooren & Norrby, 2002), found that eyes with aspheric IOLs showed spherical aberration not significantly different from zero. However, tolerance to defocus was lower in these eyes (Marcos et al., 2005, Rocha, Soriano, Chalita, Yamada, Bottós, Bottós, Morimoto & Nosé, 2006). Recent studies have addressed ocular aberrations in eyes with other types of IOLs (Chung, Lee, Lee, Seo & Kim, 2007)

While the description of the optical performance in eyes with IOLs is interesting, as it can provide insights on the visual quality of the patients, the identification of the sources of these measured optical aberrations is essential to improve surgery and IOL designs. Chapters 7, 8 and 9 of this thesis will address the measurement and understanding of the impact of each factor contributing to optical performance in pseudophakic eyes and relating those to the ocular aberrations measured on these eyes.

6. HYPOTHESIS AND GOALS OF THIS THESIS

Our hypothesis is that knowledge of the crystalline lens/intraocular lens geometry and positioning will help us to better understand the optical quality of the normal and pseudophakic eye and accommodative mechanism of the eye. We will test this hypothesis by measuring crystalline lens curvature, tilt and decentration (with Purkinje and Scheimpflug imaging techniques implemented and validated in this thesis) in young human eyes and Rhesus Monkeys, and by measuring IOL tilt and decentration, ocular surface misalignments and corneal changes in eyes after cataract surgery. With the aid of customized computer eye models we will be able to predict the role of each factor to optical aberrations.

The specific goals of this thesis are:

1.- Development of custom technology, based on Purkinje imaging, to measure phakometry and tilt and decentration of the lens in vivo (Chapter 2).

2.- Implementation of processing algorithms for Scheimpflug images of the anterior segment of the eye to obtain lens shape and position (Chapter 3).

3.- Computer and experimental validations of the technology developed in this thesis, to test the assumptions and reliability of the techniques (Chapters 2, 4 and 5)

4.- Investigation of the radii of curvature and tilt and decentration of the crystalline lens in normal young human eyes in vivo, and their changes with accommodation (Chapter 4).

5.- Investigation of the changes in radii of curvature of the anterior and posterior crystalline lens surfaces and lens tilt and decentration with accommodation in vivo, in a rhesus monkey experimental model (Chapter 6).

6.- Assessment of the lens tilt and decentration (in two dimensions) in patients implanted with intraocular lenses (Chapter 2, 8 and 9).

7.- Evaluation of the changes induced by incision in cataract surgery measuring patients before and after implanation of intraocular lenses (Chapter 7).

8.- Study of the accuracy of computer eye models to predict ocular aberrations, in comparison with ocular aberrations measured on the same patients (Chapter 8)

9.- Quantification of the relative contribution of factors contributing to optical aberrations in patients implanted with intraocular lenses: corneal topography, intraocular lens geometry, lens tilt and decentration and line-of sight misalignment, using customized computer eye models, (Chapter 8).

10.- Investigation of the effect of tilt and decentration of the lens on the optical quality of the eye, and the passive or active nature of cornea and lens compensation mechanism in the human eye (Chapter 9).

METHODS:
Custom-developed Purkinje apparatus for phakometry and lens tilt and decentration

2

2. *Phakometry and lens tilt and decentration using a custom-developed Purkinje imaging apparatus: validation and measurements*

This chapter is based on the article by Rosales et al., *"Phakometry and lens tilt and decentration using a custom-developed Purkinje imaging apparatus: validation and measurements"* Journal of the Optical Society of America A. 2006. 23: p.509-520. Coauthor of the study is Susana Marcos. The contribution of Patricia Rosales to the study was to develop the Purkinje imaging system, to carry out the experiments to validate the system and the measurements of phakometry, tilt and decentration on patients, data analysis and the discussion of the results.

RESUMEN

Objetivos: Desarrollo de un sistema de detección de imágenes de Purkinje para la medida de radios de curvatura, inclinación y descentramiento del cristalino y lentes intraoculares. Se presenta una validación de la técnica a través de simulaciones computacionales, experimentos control y primeras medidas en 17 ojos normales (edad media: 26.67 ± 2.31 años) y nueve ojos de pacientes operados de cirugía de cataratas (edad media: 74 ± 2.3 años).

Métodos: Se ha diseñado un sistema de detección de imágenes de Purkinje que consiste en dos canales de iluminación, uno para el ojo derecho y otro para el izquierdo (con luz procedente de un único LED infrarrojo), con estos canales se mide la inclinación y el descentramiento, y otro canal de iluminación que consiste en dos LEDs infrarojos, para las medidas de facometría. Estas imágenes se capturan con una cámara sensible al infrarrojo con un objetivo telecéntrico para capturar las dobles imágenes de Purkinje reflejadas por las diferentes superficies oculares con los mismos aumentos. El sistema cuenta con un sistema de fijación que consiste en un "minidisplay" con resolución SVGA y un sistema de badal para la corrección de errores refractivos. Los radios de curvatura se obtuvieron a partir de estas imágenes empleando el Teorema del Espejo Equivalente y una función de Mérito. Para la obtención de la inclinación y el descentramiento se emplearon las ecuaciones de Phillips que consideran una relación lineal entre la posición de las imágenes de Purkinje, la rotación del ojo, el tilt y el descentramiento de la lente.

Resultados: Los valores de los radios de curvatura (±SD) medidos se encuentran entre 12.7±0.37 y 8.81± 0.21 mm y entre -5.64 ± 0.44 y -7.09±0.41 mm para las caras anterior y posterior del cristalino respectivamente. Los valores de inclinación del cristalino (±SD) se encuentran entre 2.8±0.4 y -2.87±0.34 deg en dirección horizontal y entre 2.58±0.27 y -1±0.31 deg en dirección vertical. Los valores de descentramiento (±SD) del cristalino obtenidos se encuentran entre 0.09±0.03 y 0.45±0.02 mm en dirección horizontal y entre 0.39±0.03 y

-0.22±0.82 mm en dirección vertical. La inclinación de las lentes intraoculares se encuentra entre 3.6±0.03 y -1.51±1.34 deg en dirección horizontal y entre 5.97±0.82 y -1.85±0.52 deg en la dirección vertical. El descentramiento de las lentes intraoculares se encuentra entre 0.53±0.06 y -0.31±0.23 mm en dirección horizontal y entre 0.13±0.08 y -0.96±0.07 mm en dirección vertical. Las medidas obtenidas para los radios de curvatura en promedio son de 10.61±1.13 y -6.15±0.41 mm, para las caras anterior y posterior del cristalino respectivamente, y de 11.21±0.86 y -11.3±0.91 para las caras anterior y posterior de la lente intraocular.

Conclusiones: Se ha desarrollado y validado mediante simulaciones computacionales un sistema para la detección de imágenes de Purkinje para la medida de radios de curvatura, inclinación y descentramiento en ojos de sujetos jóvenes con cristalino normal, y en pacientes operados de cirugía de cataratas. Tanto las validaciones como las medidas, muestran que las medidas obtenidas mediante este sistema son precisas, siendo el principal factor limitante, la asfericidad de las superficies oculares que producen una cierta sobre estimación del radio de curvatura. Las simulaciones muestran que las estimaciones tienen una precisión de 0.85 y 0.66 mm para el radio de la cara anterior de la lente y de 1.35 y 0.75 mm para el de la cara posterior, empleando tanto el método del espejo equivalente y la función de mérito respectivamente. La reproducibilidad de las medidas del radio de curvatura del cristalino es de 0.34 y 0.28 mm para las caras anterior y posterior del cristalino. Para la inclinación, la reproducibilidad es de 0.29 y 0.33 deg para la dirección horizontal y vertical respectivamente. Para el descentramiento, la reproducibilidad es de 0.03 y 0.02 mm para la dirección horizontal y vertical respectivamente. La reproducibilidad de las medidas de radios de curvatura de las lentes intraoculares es de 0.31 y 0.61 mm para las caras anterior y posterior de la lente introcular. Para la inclinación de lentes intraoculares la reproducibilidad es de 0.33 y 0.29 deg para la dirección horizontal y vertical respectivamente, y de 0.06 y 0.05 mm para el descentramiento en dirección horizontal y vertical respectivamente.

ABSTRACT

Purpose: We present a Purkinje Imaging system for phakometry and measurement of tilt and decentration of crystalline and intraocular lenses. We present a complete validation of the technique through exhaustive computer simulations and control experiments, and measurements in 17 normal eyes (mean age 26.67 ± 2.31 years) and 9 post-cataract surgery eyes (mean age 74±2.3 years).

Methods: The Purkinje imaging system consists of two illumination channels to illuminate the right and the left eye (with a single infrared LED each), to measure tilt and decentration, and other illuminating channel (with a double infrared LED) for phakometry measurements. Images of the eye with reflection of the LED's light from the different ocular surfaces (Purkinje images), were captured on a videocamera with an infrared sensitive CCD, and a telecentric lens to capture Purkinje images with the same magnification. The system also includes a fixation channel with a minidisplay and a Badal system to correct refractive errors. Lens radii of curvature were calculated using the equivalent mirror theorem and a merit function. To obtain lens tilt and decentration Phillips' equations were used, assuming a linear relation between the Purkinje images positions, rotation of the eye and lens tilt and decentration.

Results: Crystalline lens radii (±SD) ranged from 12.7±0.37 to 8.81± 0.21 mm and from -5.64 ± 0.44 to -7.09± 0.41 mm for anterior and posterior surface respectively. Crystalline lens tilt (±SD) ranged from 2.8±0.4 to -2.87±0.34 deg horizontally and 2.58±0.27 to -1±0.31 deg vertically. Crystalline lens decentration (±SD) ranged from 0.09±0.031 to 0.45±0.02 mm horizontally and from -0.22±0.82 mm to 0.39±0.03 mm vertically. IOL tilt ranged (±SD) from 3.6±0.03 to -1.51±1.34 deg horizontally and 5.97±0.08 to -1.85±0.52 deg vertically. IOL decentration (±SD) ranged from 0.53±0.06 to -0.31±0.23 mm horizontally and from 0.13±0.08 to -0.96±0.07 mm vertically.

Conclusions: A Purkinje imaging system has been developed and computationally validated for phakometry, lens tilt and decentration measurements, in phakic and pseudophakic eyes. Simulations and computational validations show that measurements obtained with this method are accurate. The asphericity of the ocular surfaces cause a certain overestimation of the lens radius of curvature, that can be avoided if Purkinje images are obtained near the pupil center where the ocular surfaces can be considered as spherical. Computer simulations show estimates should be accurate within 0.85 and 0.66 mm for the retrieved anterior lens radius of curvature, and within 1.35 and 0.75 mm for the retrieved posterior lens radius of curvature with the equivalent mirror and merit function methods, respectively, and within 0.25 deg and 0.013 mm for the retrieved lens tilt and decentration. Average reproducibility of lens radius of curvature measurement is 0.34 mm and 0.28 mm for the anterior and posterior surfaces of the phakic eye and 0.31 mm and 0.61 mm for the anterior and posterior surfaces of the pseudophakic eye. Average reproducibility for lens tilt and decentration of the phakic eye is 0.33 and 0.29 deg for horizontal and vertical tilt, respectively, and 0.03 and 0.02 mm for horizontal and vertical decentration, respectively. For the pseudophakic eye, average reproducibility for intraocular lens tilt is 0.55 and 0.6 deg for horizontal and vertical tilt, respectively, and 0.06 and 0.05 mm for horizontal and vertical decentration, respectively.

1. INTRODUCTION

Purkinje images are reflections of the light from anterior and posterior corneal surfaces (first and second Purkinje images, PI, PII although PII is difficult to image because it is overlaped by PI), and from anterior and posterior crystalline lens surfaces (third and fourth Purkinje images, PIII, PIV). They have been used for more than a century to assess properties of the cornea and crystalline lens. A more extensive historical background is provided in the introduction of this thesis. Purkinje images I, III and IV can be captured by imaging the eye's pupil, since they are formed within close distance of the pupillary plane (particulary PI and PIV). For example, for the Le Grand Model eye, for an object placed at 1 m, with a height of 18mm, the height of PIII relative to the height of the PI image is $\frac{h_3}{h_1} = 1.96$ and the height of PIV relative to the height of the PI image is $\frac{h_4}{h_1} = 0.76$. The position of the Purkinje images relative to the anterior cornea are 3.89 mm, 10.72 mm and 4.34 mm for PI, PIII and PIV, respectively. PI and PIV are relatively near to each other, so they are approximately in the same plane of focus, while PIII image is formed in a different plane.

Therefore, to visualize the three Purkinje images, the camera of a system for Purkinje image detection should be focused at different planes or a telecentric lens used to visualize the three Purkinje images in the same plane with the same magnification. Typically, illumination is performed off-axis to avoid overlapping of the images. In this thesis we developed a Purkinje-imaging based apparatus to measure the anterior and posterior radii of curvature and tilt and decentration of the crystalline lens or intraocular lenses in vivo. One of the earlier studies by Wulfeck (Wulfeck, 1955) described a system to image the third Purkinje Image using infrared photography, and established the basis of the current systems. Van Veen and Goss (Van Veen, 1988) presented a Purkinje Image system with a still flash camera. A similar system was used by Sorsby (Sorsby, Benjamin & Sheridan, 1961) in their studies correlating refractive error and geometrical properties of the ocular components. Mutti (Mutti, Zadnik & Adams, 1992) used a video camera for the first time and introduced a telecentric stop lens (which eliminates changes in magnification when an image is defocused) to record the three Purkinje images simultaneously (Zadnik, Mutti, Mitchell, Jones, Burr & Moeschberger, 2004).

Our phakometry system is based on previous developments by Smith and Garner (Smith & Garner, 1996) , the "Equivalent Mirror Theorem", and the method reported by Garner (Garner, 1997) based on an iterative method defining a "Merit Function". Lens tilt and decentration mesurements where obtained from equations presented by Phillips (Phillips, Perez-Emmanuelli, Rosskothen & Koester, 1988), that assume a linear relationship between Purkinje images positions and eye rotation, lens tilt and decentration.

Apart from phakometry, Purkinje images can also provide information on tilt and decentration of the ocular components and the lens in particular, which can be related to the optical quality of the eye. Several methodologies have been proposed to estimate lens tilt and decentration from Purkinje imaging systems. Several works, mainly from the clinical literature, estimate lens tilt by presenting to the subject fixation targets at different eccentricities and determining the fixation angle that produces an overlap of PIII and PIV (Guyton, Uozato & Wisnick, 1990). Phillips (Phillips et al., 1988) proposed a linear relation between Purkinje images locations and rotation of the eye, tilt and decentration of the lens in patients with IOLs. This methodology was validated and extensively used by Barry et al. in several studies of the misalignment of the ocular components (Barry, Branmann & Dunne, 1997, Barry, Dunne & Kirschkamp, 2001, Kirschkamp, Dunne & Barry, 2004).

Despite the fact that the use of Purkinje images to do phakometry and to measure tilt and decentration of the lens is well known, to our knowledge the description of the practical implementation of a compact system to measure both the normal lens and intraocular lens phakometry, tilt and decentration (in all orientations) has never been presented. In this thesis we designed a portable device to provide complete information of lens phakometry and positioning, and performed a thorough analysis of its performance through computational simulations (this Chapter) and validation experiments (Chapters 5 and 6).

In this chapter we present: 1) The design of the experimental set-up of a Purkinje imaging system. 2) A description of the algorithms developed to retrieve lens radii of curvature, lens tilt and decentration, and a comparison of the performance of the Equivalent Mirror and the Merit Function methods. 3) Computational validations of the measurements: The performance of the Equivalent mirror theorem and Merit function methods for phakometry has been assessed, in particular, the limitations that arise from considering paraxial optics, spherical surfaces, or constant refractive gradient index.

Models have been developed using real data obtained for individual eyes. The same eye models are used to evaluate the performance of Phillips' linear equations to obtain lens tilt and decentration. 4) First measurements of phakometry, lens tilt and decentration on young subjects with normal crystalline lens and on patients with IOLs.

This system, or slight modifications of it (adding a channel for central fixation or adding a mirror to reflect the fixation stimulus), was used in this thesis to: 1) Measure tilt and decentration in normal eyes and patients with intraocular lenses, presented in this chapter; 2) Compare phakometry measurements from Purkinje images and Scheimpflug imaging in the same set of phakic eyes (Chapter 5); 3) Compare tilt and decentration measurements from Purkinje and Scheimpflug imaging in a model eye, phakic and aphakic eyes (Chapter 6); 4) Compare measured and simulated aberrations in eyes with intraocular lenses, to identify the contribution of different factors, including IOL tilt and decentration, on optical quality degradation with cataract surgery (Chapter 9); 5) To evaluate the active or passive nature of the compensation of corneal coma by the crystalline lens, using pseudophakic eyes as a model (Chapter 10).

2. PURKINJE IMAGING

2.1 Optical Set up

Figure 2.1 and Figure 2.2 show, respectively, a schematic diagram and a photograph of the optical implementation of the Purkinje imaging set-up at the Visual Optics and Biophotonics Lab (Instituto de Optica, CSIC). The system is mounted on a 500 x 400 mm optical table. It has a symmetrical configuration for measurements on right and left eyes. The light sources are 880-nm LEDs (SFH485, Osram, 5-mm diameter, 22-deg emission angle; Maximum Radiant Intensity 80 mW/sr). Light from LED1 and LED2 is collimated by L1 and L2 (focal length= 125 mm, diameter= 12.5 mm). These channels illuminate the eye at an angle of 12 deg and are used for lens tilt/decentration measurements. Double LEDs (D-L1 and D-L2), separated by 18 mm and mounted at a distance of 65 mm from the eye at an angle of 15 deg were used to perform phakometry. The imaging channel consists of an IR-enhanced CCD camera (CV-M50IR, JAI) provided with a 55 mm focal length telecentric lens (Edmund Optics Ltd) mounted at a distance of 260 mm from the eye and focused at the pupil plane. This configuration resulted on a scale of 0.018 mm/pixel on the CCD chip. A third channel

projects a visual stimulus (FT) for foveal and eccentric fixations. It consists of a 12 x 9 mm minidisplay (Liteye Systems, pixel size 15x15μm), subtending a visual field of 7 deg, and a Badal system to correct for refractive errors and to meet different accommodation demands. The minidisplay has SVGA resolution and allows presentation of multiple targets. The Badal system consists of three lenses (L3 and L4 and L5, focal length=125 mm) allowing refractive corrections ranging from -8 to 8 D.

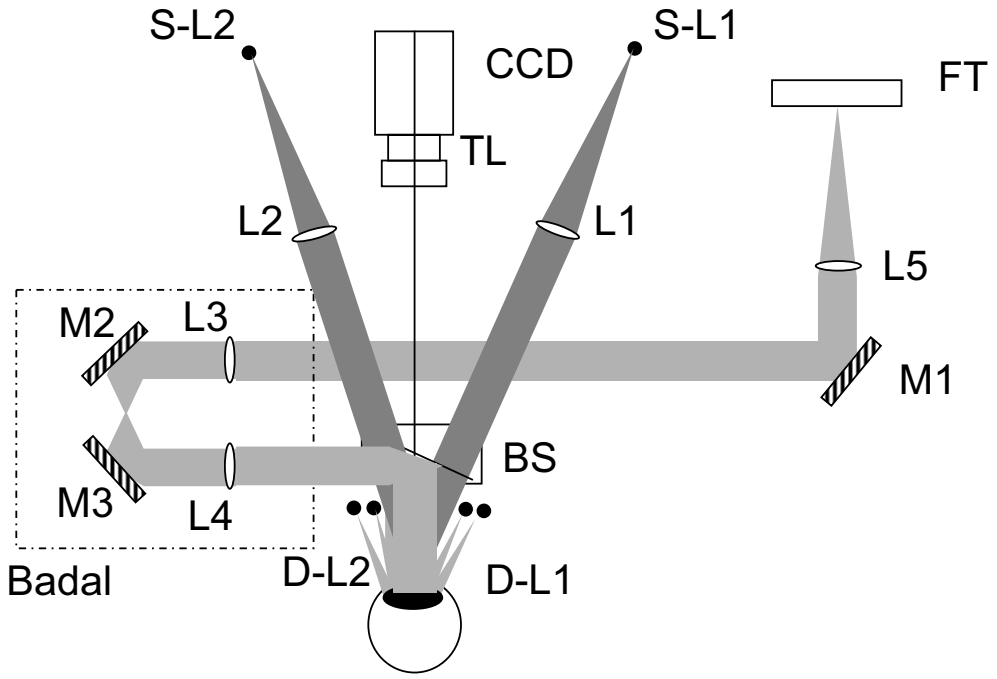

Figure 2.1. Diagram of the Purkinje Imaging system optical setup, with single LEDs (S-L1 and S-L2) collimated with achromatic lenses L1 and L2 (f=125 mm, ϕ = 25mm) for measurements of tilt and decentration on right and left eyes, and double LEDs (D-L1 and D-L2) for phakometry. Images are captured on a CCD camera with telecentric lens (TL). Fixation targets (FT) are presented on a minidisplay, collimated by L5 (f=125mm, ϕ = 38 mm) and inserted into the system with mirror M1. Illumination and imaging channels are separated by a hot mirror acting as a beam splitter (BS). A Badal system consisting of two mirrors (M2, M3) and three lenses (L3, L4 (f=125 mm, ϕ = 25mm), L5 (f=125 mm, ϕ = 38 mm)) allows for correction of refraction and for compliance of accommodative demands.

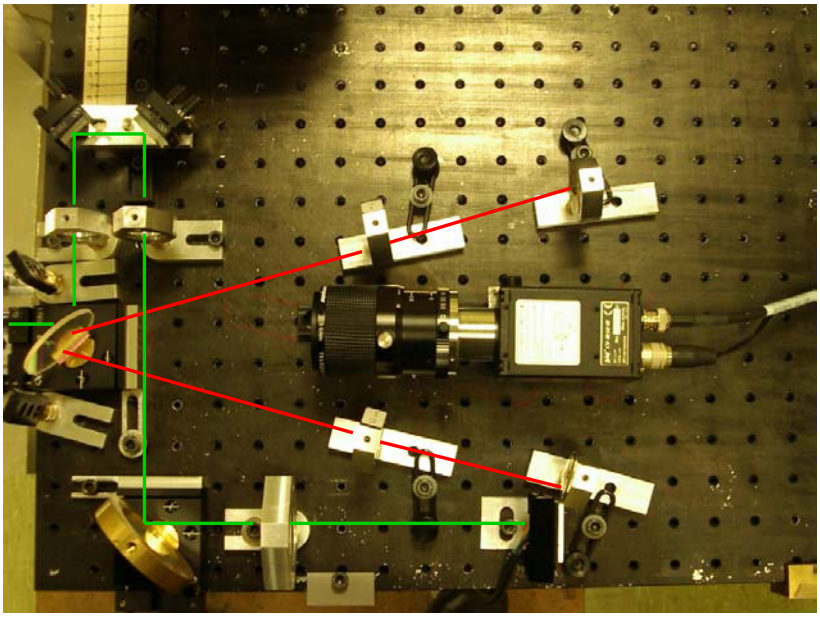

Figure 2.2. Physical set-up of the Purkinje imaging system

The system is controlled automatically with software written in Visual Basic (Microsoft Visual Studio, 6.0). The Windows-based program incorporates capture of pupillary images (by means of an acquisition board), presentation of targets on the system´s minidisplay (with a simultaneous view of the target on the controlling program), and patients data handling. For phakometry mesurements, the program controls the fixation target on the screen, so when the double Purkinje images are overlapped, the fixation target is moved until we obtain an image with separated Pukinje images. A screen capture of the software running the system is shown in Figure 2. 3.

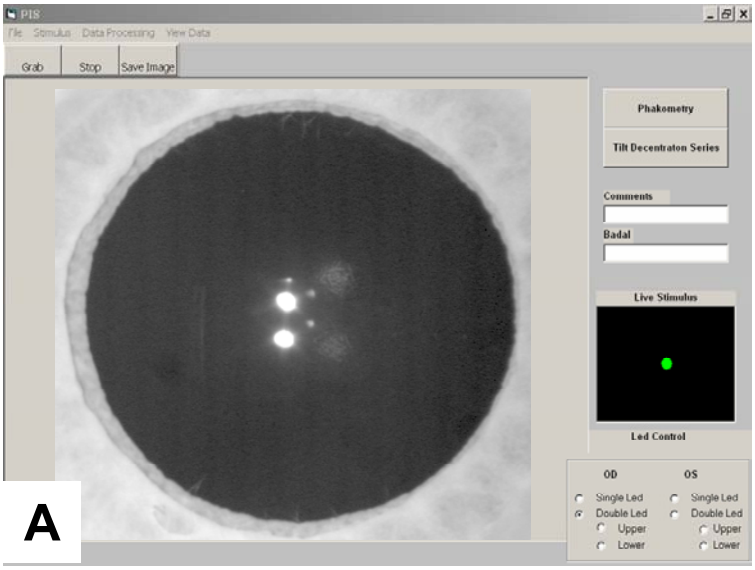

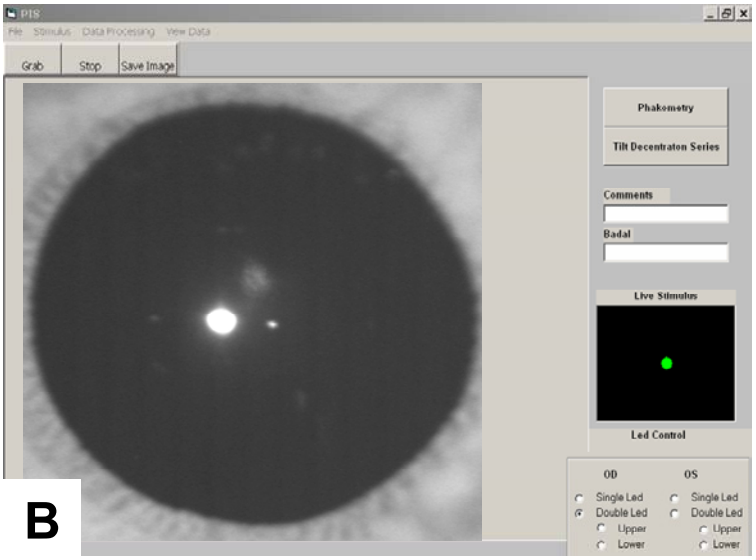

Figure 2.3.A. Image of the software running the system. Typical image of the phakometry mode. The software window contains a menu for file management, stimulus control, data processing. The pupilary image can be continuously viewed, sequences can be grabbed or images saved. **B.** Typical image of Tilt/Decentration mode. A live image of the stimulus viewed by the subject at each moment appears on the right bottom corner to the experimenter. For phakometry experiments, pushing the phakometry button activates the control of the fixation stimulus with the mouse that enables the shift of the fixation stimulus to different positions on the minidisplay. When the tilt and decentration button is clicked, the spot moves automatically to ten positions, for each of which pupilary images (such as that shown in 3.B. are grabbed). It is possible to save information about incidents during the measurement and about the Badal system in the comments and Badal boxes. Future control of the LEDs will be possible with the options that appear on the right bottom corner.

This system was modified to perform different studies. For a comparison to phakometry measurements with Scheimpflug imaging (Chapter 4), the Badal system was removed and a mirror was added. A channel for central illumination was inserted to obtain angle lambda to build a model eye to predict ocular aberrations after cataract surgery and to evaluate the compensation of spherical aberration and coma with aspheric IOLs (Chapter 9).

2.2 Purkinje image processing

We estimate the location of the Purkinje images referred to the pupil center. The center of the pupil is estimated by detection of the pupil margin which is fitted to a circle. The positions of the Purkinje images obtained from the reflection of the single

LED on the different ocular surfacesare detected through a Gaussian fitting with routines written in Matlab.

2.3 Phakometry

2.3.1. The Merit Function.

This is an iterative method, implemented by Garner (Garner, 1997), for calculation of the radius of curvature of both the anterior and posterior surfaces of the crystalline lens that can be applied to instruments with finite object distances, with objects of different heights and with stationary or mobile objects. For the context of this thesis, it will be used to the case of a stationary object.

The merit functions to evaluate are given by:

$$f_3 = \left[\left[\frac{h_3}{h_1}\right]_{theoretical}\right]^2 - \left[\left[\frac{h_3}{h_1}\right]_{\text{experimental}}\right]^2$$

$$f_4 = \left[\left[\frac{h_4}{h_1}\right]_{theoretical}\right]^2 - \left[\left[\frac{h_4}{h_1}\right]_{experimental}\right]^2 \qquad [2.1]$$

where $[h_3/h_1]_{\text{experimental}}$, $[h_4/h_1]_{\text{experimental}}$, are the experimentally obtained heights of PIII and PIV relative to PI, and $[h_3/h_1]_{\text{theoretical}}$, $[h_3/h_1]_{\text{theoretical}}$ are the height of PIII and PIV images relative to the height of PI, theoretically calculated from ray tracing. From initial values for the lens radius of curvature these are changed, until the merit function f_3 and f_4 reaches a minimum value.

To perform the ray tracing, the paraxial approximation is assumed and surfaces are considered to be spherical, therefore the image formed by refraction will be given by:

$$l'' = \frac{n_2 l r}{n_1 r + l(n_2 - n_1)}, \qquad [2.2]$$

Where l and l'' are the distances of the object in the object and image planes, respectively, n_1 and n_2 are the refractive index in the object and image space, respectively.

The reflected image can be found by substituting $n_2 = -n_1$ to obtain:

$$l'' = \frac{lr}{(2l - r)} \qquad [2.3]$$

The schematic eye used for ray tracing is given in Figure 2. 4.

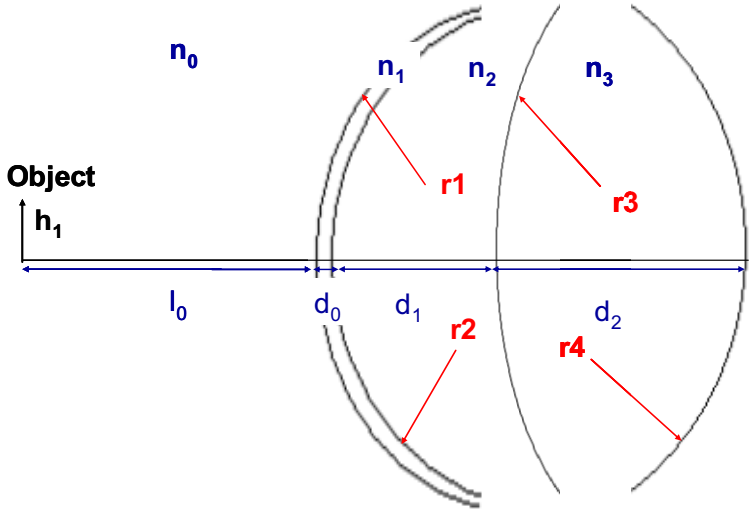

Figure 2.4. Schematic eye for paraxial ray tracing to obtain lens radius from the Merit Function.

r1, r2 are the anterior and posterior cornea radii of curvature, respectively, r3 and r4 are the anterior and posterior lens radii of curvature.

d_0= Corneal thickness, d_1 = Anterior chamber depth, d_2 = Lens thickness.

n_0 = Refractive index of the air, n_1 = Corneal refractive index, n_2 = Lens refractive index

The general paraxial equation:

$$\frac{n_2}{l''} - \frac{n_1}{l} = \frac{n_2 - n_1}{r}, \qquad [2.4]$$

can be written for refraction in the forms given by the equations 2.2 and 2.3.

The transverse magnification is given by:

$$M = -\frac{l''}{l} = \frac{r}{(r - 2l)} \qquad [2.5]$$

Where l and $l^{"}$ are as in equation 2.3.

Those equations will be applied for refraction and reflection from the different ocular surfaces.

2.3.1.1. First Purkinje image height:

Reflection in the anterior cornea:

After reflection, the position of PI relative to the anterior cornea will be given:

$$l_1^{"} = \frac{l_0 r_1}{(2l_0 - r_1)} \qquad [2.6]$$

Where l_0 and $l_1^{"}$ are the distance of the object to the anterior cornea and the first Purkinje image position, respectively, r_1 is the anterior corneal radius of curvature. Therefore, magnification of PI is:

$$M_1 = \frac{l_1^{"}}{l_0} \qquad [2.7]$$

and the height of PI is given by

$$h_1^{"} = M_1 h_1 \qquad [2.8]$$

Where h_1 is the object height.

2.3.1.2. Third double image height:

Refraction in the anterior cornea:

$$l_{3\_ant\_cornea} = \frac{n_1 l_0 r_1}{r_1 + l_0(n_1 - n_0)} \qquad [2.9]$$

Referred to the posterior cornea:

$$l_{3\_ant\_cornea}^{"} = l_{3\_ant\_cornea} - d_0 \qquad [2.10]$$

Refraction in the posterior cornea:

$$l_{3\_post\_cornea} = \frac{n_2 l'_{3\_ant\_cornea} r_2}{r_2 + l'_{3\_ost\_cornea}(n_2 - n_1)} \qquad [2.11]$$

Referred to the anterior crystalline lens:

$$l''_{3\_ant\_crystalline} = l_{3\_post\_cornea} - d_1 \qquad [2.12]$$

Reflection in the anterior crystalline lens:

$$l_{3\_ant\_crist} = \frac{-l''_{3\_post\_cornea} r_3}{r_3 - 2l''_{3\_post\_cornea}} \qquad [2.13]$$

Here r_3 is the variable to evaluate in the Merit Function until a minimum is reached.

Referred to the posterior cornea:

$$l''_{3\_ant\_crist} = l_{3\_ant\_crist} + (d_1 - d_0) \qquad [2.14]$$

Refraction in the posterior cornea:

$$l_{3\_post\_corn\_2} = \frac{n_1 l''_{3\_ant\_crist} r_2}{n_2 r_2 + l''_{3\_ant\_crist}(n_1 - n_2)} \qquad [2.15]$$

Referred to the anterior cornea:

$$l''_{3\_post\_corn\_2} = l_{3\_post\_corn\_2} + d_0 \qquad [2.16]$$

Refraction in the anterior cornea:

$$l_{3\_ant\_cornea\_2} = \frac{n_1 l''_{3\_post\_cornea\_2} r_1}{n_2 r_1 + l''_{3\_post\_cornea\_2}(n_1 - n_2)} \qquad [2.17]$$

$l_{3\_ant\_cornea\_2} \equiv$ Position in z of PIII image referred to the anterior cornea.

Thus, magnification of PIII image would be:

$$M_3 = \frac{l_{3\_ant\_cornea} l_{3\_post\_cornea} l_{3\_ant\_cryst} l_{3\_post\_cornea\_2} l_{3\_ant\_cornea\_2}}{l''_{3\_ant\_cornea} l''_{3\_post\_cornea} l''_{3\_ant\_cryst} l''_{3\_post\_cornea\_2} l''_{3\_ant\_cornea\_2}} \qquad [2.18]$$

Hence, the theoretical heights of PIII and PI are:

$$\left.\begin{array}{l} h_3^{''} = h_1 M_3 \\ h_1^{''} = h_1 M_1 \end{array}\right\} \Longrightarrow \frac{h_3^{''}}{h_1^{''}} = \frac{M_3}{M_1} \qquad [2.19]$$

To evaluate the Merit function for PIV, the same procedure is followed, taking into account refraction in the anterior lens and reflection in the posterior lens surface.

2.3.2. The Equivalent Mirror Theorem

Smith and Garner (Smith & Garner, 1996) proposed a method to calculate the lens radii of curvature using the equivalent mirror theorem that states that an optical system consisting of a number of refracting surfaces followed by a reflecting surface can be replaced by a single "equivalent mirror". The Equivalent Mirror Theorem states that the vertex and center of curvature of the equivalent mirror are conjugates of the vertex and centre of curvature of the real mirror, imaged by the refracting surfaces. If the target is at infinity, the image formed by reflection is proportional to the focal length of the surface, which is equal to one-half of the radius of curvature of the surface. Hence, the radius of curvature of the equivalent mirror, can be easily calculated from the expression:

$r_3^{''} = r_1 \left[\frac{h_3^{''}}{h_1^{'}} \right]$, where $h_3^{''}$ and $h_1^{''}$, the heights of PIII and PI.

For a practical configuration, it is better to place the light source near the eye to obtain brighter images. Also, as it has been addressed before, while PI and PIV images are formed in planes quite near to each other, PIII is formed in a different plane. Therefore focus should be adjusted to obtain a sharper PIII image. To overcome this problem, a telecentric lens is used, that allows to image PI, PIII and PIV Purkinje images (which will appeared out of focus) with the same magnification. Smith and Garner proposed methods to calculate the equivalent mirror radius of curvature in three cases:

a) The distance from the target to the corneal vertex is fixed, and the camera is focused on PI and then on PIII and PIV. b) The target is fixed to the camera, and the camera is focused on PI and then on the PIII image. c) The camera is focused on PI image, and only one recording is made. Thus, while PI will be sharp, PIII will be blurred, and it may lead to a measured image height that is different from the focused image.

For the purposes of this thesis, option a) has been used, and, since the camera used to visualize the three Purkinje images has a telecentric stop, refocus is not necessary. According to this, the scheme of the ray tracing procedure can be summarized in Figure 2. 5.

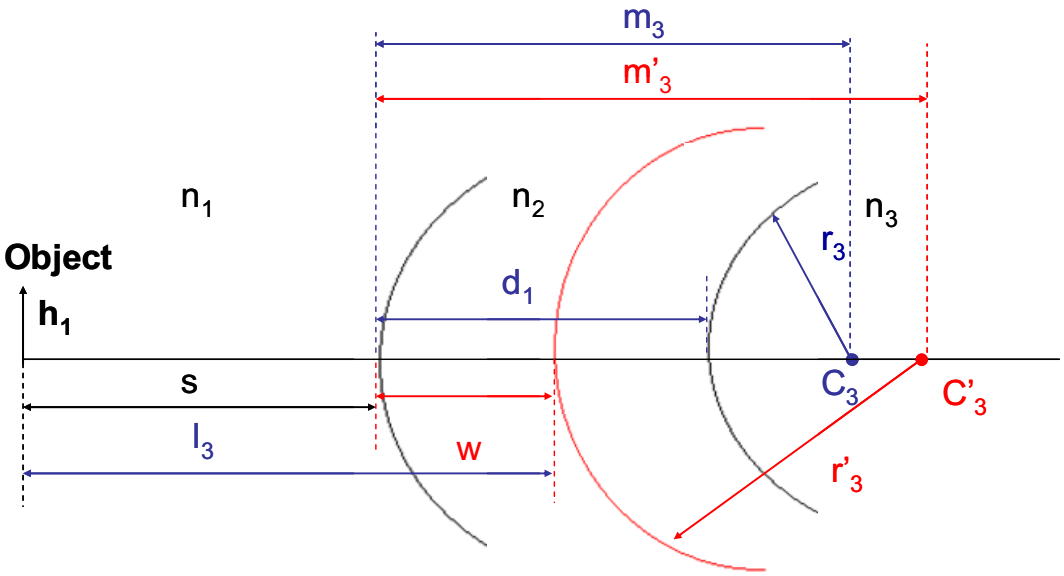

Figure 2.5. Schematic diagram for the Equivalent Mirror theorem

s is the distance of the object to the corneal vertex; l_3 is the distance of the object to the vertex of the Equivalent Mirror; w is the distance of the vertex of the anterior cornea to the vertex of the Equivalent Mirror; d_1 is the anterior Chamber depth; C_3 and C'_3 are the centers of curvature of the anterior lens and of the Equivalent Mirror for the anterior lens, respectively; r_3 and r_3'' are the radii of curvature of the anterior lens and of the Equivalent Mirror for the anterior lens, respectively; n_1, n_2, n_3, stand for the refractive index of air, cornea and lens respectively.

The radius of curvature r_3 of the anterior lens can be found using the equivalent mirror theorem by finding the positions of the vertex and centre of curvature of the equivalent mirror.

Considering that the refractive index in the object space is n_1 and the refractive index in the image space is n_2, applying equation 2.5.a, it follows that:

a) The distance w, distance from the image of the anterior surface of the lens to the corneal vertex, is given by:

$$w = \frac{n_1 d_1 r_1}{n_2 r_1 + d_1 (n_1 - n_2)} \qquad [2.20]$$

b) The distance $m_3^{"}$ from the corneal vertex to the center of curvature of the equivalent mirror is given by:

$$m_3^{"} = w + r_3^{"} \qquad [2.21]$$

where $r_3^{"}$ is the radius of the equivalent mirror.

Using equation 2.2 and given the same conditions for refractive index in image and object space, the position of the center of curvature of the anterior lens surface with respect to the corneal vertex is:

$$m_{\ 3} = \frac{n_2 m_3^{"} r_1}{n_1 r_1 + m_3^{"}\left(n_2 - n_1\right)} \qquad [2.22]$$

The equivalent anterior lens radius of curvature can be easily calculated:

The distance of the object to the corneal vertex is given by $l_1 = -s$, and the magnification after reflection in the anterior cornea is given by:

$$M_1 = \frac{h_1^{"}}{h_1} \qquad [2.23]$$

Magnification also can be expressed as:

$$M_1 = \frac{r_1}{\left(r_1 - 2l_1\right)} \qquad [2.24]$$

The vertex of the equivalent mirror is placed at $l_3 = -s - w$.

The magnification of PIII (from reflection of the "equivalent mirror" with an equivalent radius of curvature $r_3^{"}$) is given by:

$$M_3 = M_1\left[\frac{h_3^{"}}{h_1^{"}}\right], \qquad [2.25.a]$$

or alternatively by $M_3 = \frac{r_3^{"}}{\left(r_3^{"} - 2l_3\right)}$. [2.25.b]

From this expression, the radius of curvature of the equivalent mirror can be easily obtained:

$$r_3^{"} = \frac{2l_3 M_3}{\left(M_3 - 1\right)} \qquad [2.26]$$

With this expression for the radius of curvature of the equivalent mirror, the actual lens radius of curvature is given by:

$$r_3 = m_3 - d_1 \qquad [2.27]$$

The same procedure is followed to obtain the posterior lens radius of curvature.

In section 3.1 a computational study of the accuracy of the Equivalent Mirror and Merit Function methods will be presented. The assumptions made for the Merit Function are weaker than the used for the Equivalent Mirror Theorem, and can be applied under different conditions without change the procedure. Equivalent Mirror Theorem applied for finite targets, has been used in this thesis on a simpler three surfaces model eye, which can be the source of some inaccuracies although it could be used on a four surface model if the posterior corneal surface topography is known.

2.4 Lens tilt and decentration

The method to obtain lens tilt and decentration is based on that described by Phillips et al.(Phillips et al., 1988) and Barry et al. (Barry et al., 2001) in previous works. This method assumes a linear relation between Purkinje images positions and rotation of the eye, lens tilt and decentration.

$$\begin{aligned} P1 &= E\beta \\ P3 &= F\beta + A\alpha + Cd \\ P4 &= G\beta + B\alpha + Dd \end{aligned} \qquad [2.28]$$

where P1, P3 and P4 are the Purkinje images positions referred to the pupil center and β, α and d, are the rotation angle of the eye, tilt and decentration of the lens, respectively. These equations are applied to both horizontal and vertical coordinates.

To obtain the coefficients in these equations for each eye, we resort to simulated model eyes with spherical surfaces and the individual parameters available for each subject, using an optical design program (Zemax, Focus Software). The anterior corneal radius of curvature and anterior chamber depth were obtained from optical biometry, and anterior and posterior lens radii of curvatures were obtained from the phakometry

measurements. Corneal thickness, lens thickness and lens refractive index were taken as constant in all eyes, using data from the unaccommodated Gullstrand model eye. IOL parameters were obtained from published data on these lenses (Sverker, Artal, Piers, Mooren & et al, 2003) or data provided by the manufacturer. Indices of refraction for the wavelength of illumination were used, using conversion factors reported by the Herzberger formula (Herzberger, 1969) given by equation 2.31.

$$n = a + bL + cL^2 + d\lambda^2 + e\lambda^4 + f\lambda^6 \qquad [2.29]$$

with $L = \frac{1}{\lambda^2 - 0.028}$ and *a, b, c, d, e, f* being the dispersion coefficient data of the corresponding media provided by Zemax.

The optical surfaces were assumed to be spherical, although validations of the technique were performed incorporating aspheric surfaces, actual corneal topographies and gradient index of refraction into the models.

To obtain coefficients *E, F* and *G*, α and *d* are set to zero (no tilt and no decentration) in the model. We estimated the Purkinje images positions in equation [2.28] for different rotation angles, and calculated coefficients *E, F, G* by linear fitting of the slope. The same procedure was repeated for *A* and *B* (setting $\beta = 0$ and $d = 0$) and *C* and *D* (with $\beta = 0$ and $\alpha = 0$).

The rotation angle (β), tilt (α) and decentration of the lens (d) can then be solved using the individual coefficients for each eye and the experimental Purkinje image locations (P1, P3 and P4):

$$\begin{aligned} \beta &= \frac{P1}{E} \\ \alpha &= \frac{\left[\beta(DF - CG) + CP4 - DP3\right]}{\left[CB - DA\right]} \\ d &= \frac{\left[P3 - \beta F - \alpha A\right]}{C} \end{aligned} \qquad [2.30]$$

The procedure is done for both horizontal and vertical coordinates.

Horizontal tilt refers to tilt around y-axis and vertical tilt refers to tilt around the x-axis. Positive tilt around the horizontal axis (α_x) means that the superior edge of the lens moves closer to the cornea than the inferior edge, and vice versa for negative.

Positive tilt around the vertical axis (α_y) means that the nasal edge of the right lens or the temporal edge of the left lens moves backwards, and vice versa for negative.

Positive horizontal decentration (d_x) means that the right lens is shifted toward the nasal side or that the left lens is shifted towards the temporal side and vice versa for negative. Positive vertical decentration (d_y) indicates that the lens is shifted upwards and vice versa for negative. A scheme of the sign criteria for lens tilt and decentration is presented in Figure 2.6.

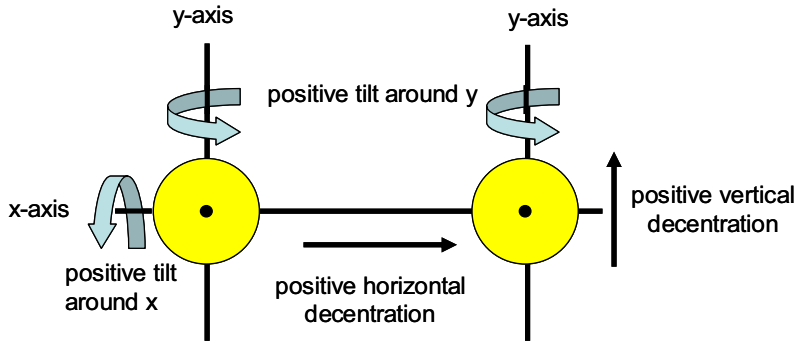

Figure 2.6. Scheme of the sign convention for lens tilt and decentration measurements as seen by the observer.

3. VALIDATION OF THE TECHNIQUE BY COMPUTER SIMULATIONS

We performed computer simulations to test individually the validity of the assumptions involved in the described procedures. Additionally, measurements in patients with IOLs allowed us to perform comparisons with nominal values and comparisons with other methods.

3.1 Test of Purkine phakometry methods using computer eye models

We performed computer simulations to test the performance of the Equivalent Mirror and Merit function approaches to obtain phakometry. Simulations are based on the same simplified eye model (spherical surfaces, constant refractive index) as the model that we used in the processing algorithms. Table 1 shows the parameters of the eye model used in the simulation, as well as the individual parameter that was varied in each case to test separately the impact of each of the assumptions. All simulations were performed in Zemax, using the actual experimental conditions for illumination (double LED, distance from the LED to the eye, and angle of illumination). The actual images

of PI, PIII and PIV were obtained by using ray tracing and intensity distribution analysis in Zemax. Figure 2.7 shows the retrieved Purkinje images positions from simulations in Zemax. As in the experiments, the locations of the double Purkinje images of PI, PIII and PIV were obtained by fitting Gaussian functions to the images. From those locations, we computed the relative heights. We used these values in the same algorithms that processed our experimental data and compared the resultant radii of curvature with the nominal values from the eye model. Table 1 shows the retrieved anterior and posterior lens radii of curvature for different combinations of anterior and posterior nominal lens radii of curvature in the model eye. For eyes with anterior lens radii ranging from 14 to 10 mm we found average discrepancies of 0.09 mm for the anterior lens and 1.12 mm for the posterior lens with the equivalent mirror method and 0.09 mm for the anterior lens and 0.33 mm for the posterior lens with the Merit function method. For eyes with posterior lens radii ranging from -4 to -6 mm, we found average discrepancies of 1.06 mm and 0.30 mm in the retrieved posterior lens radius of curvature with the merit function and equivalent mirror methods, respectively.

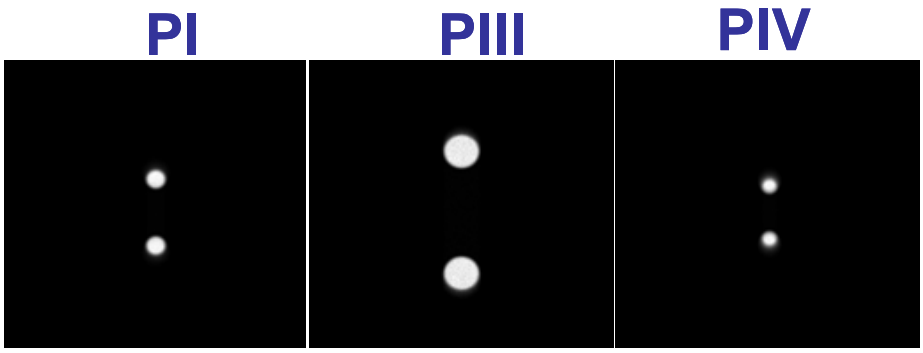

Figure 2.7. Example of simulated Purkinje images for phakometry evaluation, using Zemax.

Alternatively, we compared the experimental heights of the Purkinje images with those obtained through simulations in Zemax using the experimentally retrieved values of anterior and posterior lens radii of curvatures. We found average discrepancies of 0.009 mm for h_1, 0.131 mm for h_3, and 0.002 mm for h_4. The discrepancies in Purkinje images heights obtained experimentally and with simulations in Zemax, translated into radii of curvature differences of 0.366 mm and 0.075mm for the anterior lens (with the Equivalent Mirror method and the Merit function respectively) and 1.09 mm and 0.217 mm for the posterior lens. These discrepancies in h_1, h_3 and h_4 are close to the

distance measurement accuracy (taking into account that pixel resolution is 0.08 mm at the pupil plane).

We also performed simulations to assess the influence of possible tilt and decentration of the lens, corneal curvature, anterior chamber depth and lens thickness on the phakometry measurements.

3.1.1. Effect of lens tilt and decentration.

To evaluate possible effects of misalignment of the lens on the estimates of lens radii of curvature we simulated the same model eye with the parameters shown in Table 1, and a decentered and tilted lens. We obtained a discrepancy of 0.28 mm for the anterior lens and 1.55 mm for the posterior lens using the Equivalent Mirror method, and 0.66 mm for the anterior lens and 0.46mm for the posterior lens with the merit function method.

3.1.2. Effect of anterior and posterior corneal curvature.

We checked that the estimates were not affected by the nominal corneal curvatures. The anterior corneal radius of curvature was changed in the processing algorithm according to the nominal value of the model, while the posterior corneal radius of curvature was kept constant in the processing algorithm. For the values of the eye model shown in Table 1, and varying the anterior corneal curvature, we found average discrepancies of 0.12 and 0.29 mm for the retrieved anterior lens radius of curvature, and 1.02 and 0.21 mm and for the retrieved posterior lens radius of curvature, using the Equivalent Mirror and the Merit function methods respectively**.** For the fixed values of the model shown in Table 1, and varying the posterior corneal curvature, we found average discrepancies of 0.43 and 0.29 mm in the retrieved anterior lens radius of curvature with the Equivalent Mirror and Merit function methods respectively. For the posterior lens radius of curvature we found discrepancies of 1.14 and 0.16 mm with the Equivalent Mirror Theorem and Merit Function respectively**.**

3.1.3. Effect of Anterior Chamber depth.

When the anterior chamber depth was varied in a range consistent with values measured in real eyes (see Table 1), we found average discrepancies of 0.24 and 0.19 mm for the retrieved anterior lens radius of curvature, and of 1.33 and 0.33 mm for the

retrieved posterior lens radius of curvature, using the Equivalent Mirror and Merit function methods respectively. Additionally, we tested that discrepancies of 0.5 mm between the anterior chamber depth used in the model eye and that used in the simulation produced average discrepancies of 0.4 and 0.026 mm for the retrieved anterior lens radius of curvature, and of 1.46 and 0.41 mm for the retrieved posterior lens radius of curvature, with the Equivalent Mirror and Merit Function methods, respectively.

3.1.4. Effect of lens thickness.

We tested the effect of the assumption of a constant value for lens thickness, changing this parameter in the model eye (see Table 1) while keeping it constant in the processing algorithms. We found that discrepancies of 0.5 mm between the lens thickness value used in the model eye and that used in the simulation produced average discrepancies of 0.36 and 0.56 mm for the retrieved posterior lens radius of curvature with the equivalent mirror and merit function methods, respectively**.**

In summary, for the anterior lens radius of curvature, both methods work theoretically within accuracies <0.3 mm, and for the posterior lens the accuracies are within 1 mm for the Equivalent Mirror and 0.3 mm for the Merit function. The estimates are not significantly affected by the assumptions regarding posterior corneal radius of curvature and lens thickness, in particular when using the Merit function method.

In brief, these simulations show that, assuming spherical surfaces and for the experimental conditions of the system, the Merit Function provides accurate estimates of phakometry, while the Equivalent Mirror slightly overestimates the posterior lens radius of curvature for this model eye.

3.2 Test of lens tilt/decentratrion methods using computer eye models

We performed computer simulations to check the accuracy of the Phillips Equations retrieving tilts and decentrations. We built a computer model eye with nominal values as in Table 1 (row 7), imposing crystalline lens tilts and decentrations. Different combinations of tilt and decentrations were also tested (with eye rotations up to 3.5 deg,

lens tilts up to 5 deg and decentrations up to 0.25 mm). We estimated the coefficients of Eq. (2.28) for the model eye as described in subsection 3.1 for real eyes. Intensity distributions for Purkinje images PI, PIII and PIV were simulated as described above, for the actual experimental conditions of eye rotation and angle of illumination, and P1, P3 and P4 in Eq. (2.28) were estimated as in the experimental images. Eye rotation, lens tilt and decentration were obtained, as described for real eyes, by using Eq. (2.32). We found maximum discrepancies of 0.1 deg in eye rotation, 0.6 deg in lens tilt and 0.026 mm in decentration.

Using similar procedures, we simulated P1, P3 and P4 for measured values of anterior corneal radii of curvature, anterior and posterior crystalline lens radii of curvature, and anterior chamber depth in one of the measured patients and compared experimental locations of the Purkinje images with the predictions from Zemax. We found average discrepancies of 0.058 mm for P1 in the horizontal direction and 0.024 mm in the vertical direction, 0.024 mm for P3 in the horizontal direction and 0.03mm in the vertical direction, and 0.058 mm for P4 in the horizontal direction and 0.02 mm in the vertical direction.

Finally, we tested that discrepancies of 1 mm in the estimated anterior and posterior radii of curvature produced discrepancies of less than 0.2 deg in the tilt estimates and 0.01 mm in the decentration estimates.

3.3 Test of the validity of the assumptions in the model eye

The computer simulations presented in Table 1 were aimed at testing the validity of the procedures with the actual experimental conditions, but used simplified eye models with spherical surfaces and constant refractive index. We have performed additional simulations to test the impact of these assumptions on the estimated lens radii of curvature and lens tilt and decentration. The parameters of the model in each condition and the results are presented in Table 2. Purkinje images were simulated by using more realistic eye models, while phakometry and lens tilt and decentrations were obtained by using the same routines as those in previous simulations and in the experiments. Implicitly these tests also checked the validity of the paraxial approximation.

3.3.1. Effect of anterior corneal asphericity.

We assumed the same eye model than in previous simulations, but with anterior corneal conic constants consistent with reports from Dubbelman (Dubbelman, Weeber,

van der Heijde & Volker-Dieben, 2002) (see Table 2). The retrieved anterior lens radii differed from nominal values by 0.09 and 0.35 mm with the equivalent mirror and merit function methods, respectively, and the posterior lens radii differed by 0.94 and 0.13 mm, respectively.

3.3.2. Effect of corneal irregularities.

We replaced the theoretical cornea in the model eye by the corneal elevation map obtained with the corneal topographer in two real eyes (fit to a seventh order Zernike polynomial and described in Table 2 in terms of third and higher root-mean-square errors, excluding spherical terms). We found average discrepancies of 0.59 and 0.15 mm for the retrieved anterior lens radius of curvature and 0.9 and 0.35 mm for the retrieved posterior lens radius of curvature, using the Equivalent Mirror and Merit function methods, respectively.

3.3.3. Effect of anterior and posterior lens asphericities.

We used the same eye model as that in previous simulations but assuming lens asphericities consistent with reports from Dubbelman (Dubbelman & van der Heijde, 2001), as shown in Table 2. When the lens anterior surface asphericity was varied, we found that the estimates of anterior lens radii are only slightly affected by changes in anterior lens asphericity (average discrepancies of 0.54 and 0.16 mm with the equivalent mirror and merit function methods respectively), but that discrepancies in posterior lens radii are higher (average discrepancies of 2.19 and 0.98 mm, with the equivalent mirror and merit function methods respectively). The average discrepancies in the posterior lens radii (changing the posterior lens asphericity) were 2.3 and 1.07 mm, with the Equivalent Mirror and Merit Function methods, respectively. These simulations show that the Merit Function Method is more robust to the presence of aspheric surfaces and provides significantly better results than does the equivalent mirror method.

3.3.4. Effect of refractive gradient index in a realistic eye model.

Finally, we tested the accuracy of the phakometry methods and tilt/decentration estimates using the realistic eye model described in Table 2, rows 12-13. This included real anterior corneal elevation from corneal topography, aspheric posterior corneal surfaces, anterior and posterior aspheric lens surfaces, and, particularly, a gradient index distribution for the crystalline lens (based on the model proposed by Garner and Smith

(Garner & Smith, 1997)). With this model eye, we found a discrepancy of 0.85 and 0.66 mm for the retrieved anterior lens radius of curvature, and of 1.35 and 0.75 mm for the retrieved posterior lens radius of curvature with the equivalent mirror and merit function methods, respectively. These values are only slightly higher than the discrepancies obtained using the same eye model (with spherical surfaces and constant index of refraction) in the simulations and in the reconstructions algorithms.

We also checked that the approximations of the model did not affect the results of lens tilt and decentration. The coefficients in Phillips' equation changed by 8% on average between using the spherical model eye and the more realistic model eyes described above. These discrepancies produced differences between the estimates lower than 0.09 and 0.01 deg for horizontal and vertical tilt, and lower than 0.16 and 0.02 for horizontal and vertical decentration, respectively, for the same nominal tilts and decentrations as those used in 3.2. Finally using the same procedures described in 3.1.3 we simulated Purkinje images for a given tilt and decentration of the crystalline lens, in the realistic eye model described above, and compared the nominal values with those obtained with the algorithms. We found maximum discrepancies of 0.1 deg in eye rotation, 0.25 deg in lens tilt and 0.013 mm in decentration. Those discrepancies are comparable to those obtained in section 3.2 where the simulations were performed using the same eye model than the processing algorithms, considering spherical surfaces used in the algorithms.

Table 2.1. Model Eye with spherical surfaces; n_{cornea}=1.3687; n_{lens}=1.41; n_{aquous}=1.32854, for 880 nm in Zemax with Herzberger formula

Eye Model Nominal Values								*Retrieved values*			
								Equivalent Mirror		*Merit function*	
Anterior corneal radius (mm)	**Posterior corneal radius (mm)**	**Anterior chamber depth (mm)**	**Lens thickness (mm)**	**Lens decentration (mm)**	**Lens tilt (deg)**	**Anterior lens radius (mm)**	**Posterior lens radius (mm)**	**Anterior lens radius (mm)**	**Posterior lens Radius (mm)**	**Anterior lens radius (mm)**	**Posterior lens radius (mm)**
7.73	6.5	3.61	4	0	0	**10**	-6	10.15	-7.35	9.96	-6.51
7.73	6.5	3.61	4	0	0	**12**	-6	12.13	-7.04	11.94	-6.27
7.73	6.5	3.61	4	0	0	**14**	-6	13.99	-7.35	13.80	-6.53
7.73	6.5	3.61	4	0	0	10.45	**-6**	10.68	-7.12	10.32	-6.15
7.73	6.5	3.61	4	0	0	10.45	**-5**	10.68	-6.03	10.32	-5.28
7.73	6.5	3.61	4	0	0	10.45	**-4**	10.68	-5.06	10.32	-4.48
7.73	6.5	3.61	4	**1**	**5**	10.45	-6	10.18	-7.55	9.79	-6.46
8.5	6.5	3.61	4	0	0	10.45	-6	10.49	-7.03	10.23	-6.19
7.5	6.5	3.61	4	0	0	10.45	-6	10.55	-7.16	10.14	-6.14
6.5	6.5	3.61	4	0	0	10.45	-6	10.69	-6.88	10.08	5.69
7.73	**6.5**	3.61	4	0	0	10.45	-6	10.56	-7.24	10.19	-6.24
7.73	**6**	3.61	4	0	0	10.45	-6	10.57	-7.21	10.19	-6.22
7.73	**5.5**	3.61	4	0	0	10.45	-6	10.48	-6.97	10.11	-6.03
7.73	6.5	**4**	**4**	0	0	10.45	-6	10.92	-7.52	10.54	-6.47
7.73	6.5	**3.5**	**4**	0	0	10.45	-6	10.58	-7.27	10.21	-6.27
7.73	6.5	**2**	**4**	0	0	10.45	-6	10.57	-7.19	10.19	-6.26
7.73	6.5	3.61	**3**	0	0	10.45	-6	10.7	-5.91	10.84	-5.17
7.73	6.5	3.61	**3.5**	0	0	10.45	-6	10.7	-6.64	10.84	-5.75
7.73	6.5	3.61	**4**	0	0	10.45	-6	10.7	-6.97	10.84	-6

Table 2.2. Model eye with aspheric surfaces, real corneal topography and/or GRIN

1) Asphericity defined for this surface: $h^2 + (1+Q)Z^2 - 2ZR = 0$ where the Z axis is the optical axis, $h^2 = X^2 + Y^2$, R is the vertex radius of curvature and Q is the surface asphericity.

2) 3rd order and higher corneal surface RMS (fitted to a seventh- order Zernike polynomial), without spherical terms c12 and c24.

3) Gradient index profile in the equatorial plane defined by Garner (Garner & Smith, 1997): $n(y) = n_c + c_1\left(\frac{y}{b}\right)^2$ where $n_c = 1.406$ refractive index in the center of the lens, b is the equatorial radius and c_1 is the CRIN shape distribution inside the lens.

Eye Model Nominal Values

Retrieved values

Anterior corneal			Posterior cornea		Anterior lens		Lens				Posterior lens		*Equivalent Mirror*		*Merit function*	
Radius (mm)	Aspher.[1]	RMS[2]	Radius (mm)	Aspher	Radius (mm)	Aspher	Refractive Index (IR) [3] const	Refractive Index (IR) [3] Grad (equ. index)	Tilt	Dec en.	Radius (mm)	Aspher	Anterior lens radius (mm)	Posterior lens Radius (mm)	Anterior lens radius (mm)	Posterior lens radius (mm)
7.73	**-0.5**	0	6.5	-0.28	10.45	0	1.41	0	0	0	-6	0	10.39	-6.99	10.03	-6.04
7.73	**-0.3**	0	6.5	-0.28	10.45	0	1.41	0	0	0	-6	0	10.39	-7.06	10.03	-6.10
7.73	**-0.2**	0	6.5	-0.28	10.45	0	1.41	0	0	0	-6	0	10.61	-7.37	10.24	-6.34
7.73	-	0.84	6.5	-0.28	10.28	0	1.41	0	0	0	-6.53	0	10.82	-7.11	10.45	-6.14
7.84	-	0.42	6.5	-0.28	11.95	0	1.41	0	0	0	-5.75	0	11.32	-6.97	11.82	-6.04
7.73	0	0	6.5	0	10.45	**-5**	1.41	0	0	0	-6	-3.25	11.14	-8.25	10.76	-7.03
7.73	0	0	6.5	0	10.45	**-3**	1.41	0	0	0	-6	-3.25	10.94	-8.28	10.56	-7.05
7.73	0	0	6.5	0	10.45	**-2**	1.41	0	0	0	-6	-3.25	10.89	-8.06	10.52	-6.88
7.73	0	0	6.5	0	10.45	-4.25	1.41	0	0	0	-6	**-3**	11.28	-8.3	10.89	-7.07
7.73	0	0	6.5	0	10.45	-4.25	1.41	0	0	0	-6	**-2**	11.28	-7.72	10.89	-6.62
7.73	0	0	6.5	0	10.45	-4.25	1.41	0	0	0	-6	**-1**	11.28	-7.51	10.89	-6.46
7.73	-	0.84	6.5	-0.28	10.28	-4.25	0	1.425	0	0	-6.53	-3.25	12.59	-8.25	10.93	-7
7.84	-	0.42	6.5	-0.28	11.95	-4.25	0	1.419	0	0	-5.75	-3.25	13	-7.84	12.59	-6.69
7.73	-	0.84	6.5	-0.28	10.28	-4.25	0	1.425	**5**	**1**	-6.53	-3.25	11.53	-8.06	11.12	-6.86

4. PRELIMINARY TESTS IN PHAKIC AND PSEUDOPHAKIC EYES

4.1 Data acquisition

Subjects are aligned to the system while looking foveally at a fixation crosstarget presented on the minidisplay. The subject´s pupil is aligned to the optical axis of the CCD camera while moving the subject´s head on a X-Y-Z stage. The subject´s head is stabilized by means of a dental impression. Spherical refractive error was corrected with the Badal system which was set in the position for which the subject reported that the stimulus looked sharpest. In subjects with accommodative capability, special care was taken to ensure that the eye was not accommodating. Measurements were typically done under normal viewing conditions in the young eyes and mydriasis (tropicamide 1%) in patients with IOLs.

A set of pupillary images showing PI, PIII and PIV are captured, with SL1 (for OD) or SL2 (for OS) on, for ten different fixations on the minidisplay (green spots on a black background). Fixation locations ranged from +3.5 to -3.5 deg in the horizontal direction, and from +2.5 to -2.5 deg in the vertical direction. These images were used for estimations of lens tilt and decentration. We captured three sets of images for statistical purposes.

Pupillary images showing double PI, PIII and PIV were also captured with D-LED1 (for OD) or D-LED2 (for OS) on, with the patient fixating foveally. Occasionally, the fixation target had to be moved off-axis to allow proper visualization of the images (a special module in the software allows easy shift and documentation of the fixation location). These images were used for estimations of lens radii of curvature. We captured three sets of images (for vertical and horizontal directions) for statistical purposes. Additional measurements on the subjects included corneal topography (Atlas, Humphrey Instruments) axial length, anterior chamber depth and keratometry (IOL Master, Zeiss), and autorefraction (Automatic Refractor Model 597, Zeiss). IR (780 nm) retro-illumination images (from a pupil imaging channel in the Laser Ray Tracing system developed in our laboratory (Llorente, Barbero, Cano, Dorronsoro & Marcos, 2004) were also captured in patients with implanted IOLs. Figure 2.8 shows typical images for phakometry obtained in normal eyes and patients with IOLs. Figure 2.9 shows typical images used to estimate tilt and decentration in normal eyes and in patients with IOLs.

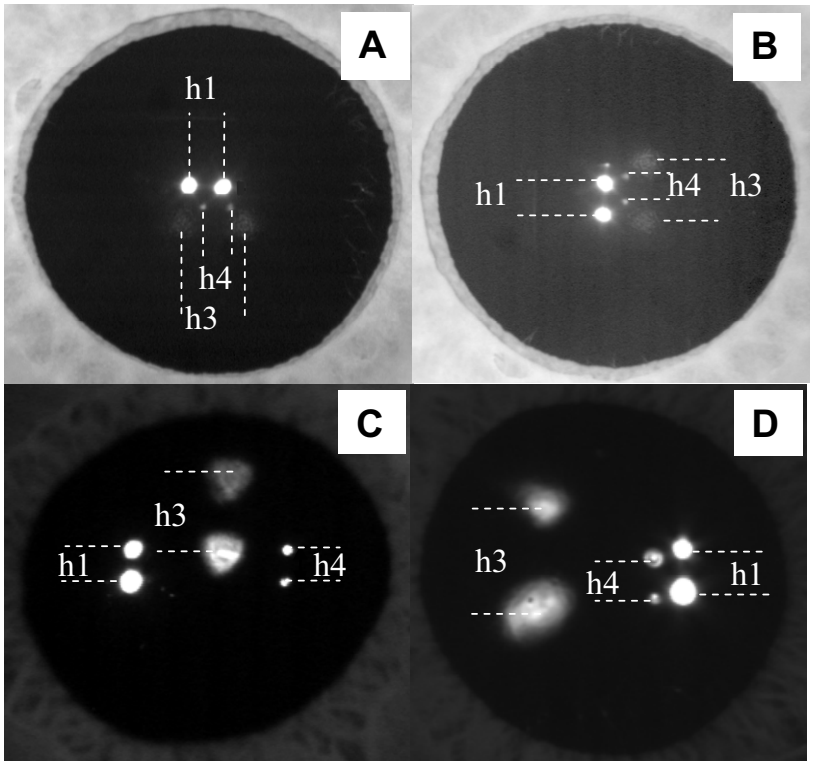

Figure 2.8. Examples of pupillary images showing double PI, PIII and PIV used to obtain phakometry. **A.** Eye with normal crystalline lens (eye #1, OD), in the horizontal direction. **B.** Eye with normal crystalline lens (eye #1, OD), in the vertical direction. **C.** Eye with IOL (eye #2, OS). **D.** Eye with IOL (eye #2, OS).

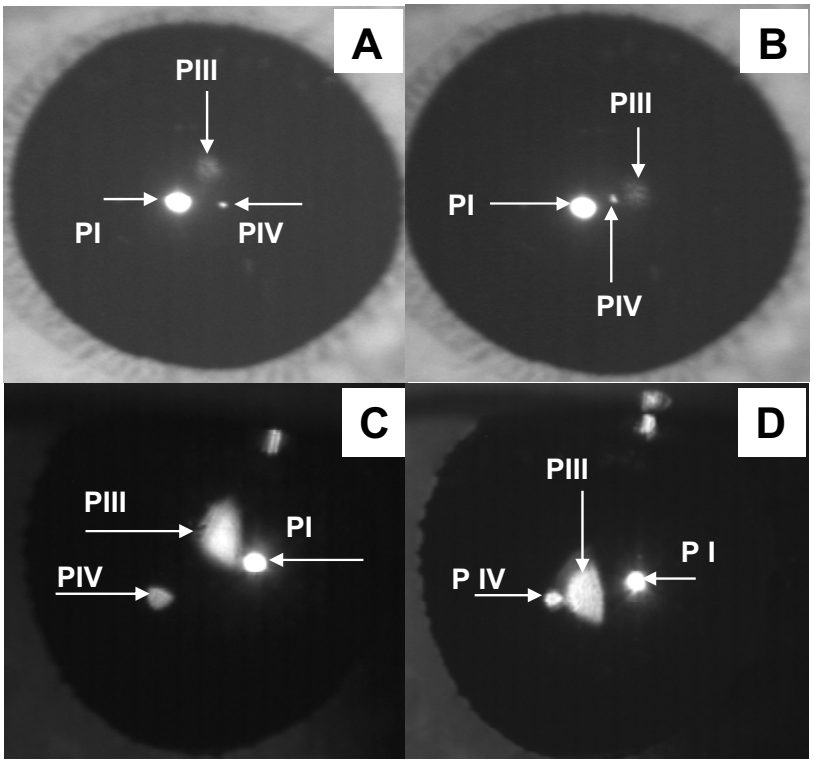

Figure 2.9. Examples of pupillary images showing PI, PIII and PIV used to obtain tilt and decentration, for different fixation angles. **A.** Eye with normal crystalline lens (subject #15, OD) fixating at -3.5 deg temporal. **B.** Eye with normal crystalline lens (subject #15, OD) fixating at 3.5 deg inferior **C.** Eye with IOL (eye #2, OS) fixating at 1.7deg superior. **D.** Eye with IOL (eye #2, OS) fixating at 1.7 deg inferior.

4.2 Subjects

Measurements were made on 17 eyes from normal subjects, moderately myopic with spherical errors ranging from 1.25 to -7 D (mean= -1.71±2.39 D) and ages ranging from 24 to 30 years (mean= 26.67±2.31 yr). Additionally, in this preliminary study, we measured nine eyes of five subjects implanted with IOLs (with both aspheric and spherical designs), with ages ranging from 71 to 79 years (mean=74±2.3 yr.). All subjects were informed of the nature of the study before the experiments and signed a consent form. The study followed the tenets of the declaration of Helsinki.

4.3 Results of phakometry measurements in young eyes and on eyes of patients with IOLs

Figure 2.9 shows the anterior and posterior radii of curvature for 12 young subjects. Radii of curvature of the anterior lens surface ranged from 8.81 ± 0.21 to 12.69± 0.37 mm, and radii of curvature of the posterior lens ranged from -7.09 ± 0.41 to -5.64 ± 0.44 mm, with use of the merit function method. The equivalent mirror method yielded similar radii for the anterior lens (ranging from 8.83 ± 0.39 to 12.86 ± 0.38) mm, and slightly values for the posterior lens (ranging from -8.43 ± 0.66 to -6.47± 0.16) mm, consistent with the predictions from the simulations.

We measured radii of curvature in the vertical and in the horizontal directions in five subjects. Differences across meridians were not significant, except for two subjects, where we found differences of 0.82 mm for the anterior lens and 0.84 mm for the posterior lens across meridians. Reproducibility of the measurements are 0.34 and 0.28 mm for the anterior and posterior lens radius of curvature respectively.

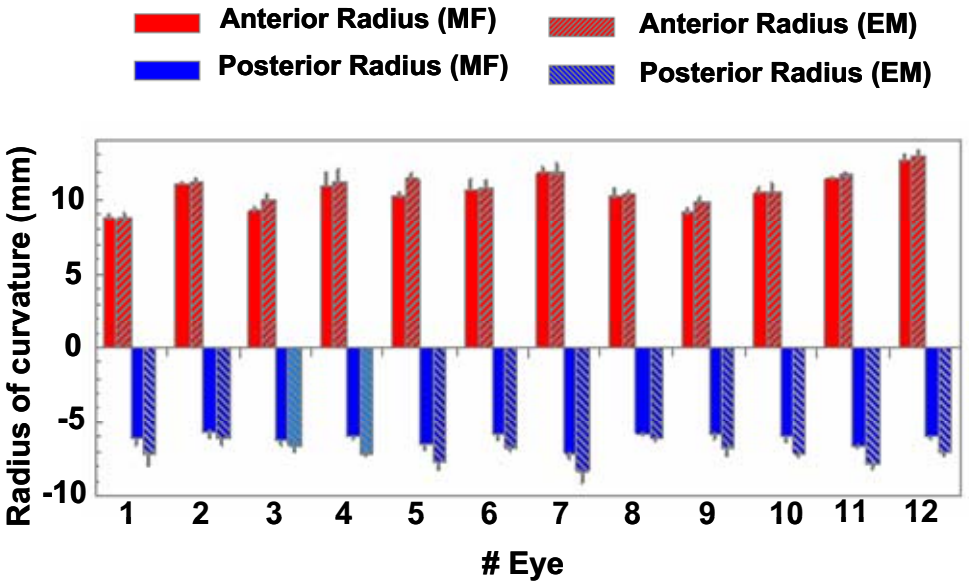

Figure 2.10. Anterior and posterior radii of curvature, estimated using the Merit function (MF) and the Equivalent Mirror (EM) methods. Eyes (right eyes from 12 subjects) are ranked by increased myopic error. Values are average of at least three measurements. Error bars stand for standard deviations.

4.4 Crystalline Lens tilt and decentration

Figure 2.11.A shows horizontal and vertical crystalline lens tilt, and Figure 2.12.B shows horizontal and vertical crystalline lens decentration on 17 eyes of 14 subjects. Solid symbols stand for right eyes and open symbols stand for left eyes.

Horizontal tilt ranged from -1.13 ± 0.43 to 2.8 ± 0.40 deg in right eyes and from -1.96 ± 0.36 to -2.87 ± 0.34 deg in left eyes. Vertical tilt ranged from –1 ± 0.31 to 2.58± 0.27 deg in right eyes, and from 0.66 ± 0.20 to 1.99 ± 0.43 deg in left eyes. Crystalline lens tilt tended to be mirror-symmetric in left/right eyes of the same subject. Crystalline lens decentrations ranged, in the horizontal direction, from -0.098 ± 0.031 to 0.445 ± 0.023 mm in right eyes and -0.36 ± 0.013 to 0.39 ± 0.032 mm in left eyes. Vertical decentrations ranged from -0.22 ± 0.02 to 0.04 ± 0.02 mm in right eyes and from -0.18 ± 0.003 to 0.06 ± 0.01 mm in left eyes. Reproducibility of the measurements are 0.29 deg and 0.33 deg for horizontal and vertical tilt, and 0.03 mm and 0.02 mm for horizontal and vertical decentration.

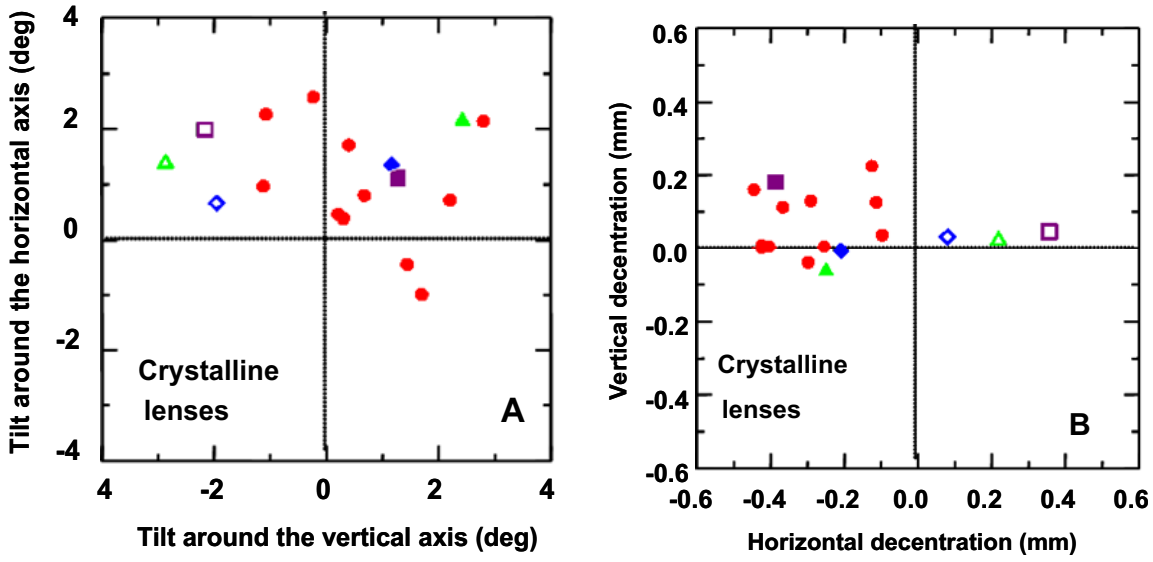

Figure 2.11. A. Tilt around the horizontal and vertical axis of the crystalline lens in 17 eyes of 14 subjects. Solid symbols correspond to right eyes, and open symbols to left eyes. Circles correspond to subjects 1-11; squares, triangle and diamonds to subjects 12, 13 & 14 respectively. Horizontal tilts represent tilts around the y-axis, and vertical tilts around x-axis. **B.** Horizontal and vertical decentration of the crystalline lens in 17 eyes of 14 subjects. Solid symbols correspond to right eyes, and open symbols to left eyes, labeled as in Figure 2.11.A. Positive horizontal decentrations represent temporal shifts from the pupil center for the right eye, and nasal for left eyes.

4.5 Intraocular lens tilt and decentration

Figure 2. 12.A shows IOL tilt, and Figure 2. 12.B shows decentration, in eight eyes of five subjects. The sign convention is the same as that for the crystalline lens. IOL horizontal tilt ranged from -0.72 ± 0.08 to 3.6 ± 0.031 deg in right eyes and from -1.51 ± 1.34 to 3.48 ± 0.42 deg in left eyes. Vertical tilt ranged from –1.85 ± 0.52 to 5.97 ± 0.82 deg in right eyes and from 0.75 ± 0.43 to 3.83 ± 0.58 deg in left eyes. IOL decentrations ranged, in the horizontal direction, from -0.31 ± 0.23 to 0.53 ± 0.06 mm in right eyes and 0.23 ± 0.032 to 0.51± 0.04 mm in left eyes. Vertical decentrations ranged from -0.96 ± 0.07 to 0.13± 0.08 mm in right eyes and from -0.96 ± 0.07 to -0.33 ± 0.02 mm in left eyes. Reproducibility of the measurements are 0.6 and 0.55 deg for horizontal and vertical tilt respectively, and 0.06 and 0.05 mm for horizontal and vertical decentration respectively.

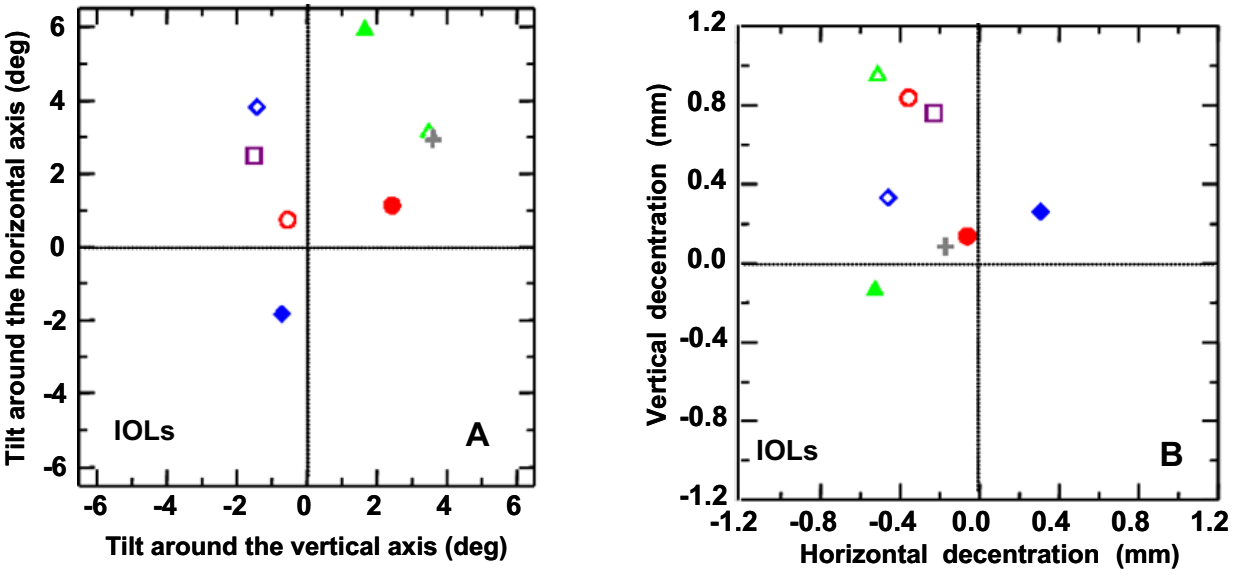

Figure 2.12. A. Tilt around the horizontal and vertical axis of the IOL in eight eyes of five subjects after cataract surgery. Solid symbols correspond to right eyes and spherical IOLs and open symbols correspond to left eyes and aspheric IOLs. Each shape correspond to a different subject. **B.** Horizontal and vertical decentration of the intraocular lens in eight eyes of five subjects after cataract surgery. Solid symbols correspond to right eyes and spherical IOLs and open symbols correspond to left eyes and aspheric IOLs. Each shape corresponds to a different subject. Signs are as in Figure 2.12.A. Error bars are smaller than the symbol size.

5. DISCUSSION

5.1 Comparison with previous studies

A new system is presented, suited for phakometry/positioning measurements of both the crystalline lens and IOLs. The instrument is very compact and well adapted to clinical use. The incorporation of a Badal system and flexible fixation targets can ensure relaxed accommodation. Also, a thorough validation has been performed, using both realistic simulations of the actual intensity distributions of PI, PIII and PIV in the pupillary image, and for the first time, to our knowledge, tilt and decentration data in both the horizontal and vertical directions.

Our analysis shows that the Merit Function provides more accurate data than the Equivalent Mirror method. Our average phakometry results using the merit function method (10.61 ± 1.13mm and -6.15 ± 0.41 mm, for the anterior and posterior lens respectively) can be compared with those reported by other authors. Kirschkamp et al (Kirschkamp et al., 2004) using Barry et al (Barry et al., 2001) Purkinje-image system and the equivalent mirror, reported for the un-acommodated eye (n=9 with age

ranging from 20 to 38 years) radii of 12.3 ± 0.8 mm and -6.01 ± 0.2 mm for the anterior and posterior lens respectively. While the differences are not statistically significant for the posterior lens, our anterior lens radii of curvature are significantly lower. Part of the difference might be due to differences in the age range of both groups. Our phakometry data are comparable with those reported by Smith and Garner (Garner & Smith, 1997) (n=11 with age ranging from 18-38 yr) with average lens radii of curvature of 11.54 ± 1.27 mm and -6.67 ± 0.97 mm for the anterior and posterior lens, respectively. Our data are also consistent with recent reports using different methods. Using distortion-corrected Scheimpflug images in subjects of similar age. Dubbleman and van der Heijde´s (Dubbelman & van der Heijde, 2001) empirical equation yields average anterior and posterior lens radii of 11.37 and -5.87 mm, respectively, for the average age of our subjects. Differences in the posterior lens are not significant. The slight differences in the anterior lens may be due to the fact that Scheimpflug crosssections are fit to conic surfaces, and the apical radius is reported, while the Purkinje system samples more peripheral areas. Also, it should be noted that Scheimpflug images were captured with the subject viewing the fixation stimulus with the contralateral eye. Further analysis of phakometry on a larger sample of young eyes (n=46) will be presented in Chapter 5.

To our knowledge, the only data available in the literature on tilt and decentration of the crystalline lens are those reported by Kisrschkamp (Kirschkamp et al., 2004) and Dunne (Dunne, Davies, Mallen, Kirschkamp & Barry, 2005) for the horizontal direction in two young groups. We report slightly higher values of crystalline lens tilt and larger intersubject variability (1.05 ± 1.12 deg for the horizontal direction and 0.77 ± 1.27 deg for the vertical direction than those reported by Kirschkamp (Kirschkamp et al., 2004) (0.2 ± 0.8 deg, horizontal direction) and Dunne (Dunne et al., 2005) (0.2 ± 1.8 deg, horizontal direction). We also found slightly higher decentrations (0.28 ± 0.12 mm for horizontal decentration and -0.06 ± 0.08 mm for vertical decentration) as opposed to 0.1 ± 0.2 mm reported by Kirschkamp (Kirschkamp et al., 2004) and -0.1 ± 0.1 mm reported by Dunne (Dunne et al., 2005).

Our measurements of IOL tilt and decentrations (0.87 ± 2.16 deg for horizontal tilt, 2.3 ± 2.33 deg for vertical tilt, and, 0.25 ± 0.28 deg for horizontal decentration and -0.41 ± 0.39 mm for vertical decentration) can be compared with those of a few reports using Purkinje imaging or other methods. Those studies typically do not report the direction and sign of tilts and decentrations. Phillips (Phillips et al., 1988) used a Purkinje

imaging system to measure tilt and decentration of posterior chamber IOLs in 13 patients and found average tilts of 7.8 ± 3 deg and decentration of 0.7 ± 0.3 mm. While those estimates are larger than the ones obtained in our study, IOL designs and surgical techniques have evolved tremendously in the last 18 years, and the accuracy in lens positioning has potentially improved. A more recent clinical study measured tilt and decentration after primary and secondary transsclerally sutured posterior chamber IOLs evaluating the Purkinje reflections while the subject was fixating at different locations in a Goldman perimeter (Ismet, 2000). This study reported an average IOL tilt of 5.71 ± 3.41 deg in the first group (14 eyes) and 6.22 ± 3.94 deg in the second group (42 eyes) and average decentrations of 0.67±0.43 mm and 0.59 ±0.43 mm respectively. Those values are larger than those reported in the present study, potentially due to the surgical procedure and implicit assumptions in the methodology using perimetry. More recent studies used commercial Scheimpflug photography to assess tilt and decentration on different types of IOLs, and found estimates consistent with our results. One study (Meng-Chi, Lin-Chung, Chao-Yu & Han-Chin., 1998) reported tilts and decentrations of PMMA and silicone IOLs in 70 eyes, and found average tilts of 2.93 ± 2.68 deg and 3.4 ± 2.02 deg and average decentrations of 0.37 ± 0.19 mm and 0.29 ± 0.26 for the the PMMA and silicone groups respectively). Another study (Kim & Shyn, 2001) evaluated PMMA (n=65), 3-piece silicone (n=47), and 3-piece acrylic (n=25) IOLs, and found average tilts of 2.67 ± 0.84 deg, 2.61± 0.84 deg and 2.69± 0.87 deg, and average decentrations of 0.31 ± 0.15mm, 0.32 ± 0.18 mm, 0.33 ± 0.19 mm, respectively. The average estimates are very similar to those of our study. However the intersubject variability, despite the larger sample of the Scheimpflug studies, seems excessively low. Further analysis of tilt and decentration of IOLs in a larger sample of pseudophakic eyes (n=38) will be presented in Chapter 10.

5.2 Limitations of the technique and implication of the results

A compact optical system has been developed to measure phakometry, and lens tilt and decentration, and demonstrated its use in both normal eyes and eyes with intraocular lenses. Computer simulations have allowed us to test the methodology, the performance of the system, and the validity of the assumptions. The main limitation of the technique comes from the fact of considering spherical surfaces for the lens that produces an overestimation of the lens radii of curvature. Although this limitation may

be important in providing accurate phakometry measurements when larger asphericities are present, we have demonstrated that these differences do not affect tilt and decentration measurements. While this issue could be overcome ensuring that the Purkinje images are formed in the apical zone, in general this is not practically possible since for those angles the Purkinje images typically overlap. Other alternatives are the use of multiple double LEDs with different separations which would allow estimates of radii of curvature as a function of radial distance and therefore estimates of asphericities, and the use of more sophisticated models for equivalent mirror (or better, for the merit function since we have demonstrated that the latter gives more accurate phakometry) incorporating aspheric surfaces. The rest of the factors tested (gradient index of the lens, anterior chamber depth, lens thickness or corneal irregularities) do not seem to have major impact on the measurements.

Although in most of the patients we could successfully measure phakometry, tilt and decentration, there were several eyes with IOLs (not presented here) for which phakometry of the anterior lens was not possible, because the distance between the double PIII exceeded the pupil diameter. Presumably, these IOLs show very flat anterior surfaces. We have estimated that lenses with radii of curvature larger than 20 mm will produce that problem, with the current configuration of LED separation, and for a pupil diameter of 6 mm. Tilt and decentration measurements are possible, provided that nominal anterior radius of curvature is known and that tilt does not exceed 10 deg (for 0 mm decentration and for anterior lens radius of curvature of 10.45mm).

While measurements of phakometry, tilt and decentration of crystalline lenses /IOLs are informative to characterize the normal eye or the outcomes of intraocular surgery, they will become particularly relevant in combination with other optical and geometrical data, to model individual eyes and predict their optical quality, to understand the sources of aberrations, to shed light into the mechanisms of accommodation and to evaluate the potential benefits of different intraocular lens designs.

Scheimpflug imaging: Optical distortion correction

3

3. Scheimpflug imaging: Optical distortion correction

The contribution of Patricia Rosales to this study was the implementation of optical distortion correction algorithms, particularly adapting them to the Scheimpflug system available in the laboratory (Pentacam, Oculus), development of a method to infere the camera nodal points and tests on artificial eyes of known dimensions and on a normal eye. Previous experience and suggestions from Michael Dubbelman and Rob van der Heijde who had developed optical distortion correction algorithms on other Scheimpflug systems have been essential. Suggestions from Susana Marcos, Alberto de Castro, Lucie Sawides, Alfonso Fernandez Escudero and Carlos Dorronsoro have been very valuable in important points to develop the algorithms.

RESUMEN

Objetivos: Desarrollar algoritmos de corrección para la cámara comercial de Scheimpflug Pentacam, Oculus.

Métodos: Para la obtención del punto nodal de la cámara se tomaron imágenes de esferas calibradas de radios conocidos: 9.65 mm, 8 mm y 6 mm, y una imagen de un papel milimetrado. Mediante funciones de minimización, se fue variando la posición del punto nodal, hasta que el radio proyectado en el plano objeto coincidía con los radios nominales de las esferas. Una vez hallados los puntos nodales, se aplicaron los algoritmos de corrección de la distorsión sobre imágenes de un ojo artificial de dimensiones conocidas y un ojo normal medido anteriormente con una cámara de Scheimpflug con la distorsión óptica corregida (Topcon SL-45, Vrije University, Amsterdam, The Netherlands).

Resultados: Los puntos nodales obtenidos recuperan el radio nominal de la esfera calibrada al 100% y la distancia entre dos puntos consecutivos del papel milimetrado con una precisión del 95%. Los radios de curvatura de las superficies oculares de las imágenes sin corregir eran mayores que las de las imágenes corregidas. El error promedio en la recuperación de los radios de curvatura nominales fue de 0.18 mm y 0.27 mm para las caras anterior y posterior de la córnea y de 0.37 y 0.46 mm para las caras anterior y posterior del cristalino. El error promedio cometido al recuperar las distancias intraoculares fue de 0.015mm, 0.385mm y 0.048 mm para el espesor de la córnea, la cámara anterior y el espesor del cristalino respectivamente.

Conclusiones: Los resultados sugieren que los algoritmos corrigen con bastante precisión las distorsiones geométrica y óptica de la cámara de Scheimpflug. Sin embargo, el conocimiento exacto de los puntos nodales de la cámara (ahora estimado mediante un método de mínimos cuadrados) mejoraría la precisión del método.

ABSTRACT

Purpose: To develop algorithms for the optical and geometrical distortion correction of the commercial Scheimpflug camera Pentacam, Oculus.

Methods: To obtain the camera nodal points, images of calibrated espheres and an image of millimetre paper were obtained with the Scheimpflug camera. The radius of those spheres were of 9.65, 8 and 6 mm. Using a merit function and a least-mean square procedure, several nodal point positions were tested, until the projected radius on the object plane matched the nominal radius values of the espheres. Once the nodal points were obtained, the correction distortion algorithms were applied on Scheimpflug images of an artificial eye with known dimensions and images of a normal eye previously measured with an optical and geometrical distortion corrected Scheimpflug camera (Topcon SL-45, from the Vrije University, Amsterdam, Holland).

Results: The estimated nodal points allowed to obtain the nominal radius of the calibrated ball with an accuracy of 100%, and distances in the images with an accuracy of 95%. The radius of curvature of the ocular surfaces of the uncorrected surfaces were higher than the corrected images. The average error in the retrieved radius of curvature were of 0.18 and 0.27 mm for the anterior and posterior cornea radius of curvature respectively, and of 0.37 and 0.46 mm for the anterior and posterior crystalline lens radius of curvature respectively. The average error in the retrieved intraocular distances were of 0.015mm, 0.385 mm and 0.048 mm for corneal thickness, anterior chamber depth and lens thickness respectively.

Conclusions: The results suggest that the distortion correction algorithms are quite accurate, although inaccuracies to retrieve the nominal radius of curvature and intraocular distances, can be minimized by a more precise knowledge of the nodal points.

1. INTRODUCTION

Scheimpflug imaging is a powerful tool for anterior segment imaging, but special care must be taken in correcting the images for the geometrical distortion (caused by the tilt of the object plane with respect to the optical axis) and for the optical distortion (caused by refraction from the different ocular surfaces, i.e, the posterior cornea is seen refracted from anterior cornea, anterior crystalline lens is seen refracted by posterior and anterior cornea, and posterior crystalline lens is seen refracted by anterior crystalline lens and anterior and posterior cornea).

The first Scheimpflug imaging set up systematically used in the lab for investigation of the crystalline lens was developed by Brown (Brown, 1973, Brown, 1974). While these authors did introduce corrections for the geometrical distortion, the optical distortion did not seem to be fully corrected. Brown's study reports a decrease of the anterior and posterior lens radius of curvature with age (Brown, 1974). More recent studies also show a decrease in the anterior and posterior lens radii of curvature with age, but to a lesser extent. Whereas Brown found a decrease in the anterior lens radius of curvature of 100 μm/year. Dubbelman (Dubbelman & van der Heijde, 2001), using a distortion corrected Scheimpflug camera found a decrease of 57 μm/year, while findings for the posterior lens radius of curvature are similar for both authors. Dubbelman also found smaller values for the absolute value for the anterior and posterior lens radius of curvature.

Different methods have been applied in order to correct for the optical distortion. Cook (Cook & Koretz, 1998) proposed a method based on a Hough transform in order to obtain corrected surfaces from Scheimpflug images. This method has been validated through comparison with MRI (Koretz, Strenk, Strenk & Semmlow, 2004) but on a different set of subjects.

Dubbelman (Dubbelman & van der Heijde, 2001, Dubbelman, van der Heijde & Weeber, 2001) have conducted thorough developments of correcting algorithms and validations on refurbished prototypes of the Topcon SL-45 and Nidek Eas-1000 systems. These systems were developed in the 80’s and 90’s respectively, and were commercially available for some time, although both are now discontinued. Figure 3.1 and 3.2 show the optical configuration of both systems. Some of the hardware modifications in the systems performed by Dubbelman and collegues include the

replacement of the original camera by high-resolution scientific grade CCD cameras. In both cases, images are taken along one meridian, which can be manually changed of orientation. Typically, data are obtained on the horizontal and vertical meridians. The geometrical distortion in this system is corrected by projecting the CCD chip from the image plane to the object plane passing through the nodal points. The optical distortion is corrected by means of ray tracing. The anterior surface of the cornea only suffers from geometrical distortion. Tracing this surface back from the image plane (CCD-chip) through the optics of the camera (with the critical dimensions of the optical layout being provided by the manufacturer) to the object plane (slit beam) gives the corrected anterior corneal surface. The posterior corneal surface is traced through the nodal point and the anterior cornea to obtain the undistorted coordinates of the posterior corneal surface on the object plane. The anterior surface of the lens is then traced through the nodal points and the anterior and posterior corneal surfaces. A similar procedure is followed for the posterior lens surface.

Figure 3.3 shows an example of a typical raw image obtained with the Topcon SL system in a young (16 years old) dilated human eye, and after correction for geometrical and optical distortion. Measurements on an artificial eye (Dubbelman & van der Heijde, 2001) show differences between corrected and uncorrected images that can be summarized in Table 3.1.

Table 3.1. Radius of curvature and thickness of both elements of the artificial eye. (Dubbelman & van der Heijde, 2001).

	Nominal Values	Before correction	After correction
Anterior cornea	8.9 ± 0.05	9.34±0.08	8.93±0.08
Posterior cornea	8.29± 0.05	9.17±0.08	8.27±0.12
Cornea thickness	0.501±0.001	0.28±0.02	0.50±0.02
Anterior lens	13.07±0.05	15±1.1	13.0±0.16
Posterior lens	13.06±0.05	26±2.8	12.29±
Lens thickness	4.285±0.001	4.0±0.14	4.24±0.06

The Scheimpflug imaging phakometry data presented in Chapter 4 of this thesis was performed using a Topcon SL-45 system, with correcting algorithms developed by Dubbelman (Dubbelman, van der Heijde & Weeber, 2005) .

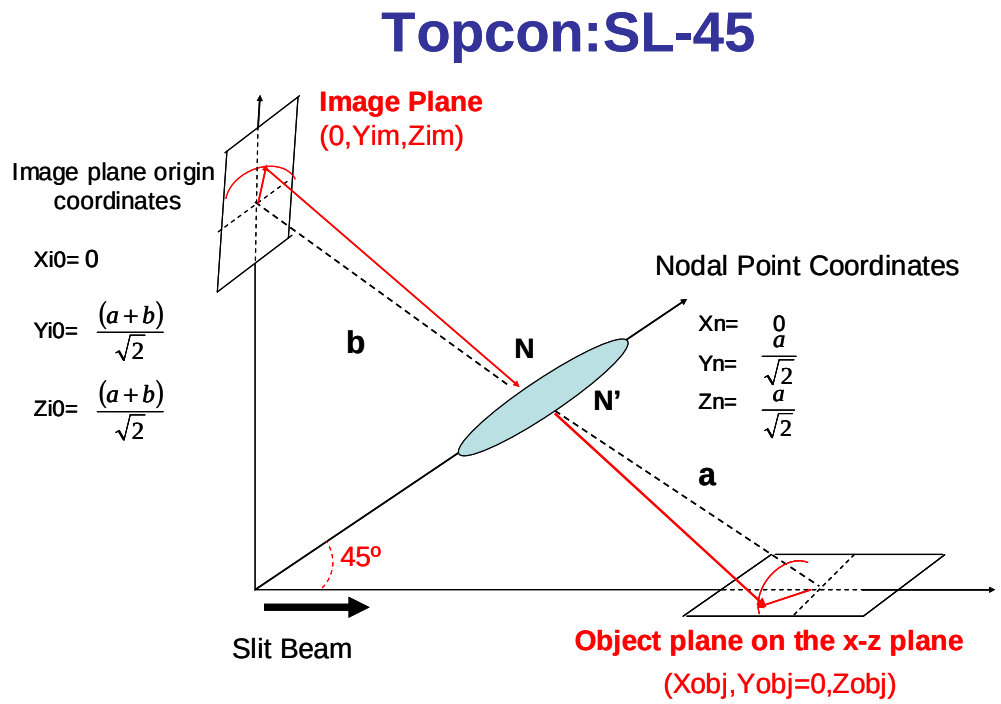

Figure 3.1. Configuration of the Scheimpflug camera Topcon SL-45. The image plane and the object plane (the anterior segment of the eye) form an angle of 90º

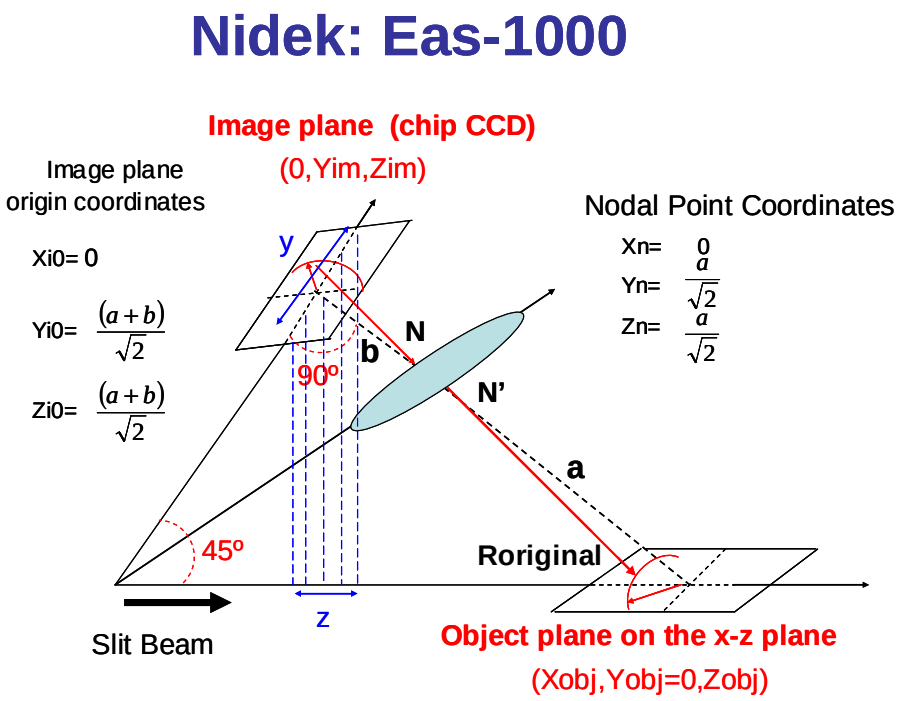

Figure 3.2. Configuration of the Scheimpflug camera Nidek EAS. It can be noticed that the image plane and the object plane form an angle of 45º

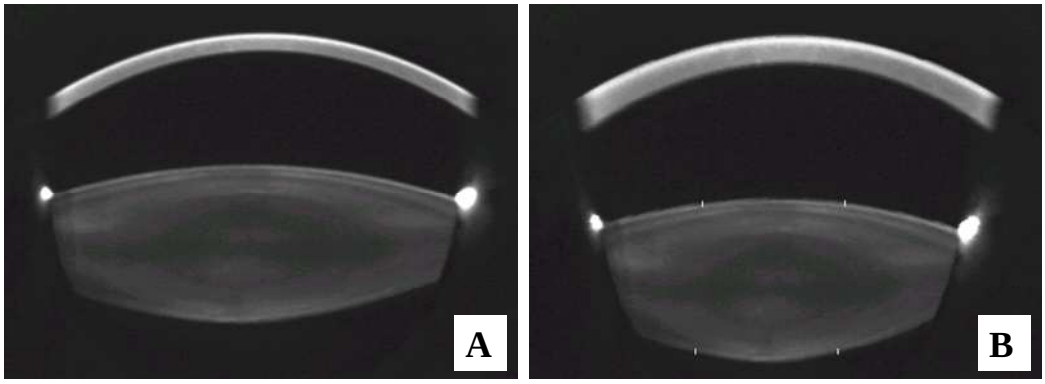

Figure 3.3. Optical and geometrical distortion correction. **A.** Shows a Scheimpflug photo of a 16 years old female before correction. **B.** shows the same photo after correction.

To our knowledge, the only Scheimpflug imaging system commercially available today is the Pentacam system by Oculus. The Pentacam images the anterior segment of the eye by a rotating Scheimpflug camera measurement. This rotating process allows rapid capture of images in different meridians, and therefore three-dimensional elevations.

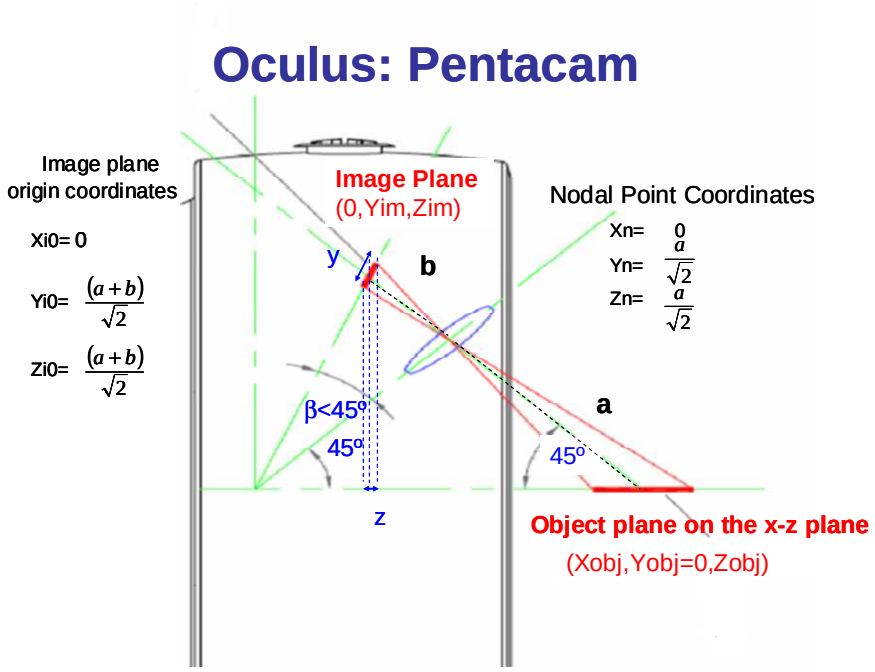

Figure 3.4. Configuration of the Scheimpflug camera Pentacam (Oculus). In this case, the object and image planes form an angle smaller than 90º. This angle was not provided by the manufacturer and it will be an unknown to obtain.

The Pentacam provides optical distortion corrected data of the posteior cornea, although it does not perform any distortion correction on the crystalline lens surfaces.

Figure 3.4 shows the optical layout of the system, as reconstructed from the specifications provided by the manufactured upon request. The Scheimpflug images of Chapter 5 of this thesis were performed using the Pentacam system.

In this Chapter we present the algorithms developed in this thesis for geometrical, and particularly, optical correction of anterior segment images obtained with the Pentacam Scheimpflug system. These algorithms are based on to those developed by Dubbelman for the Topcon and Nidek systems, adapted to the particular configuration of the new system. Since the manufacturer did not provide some critical specifications of the system (CCD pixel size or nodal point distances) additional work was conducted to infer this information.

2. METHODS

In this chapter a method to correct the optical distortion of the Pentacam is proposed.

2.1 Obtaining images from the raw data

The Pentacam stores raw images of the anterior segment of the eye in *.src files. However, the extraction of the raw images from those files is proprietary. An algorithm to obtain original images from the raw data was provided by D. Atchison and S. Kasthurirangan from the School of Optometry, Queensland University of Technology (Australia). The processing algorithms therefore work on the raw images obtained by the system's CCD camera (Oculus, Pentacam).

2.2 Image Processing

Ocular surfaces were detected using a Canny filter in most cases, on images from one single meridian and resulting from an average of 15 identical images. In those images where the lens surfaces were not properly detected using the Canny filter, a manual detection was used instead.

2.3 Obtaining information about the Pentacam's configuration

The application of the correction distortion algorithms requires knowledge of the camera's nodal points and the angle between the image and object plane of the camera (*a, b, angle*), respectively where *a* is the distance between the lens and object planes, and *b* is the distance between the image and the lens planes, those distances give the

nodal point position. However, these parameters have not been provided by the manufacturer.

In order to obtain those values, the following procedure has been followed. Calibrated spheres of known radii of curvature (9.65, 8 and 6 mm) have been placed in different positions along the image plane (Figure 3.4), and imaged with the Scheimpflug system at a given meridian. Ray tracing was recursively performed with varying values of *a*, *b*, and *angle*. A minimization procedure (mean least squares) was applied to obtain the *a*, *b*, and *angle* values that minimized the difference between the estimated and nominal radius of curvature of the calibrated sphere (Figure 3.5). As a proof that the estimated nodal point was correct, a projection of two consecutive points from a millimeter paper was obtained in order to check if the distance between two consecutive points projected was 1 mm. The minimization routine was performed with randomized initial conditions for values of *a* and *b*, with combination of values between 63 and 250 mm, until two conditions were reached:

1) Difference between nominal and obtained radius was 0 mm.
2) Distance between two consecutive points in the millimeter paper was 1 mm.

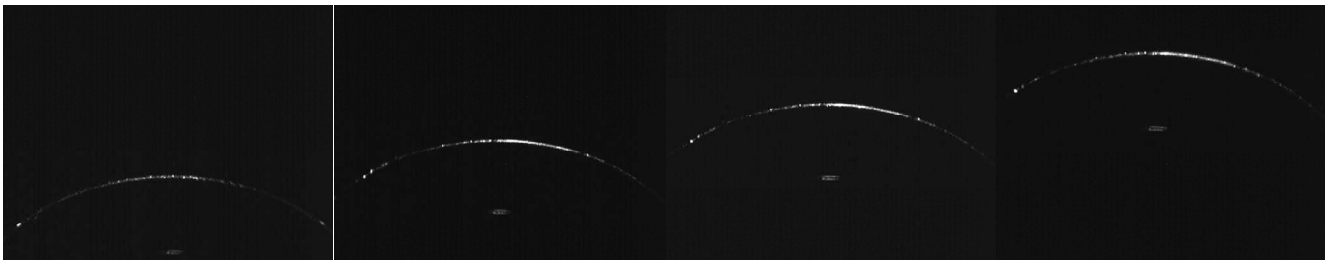

Figure 3.5. Image of the 9.65 mm sphere in different Y positions in the object plane.

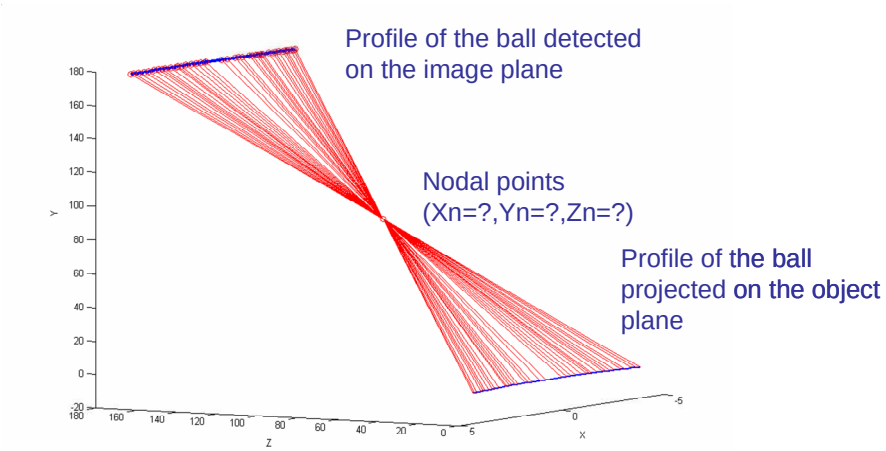

Figure 3.6. Ray tracing back from the image plane to the object plane passing through the nodal points.

2.3. Applying the distortion's correction algorithm

In the ray tracing technique, the slit beam projected on the anterior eye segment is regarded as the object plane, and the CCD- chip as the image plane. The steps followed for the distortion correction are:

a) The anterior surface of the cornea is traced from the image plane, through the nodal points of the camera, to the object plane to obtain its real coordinates.

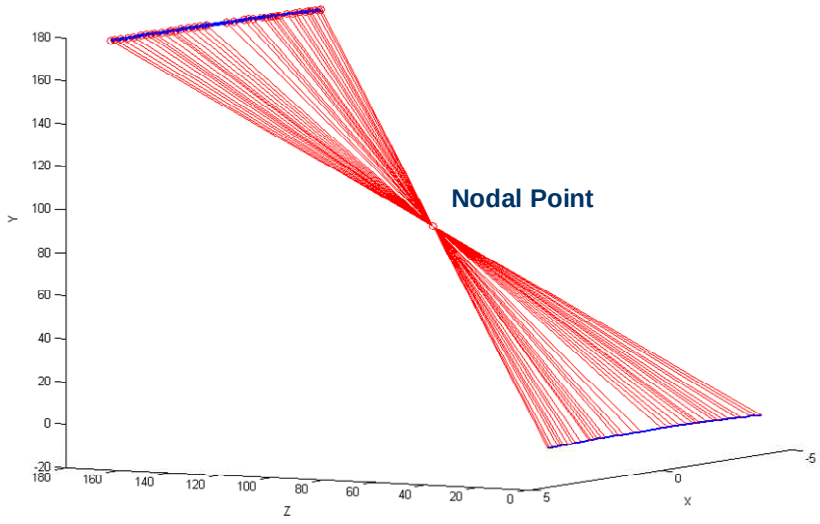

Figure 3.7. Projection of the anterior cornea surface to the object plane passing through the nodal points using a ray tracing procedure.

b) A conic of revolution is fitted to the anterior corneal surface (a sphere in the example).

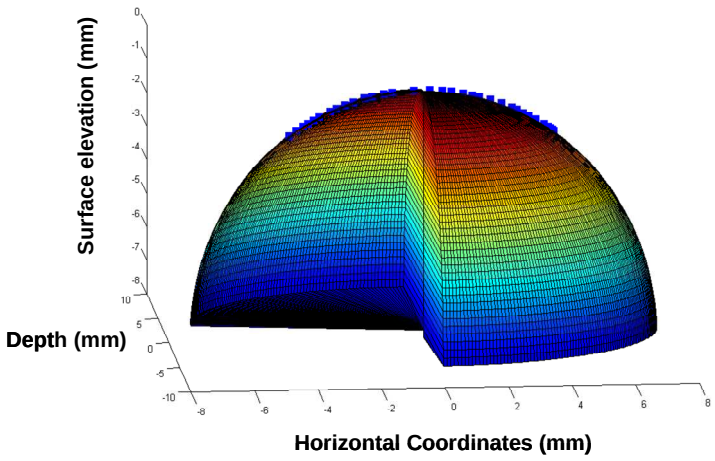

Figure 3.8. The projected points in the object space are fitted to a circle. Considering revolution symmetry, a sphere is raised.

c) Assuming that the surface is rotationally symmetric, the posterior surface is traced from the image plane through the nodal point of the camera and refracted by the anterior cornea, and then projected on the object plane. The projected points are fitted to a conic of revolution (a sphere in the example).

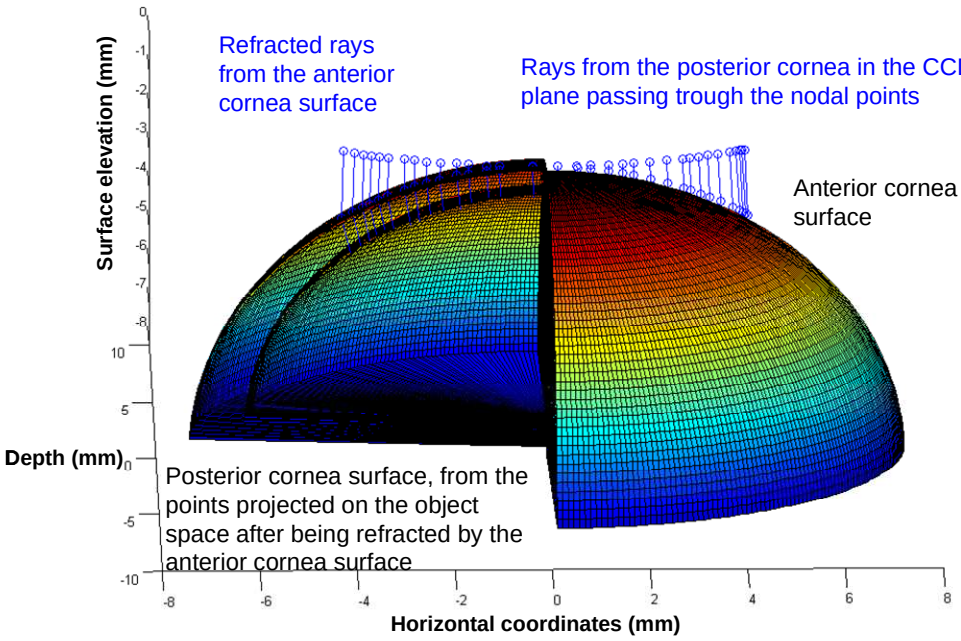

Figure 3.9. The projected points in the object space from the posterior cornea and refracted by the anterior cornea. The surface obtained from the image plane, passing through the nodal points and being refracted by anterior surfaces will be the corrected surface.

d) The same procedure is followed for the anterior and posterior lens surfaces.

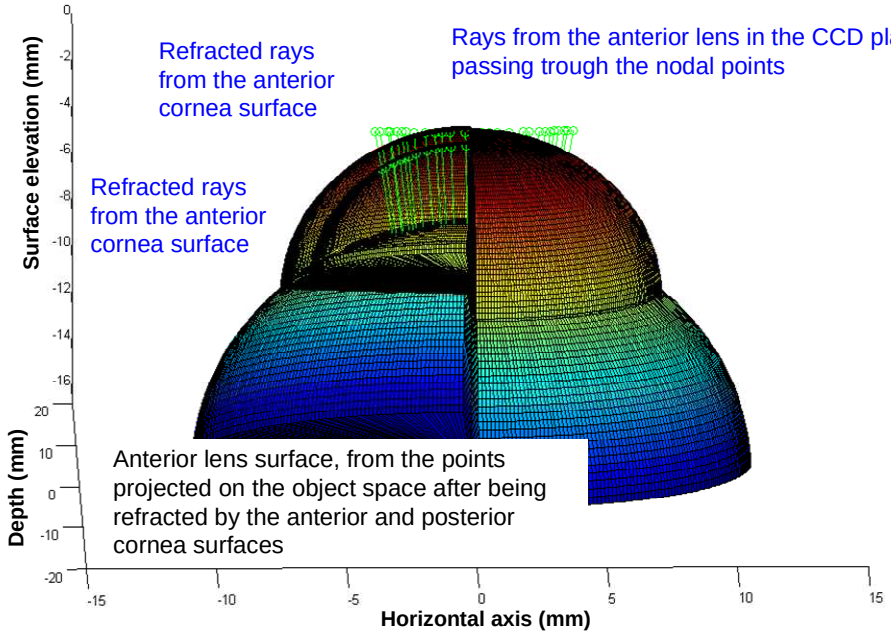

Figure 3.10. The projected points in the object space from the anterior crystalline lens, refracted by the anterior and posterior cornea surfaces.

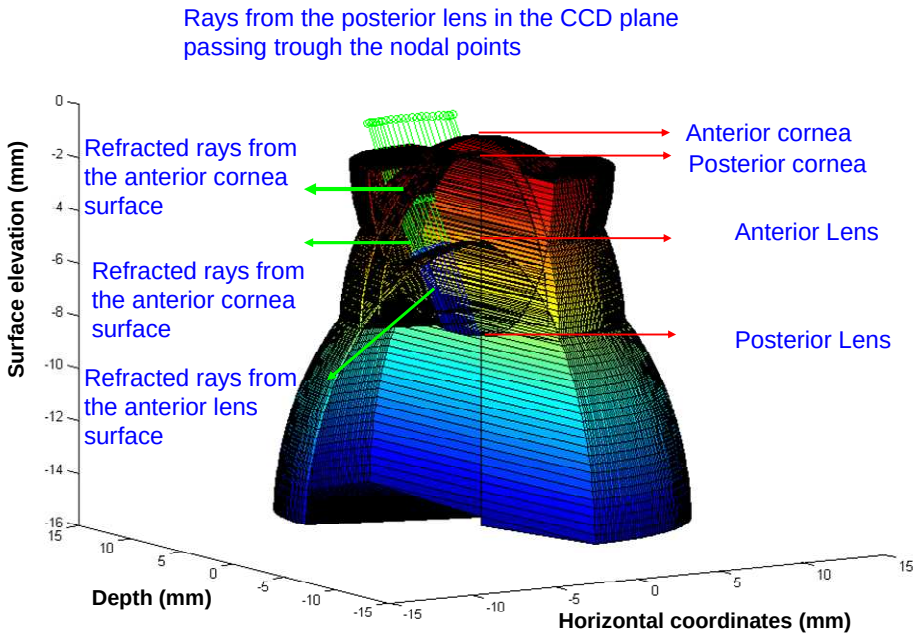

Figure 3.11. The projected points in the object space from the posterior crystalline lens, refracted by the anterior and posterior cornea surfaces and by the anterior crystalline lens

3. RESULTS

3.1 Nodal Points

Using the minimization procedure previously described, the position of the nodal points that reproduces the nominal radii of curvature of the calibrating spheres in the least-squares sense were obtained. The retrieved parameters are: a = 74. 83 and b = 86.09 mm. With those values, radii of curvature of the spheres agreed 100% with the nominal values while the distance between consecutive points in the projected millimetre paper marks was underestimated in 0.05 mm.

3.2 Correction distortion algorithms

In order to estimate the accuracy of the distortion correction algorithms, measurements were performed on an physical model eye and a real human eye. The physical model eye consisted of a PMMA cornea and a spherical intraocular lens (CeeOn, 19D, Pharmacia) (Sverker, Artal, Piers & van der Mooren, 2003), in place of the crystalline lens, with known radii of curvature and known refractive index (Figure 3.12). The normal human eye used as a reference had been previously measured with the distortion corrected Scheimpflug Topcon-SL in the Vrije University, Amsterdam.

Figure 3.13 shows an uncorrected Scheimpflug image obtained with the Nidek EAS-1000 **(A)** and with the Pentacam system **(B)**.

Figure 3.12. Scheimpflug image of an artificial eye of known dimensions (mm).

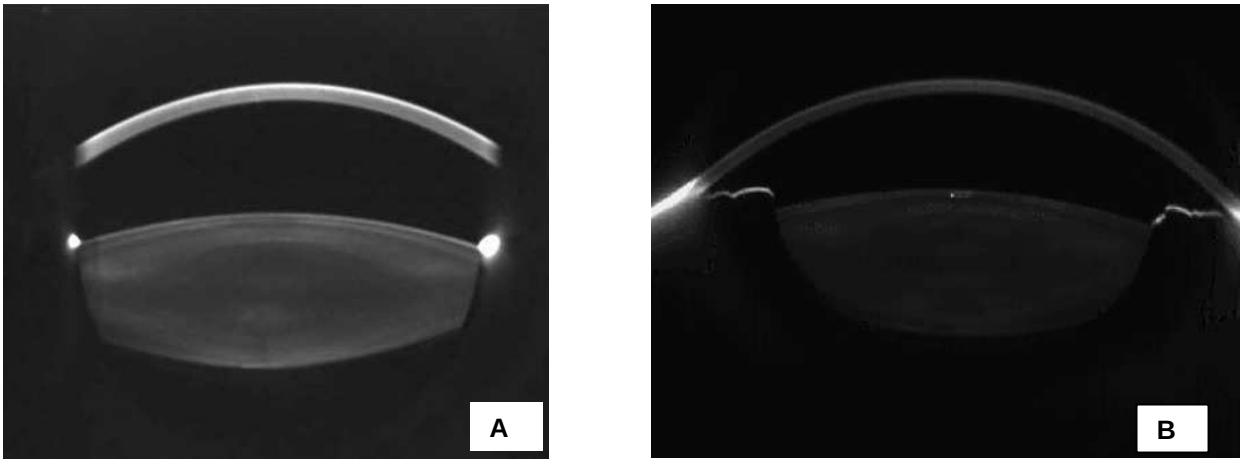

Figure 3.13. A. Distortion uncorrected image obtained with the Nidek EAS-1000 Scheimpflug camera and **B.** Distortion uncorrected image obtained with the Pentacam (Oculus) Scheimpflug camera.

Figure 3.14 shows images of the artificial eye (A) and the normal eye with the uncorrected surfaces detected (blue lines) and the position of the corrected surfaces (B) (red lines) after application of the developed distortion-correction algorithms.

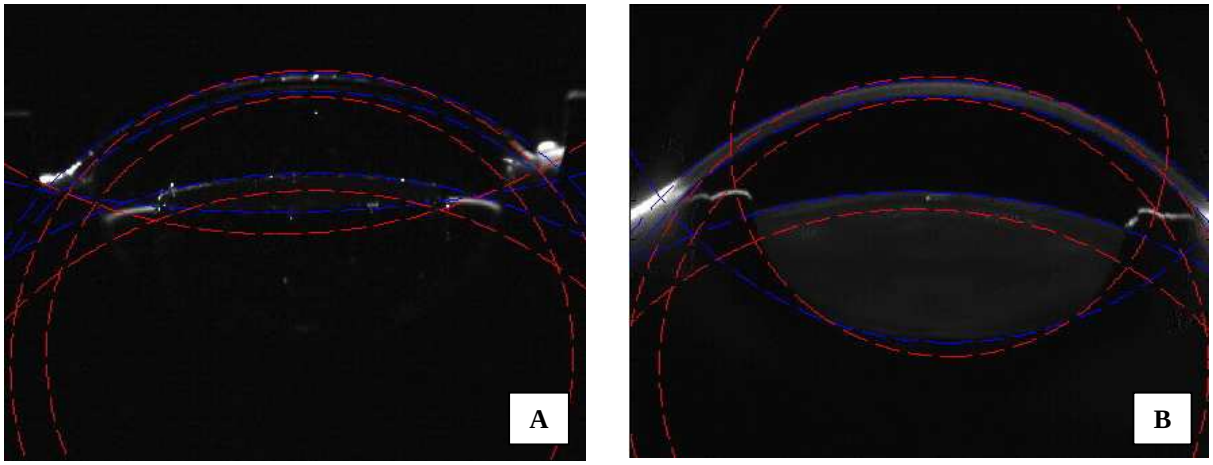

Figure 3.14. Corrected Scheimpflug images. Blue lines represent the detected edges on the uncorrected image. Red lines represent the corrected surfaces for the artificial eye. **A.** Artificial eye. **B.** Normal human eye.

Tables 3.2 and 3.3 show the radii of curvature of the anterior and posterior cornea and anterior and posterior lens and inter ocular distances of the physical and human eye respectively, and those obtained before and after applying the developed distortion correction algorithms for the Pentacam Scheimpflug.

Table 3.2. Radii of curvature of the ocular surfaces and intraocular distances of the artificial eye and the normal human eye before and after distortion correction.

	ARTIFICIAL EYE	NORMAL EYE
Anterior Cornea Radius (mm)	7.8	7.72
Cornea thickness (mm)	0.55	0.54
Posterior cornea radius of curvature (mm)	6.48	6.48
Anterior Chamber Depth (mm)	3	3.15
Anterior Lens Radius of curvature (mm)	12.25	10.54
Lens Thickness (mm)	1.164	4.04
Posterior Lens Radius of curvature (mm)	12.25	5.80

Table 3.3. Radii of curvature of the ocular surfaces and intraocular distances of the artificial eye and the normal human eye

	ARTIFICIAL EYE		NORMAL EYE	
	Before Correction	**After Correction**	**Befote Correction**	**After Correction**
Anterior Cornea Radius of curvature (mm)	8.98	7.59	9.43	7.86
Cornea thickness	0.31	0.53	0.43	0.55
Posterior cornea radius of curvature (mm)	8.48	6.43	8.99	6.97
Anterior Chamber Depth (mm)	2.15	2.52	2.48	2.86
Anterior Lens Radius of curvature (mm)	15.85	11.68	14.68	10.37
Lens Thickness	0.99	1.24	3.83	4.06
Posterior Lens Radius of curvature (mm)	24.26	11.59	8.87	5.55

4. CONCLUSION

We have developed distortion correction algorithms for the Pentacam Scheimplug system. These algorithms have proved to recover the radii of curvature of the different ocular surfaces of a physical model eye, and real eye previously measured with other techniques. Minimization algorithms have been necessary to obtain the location of the nodal points of the camera. The lack of information on the optical parameters of the Pentacam Scheimpflug system has imposed a limitation on the correction algorithms with respect to those developed by other authors for previous Scheimpflug systems.

Crystalline lens radii of curvature from Purkinje and Scheimpflug imaging

4

4. Crystalline Lens radii of curvature from Purkinje and Scheimpflug imaging

This chapter is based on the article by P. Rosales et al., *"Crystalline Lens radii of curvature from Purkinje and Scheimpflug imaging"* Journal of Vision Vol 6(10), 1057-1067. Coauthors of the study are M. Dubbelman, S. Marcos and GL. Van der Heijde. The contribution of Patricia Rosales to the study was to adapt the Purkinje imaging system to do the comparison with Scheimpflug imaging, measurements of phakometry, data analysis of the Purkinje images and the discussion of the results after comparison between Purkinje and Scheimpflug imaging analysis data. Part of the study was conducted at VU Medical Center, the Vrije University, Amsterdam, The Netherlands Rob van der Heijde's lab.

RESUMEN

Objetivos: Comparación de las medidas de los radios de curvatura de las caras anterior y posterior del cristalino en estado desacomodado y en función de la demanda acomodativa (de 0 a 7D), medidos mediante los sistema de imágenes de Purkinje y de Scheimpflug corregida de distorsiones geométrica y óptica.

Métodos: La medida de los radios de curvatura del cristalino se realizó empleando un sistema de imágenes de Purkinje y una cámara de Scheimpflug corregida de distorsiones óptica y geométrica. Las medidas con ambos sistemas se realizaron en un mismo grupo de sujetos (46 ojos para la medida del radio de curvatura de la cara anterior del cristalino y 34 para la medida del radio de curvatura de la cara posterior del cristalino, ojos derechos en todos los casos) en estado desacomodado. También se realizó la comparación en función de la acomodación en 11 ojos. Las imágenes se procesaron empleando algoritmos propios, para la corrección de las distorsiones geométrica y óptica de la cámara de Scheimpflug y empleando los métodos del Teorema del Espejo Equivalente y una Función de Mérito para obtener los radios de curvatura del cristalino a partir de las imágenes de Purkinje. Las imágenes de Purkinje se analizaron teniendo en cuenta parámetros biométricos promedio (del modelo de ojo de Le Grand) y datos biométricos individuales obtenidos mediante la cámara de Scheimpflug. Los resultados obtenidos mediante ambos métodos se analizaron mediante un test ANOVA para medidas repetidas.

Resultados: Se evaluó la correlación entre el radio de la cara anterior del cristalino obtenidos mediante Scheimpflug y Purkinje utilizando correlaciones lineales y se obtuvieron pendientes, muy similares con ambos métodos (Teorema del Espejo Equivalente y Función de Mérito, empleando tanto datos biométricos individualizados como los del modelo de ojo), con pendiente entre 0.752 y 0.827; y r entre a 0.58 y 0.60, con una correlación estadísticamente significativa en todos los casos ($p<0.0001$). Individualmente se encontraron diferencias

estadísticamente significativas entre ambas técnicas en 4 de los 46 ojos medidos (con datos biométricos individualizados) y en 10 ojos (con datos biométricos del modelo de ojo genérico), empleando el teorema del Espejo Equivalente (EE) y en 7 y 11 ojos respectivamente empleando la Función de Mérito (MF). En las correlaciones entre Scheimpflug y Purkinje para el radio de la cara posterior del cristalino se obtuvieron pendientes entre 1 y 1.09 y r entre 0.48 y 0.43, $p<0.0001$. Se encontraron diferencias estadísticamente significativas en 17 y 19 ojos de los 34 medidos empleando biometría individualizada y datos del modelo de ojo respectivamente, para el método del Espejo Equivalente y en 10 y 19 ojos respectivamente empleando la Función de Mérito. En el caso de los cambios de los radios de curvatura con la acomodación, con un análisis de la varianza (ANOVA) no se encontraron diferencias estadísticamente significativas ($F = 3.7$, $df = 1$, $p = 0.083$). Se encontró que el radio anterior del cristalino desacomodado, obtenido mediante las diferentes técnicas, empleando tanto datos biométricos como datos genéricos del modelo de ojo varía entre 7.23 ± 0.04 mm y 13.45±0.59 mm para la cara anterior del cristalino y entre 4.73 ±0.43 mm y 9.49±0.18 mm para la cara posterior del cristalino. Ambas superficies se hacen más curvas con la acomodación, a razón de 0.59 mm/D para el radio anterior y 0.27 mm/D para el radio posterior, en promedio empleando las diferentes técnicas y empleando tanto datos biométricos individuales como genéricos del modelo de ojo.

Conclusiones: Con ambas técnicas se obtienen medidas rápidas y fiables de la curvatura del cristalino. Los datos obtenidos con la cámara de Scheimpflug son ligeramente menos variables que los obtenidos con las imágenes de Purkinje. Con la cámara de Scheimpflug, además, se puede obtener información mucho mas completa sobre la biometría de la cámara anterior y la geometría del cristalino. Sin embargo, es necesaria la dilatación de la pupila para mejorar la visibilidad de la cara posterior del cristalino que en algunos casos es imposible de detectar, mientras que con las imágenes de Purkinje ha sido posible realizar medidas robustas de la cara posterior del cristalino en todos los casos del estudio.

ABSTRACT

Purpose: We present a comparison between two methods to measure the radius of curvature of the anterior and posterior lens surfaces, corrected Scheimpflug Imaging and Purkinje Imaging in the same group of subjects (46 for the anterior lens, and 34 for the posterior lens). Comparisons were also made as a function of accommodation (0 to 7 D) in a subset of 11 eyes.

Methods: Data were captured and processed using laboratory prototypes and custom processing algorithms (for optical and geometrical distortion correction in the Scheimpflug system, and using either Equivalent Mirror or Merit Function methods for Purkinje). Analysis of Purkinje images was performed according to biometric parameters obtained from a model eye (Le Grand) and from individual biometric data obtained from Scheimpflug camera. Results from both methods are compared with an ANOVA test for repeated measurements.

Results: For anterior lens radius of curvature, slopes and correlation coefficients of a linear regression between anterior radii from Scheimpflug and Purkinje are very similar in all cases (slope ranging from 0.752 to 0.827, and r from 0.58 to 0.60), and the correlation is statistically significant in all cases ($p < 0.0001$). We found statistically significant differences in the anterior radii of curvature between techniques in 4 out of the 46 eyes (using individual biometry) and 10 eyes (using model eye data), with the Equivalent Mirror (EM) procedure, and 7 and 11 eyes respectively using the Merit Functon (MF). For the posterior lens radius of curvature we found statistically significant differences in the posterior radii of curvature. Slopes and correlation coefficients of a linear regresion between the posterior radius of curvature obtained with Scheimpflug and Purkinje imaging are very similar in all cases (ranging from a slope of 1 to 1.09, and r from 0.48 to 0.43, $p<0.0001$). Differences between techniques were found in 17 and 19 out of 34 using individual biometry and model data respectively, for

the EM method, and in 10 and 9 subjects respectively for the MF. For lens radii of curvature during accommodation comparison, an analysis of variance (ANOVA) demonstrated that the difference in the anterior and posterior radius of curvature obtained with the two methods was not significant ($F=3.7, df=1, p=0.083$).

For the unaccommodated state, the average anterior lens radius of curvature with the different methos, using biometric data as well as data from the model eye was in the range between 7.23 ± 0.04 mm to 13.45±0.59 mm for the anterior lens radius of curvature and between 4.73 ±0.43 mm to 9.49±0.18 mm for the posterior lens radius of curvature. Both surfaces became more steeply curved with accommodation at a rate of 0.59 mm/D for the anterior lens radius of curvature and 0.27 mm/D for the posterior lens radius of curvature, on average using the different techniques and using custom biometric data as well as data from the model eye

Conclusions: Both techniques provided rapid and reliable data in a clinical/laboratory setting. Scheimpflug imaging is slightly less variable than Purkinje imaging and provides more complete information on anterior chamber biometry and the crystalline lens geometry, however it requires pupil dilation in order to improve the visibility of the posterior lens surface while with Purkinje imaging accurate measurement of the posterior lens surface is possible without pupil dilation.

1. INTRODUCTION

We have implemented techniques for phakometry measurements based on Purkinke imaging (with two different algorithms, the Equivalent Mirror Theorem and the Merit Function), and worked with images of the crystalline lens from Scheimpflug imaging systems. Despite Scheimpflug and Purkinje Imaging having been used by several authors to perform in vivo phakometry, to our knowledge a direct comparison between radii of curvature obtained with these two techniques on the same eyes has been never done. Koretz et al (Koretz, Strenk, Strenk & Semmlow, 2004) performed a comparative study between Scheimpflug and high-resolution magnetic resonance imaging (MRI) of the anterior segment of the eye. In that study each technique was performed on a different group of subjects, and only a comparison could be made on the trends of the cross-sectional changes with age. Furthermore, there has been discussion on the statistical methods used and the conclusions drawn from the results (Dubbelman, van der Heijde & Weeber, 2005). Cross-validation of Purkinje and Scheimpflug imaging on the same set of subjects during the same experimental session is important in order to validate both methods and shed light on the validity of both techniques on phakometry measurements.

In this chapter we compare phakometry from Purkinje imaging (developed at the Instituto de Optica, Madrid, and modified in order to obtain a similar configuration for fixation as the one used with Scheimpflug camera) and from a Scheimpflug imaging system (implemented at VU Medical Center, Amsterdam) on the same set of subjects for relaxed accommodation, and as a function of accommodation in a subsample of eyes. For comparison, Merit Function and Equivalent Mirror Theorem algorithms were evaluated, using custom biometric data from Scheimpflug imaging and model eye data from a Le Grand model eye to evaluate the accuracy of both methods and the influence of biometrical data on the precision of the measurement.

2. METHODS

2.1 Purkinje imaging.

The Purkinje imaging system developed in this thesis was used to perform phakometry. The optical set-up and data analysis, as well as experimental and computational validations, have been described in detail in Chapter 2. The system is

compact and was easily transported to the VU University Medical Center, Amsterdam, The Netherlands, where the experiments were conducted. For comparative measurements with the Scheimpflug system, a slight change was incorporated with respect to the described implementation used in other experiments: a mirror was inserted in the fixation channel in order to offer the left eye an accommodation stimulus, while the right eye is being imaged.

Heights of the double Purkinje images were computed and processed to obtain radii of curvature in the vertical meridian. The anterior and posterior lens radius of curvature were obtained using both the EM, (Smith & Garner, 1996) and the MF, methods (Garner, 1997), with custom-developed routines written in Matlab (detailed explanation of those methods is in Chapter 2). As described in that chapter, our typical experimental protocol involved measurement of corneal radius of curvature with videokeratography and optical biomety form the IOL master to process the data. In the study presented in this chapter, we obtained both optical biometry and anterior cornea radius of curvature from Scheimpflug imaging or constant data from a model eye and both results are reported.

2.2 Scheimpflug imaging

The set-up of the Scheimpflug camera as well as the necessary corrections of the Scheimpflug images, implemented at the VU Medical Center in Amsterdam, has been described previously in detail (Dubbelman M, Sicam VA & van der Heijde G. L, 2006, Dubbelman M, van der Heijde G.L & HA., 2001, Dubbelman et al., 2005), and in Chapter 3. Images were obtained with the Topcon SL-45 Scheimpflug camera, the film of which was replaced by a CCD-camera. Correction and analysis of the Scheimpflug images were done using custom developed software as described in Chapter 3. Conic of revolution were fitted to the anterior and posterior lens surfaces in order to find the asphericities of the surfaces. Furthermore, a circle was fitted to the central 3 mm zone of both lens surfaces and it is this radius of curvature that will be compared with the results of the Purkinje imaging. As a result, at least 3 mm of the lens surface should be visible on the Scheimpflug image in order to obtain its radius of curvature. For the posterior lens surface, this was not always the case, especially when only phenylephrine was used to dilate the pupil. Dubbelmann (Dubbelman & van der Heijde, 2001) validated the method in vitro, with an artificial eye and in vivo with four subjects with intraocular

lenses. The combination of the reproducibility and systematic errors has been estimated as approximately 0.3 mm for the anterior lens and 0.25 mm for the posterior lens surface.

2.3 Subjects

Experiments were performed on the right eye of 46 normal subjects with ages ranging between 22 and 60 years (30 ± 9 yrs, mean and standard deviation). Spherical equivalent ranged from -7.25 to 4.25 D (-1.5 ± 2.5 D). The experimental protocols followed the tenets of the declaration of Helsinki and had been approved by institutional review boards. Subjects were informed on the nature of the experiments and provided written consent.

A sub-sample of 11 subjects (ages ranging from 22 to 36 years, mean 28.5 years) was also examined as a function of accommodation stimulus.

2.4 Experimental procedures

The right eye of the subjects was dilated with one drop of tropicamide and one drop of 5% phenylephrine HCl. For those 11 subjects who were also measured as a function of accommodation stimulus, only two drops of 5% phenylephrine were used. Subsequently, refractive error and keratometry was measured with a Topcon KR-3500 autokerato-refractometer. Purkinje and Scheimpflug measurements were obtained in turns in the same experimental session. The subject was seated with the head in upright position, and the slit beam of the Scheimpflug was vertically oriented. The left eye was used to focus a fixation stimulus, while the right eye was photographed. The fixation stimulus was an illuminated black Maltese star (diameter: 5 cm), which was located 0.5 m from the left eye. Refractive error was corrected with trial lenses in a lens holder directly in front of the left eye and a +2 D lens was added as well in order to obtain the unaccommodated state of the eye. Subjects wearing contact lenses kept the left lens in. First of all, the subject fixated with the right eye the fixation light in the Scheimpflug camera, while the slit of the camera was aligned along the optical axis of the right eye. Then, the subject fixated with the left eye the Maltese star, the position of which can be adjusted horizontally and vertically by a remote control until the subject reports that the fixation light of the Scheimpflug camera is superimposed on the center of the Maltese star. Subsequently, the internal fixation light of the camera was turned off. At that time,

the subject was asked to focus on the Maltese star and two images were obtained. For 11 subjects, Scheimpflug images of the right eye were also obtained as a function of accommodation. For these images, the same procedure was followed except for the fact that in order to induce accommodation the power of the lens in front of the left eye was reduced in steps of 1 D with the trial lenses. Measurements were performed until the subject indicated that it was no longer possible to focus sharply on the star.

Purkinje images were obtained with the double vertical LEDs. The right eye's pupil was aligned to the optical axis of the camera by means of a X-Y-Z stage to which a chin rest was mounted. For the left eye, the set-up (lens holder, trial lenses, Maltese cross) and protocol for the accommodation experiments were identical to that used during the Scheimpflug imaging. The pupil was continuously monitored to ensure centration and convergence was corrected by changing the lateral position of the Maltese star, until the pupil was in the center of the screen.

Each measurement was repeated at least three times for each method for statistical analysis.

2.5 Statistical analysis

Statistical differences of the radii of curvature between techniques for the global sample were tested using a general linear model and analysis of variance (ANOVA) for repeated measurements. To test statistical differences between techniques for each individual eye we performed a Test of Homogeneity of Variances (for repeated measurements with the same technique). As a result, we applied ANOVA with the Bonferroni post hoc test if the variances were equal and Welch-ANOVA with the Tamhane post hoc test if the variances were unequal. The change of radii of curvature with accommodation, and differences of those between techniques were tested using ANOVA. In all cases a significance level (p) of 0.05 was considered (or a confidence interval of 95%).

3. RESULTS

Figure 4.1 shows a typical example of a Purkinje image showing double PI, PIII and PIV (A) and an example of a corrected Scheimpflug image (B), for the same unaccommodated eye.

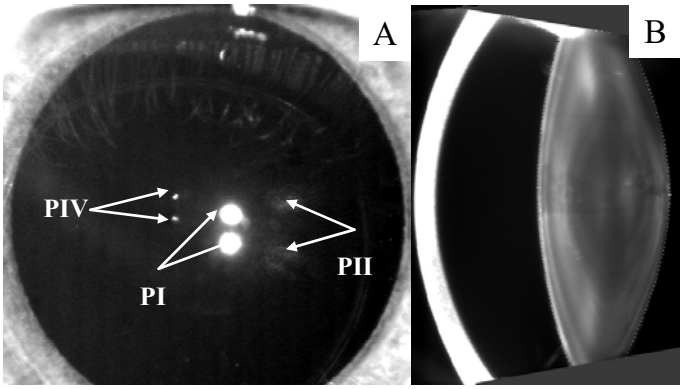

Figure 4.1. Examples of **A.** Purkinje Images **B.** Scheimpflug Image for the same unaccommodated eye.

3.1 Lens radii of curvature of the unaccommodated eye

Table 4.1 shows that there is a good match between anterior lens radius of curvature measurement from Purkinje imaging and Scheimpflug imaging.

Anterior Lens Radius	SCHEIMP FLUG CAMERA	PURKINJE IMAGING SYSTEM			
		Individual Biometric Data (I)		Model Eye (ME)	
		MF	EM	MF	EM
Average	11.1 ± 1.1	10.8 ± 1.1	10.95 ± 1.1	10.8 ± 1.3	10.9± 1.25
Range	[8.1, 13.8]	[7.9 , 13.3]	[8.1 , 13.6]	[7.2 , 13.45]	[7.4 , 13.5]

Table 4.1. Comparison of the anterior lens radii of curvature in mm (mean and standard deviation) obtained with Scheimpflug and Purkinje imaging.

There are no significant differences between Purkinje imaging anterior radii with data processed using individual biometric (I) or model eye data (LG) ($p=0.072$ for EM, and $p=0.113$ for MF). The average (±SD) difference between the anterior lens radius of curvature obtained with Scheimpflug and Purkinje imaging is 0.36 ±0.76mm (MF) and 0.13 ±0.77mm (EM).

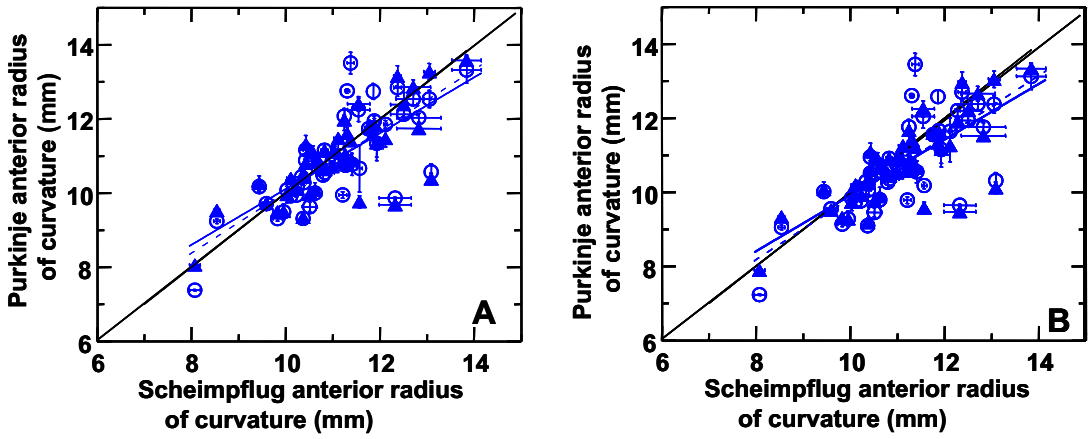

Figure 4.2. Anterior radii of curvature from Scheimpflug imaging vs Purkinje imaging using **A.** Equivalent Mirror **B.** Merit function. Solid triangles are for Purkinje imaging using individual biometry and open circles using biometry from a model eye. It is remarkable the similarity between both graphics.

Figure 4.2 A shows the anterior lens radii of curvature obtained from Scheimpflug measurements versus those obtained from Purkinje imaging using the EM theorem. Solid symbols are for Purkinje imaging data using individual biometric data of anterior chamber depth and lens thickness, and open symbols are for Purkinje imaging data using fixed data from the model eye. Similarly, Figure 4.2 B shows the same data, but with Purkinje imaging using the Merit Function (MF) algorithm. In this figure, vertical error bars represent individual variability (standard deviation) for repeated Purkinje imaging anterior radii estimates. Average (across-subjects) standard deviation for repeated measurements was 0.5 mm. This variability arises from an average measurement variability in h_3 (separation of PIII double images) and h_1 (separation of PI double images) of 0.11 mm in both cases. Horizontal error bars represent individual variability for repeated Scheimpflug imaging (and was 0.10 mm on average).

Slopes and correlation coefficients of a linear regression between anterior radii from Scheimpflug and Purkinje are very similar in all cases (slope ranging from 0.752 to 0.827, and r from 0.58 to 0.60), and the correlation is statistically significant in all cases ($p< 0.0001$). In an ANOVA for repeated measurements the difference across the entire sample was not statistically significant using the EM (for both individual biometry, $p=0.221$ and model eye biometry, $p=0.231$). This statistical test found differences for the MF ($p=0.003$ and $p=0.011$ for individual and model eye biometry, respectively). On an individual basis, we found statistically significant differences in the anterior radii of

curvature between techniques in 4 out of the 46 eyes (using individual biometry) and 10 eyes (using model data), with the EM procedure, and 7 and 11 eyes respectively using the MF.

Table 4.2. Comparison of the posterior lens radii of curvature in mm (mean and standard deviation) obtained with Scheimpflug and Purkinje imaging**.**

Posterior Lens Radius	SCHEIMPFLUG CAMERA	PURKINJE IMAGING SYSTEM			
		Individual Biometric Data		Model Eye	
		MF	EM	MF	EM
Average	6.1 ± 0.55	6.7 ± 0.8	7.6 ± 1.0	6.5 ± 1.0	7.4 ± 1.2
Range	[5.1 , 7.15]	[5.2 , 8.65]	[5.7 , 10.2]	[4.8 , 9.5]	[5.2 , 11.15]

Table 4.2 shows posterior lens radii of curvature (average ± SD and range) obtained from Scheimpflug, and Purkinje imaging (with the MF, and EM, and individual phakometry, I, or model eye data, LG, respectively). Unlike results for the anterior lens, posterior lens radii of curvature from the MF and EM are significantly different. The average (±SD) differences between the posterior lens radius of curvature obtained with Scheimpflug and Purkinje imaging are -0.57 ± 0.58 mm (MF) and -1.47± 0.84 mm (EM). The difference is not increased when using non-individual data (-0.42 mm), as can be seen in Table 4.2.

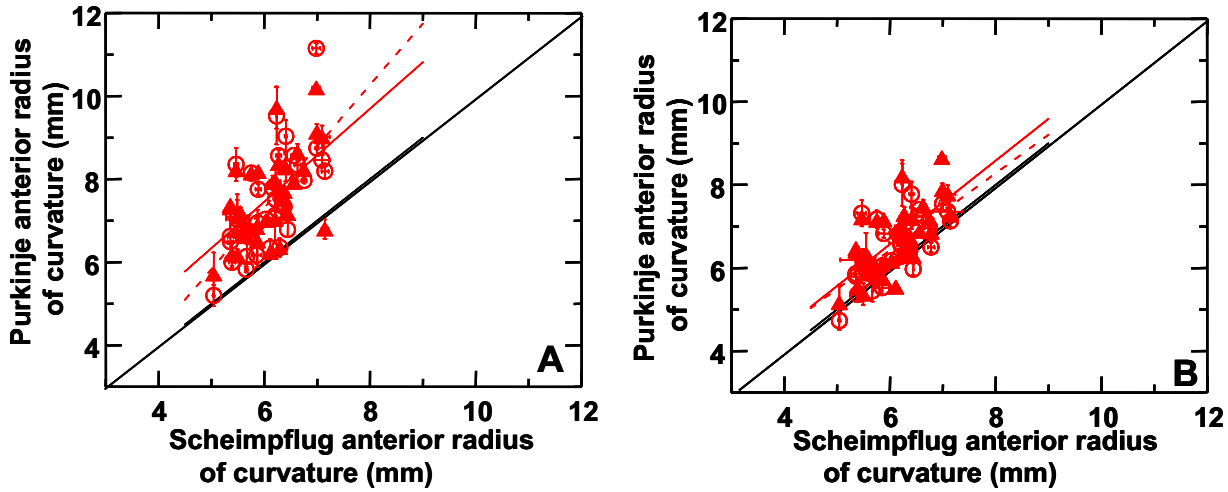

Figure 4.3. Posterior radii of curvature from Scheimpflug imaging vs Purkinje imaging using **A.** Equivalent Mirror **B.** Merit Function. Solid triangles are for Purkinje imaging using individual biometry and open circles are for Purkinje imaging using biometry from a model eye.

Figure 4.3 shows posterior radii of curvature from Scheimpflug imaging versus Purkinje imaging in a similar format to that of Figure 4.2. For simplicity, we show absolute values, whereas the posterior radii of curvature are always negative. Vertical error bars represent individual variability (standard deviation) for repeated Purkinje imaging posterior radii estimates. Average (across-subjects) standard deviation for repeated measurements was 0.31 mm. This variability arises from a average variability in h_4 (separation of PIV double images) and h_1 (separation of PI double images) measurements of 0.02 mm in both cases. Horizontal error bars represent individual variability for repeated Scheimpflug imaging (and was 0.22 mm on average).

We have also estimated the differences in crystalline lens surface power resulting from the differences in anterior and posterior radii of curvature across techniques. We have used the lens maker formula, using individual data of lens thickness and equivalent refractive index obtained from Scheimpflug. For MF and LG we estimated that Purkinje/Scheimpflug differences in anterior lens radius of curvature of 0.3 mm and posterior lens radius of curvature of –0.45 mm will result in differences in lens power of 0.61 D.

Slopes and correlation coefficients of linear regressions between the posterior radius of curvature obtained with Scheimpflug and Purkinje imaging are very similar in all cases (ranging from a slope of 1 to 1.09, and r from 0.48 to 0.43, $p<0.0001$). In an analysis of variance the difference across the entire samples was statistically significant, for both the EM and MF ($p<0.01$ in all cases). On an individual basis, we found statistically significant differences in the posterior radii of curvature between techniques in 17 and 19 out of 34 using individual biometry and model data respectively, for the EM method, and in 10 and 9 subjects, respectively, for the MF.

3.2 Lens radius of curvature during accommodation

Figure 4.4 shows changes in the anterior and posterior radius of curvature as a function of accommodation in the same eyes for three subjects of whom it was possible to measure the radius of curvature of the posterior lens surface across the full accommodative range. All Purkinje imaging data are for the MF algorithm. No significant differences were found between using individual or model biometric data, despite the fact that ACD and lens thickness vary significantly with accommodation. Both the radius of curvature of the anterior and posterior lens surface show similar trends individually, although for some individual subjects there seems to be an almost

constant offset (for example anterior radius of curvature for S1, or posterior radius of curvature for S7).

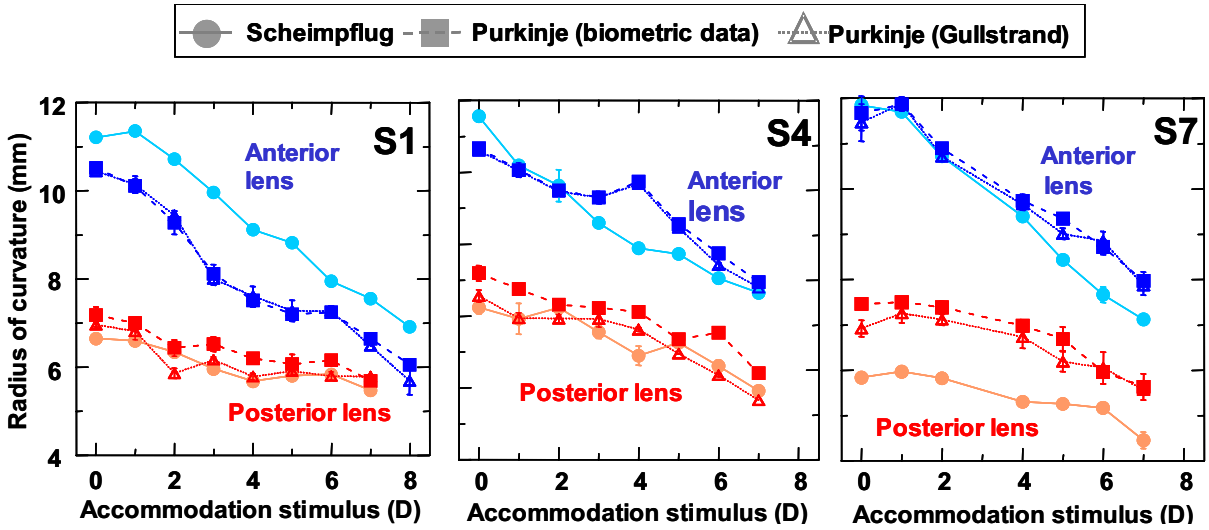

Figure 4.4. Change of anterior and posterior lens radii of curvature as a function of accommodation in three individual eyes. Each colour stands for a different subject.

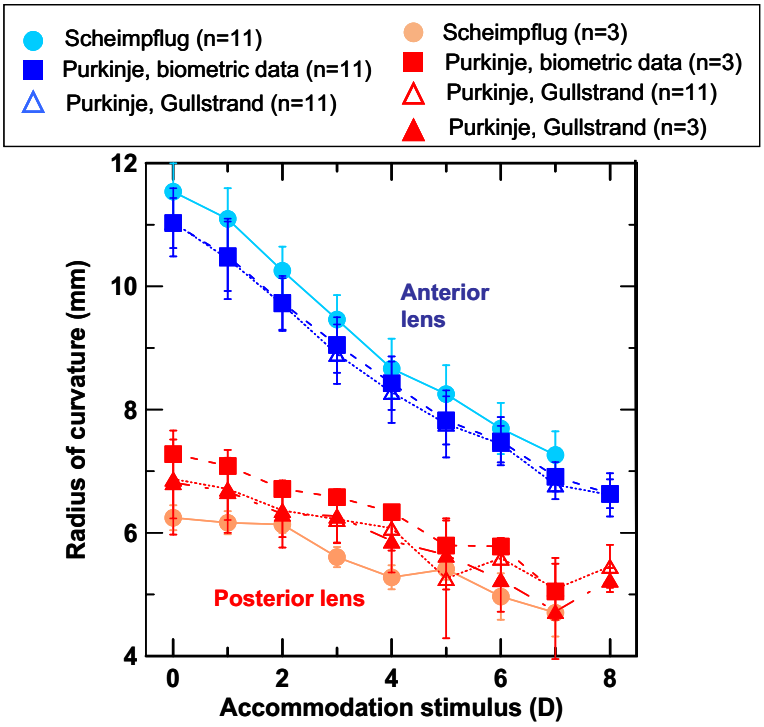

Figure 4.5. Change of anterior and posterior lens radius of curvature as a function of accommodation, averaged across eyes.

We did not observe a consistent trend of Scheimpflug/Purkinje discrepancy as a function of accommodation (Figure 4.5). For the anterior lens, the Purkinje radii were slightly lower than those of the Scheimpflug in all eyes (on average across subjects and accommodation by 0.39±012 mm and 0.46±014 mm, using individual biometry and

model eye data respectively). For the posterior lens, the Purkinje radii were slightly higher than those of the Scheimpflug in all eyes (average ± SD. across subjects and accommodation was 0.38±0.24mm). Table 4.3 shows the range of variation of anterior and posterior radii of curvature from 0 to 8 D of accommodation and slope of the linear regresion to the data using Scheimpflug and Purkinje imaging.

In an analysis of variance (ANOVA) the difference in the anterior and posterior curvature radius of curvature obtained with the two methods was not significant ($F = 3.7$, $df = 1$, $p = 0.083$) whereas the difference of radii of curvature across the different accommodative states was significant ($F = 231.8$, $df = 6$, $p < 0.001$).

Table 4.3. Range of variation of the anterior and posterior radii of curvature between 0 and 8 D and slope of the linear regression to the data, from Scheimpflug and Purkinje imaging.

	SCHEIMPFLUG	PURKINJE IMAGING SYSTEM (MF)	
		Individual Biometry	Model Eye
ANTERIOR LENS RADIUS (mm)			
Range	(11.54, 7.26)	(11.03, 6.9)	(11.04, 6.78)
slope	-0.64	-0.57	-0.57
POSTERIOR LENS RADIUS (mm)			
Range	(6.24, 4.7)	(7.28, 5.05)	(6.81, 5.23)
slope	-0.23	-0.29	-0.29

4. DISCUSSION

We found good correspondence of lens radii of curvature with our implementations of Scheimpflug and Purkinje imaging systems on the same group of eyes. The ranges of radii of curvature found with both techniques are consistent to those reported before in normal eyes for the unaccommodated eye and under different levels of accommodation stimuli. Although previous studies on different populations and different experimental protocols, and the lack of a gold standard for calibration, prevented validation of the accuracy of the different techniques used for phakometry, our comparison on an individual basis allows us to identify potential systematic errors associated to a given technique and assess the potential advantages or limitations of the different techniques.

We found that Scheimpflug and Purkinje imaging (with EM) provided statistically similar results for the anterior radius of curvature. We have also shown that using individual biometry data increases slightly the similarity between techniques for the anterior radius of curvature, and only marginally for the posterior radius of curvature, with respect of using general data from the model eye.

We have performed computer simulations to assess whether there are systematic differences that can be attributed to the Purkinje imaging method, or whether the errors do not follow any particular trend and can be attributed to both methods. The details of the ray tracing of our apparatus and computer simulations of Purkinje images were described in the Chapter 2 of this thesis. In brief, we simulated with Zemax the configuration of the optical system and simulated the intensity distributions of the Purkinje images for a model eye. The simulated Purkinje images were processed as the experimental images, using the MF. For the present simulations, we used as nominal values for the model eyes (biometry and radii of curvature of the cornea and anterior and posterior lens) those obtained from Scheimpflug imaging. We performed simulations for model eyes with spherical surfaces (as assumed in the processing algorithms) and also aspherical surfaces, with asphericities (Q-values) obtained from Scheimpflug imaging in each individual eye (-0.26 ± 0.19 for the anterior cornea, -0.49 ± 0.19 for the posterior cornea, -2.00 ± 0.15 for the anterior lens, -2.65 ± 1.42 for the posterior lens). The simulations were performed for 31 eyes. For the anterior radii of curvature, predictions using spherical surfaces in the model eye reveal a slight underestimation of Purkinje radii compared to Scheimpflug radii of curvature (nominal values in the model). However, similarly to the experimental findings, these differences are not significant. The average differences between Purkinje imaging and Scheimpflug anterior radii of curvature were 0.28±0.67 mm for the experimental values in these set of eyes, -0.50±0.16 mm for the predicted values using spherical surfaces and –0.34±0.25 mm for the predicted values using aspherical surfaces. There are good correlations between Scheimplug and Purkinje data. For the spherical surface model, we found a slope closer to 1 (0.93) than for the experimental (0.81) or predictions (0.87) using the aspheric model. For the posterior radius of curvature predictions with the aspheric model reproduce a systematic overestimation of Purkinje imaging data from the nominal Scheimpflug data. A lower overestimation is found for the spherical model eye. The average differences between Purkinje imaging and Scheimpflug posterior radii of curvature were 0.60±0.57 mm for the experimental values, 0.48±0.43 mm for the predicted values using spherical surfaces, and 1.04±0.69 mm for the predicted values using aspherical surfaces. These simulations indicate that the discrepancies found between the Purkinje and Scheimpflug posterior radii are partly inherent to the method, and also to the fact that the surface of the crystalline lens is not spherical, but exhibits a

negative asphericity (with nominal values obtained from Scheimpflug). The larger the asphericity, the larger the discrepancy. Thus, the simulations predict a higher overestimation of the lens radii respect to nominal values, whereas the experimental values lie in between predictions from spherical and aspheric surfaces. This could indicate that the asphericity of the lens is actually lower (more spherical) or that the gradient index of the lens could play a counteractive role. The asphericity of the anterior surface does not seem to affect the estimation of the anterior lens radius of curvature using Purkinje imaging, but the asphericity of the anterior lens surface, posterior lens surface, or both, do play a substantial large role in the slight overestimation of the Purkinje radii of curvature. The asphericity of the crystalline lens surfaces in young eyes is usually negative (Dubbelman et al., 2005), but varies significantly across subjects, and as a function of accommodation. The MF could incorporate an aspheric eye model to account for some of this effect, although a fixed asphericity will probably not account for all the individual effects.

Intraocular lens tilt and decentration measurements: Purkinje imaging versus Scheimpflug imaging

5

5 IOL tilt and decentration measurements: Purkinje imaging versus Scheimpflug imaging

This chapter is based on the article by de Castro. A et al., *"Tilt and decentration of intraocular lenses in vivo from Purkinje and Scheimpflug imaging: a validation study"* J. Cataract Refractive Surg. Vol 33, 418-429. Coauthors of the study are S.Marcos and P.Rosales. The contribution of Patricia Rosales to the study was data acquisition and processing of Purkinje images on the artificial eye, on normal subjects and on patients with IOLs.

RESUMEN

Objetivos: Se presenta una comparación de medidas de inclinación y descentramiento de la lente, obtenidas a partir de imágenes de Scheimpflug tomadas con una cámara de Scheimpflug comercial (Pentacam, Oculus) e imágenes de Purkinje.

Métodos: Las medidas de inclinación y descentramiento de la lente se realizaron empleando una cámara de Scheimpflug comercial (Pentacam, Oculus), con algoritmos propios para calcular la inclinación y el descentramiento de la lente y un sistema de imágenes de Purkinje desarrollado en el laboratorio. Las medidas se realizaron sobre un ojo artificial, y en veinte y un ojos de 12 pacientes operados de cirugía de cataratas.

Resultados: Las medidas realizadas sobre el ojo artificial, presentaban una discrepancia en valor absoluto, respecto del valor nominal de 0.279 deg (Purkinje) y 0.243 deg (Scheimpflug) para medidas de inclinación, y 0.0094 mm (Purkinje) y 0.228 mm (Scheimpflug) para descentramiento. En medidas realizadas sobre pacientes con lentes intraoculares implantadas se encontró una inclinación promedio menor que 2.6 deg y un valor de descentramiento promedio menor que 0.4 mm. Se observa una simetría entre ojos derecho e izquierdo para inclinación y descentramiento horizontal, tanto empleando ambos métodos.

Conclusiones: Ambos sistemas muestran una alta reproducibilidad. Las medidas realizadas sobre el ojo artificial muestran una mayor precisión empleando el sistema de imágenes de Purkinje que los algoritmos aplicados a las imágenes de Scheimpflug. Las medidas de inclinación y descentramiento en dirección horizontal están muy correlacionadas. Las medidas muestran que las lentes intraoculares tienden a estar inclinadas y descentradas nasalmente en la mayoría de los pacientes.

ABSTRACT

Purpose: To measure tilt and decentration of intraocular lenses (IOLs) with Scheimpflug and Purkinje imaging systems.

Methods: Measurements of IOL tilt and decentration were obtained using a commercial Scheimpflug system (Pentacam, Oculus) and custom algorithms, and a custom-built Purkinje imaging apparatus. Both methods were validated with a physical model eye where tilt and decentration can be set nominally. Twenty-one eyes of 12 patients with IOL implanted were measured with both systems.

Results: Slopes and correlation coefficients of measurements on the physical model eye showed an absolute discrepancy between nominal and measured values of 0.279 deg (Purkinje) and 0.243 deg (Scheimpflug) for tilt and 0.094 mm (Purkinje) and 0.228 mm (Scheimpflug) for decentration. In patients, we found an average tilt less than 2.6 deg and average decentration less than 0.4 mm. We found mirror symmetry between right and left eyes for tilt around vertical axis and for decentration in the horizontal axis, as revealed by both techniques.

Conclusions: Both systems show a high reproducibility. Validation experiments on physical model eyes shows slightly higher accuracy with the Purkinje than the Scheimpflug imaging method. Horizontal measurements on patients from both techniques are highly correlated. IOLs tend to be tilted and decentered nasally in most patients.

1. INTRODUCTION

Although some studies reporting measurements of IOL tilt and decentration in vivo with Purkinje imaging and Scheimpflug imaging have been published, to our knowledge no validation studies of these techniques have been presented. The Purkinje imaging system developed in this thesis to measure tilt and decentration of the crystalline lens has been described in detail in Chapter 2. In research projects undergoing at the Visual Optics and Biophotonics lab, routines to measure tilt and decentration from Scheimpflug imaging have been developed in parallel by Alberto de Castro (de Castro, Rosales & Marcos, 2007). The Scheimpflug camera provides images of the anterior chamber of the eye. Its configuration is such that the image, lens and object plane intersect in one point, so that sections of the eye appear with large depth-of-focus. Scheimpflug images suffer from geometrical distortion (due to tilt of the object, lens and image planes), and optical distortion (due to the fact that the different surfaces are viewed through anterior refracting surfaces). Ray-tracing techniques are therefore required to obtain more reliable crystalline surface geometry (Dubbelman & van der Heijde, 2001, Lapuerta & Schein, 1995). Scheimpflug research instruments (Brown, 1973, Dubbelman & van der Heijde, 2001, Koretz, Cook & Kaufman, 1997) have been used to study the shape of the crystalline lens and how it changes with accommodation (as shown in Chapter 4) or aging (Dubbelman & van der Heijde, 2001, Dubbelman, van der Heijde & Weeber, 2005). In the clinical literature, there are numerous reports of intraocular lens tilt and decentration measurements either longitudinally or comparing different types of lenses using commercial Scheimpflug instruments reports (Baumeister, Neidhardt, Strobel & Kohnen, 2005, Hayashi, Hayashi, Nakao & Hayashi, 1998, Jung, Chung & Baek, 2000, Kim & Shyn, 2001, Nejima, Miyata Honbou, Tokunaga, Tanabe, Sato & Oshika, 2004, Sasaki, Sakamoto, Shibata, Nakaizumi & Emori, 1989, Meng-Chi, Lin-Ghung, Chao-Yu & Han-Chin., 1998). In these instruments the optical distortion is presumably not corrected. Only a recent study of IOL tilt and decentration in eyes with phakic lenses (Coopens, Van den Berg & Budo, 2005), using a Nidek Scheimpflug system, mentions that images were corrected using custom algorithms.

The availability of new Scheimpflug commercial instruments may make the measurement of IOL tilt and decentration more accessible. However, powerful data

processing routines, a careful assessment of the limitations of the technique, and experimental validations are necessary before this information can be used reliably.

In this chapter we present measurements of IOL tilt and decentration of intraocular measurements in a water cell model eye and in patients, using a custom-built Purkinje imaging system and a Pentacam Scheimpflug imaging with custom algorithms. To our knowledge, this represents the first assessment of the accuracy of the techniques to measure IOL tilt and decentration, and the first cross-validation of Scheimpflug and Purkinje imaging to measure tilt and decentration.

2. METHODS

2.1 Purkinje imaging

A system for phakometry and lens tilt and decentration measurements based on phakometry and implemented at the Instituto de Optica (CSIC) was used in the study. The optical set up, processing algorithms and validations have been described in the chapter 2 of this thesis. In brief, the system consists of 1) two illuminating channels (for measurements on right and left eyes) with collimated light from IR LEDs, at an angle of 12 deg, horizontally; 2) an imaging channel with an IR-enhanced CCD camera provided with a telecentric lens mounted in front of the eye and conjugate with the eye´s pupil; 3) a fixation channel with a minidisplay, a collimating lens and a Badal system, which allows projection of visual stimuli both foveally and at different eccentricities, as well as correction of refraction. The system sits on a 500 × 400 mm optical table. Software written in Visual Basic (Microsoft Visual Studio 6.0, Redmond, WA) controls automatically the image acquisition, LED switching and stimulus display. Data processing is performed using Matlab (Mathworks Inc., Natick, MA) and the optical design program Zemax (Focus Software, Tucson, AZ). The detection of Purkinje images PI, PII and PIII and pupil center in the pupillary images is performed using Gaussian fitting with routines written in Matlab. The processing routines assume that P1, P3 and P4 (positions of PI, PII and PIII relative to the center of the pupil) are linearly related with eye rotation (β), lens tilt (α) and lens decentration (*d*).

$$P1 = E\,\beta$$
$$P3 = F\,\beta + A\,\alpha + C\,d$$
$$P4 = G\,\beta + B\,\alpha + D\,d,$$

These equations are applied to both horizontal and vertical coordinates. Coefficients A-G are obtained using a computer model eye (simulated using biometric data available

for each eye). IOL decentration is referred to the pupil center. IOL tilt is referred to the pupillary axis.

2.2 Scheimpflug imaging

A commercial Scheimpflug imaging System (Pentacam, Oculus) was used to image sections of the anterior segment of the eye at different meridians (25), by projecting a slit (blue light). The software of the system corrects geometrical distortion but shows uncorrected images. Since we work directly on the images captured, a routine to correct this distortion was implemented (de Castro et al., 2007). The commercial software provides quantitative information of the anterior and posterior corneal surfaces, but not the crystalline lens/IOL. In addition, the edge detection routines of this software usually fail to detect the edges of certain types of IOLs (i.e. acrylic) due to their different scattering properties from the crystalline lens. We have developed algorithms that work directly on the raw images and calculate IOL tilt and decentration. These include:

1) Correction of the geometrical distortion of the images.

2) Routines to find the edges of cornea and intraocular lenses.

3) Routines fitting the edges of the pupil and the lens to find the pupil center, IOL center, IOL tilt, and eye rotation.

4) These procedures are applied to each of the 25 sections obtained at each meridian.

5) IOL decentration is obtained from the distance between the IOL center and the pupillary axis.

2.3 Physical model eye

A physical model eye was built by Alberto de Castro (de Castro et al., 2007) especifically for this study, where nominal values of IOL tilt and decentration can be set. Figure 5.1 shows a photograph (A) and a schematic diagram (B) of the model eye. It consists of a PMMA water cell model, with a PMMA contact lens simulating the cornea and IOL lenses on a XYZ micrometer stage and rotational stage. The cornea was built by a contact lens manufacturer (AR3 Vision, Madrid, Spain) with parameters similar to the Gullstrand eye model (corneal diameter: 11.20 mm, anterior corneal radius: 7.80 mm, posterior corneal radius: 6.48 mm, central thickness: 500 μm). Different intraocular lenses with spherical or aspheric designs from different manufacturers (Pharmacia, Alcon and A.M.O.) with IOL powers of 19, 22 and 26 D were used in place

of the crystalline lens. Decentration was achieved in the horizontal direction, with a precision of 0.1 mm. Tilt of the IOL was achieved in the horizontal direction, with a precision of 0.01 degrees. The anterior chamber depth could be varied, but for the purpose of this study we kept it constant at 5 mm.

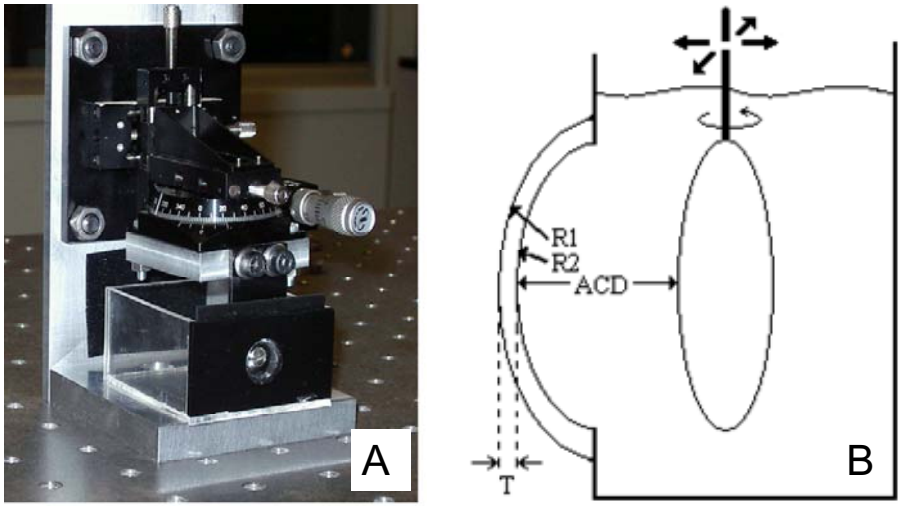

Figure 5.1. A. Photograph and **B.** schematic diagram of the physical model eye developed for this study. A PMMA contact lens simulates the cornea (R1= 7.80 mm, R2= 6.48 mm, T= 500 mm). IOLs are positioned with an XYZ micrometer stage and rotational stage.

2.4 Patients

For this study 21 eyes from 12 patients (average age 72 ± 8 years) with intraocular lenses implanted were measured. Time after surgery was at least six months. IOLs had aspherical designs. All protocols adhered to the declaration of Helsinki and followed protocols approved by Institutional Review Boards. All patients signed informed consents after receiving an explanation of the purposes of the study.

2.5 Experimental protocols

The artificial eye is fixated in a translational XYZ and then aligned with the system. The main difference with respect to measurements on patients is that the optical axis of the model eye is collinear with the optical axis of the instrument (as opposed to the line of sight).

Measurements were done for horizontal decentrations ranging from 0 to 2 mm (every 1 mm) and horizontal tilts (around the vertical axis) ranging from 0 to 4 degrees (every

1 deg). Since the IOL does not rotate around its own axis, induced decentration was compensated for the tilted conditions. Alternate measurements with both the Purkinje and Scheimpflug systems were made for each condition of tilt and decentration.

Measurements on patients were performed under pupil dilatation with tropicamide 1%. In the Purkinje apparatus, subjects were aligned with respect to the line of sight while they viewed foveally a fixation target presented in the minidisplay. Stabilization was achieved with a dental impression. Series of images were captured for different fixation angles (with fixation stimuli presented from -3.5 to 3.5 deg horizontally and from -2.5 to 2.5 deg vertically). Although only a snapshot is necessary to obtain IOL tilt and decentration, different eccentricities were tested to avoid overlapping of the Purkinje images. To assess the measurement reproducibility the whole procedure was repeated 3 times. For Scheimpflug imaging the subject fixates foveally a fixation target. Three series of 25 images were obtained per eye.

Data processing of Purkinje imaging data requires several individual ocular biometry data to obtain coefficients A-G in the Phillips equations. For the artificial eye these were taken from nominal values. In patients we measured anterior corneal radius and anterior chamber depth from optical biometry (IOLmaster, Zeiss). The radii of curvature of the anterior and posterior IOL surfaces were measured using the phakometry mode of our Purkinje imaging system (see (Rosales & Marcos, 2006)) if the geometry of the lens was not known.

3. RESULTS

3.1 Purkinje imaging and Scheimpflug raw data

Figure 5.2 shows typical images for the artificial eye captured with the Purkinje imaging system (top) and the Scheimpflug camera (bottom) respectively. Left images correspond to an eye with a 2-mm decentered silicone IOL, and right images to an eye with a 3-deg tilted acrylic IOL. Nominal decentration and tilt were set with the micrometer stages in the artificial eye. Purkinje images PI, PIII and PIV have been marked on Figure 5.2, and the detected edges and fitting circumferences are superimposed on the Scheimpflug sections of Figure 5.2. Figure 5.3 shows typical examples of Purkinje (left) and Scheimpflug (right) images for one real eye. Differences in the diffusing properties of the real cornea and PMMA cornea of the artificial eye can be observed.

The relative positions of PI, PIII and PIV with respect to the center of the pupil are detected from images like those shown in Figure 5.2 and 5.3, and data are processed as explained above to obtain Purkinje tilt and decentrations. The centers of curvature of the corneal and lens surfaces and pupil center are computed from each of the 25 Scheimpflug sections as those shown in Figure 5.2 and 5.3.

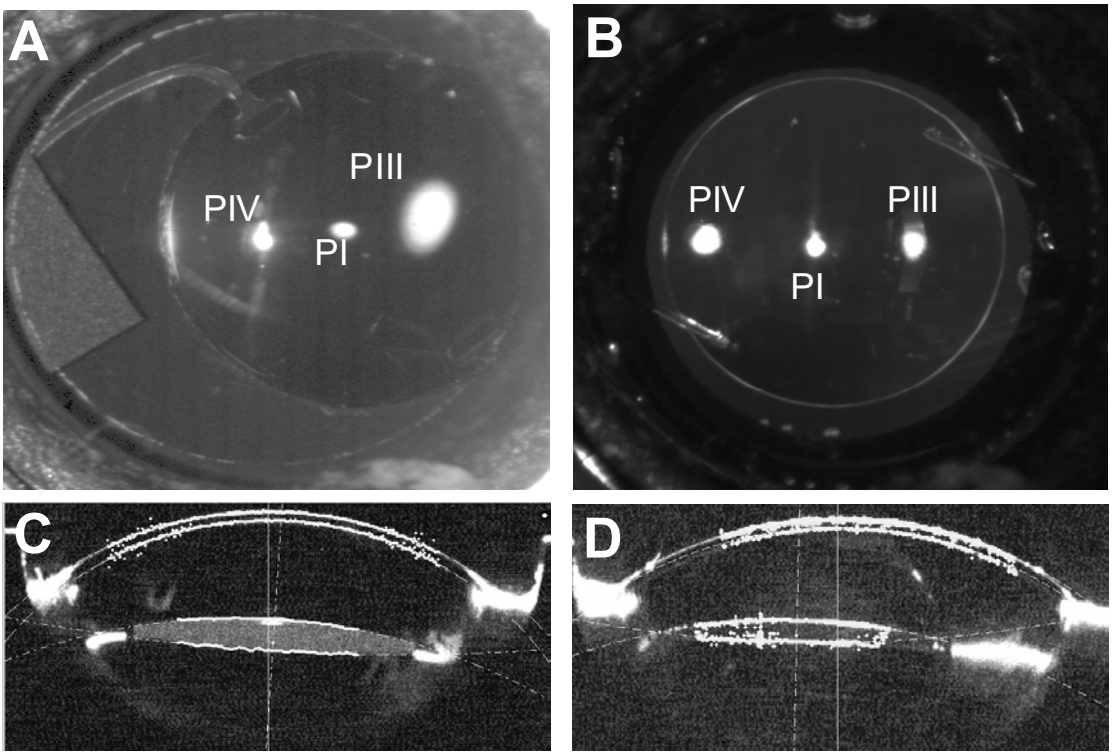

Figure 5.2. **A. B.** Raw images obtained using the Purkinje imaging system and Scheimpflug system **C. D** from the model eye. The examples correspond to a tilted silicone IOL **(A, C)** and a decentered acrylic IOL **(B, D)**. PI, PIII and PIV are marked on the image from the Purkinje system. The fitted curves and calculated axes have been superimposed on the Scheimpflug image.

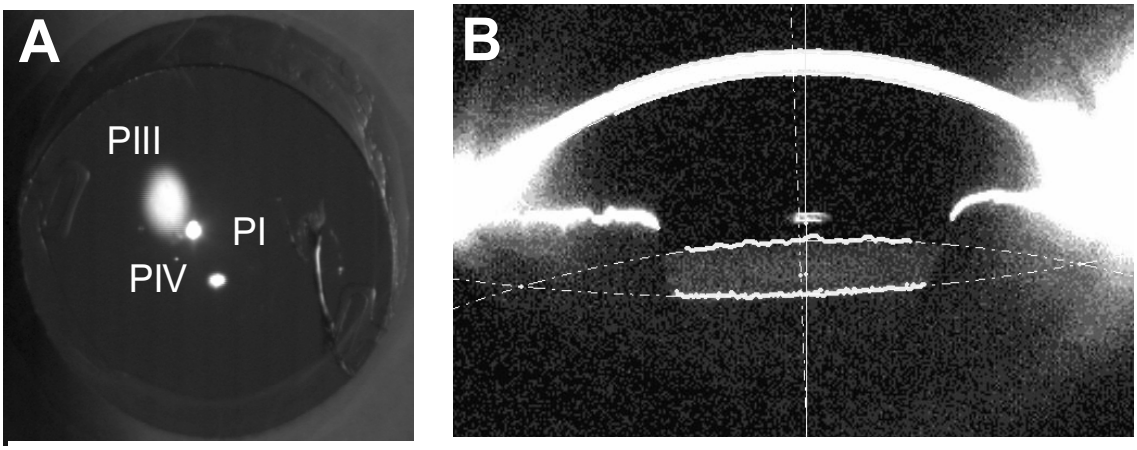

Figure 5.3. Raw images from the Purkinje **(A)** and Scheimpflug **(B)** systems in a real eye. As in Figure 2, the Purkinje images locations and fitted curves and calculated axis have been superimposed.

3.2 IOL tilt and decentration in the physical model eye

Figure 5.4.A shows measured tilt from Purkinje imaging, and 5.4.B measured tilt from Scheimpflug imaging as a function of nominal tilt in the artificial eye, for three different IOLs. The solid line represents the ideal results. There is a good correspondence between nominal and measured values for both Purkinje imaging (average slope= 1.088, average absolute discrepancy= 0.279 deg) and Scheimpflug imaging (average slope= 0.902 average absolute discrepancy= 0.243 deg). Error bars represent the standard deviation of repeated measurements. Figure 5.4.C shows measured decentration from Purkinje imaging, and 4.D measured decentration from Scheimpflug imaging as a function of nominal decentration in the artificial eye, for three different IOLs. There is a good correspondence between nominal and measured values for Purkinje imaging (average slope = 0.961, average absolute discrepancy = 0.094 mm and a higher disagreement for Scheimfplug imaging (average slope= 1.216, average absolute discrepancy= 0.228 mm), where there is a consistent overestimation for two of the measured lenses.

3.3 IOL tilt and decentration in patients' eyes

Figure 5.5 shows tilt (A & B) and decentration (C & D) of intraocular lenses for right eyes (A & C) and left eyes (B& D) of real patients. Results from Purkinje imaging are shown as open symbols and from Scheimpflug imaging as solid symbols. Positive tilts around X-axis indicate that the superior edge of the lens is moved forward and viceversa for negative tilts around X-axis. Positive tilts around Y-axis stand for nasal tilt and indicate that the nasal edge of the lens is moved backwards) and viceversa for a negative tilt around Y-axis, in right eyes. A positive tilt around Y-axis stands for temporal tilt (nasal edge of the lens moves forward) in left eyes. A positive horizontal decentration stands for a nasal decentration in right eyes and temporal in left eyes. Positive vertical decentration (d_y) indicates that the lens is shifted upwards and vice versa for negative. There is clear mirror symmetry in tilt (as measured with both techniques) and less systematic trend for decentration in this group of eyes.

We found average absolute tilts around X of 1.89±1.00 deg (Purkinje) and 1.17±0.75 deg (Scheimpflug), average absolute tilts around Y of 2.34±0.97 deg (Purkinje) and 1.56±0.82 deg (Scheimpflug), and average absolute horizontal decentration of 0.34±0.19 mm (Purkinje) and 0.23±0.19 mm (Scheimpflug), and average absolute

vertical decentration of 0.17±0.23 mm (Purkinje) and 0.19±0.20 mm (Scheimpflug). Figure 5.6 compares tilts and decentrations measured with Scheimpflug and Purkinje imaging. The results with both techniques are highly significantly ($p<0.001$) correlated for horizontal decentration ($r=0.764$) and tilt around Y axis ($r=0.762$), i.e. horizontal displacements of the lens. For vertical decentrations and tilts around X, the correlations are not significant, and the estimated values are close to the measurement error and method accuracy.

Repeatibility of both the Purkinje and Scheimpflug methods were found to be high: mean average standard deviation of repeated measurements were 0.61 and 0.20 degrees for tilt and 0.05 and 0.09 mm for decentration, for Purkinje and Sheimpflug respectively. An ANOVA for repeated measures was used to test whether the mean value (for each type of measurement) is representative of data. We found this to be the case in all conditions.

After this analysis, intraclass correlation coefficients were calculated to assess the reliability of the methods (since the intraclass is sensitive both to random error and to systematic bias). We found that the methods were reliable for tilt around Y (intraclass coefficient= 0.830) and for decentration in X (intraclass coefficient= 0.836).

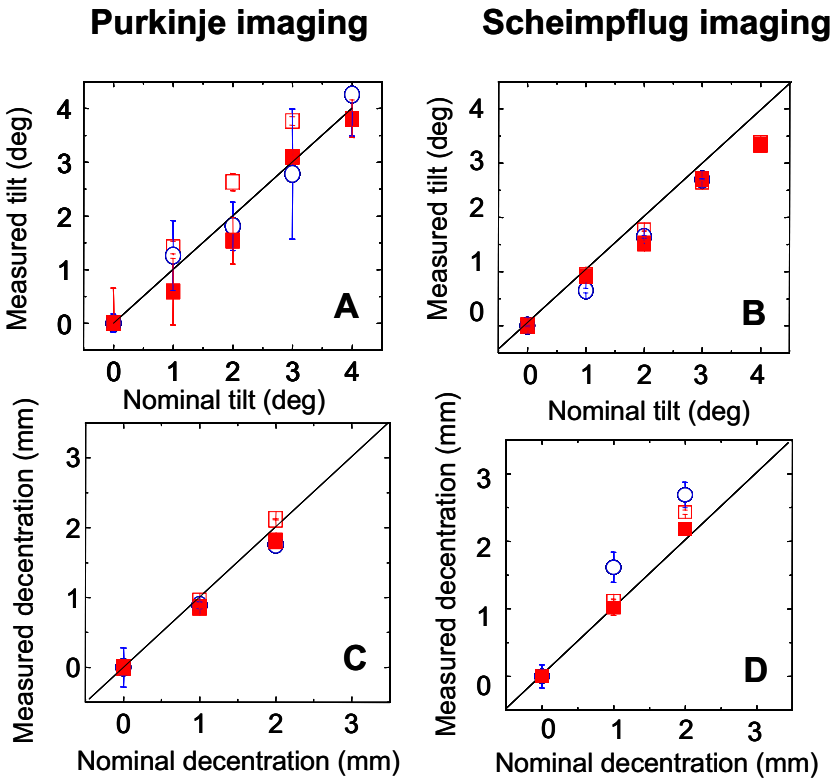

Figure 5.4. Experimental IOL tilt **(A, B)** and decentration **(C, D)** for the model eye for three different lenses (plotted with different symbols) as a function of nominal values of tilt and decentration using Purkinje imaging **(A, C)** and Scheimpflug imaging **(B, D)**. Nominal tilt ranged from 0 to 4 degrees and nominal decentration ranged from 0 to 2 mm. The ideal X=Y line has also been plotted.

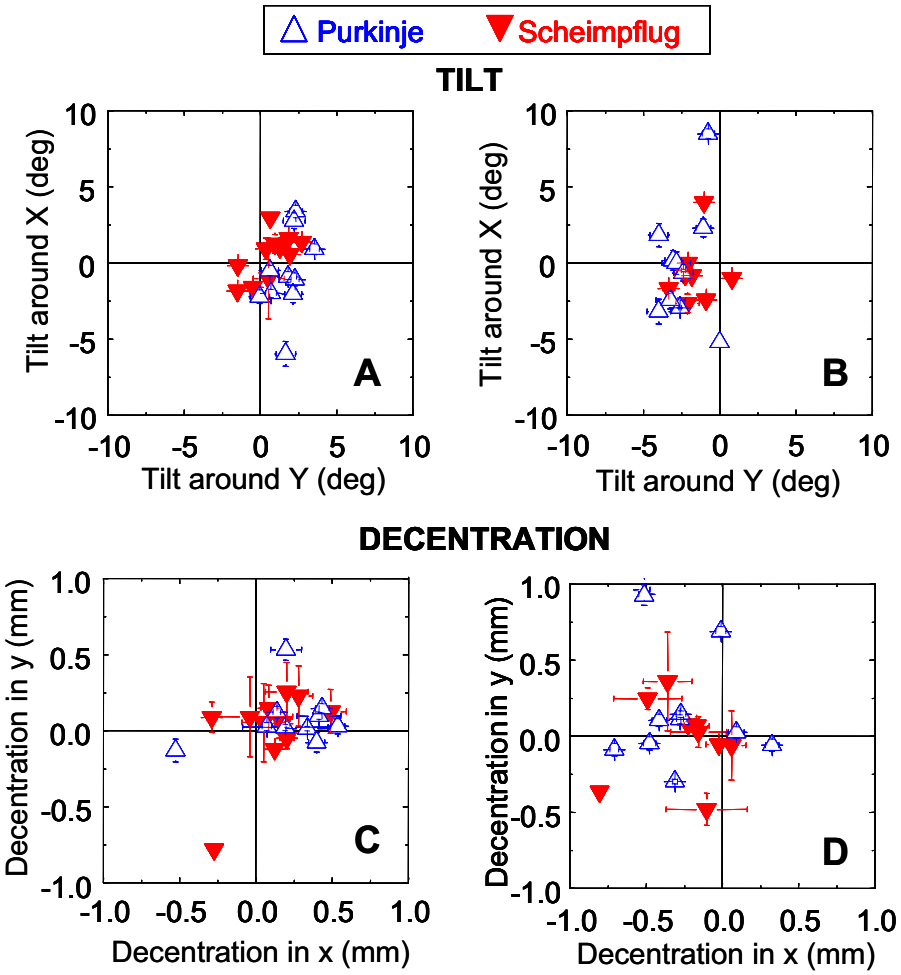

Figure 5.5. Tilt **(A, B)** and decentration **(C, D)** for right and left eyes of patients, using Purkinje (open symbols) and Scheimpflug (solid symbols) imaging. Refer to the text for details on sign conventions. The sign of the tilt around x-axis has been changed to allow a more graphical representation of lens positioning, assuming a frontal view of the patients' eyes. Both techniques show a forward (toward the cornea) tilt of the nasal side of the IOL, and a clear mirror horizontal symmetry of tilt across right and left eyes. Also, both techniques show a nasal displacement of the IOLs, and a clear mirror horizontal symmetry of tilt across right and left eyes.

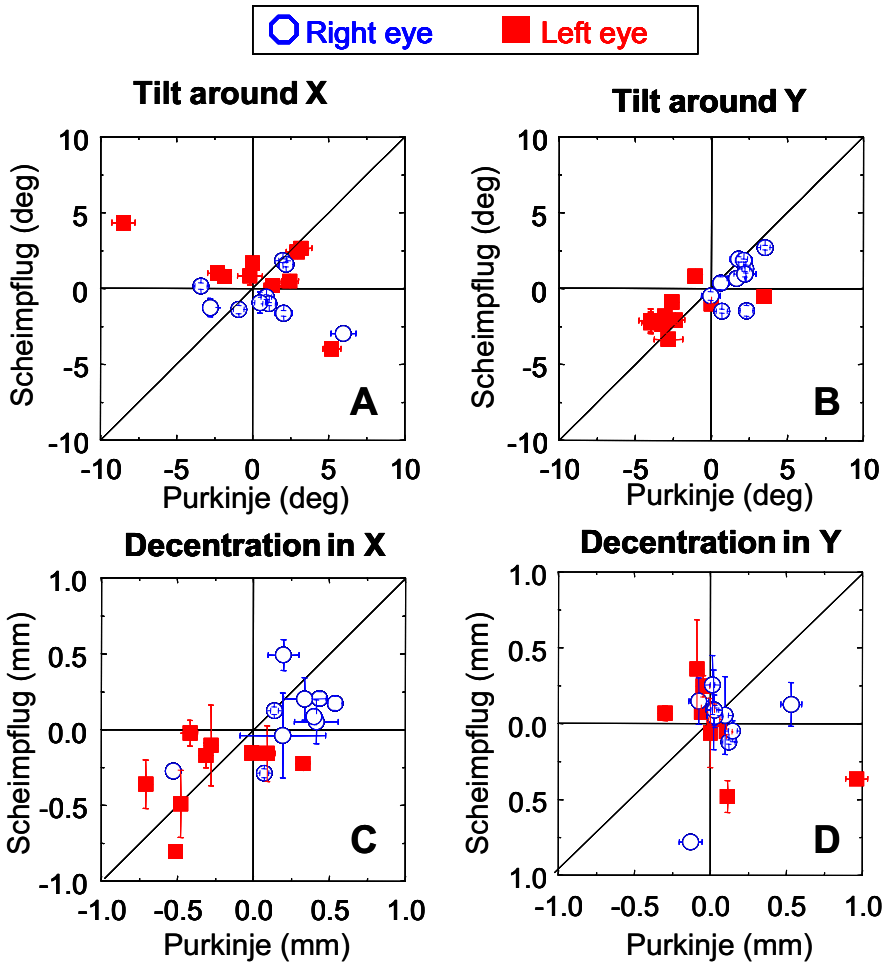

Figure 5.6. Comparison of the horizontal and vertical components of IOL tilt and decentration between Scheimpflug and Purkinje techniques. The ideal X=Y line is also shown. The correlations are statistically significant ($p<0.001$) for the tilt around x-axis and horizontal decentration.

4. DISCUSSION.

4.1 Limitations of the techniques

The Purkinje imaging system has been extensively validated computationally and experimentally in previous studies (Rosales, Dubbelman, Marcos & Van der Heijde, 2006), as has been shown in Chapters 2 and 3 of this thesis. Computer simulations using eye models and the actual optical configuration of the system show that deviations from spherical model eyes due to corneal asphericity or corneal irregularities and anterior and posterior lens surfaces asphericities did not affect significantly the results of lens tilt and decentration.

Scheimpflug images from the Pentacam system are not corrected from optical distortion, and the CCD images also suffer from geometrical distortion. The former is corrected by software at the corneal level, but not at the crystalline or IOL lens level. The second can be compensated using calibration grids. This is implemented in the commercial software to provide corrected biometry values, and a routine to compensate the raw images has been developed.

Our measurements with both techniques show a high reproducibility. The Purkinje imaging system has some limitations when lenses are very flat, for which PIII is quite large. The system also relies on the appropriate measurement of the anterior and posterior lens radii of curvature. Scheimpflug imaging requires sufficient pupil dilation to visualize the posterior lens surface and collaboration from the patients to fixate for 1.5 seconds without moving while illuminated with a blue light (a opposed to IR illumination and 30 exposure times in the Purkinje imaging system). Scheimpflug imaging also poses some challenges with low diffusing IOLs. Optical and geometrical distortion of the Scheimpflug images (as obtained directly from the CCD) produce slight discrepancies of the measured tilt and decentration, which improve with the correction of the geometrical distortion.

In real eyes, both techniques agree well, in general, for the horizontal IOL tilt and decentrations. The larger discrepancies, particularly for vertical decentration may be attributed to the proximity of the decentration measurements to the nominal accuracy of the techniques.

4.2 Comparisons to previous studies and implications

In this study we present an experimental validation of the Purkinje imaging system developed in this thesis to measure tilt and decentration of IOLs using a physical model eye. We also proposed a new robust method to calculate tilt and decentration of an IOL using a commercial Scheimpflug imaging system, which is validated using the same physical model eye. A comparison of tilt and decentration measurements in real eyes using both techniques is also presented.

Purkinje and Scheimpflug methods have been used before to measure tilt and decentration of IOLs. To our knowledge, only the reports of Barry (Barry, Dunne & Kirschkamp, 2001) and Rosales (Rosales & Marcos, 2006) were based on thoroughly validated Purkinje imaging methods. Several studies report tilt and decentration measured with Scheimpflug imaging, in most cases from two sections of the anterior

segment captured at perpendicular meridians. Coopens et al (Coopens et al., 2005), working with a modified Nidek system, used two or more images to create a redundant data set to check the procedure. In the present study we used combined information from 25 meridians. To our knowledge, only Coopens et al. corrected the Scheimpflug images from geometrical and optical distortion to measure tilt and decentration of intraocular lenses. We have found that not correcting for geometrical distortion cause slight discrepancies in the measured values.

Our results (mean values with Scheimpflug and Purkinje in this study are decentrations of 0.21±0.28 mm horizontally and 0.03±0.38 mm vertically and tilts of -0.26 ±2.63 deg around x-axis and 1.54±1.50 around y-axis. Decentrations in X and tilts around Y being nasal for both eyes. In general, the amounts of tilt and decentration that we report are lower than the earliest reports in the literature. For example, Philips (Phillips, Perez-Emmanuelli, Rosskothen & Koester, 1988) reported average decentrations of 0.7±0.3 mm and tilts of 7.3±3.0 deg without specifying direction of tilt or decentration. One report of IOL position after transcleral implantation show systematically high amounts of tilt and decentration (an average IOL tilt of 5.97±3.68 deg and average decentrations of 0.63±0.43 mm), which the authors attribute to the implantation technique (Ismet, 2000). Our results are more comparable with those from more recent studies, reporting lower values of tilt and decentration, and are probably associated with an improvement of the surgical procedure. These results are close to the pilot data of IOL tilt and decentration presented in Chapter 2 (Rosales & Marcos, 2006): 0.87±2.16 deg for tilt around X-axis, 2.3±2.33 deg for tilt around Y-axis, and 0.25±0.28 mm for horizontal decentration and -0.41±0.39 mm for vertical decentration.

Other studies using non-corrected Scheimpflug images reported average tilts between 2.61±0.84 deg (three-piece acrylic IOLs, (Meng-Chi, Lin-Chung, Chao-Yu & Han-Chin, 1998) and 3.4±2.02 deg (silicone IOLs, (Kim & Shyn, 2001)) and average decentrations of 0.29±0.26 mm to 0.37±0.19 (Meng-Chi et al., 1998). To our knowledge only one study mentions interocular mirror symmetry for tilt and decentration, with phakic IOLs (Coopens et al., 2005). While most studies and techniques provide similar average values, which agree well with the average values reported here using both Purkinje and Scheimpflug, we have shown that in individual patients some discrepancies across techniques may be found. This is particularly important when using Scheimpflug images that have not been corrected for geometrical and optical

distortion, as are the raw images provided by commercially available instruments such as the Pentacam.

Finally, the amounts of tilt and decentration found in patients are in general low, and particularly for the decentration are of the order of the resolution of the techniques in many patients. The clinical relevance of tilts and decentrations of these amounts is likely limited (Rosales & Marcos, 2007) although there are case reports in the literature where they result in decreased visual function (Oshika, Kawana, Hiraoka, Kaji & Kiuchi, 2005). The impact of IOL tilt and decentration on optical aberrations of pseudophakic eyes will be addressed in Chapter 8.

Changes in crystalline lens radii of curvature and lens tilt and decentration during dynamic accommodation in Rhesus Monkey

6

6. Changes in crystalline lens radii of curvature and lens tilt and decentration during dynamic accommodation in Rhesus Monkey

This chapter is based on the article by de P. Rosales et al., *"Changes in crystalline lens radii of curvature and lens tilt and decentration during dynamic accommodation in Rhesus Monkey"* (Journal of Vision In press). Coauthors of the study are M. Wendt, S. Marcos, A. Glasser. The contribution of Patricia Rosales to the study was to prepare the processing algorithm for dynamic measurement of phakometry, and to measure lens tilt and decentration for each accommodative state in Rhesus Monkeys. Part of the study was conducted in the University of Houston College of Optometry (Adrian Glasser's lab).

RESUMEN

Objetivos: Estudiar cómo cambian los radios de curvatura del cristalino del Rhesus Monkey en función de la acomodación dinámica y medir los cambios en la inclinación y descentramiento del cristalino para cada estado acomodativo.

Métodos: Las medidas de los cambios en los radios de curvatura del cristalino y de la inclinación y descentramiento durante la acomodación dinámica centralmente estimulada, se realizaron en cuatro ojos de dos monos adolescentes. Las medidas dinámicas de facometría se realizaron mediante un video facómetro basado en imágenes de Purkinje. Los radios de curvatura de las caras anterior y posterior del cristalino se calcularon a partir de reflexiones de dobles LEDs procedentes de las diferentes superficies oculares (Imágenes de Purkinje PI, PIII y PIV). La inclinación y descentramiento del cristalino se calcularon asumiendo una relación lineal entre las posiciones de las imágenes de Purkinje, rotación del ojo, inclinación y descentramiento del cristalino. Como los ojos del mono estaban iridectomizados, se tomó como referencia para las posiciones de las imágenes de Purkinje el punto medio de la primera doble imagen de Purkinje (PI).

Resultados: El valor medio obtenido de los radios de curvatura de las caras anterior y posterior del cristalino en estado desacomodado fue 11.11±1.58 mm y -6.64±0.62 mm, respectivamente. Se encontró una disminución de los radios de curvatura aproximadamente lineal con la acomodación para todos los ojos, a razón de 0.48±0.14 mm/D y 0.17 ± 0.03 mm/D para las superficies anterior y posterior del cristalino, respectivamente. Para la inclinación y el descentramiento no se encontraron cambios significativos con la acomodación, excepto para la inclinación vertical (0.147± 0.25 deg/D).

Conclusiones: Se ha desarrollado un sistema de medida y procesado de los cambios de los radios de curvatura, inclinación y descentramiento

del cristalino durante la acomodación dinámica, encontrándose un cambio lineal de los radios de curvatura del cristalino durante la acomodación, mientras que la inclinación y descentramiento del cristalino apenas cambian durante la acomodación, excepto para la inclinación vertical. Estos resultados son importantes para una completa caracterización del proceso acomodativo en el Rhesus Monkey.

ABSTRACT

Purpose: To measure dynamic changes in crystalline lens radii of curvature and lens tilt and decentration during centrally stimulated accommodation in four iridectomized eyes of two adolescent rhesus monkeys.

Methods: Phakometry measurements were performed dynamically using a custom-built, video-based, Purkinje-image instrument. Lens anterior and posterior radii were calculated from reflections of paired light sources from the ocular surfaces (Purkinje images PI, PIII and PIV). Lens tilt and decentration were calculated assuming linearity between Purkinje image positions, eye rotation, lens tilt and decentration. Because the monkey eyes were iridectomized, Purkinje images were referred to the mid-point of the double first Purkinje image (PI).

Results: Mean unaccommodated values of anterior and posterior lens radii of curvature were 11.11±1.58 mm and -6.64±0.62 mm respectively, and these decreased relatively linearly with accommodation in all eyes, at a rate of 0.48±0.14 mm/D and 0.17 ± 0.03 mm/D for anterior and posterior lens surfaces respectively. Tilt and decentration did not change significantly with accommodation except for tilt around the horizontal axis which changed at a rate of 0.147± 0.25 deg/D.

Conclusions: A system and a method to measure and to process dynamic changes in lens radii of curvature and lens tilt and decentration during centrally stimulated accommodation has been presented, finding a linear change of lens radii during accommodation, while lens tilt and decentration did not change significantly during accommodation, except for vertical tilt. Those results are important to fully characterize the accommodative process in the rhesus monkey.

1. INTRODUCTION

Accommodation is an increase in the dioptric power of the eye that enables the image of near objects to be focused on the retina. As described in the Introduction, according to the classic Helmholtz mechanism of accommodation (Von Helmholtz, 1855), during distant vision (when the lens is unaccommodated), the ciliary muscle is relaxed, the zonular fibers are under tension and the lens is pulled flat. During accommodation, the ciliary muscle contracts, releasing tension on the zonular fibers at the lens equator, allowing the lens equatorial diameter to decrease, the lens thickness to increase, and the lens anterior surface to become more steeply curved.

While axial changes in lens position, and centripetal movements of the crystalline lens have been studied in detail, to our knowledge only one human study has looked at possible changes in crystalline lens tilt and decentration (in the horizontal direction) for unaccommodated and accommodated eyes (Kirschkamp, Dunne & Barry, 2004), for an accommodative demand of 4 D. The change in crystalline lens shape and alignment has implications for the accommodative mechanism and for accommodative optical performance. Optical aberrations have been measured for different accommodative demands in humans, both statically (Cheng, Barnett, Vilupuru, Marsack, Kasthurirangan, Applegate & Roorda, 2004, He, Burns & Marcos, 2000) or dynamically (Hofer, Artal, Singer, Aragon & Williams, 2001) as well as in enucleated monkey eyes (Roorda & Glasser, 2004) and dynamically in iridectomized centrally stimulated monkeys (Vilupuru, Roorda & Glasser, 2004). These studies all report a consistent shift of spherical aberration with accommodation toward more negative values (which must be related to changes in the lens shape and/or gradient index distribution). An increase in vertical coma with accommodation is shown in some humans (Cheng et al., 2004, Plainis, Ginis & Pallikaris, 2005) and monkeys (Vilupuru et al., 2004), suggesting an increase in the lens vertical decentration and/or tilt. Other studies have examined the potential role of monochromatic aberrations on accommodation dynamics (Chen, Kruger, Hofer, Singer & Williams, 2006, Fernandez & Artal, 2005, Radhakrishnan & Charman, 2007).

In the study presented in this Chapter, ocular biometry and infrared photorefraction were measured dynamically during Edinger-Westphal (EW) stimulated accommodation in anesthetized, iridectomized rhesus monkeys for identical stimulus current amplitudes. Changes in anterior and posterior crystalline lens radii, lens tilt and decentration were

also measured dynamically for the same stimulus amplitudes using a custom-built phakometry Purkinje imaging technique. Those measurements, together with biometric and photorefractive measurements in monkey eyes (Vilupuru & Glasser, 2005), are useful to fully characterize the accommodative mechanism in a widely accepted animal model for human accommodation and presbyopia (Glasser & Kaufman, 1999, Glasser, Wendt & Ostrin, 2006, Koretz, Bertasso, Neider, True-Galbelt & Kaufman, 1987a).

2. METHODS

2.1 Animals

The left and right eyes of two anesthetized rhesus monkeys (#54 and #58) were imaged during EW stimulated accommodation. The monkeys were aged 9 years, 1 month and 9 years, 3 months respectively and had previously undergone complete, bilateral removal of the irides (Kaufman & Lütjen-Drecoll, 1975) and surgical implantation of stimulating electrodes into the EW nucleus (Chen & Makous, 1989). All experiments followed the ARVO Statement for the Use of Animals in Ophthalmic and Vision Research and were performed in accordance with institutionally approved animal protocols.

2.2 Measurement of current stimulus /accommodative response

At the start of each experiment, a Hartinger coincidence refractometer (Zeiss, Jena, Germany) was used to measure the static accommodative response for each eye as a function of increasing stimulus amplitudes. Baseline refraction and maximal accommodated refraction achieved at each stimulus amplitude was recorded. Accommodative amplitude at each stimulus current amplitude was the difference between these two refractions.

2.3 Dynamic measurement of accommodation

Infrared photorefraction was used to measure dynamic changes in refractive state during centrally stimulated accommodation (Glasser & Kaufman, 1999, Schaeffel, Farkas & Howland, 1987, Schaeffel, Howland & Farkas, 1986, Vilupuru & Glasser,

2002). In each experiment, a calibration curve was generated to relate the slope of the vertical brightness profile through the pupil to the absolute refractive state of the eye obtained with the previous Hartinger coincidence refractometer measurements. The dynamic photorefractive optical change occurring in the eye during centrally stimulated accommodation was recorded onto videotape, and subsequent image analysis was performed to measure the pupil brightness profile. The calibration curve was then used to relate the dynamic changes in the pupil brightness profile to the accommodative amplitude.

2.4 Dynamic biometric measurements

Biometric changes were measured with continuous high-resolution A-scan ultrasound biometry (CUB) (Beers & van der Heijde, 1994, Vilupuru & Glasser, 2005). Biometric measurements were recorded to a computer at 100 Hz, using a 10-MHz transducer. The transducer contacted the cornea through ultrasound transmission gel to generate sharp A-scan peaks representing the anterior and posterior cornea surfaces, anterior and posterior lens surfaces, and the retina. The CUB measures the time between peaks associated with the intraocular surfaces. These times are converted to distances using standard, accepted sound velocities: anterior and vitreous chambers, 1532 m/s and lens, 1641 m/s (van der Heijde & Weber, 1989, Vilupuru & Glasser, 2005). Biometric changes were recorded during a sequence of increasing EW-stimulated accommodative responses. The same stimulus current amplitudes used during the photorefraction described earlier were used for the CUB measurements.

2.5 Dynamic measurement of phakometry and lens tilt and decentration

A custom-built dynamic (30 Hz) video-based phakometer was used to measure lens radii of curvature and lens tilt and decentration. The set-up included a broad spectrum, white light source, two collimated optic fibers (to assure that the Purkinje images are in focus) and a video camera with a telecentric lens to capture the reflections produced by the anterior cornea (PI), and the anterior and posterior lens surfaces (PIII, PIV). This system was modified from that described previously in the literature (Mutti, Zadnik & Adams, 1992). The collimated light sources used for illumination were adjustable and were separated horizontally between 5-10 deg from the optical axis of the camera for

the measurements. Both phakometry and lens tilt and decentration data were calculated from the same measurements using the double light sources. Measurements were performed with a plano perfusion speculum lens filled with saline solution placed over the monkey's cornea to effectively neutralize the cornea and improve Purkinje image visibility. This was a custom made lens with an open circular base designed to fit under the eye lids against the conjunctiva concentrically around the limbus. The lens held a 5 ml volume chamber in front of the cornea with a plano clear glass cover slip on the front with an inlet and an outlet tube to fill the chamber in front of the cornea with normal buffered saline. To calculate anterior and posterior lens radii of curvature, the heights of PIII and PIV relative to PI (h3/h1 and h4/h1 respectively), were measured frame-by-frame from the recorded video phakometry images. Corneal curvature, measured from a linear calibration curve obtained from calibrating the phakometer on a set of steel calibration ball bearings of different, known radii, and lens thickness and anterior chamber depth measured with A-scan ultrasound biometry, were used in the calculations, using the equivalent mirror theorem (Smith & Garner, 1996) and an iterative method (Garner, 1997) with custom routines written in Matlab (Rosales & Marcos, 2006).

To measure lens tilt and decentration a linear relationship between Purkinje image locations, eye rotation β, lens tilt α and lens decentration d was assumed according to Phillips' linear equations (Phillips, Perez-Emmanuelli, Rosskothen & Koester, 1988).

$P1 = E\beta;\ P3 = F\beta + C\alpha + Ed;\ P4 = G\beta + D\alpha + Fd$; $P1$, $P3$ and $P4$ are the relative locations of the midpoint of the double PI, PIII and PIV Purkinje images and A, B, C, D, E, F and G are coefficients that depend on the individual ocular biometry, (see Chapter 2 for details). Since the eyes were iridectomized, the pupil center could not be located and therefore be used as a reference for PI, PIII and PIV. Alternatively, we used the midpoint of the double PI as a reference. Considering that the head was not rotated, and head and eye rotation did not change with accommodation (the first Purkinje image did not move significantly with accommodation (less than 0.0001mm) this approximation should be appropriate. To calculate the coefficients of the Phillips equations, eyes were modeled using Zemax with measured A-scan biometric parameters and lens radii obtained from phakometry measurements following the procedures described in detail previously (Rosales & Marcos, 2006), Chapter 2.

To evaluate the validity of these algorithms on a monkey eye with the corneal neutralizing profusion lens in front of the eye, computer simulations were performed with the lens on the eye. A model eye was built in Zemax with anterior and posterior lens radii of 9.09 mm and -5.93 mm respectively. The Purkinje images for the monkey eye and the experimental configuration were simulated and the simulated images were processed with the same algorithms used for processing the real images. Anterior and posterior lens radii were calculated with an accuracy of 0.11 and 0.07 mm respectively. Similarly, an eye was simulated with nominal values for tilt and decentration of 1 deg and 5 deg for tilt around the vertical axis and tilt around the horizontal axis, and 0.5 mm and 0.1 mm for horizontal and vertical decentration. Tilt and decentration were calculated with an accuracy of 0.089 deg and 0.009 mm respectively with respect to the nominal values.

2.6 Experimental protocols

Monkeys were initially anesthetized with intramuscular ketamine (10 mg/kg) and acepromazine (0.5 mg/kg). Surgical depth anesthesia was induced with an initial bolus of 1.5 mg/kg followed by constant perfusion at 0.5 mg/kg/min of intravenous propofol (Propoflo, Abbott Laboratories, North Chicago, IL).

The anesthetized monkeys were placed prone with the head held in a head holder, upright and facing forward for all measurements. At the beginning of each experimental session, sutures were tied beneath the medial and lateral rectus muscles of the monkey eye and light tension applied by micrometers to reduce convergent eye movements. The eyelids were held open with lid speculums. A plano polymethyl-methacrylate contact lens was placed on the cornea for refraction measurements to maintain optical quality and prevent dehydration. Five, four-second duration stimulus trains (600-μs pulse duration, 72 Hz, amplitude range 10 to 2,000 μA) with a four-second inter stimulus interval were used to induce varying amplitudes of accommodation. The accommodative response to three different current amplitudes was first measured using a Hartinger coincidence refractometer. The same increasing stimulus amplitudes were used for the same monkey throughout the session. Infrared video photorefraction was performed with a contact lens on the cornea. Video phakometry was then performed, with the corneal neutralizing perfusion speculum. Finally, because it was a contact procedure, A-scan ultrasound biometry was performed with ultrasound transmission gel

on the cornea. For monkey #54, one eye was measured per session over approximately 2 hours, one month apart. For monkey #58 both eyes were measured in the same session. For each procedure and for each stimulus amplitude, only the last three of the five stimulus trains were analyzed.

Lens tilt and decentration were calculated for the un-accommodated state and accommodative responses for the different current stimuli. Because the tilt and decentration calculations were more computationally demanding, this analysis was not done on all dynamic data traces. Instead, a total of 15 images were analyzed from the last three stimuli. Six images were captured when the stimulus was OFF and 9 images were captured when the stimulus was ON near the end of the stimulus train when the eye was in a stable and maximally accommodated state for each of three different increasing stimulus amplitudes. The images were captured during each of the last three stimuli. The corresponding averaged optical biometry data, for the corresponding stimulation sequences were used for data processing.

3. RESULTS

3.1 EW stimulated accommodation

Figure 6.1 shows the Hartinger measured accommodative response for each stimulus current amplitude for the four eyes. These functions were used to convert the stimulus current amplitudes into actual accommodative response for the photorefraction calibration procedures.

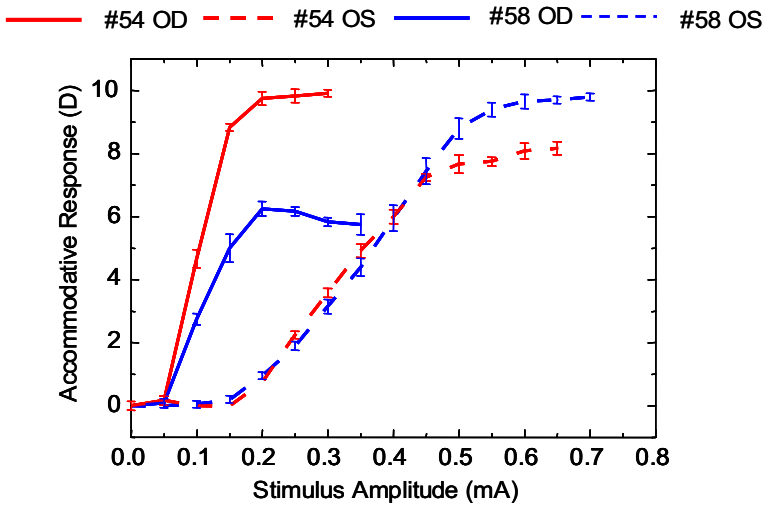

Figure 6.1. Accommodative response for each current stimulus for the four eyes of the two monkeys used in this experiment. Each point is the average of three measurements. Error bars are standard deviations.

Maximum accommodative response amplitudes were 9.91 D for monkey #54 OD, 7.75 for monkey #54 OS, 5.75 D for monkey #58 OD and 9.65 for monkey #58 OS.

In this experiment, the accommodative response for a given current stimulus varied across eyes, and between eyes of the same monkey, dependent on the anatomical position of the stimulating electrode.

3.2 Dynamic photorefraction and biometry

Photorefraction, anterior chamber depth and lens thickness, were recorded dynamically at 30 Hz. These measurements, along with the dynamic recording of the Purkinje images, allowed dynamic changes in lens curvatures to be calculated. Figure 6.2 shows an example of dynamic recoding of photorefraction, and optical biometry for monkey #54 OS, for one stimulus (off-on-off). The abrupt step trace at the bottom of the graph indicates the start, duration (four seconds) and termination of the stimulus train. Anterior chamber depth (ACD) decreases systematically and lens thickness (LT) increases systematically with accommodation. These dynamic data recorded at 30Hz were used, along with 30 Hz phakometry images, for calculations of lens radii of curvature and lens tilt and decentration for the same accommodative levels. The repeatability of EW stimulated accommodative responses has been demonstrated in previous studies (Glasser et al., 2006, Vilupuru & Glasser, 2005), temporal registration of the different measurements is possible to within 1/30 of a second (i.e., at the video frame rate).

Figure 6.3 shows dynamic biometric changes (anterior chamber depth and lens thickness) with accommodation for all eyes. Data are from the last stimulus producing the maximum accommodative amplitude.

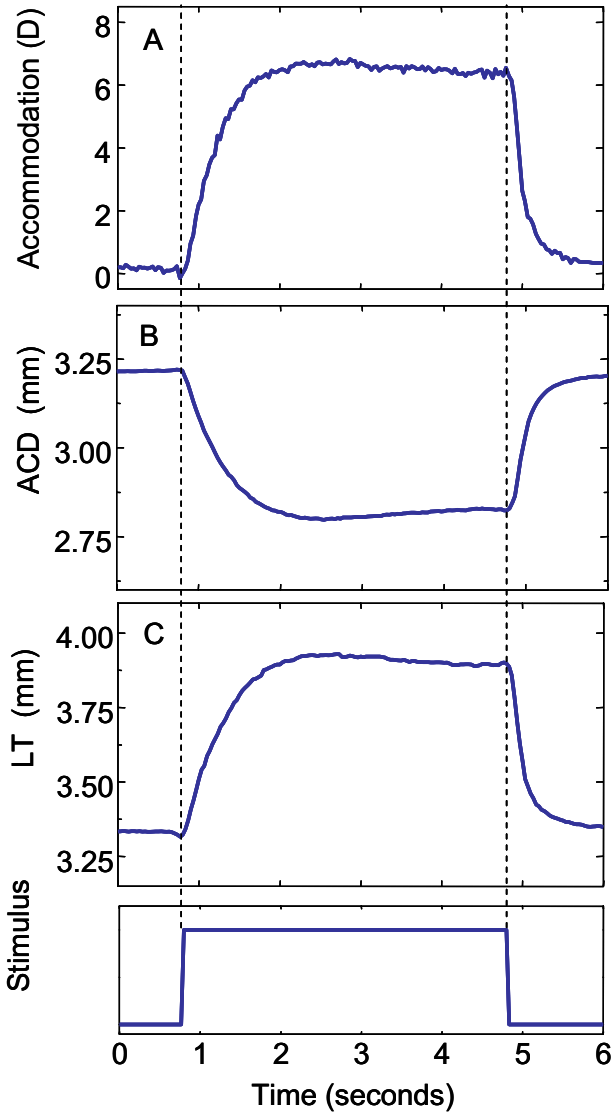

Figure 6.2. Dynamic recordings of accommodation from photorefraction and lens thickness (LT) and anterior chamber depth (ACD) from continuous ultrasound biometry (CUB) from monkey #54 OS, for an accommodation response of 7.75D. Photorefraction was measured first, followed by the CUB measurements for the same stimulus amplitude. This example corresponds to a single response (the 5th response to five, four-second long stimuli).

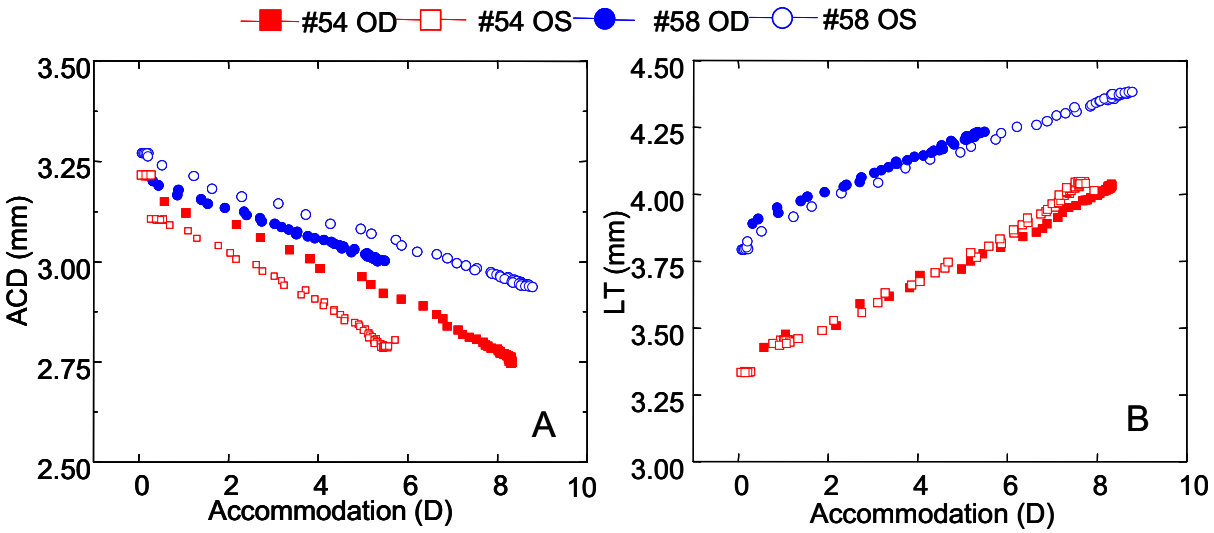

Figure 6.3. Dynamic biometric changes (anterior chamber depth and lens thickness) with accommodation for all eyes. Data are from the last stimulus producing the maximum response with accommodation recorded first with photorefraction and ACD and LT recorded subsequently with the CUB.

Figure 6.4 shows an example of changes in anterior and posterior lens radii of curvature for monkey #54 OS for the same stimulus sequence as shown in Figure 6.2.

Average unaccommodated anterior and posterior lens radii were 11.11±1.58 mm and -6.64±0.62 mm respectively and decrease (in absolute values) systematically with accommodation in all eyes (Figure 6.5). Average values were obtained from the last three of the five stimuli applied. For the same accommodative level there are individual differences in the anterior and posterior radii of curvatures. The amounts and rate of change tend to be similar across eyes of the same monkey.

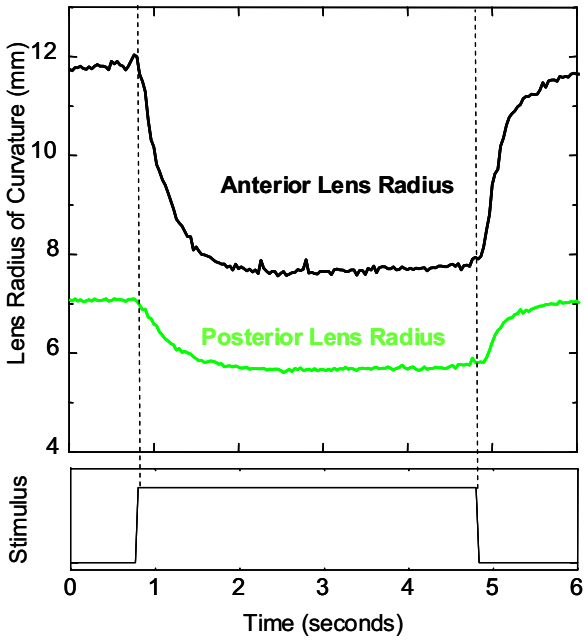

Figure 6.4. Anterior and posterior lens radii of curvature as a function of accommodation, for a phakometry sequence (5th stimulus). Phakometry data were calculated using individual biometry data shown in Figure 2, for monkey #54 OS.

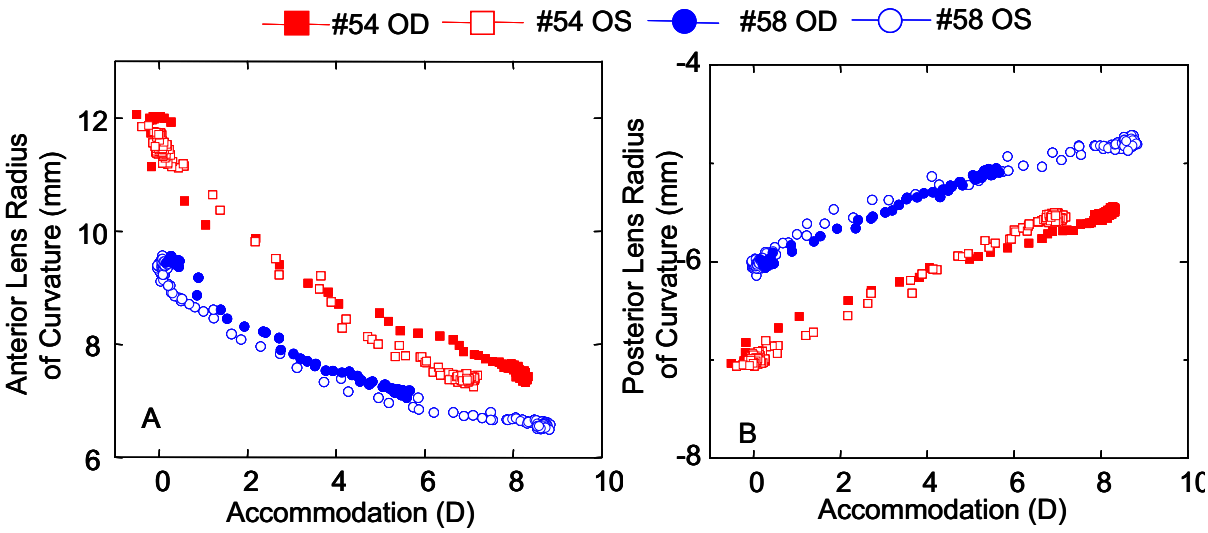

Figure 6. 5. Anterior and posterior lens radii of curvature as a function of accommodation for both eyes each of monkey #54 and monkey #58. Data are from the 5th stimulus for the maximum accommodative response in the phakometry sequence. Biometry and photorefraction data from each individual eye, corresponding to that shown in Figure 2, were used in the data processing.

A better comparison of the rate of decrease in radii of curvature across eyes can be performed by relating all values to the unaccommodated state. Figure 6.6 shows average changes in radii of curvature as a function of accommodation, relative to the unaccommodated state, averaged across eyes. Since the accommodative responses differed across eyes, spline fitting to the data was performed to average across the individual data from each eye. The curves in Figure 6.6 show similar slopes for the anterior and posterior surface (0.0058 mm^{-1}/D and 0.0056 mm^{-1}/D respectively, averaging across eyes and monkeys), indicating that both surfaces contribute similarly to change in power. The curves are relatively linear for the first 4 D indicating that the relative contribution of the surfaces to the lens power change is rather constant with accommodation.

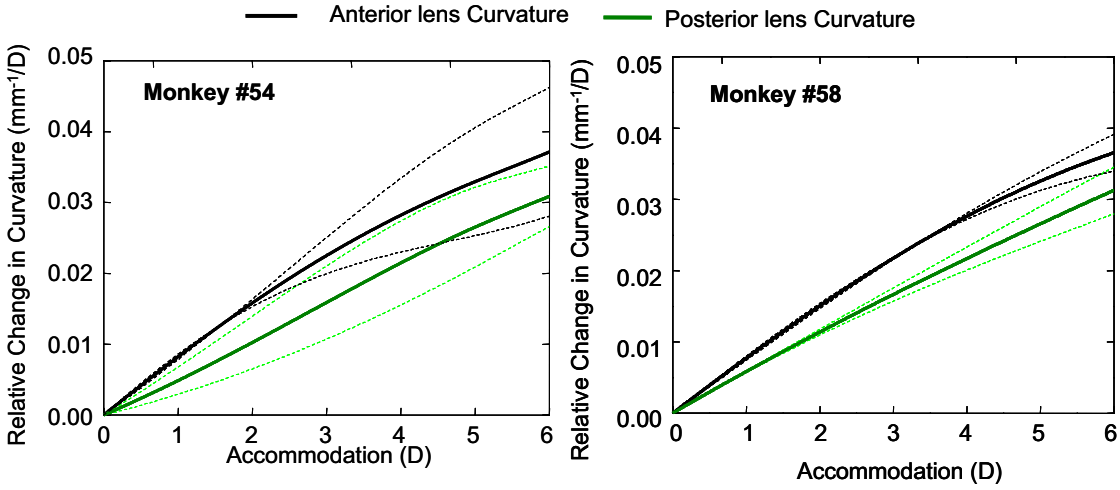

Figure 6.6. Average changes in anterior and posterior curvature relative to the un-accommodated state from the two monkeys. Data for each eye was fitted using a spline function, and then averaged across eyes for each monkey at different accommodation levels. Dashed lines represent ± 1 standard deviation.

3.3 Changes in lens tilt and decentration with accommodation

Table 6.1.a and Table 6.1.b show measurements of tilt and decentration (horizontal and vertical components) for each eye. See Chapter 2 (page 56, Figure 2.6) for sign conventions.

Table 6.1.a Lens tilt (α in degrees) and decentration (d in mm) for 0 D of accommodation for all eyes

	α_x	α_y	d_x	d_y
#54 OD	8.97±0.03	-1.09±0.03	0.17±0.01	1±0.01
#54 OS	8.08±0.04	-1.81±0.04	0.17±0.01	0.56±0
#58 OD	3.22±0.06	0.25±0.05	-0.05±0.01	0.95±0.01
#58 OS	2.48±0.05	-0.13±0.15	0.13±0.02	0.79±0.01

Table 6.1.b Lens tilt (α in degrees) and decentration (d in mm) for the maximum accommodation amplitude for all eyes

	α_x	α_y	d_x	d_y
#54 OD	9.63±0.11	-1.3±0.12	0.18±0.02	0.94±0.02
#54 OS	6.69±0.2	-0.99±0.12	0.04±0.01	0.44±0.02
#58 OD	5.08±0.15	0.73±0.12	-0.07±0.02	1.03±0.02
#58 OS	6.24±0.18	-1.03±0.13	0.11±0.02	0.92±0.01

Average unaccommodated lens tilt around the vertical axis was 5.69±3.31 deg and average tilt around the horizontal axis was -0.69±0.93 deg. Average unaccommodated lens decentration was 0.10 ± 0.11 mm horizontally and 0.82 ± 0.20 mm vertically. With accommodation, tilt around the horizontal axis increases significantly ($p<0.0044$) for all eyes except for #54 OD. The largest increase occurred for eye #58 OS, for which tilt around the horizontal axis increased at a rate of 0.39 deg/D (a total increase of 3.77 deg between 0 and 9.7 D of accommodation). Tilts around the vertical axis were much smaller than tilts around the horizontal axis. Decentration did not change significantly with accommodation in any of the eyes.

4. DISCUSSION

Dynamic accommodative measurements of the anterior and posterior lens radii of curvature and lens tilt and decentration have been presented for the first time in monkey eyes. These measurements are important to fully characterize the accommodative mechanism in Rhesus Monkey eyes. Comparisons of the ocular changes measured here during accommodation in monkeys with those measured in humans will further serve to test the extent of the similarity. This study was primarily directed at measuring lens radius of curvature, tilt and decentration, and how they change during accommodation. For the unaccommodated state, average anterior lens radius of curvature of 11.11±1.58

mm and posterior lens radius of curvature of -6.64±0.62 mm were found from the four eyes of the two monkeys. These values are close to the values reported for a four-surface schematic eye of macaque monkey obtained by an optical method (Lapuerta & Schein, 1995). Results obtained here for the anterior and posterior lens radii in monkeys using a collimated light source were not significantly different between the equivalent mirror theorem and the merit function. In previous studies (Rosales, Dubbelman, Marcos & Van der Heijde, 2006, Rosales & Marcos, 2006) a difference between the two algorithms was found, very likely due to the use of an uncollimated light source. Accommodative changes in monkeys of -0.48±0.14 mm/D and 0.17±0.03 mm/D for the anterior and posterior lens radii of curvature were found using a Purkinje imaging method in the present study. In terms of changes of curvature per diopter of accommodation, those slopes would be 0.006 mm^{-1}/D and 0.00485 mm^{-1}/D for the anterior and posterior lens respectively. A prior study using drug stimulated accommodation in monkey eyes found approximately -0.272 mm/D and 0.215 mm/D for the anterior and posterior lens using Scheimpflug imaging in two eyes of one monkey (Koretz, Bertasso, Neider, True-Galbelt & Kaufman, 1987b).

Changes in lens radii of curvature with accommodation in human eyes differ across studies. Some studies found changes in the human eye which are close to the results of the present study in monkey eyes. For example, Koretz (Koretz, Cook & Kaufman, 2002), using Scheimpflug on one 19 year old human subject found a mean change of -0.33 mm/D and 0.15 mm/D, for the anterior and posterior lens radii of curvature, respectively.

However, while most studies report similar changes for the posterior lens, in general larger changes are measured for the anterior lens in humans than those found in the present study for monkeys. Garner (Garner & Yap, 1997) using Purkinje imaging found a value of -0.62 mm/D and 0.17 mm/D for anterior and posterior lens radii on average in a group of 11 young eyes (21.2±2.6 years). Dubbelman (Dubbelman, van der Heijde & Weeber, 2005), also using Scheimpflug imaging, found changes of -0.62 mm/D and 0.13 mm/D for the anterior and posterior lens radius of curvature respectively (0.0067 mm^{-1}/D and 0.0037 mm^{-1}/D in terms of curvature).

Differences across studies are not necessarily associated with the technique (Scheimpflug or Purkinje imaging). In a recent study, similar values for anterior and posterior lens radii of curvature with accommodative effort were found using Scheimpflug (-0.64±0.04 and 0.23±0.08 mm/D for the anterior and posterior lens

radius of curvature respectively) or Purkinje imaging (-0.57±0.05 and 0.29±0.04 mm/D for the anterior and posterior lens radius of curvature) on the same human eyes (mean age: 28.5) (Rosales et al., 2006).

The fact that most previous human studies relate phakometry measurements to accommodative demand rather than to the actual accommodative response, cannot be the cause for the discrepancy, since compensation for the accommodative lag would increase the relative mm/D accommodative changes of the radii of curvature, rather than decrease them. Although a direct comparison between results obtained from monkey and human eyes can not be done, due to differences in eye size and different experimental protocols (contralateral accommodation; pharmacological, natural or centrally stimulated accommodation or differences in the ages of the subjects) the results presented here suggest that change in anterior radius of curvature per diopter of accommodation is lower in iridectomized monkeys than in human eyes, indicating than other factors (i.e. gradient index distribution or lens surface asphericity) may play a role in the change of lens power with accommodation.

When the unaccommodated radii of curvature and the accommodative change in lens curvatures for 10 D of accommodation found in the present study are applied to a monkey schematic eye (Lapuerta & Schein, 1995) using the Bennett-Rabbets schematic eye model (Bennett & Rabbetts, 1984), with a uniform equivalent refractive index lens, this accounts for only 7.8 D of accommodation. If a gradient refractive index (GRIN) model was used, the reported differences in lens radii of curvature between monkeys and humans would be even larger and would result in a relatively larger contribution of GRIN to the crystalline lens power change with accommodation in monkeys than in humans.

Some authors have attributed a role of the iris in modifing the shape of the anterior lens with increased accommodation (McWhae & Reimer, 2000). However, the absence of iris in the monkeys in this study cannot be the cause of any differences between humans and monkeys. It has been shown that removal of the iris does not affect the EW stimulated accommodative amplitude in monkeys (Crawford, Kaufman & Bito, 1990). Further, in the present study the optical accommodative response, as well as the accommodative biometric changes were actually measured, so the calculated changes in curvature were related to the actual accommodative change in refraction, lens thickness and anterior chamber depth that occurred.

A factor that may produce an underestimation of lens radii of curvature is the fact that primate lenses are in fact aspherical surfaces. The influence of asphericity on the Purkinje estimates of lens radii was analyzed in depth in a previous study (Rosales & Marcos, 2006). This study found that, particularly for the anterior surface, asphericity had a minimal influence on the lens radius of curvature estimates. However, in the previous study the lens area was limited by the pupil, and therefore probably closer to the apical region. In the iridectomized monkey eyes, where no constraints are imposed by the iris, the Purkinje images were reflected off more peripheral regions of the lens where the asphericity may be a more important factor.

The values obtained for tilt and decentration in this study on monkeys are larger than those found in prior studies in humans (Chapter 2). Part of the differences may be due to a systematic accommodative decentration of the pupil center (used as a reference in the previous study) with respect to the midpoint of the first double Purkinje image (used as a reference in the present study, due to the absence of the pupil in the iridectomized eye). Pupil decentration affects both the reference for decentration, as well as the reference axis for tilt (which was the pupillary axis in previous studies). In the monkey experiments the eye did not converge during accommodation**.** Therefore, while the absolute values of tilt and decentration are likely affected by the choice of reference axis, the relative changes of lens tilt and decentration with accommodation are not. The relative changes of decentration and tilt with accommodation were systematic except for one monkey eye and higher for tilt around the horizontal axis than tilt around the vertical axis and decentration. To our knowledge the only report of lens tilt and decentration in human eyes for unaccommodated versus accommodated states was unable to find statistical differences (Kirschkamp et al., 2004). Data in that study were only for the horizontal meridian, for an accommodative demand of 4D.

Lens tilt and decentration can have an effect on ocular aberrations. In Chapter 8 (Rosales & Marcos, 2007) we will study the effect of real amounts of tilt and decentration in human eyes with intraocular lenses. In normal human eyes, asymmetric aberrations (such as coma) do not change systematically with accommodation (He et al., 2000), although one study reports minor changes of coma in some subjects, particularly in the vertical direction (Plainis et al., 2005). Also, previous observations in monkeys during centrally stimulated accommodation are consistent with significant changes in lens tilt and decentration, particularly in the vertical direction (Glasser & Kaufman, 1999). The greater tilt of the lens around the horizontal axis reported in the present

study is consistent with the observation that gravity influences the movement of the crystalline lens during accommodation in monkeys (Glasser & Kaufman, 1999). Also the change in tilt with accommodation may affect high order aberrations, particularly coma. Vertical coma has been shown to increase significantly and systematically with increasing accommodation compared to the unaccommodated state in some centrally stimulated iridectomized monkey eyes (Vilupuru et al., 2004). Changes in horizontal coma were not significant (Glasser personal communication), which is supported by the small amounts of tilt around the vertical axis and horizontal decentration found in the present study. Customized computer eye modelling shows that lens tilt tends to compensate the optical effects produced by eye rotation (Rosales & Marcos, 2007). It is certainly possible that the tension induced with sutures to minimize accommodative convergent eye movements as used in this study, may impact the tilt and decentration results reported here. Also, the systematic changes in tilt that appear to occur with EW stimulated accommodation in at least some anesthetized rhesus monkeys may stem from several factors. EW stimulation may produce greater contractions of the ciliary muscle than could occur with voluntary accommodation. The rhesus monkey ciliary muscle may be capable of far greater accommodative excursions than the human ciliary muscle. EW stimulated accommodation in young rhesus monkeys can produce 15 D or more of accommodation, whereas 10 D is nearing the upper limit of voluntary accommodation in young humans. Further, the presence of the iris, especially when constricted during accommodation, may provide greater stability to the lens than in iridectomized eyes.

In conclusion, dynamic phakometry, tilt and decentration were measured for the first time in monkey eyes during accommodation using Purkinje imaging. Changes in the lens radii of curvature with accommodation are consistent with those found in human eyes, with the anterior lens getting steeper at a faster rate. Tilt, particularly around the horizontal axis, changed significantly with accommodation in some eyes, apparently more than in human eyes. No significant changes in lens decentration were found. These results are important to fully characterize the accommodation mechanism in monkey eyes, to understand the age changes that occur in the accommodative mechanism, as well as for the evaluation and design of strategies for presbyopia correction, for example lens refilling (for which the relative contribution of lens curvature and refractive index is critical).

Change of optical quality with Intraocular lens implantation: Corneal aberrations

7

7. Change of optical quality with IOL implantation: corneal aberrations

This chapter is based on the article by S.Marcos et al. *"Change in corneal aberrations after cataract surgery with 2 types of aspherical intraocular lenses"* Journal of Cataract Refractive Surgery Vol 33, 217226-1067. Coauthors of the study are Lourdes Llorente, Ignacio Jiménez-Alfaro and Patricia Rosales. The contribution of Patricia Rosales to the study was participation in data collection, processing and analysis of corneal aberrations of patients.

RESUMEN

Objetivos: Estudiar el efecto de la incisión corneal sobre las aberraciones corneales en pacientes operados de cirugía de cataratas, con dos tipos de lentes intraoculares (LIO) monofocales, de diseño asférico.

Métodos: Se toman topografías corneales en 43 ojos, antes y después de la cirugía de cataratas con incisión corneal superior. Veinte y dos ojos fueron implantados con una lente intraocular asférica de silicona (Tecnis Z9000, Advanced Medical Optics) y veinte y un ojos una lente intraocular asférica acrílica (AcrySof IQ SN60WF, Alcon Research Labs) empleando el tipo de inyector recomendado para cada tipo de LIO. El tamaño de la incisión corneal (3.2 mm) fue similar en los dos grupos. Las aberraciones corneales se evaluaron empleando algoritmos propios (basados en trazados de rayos) para tamaños de pupila de 10.0 y 5.0 mm. Las comparaciones entre medidas pre-cirugía y post-cirugía y entre grupos se realizó para términos de Zernike individuales y para el error cuadrático medio (RMS) del frente de onda.

Resultados: La RMS (excluyendo prisma y desenfoque) del grupo con la LIO AcrySof IQ no cambió, incrementando en cambio para el grupo de las LIO Tecnis para diámetros de pupila de 10.0 y 5.0 mm. La aberración esférica, y términos de coma, no cambiaron significativamente; sin embargo, el astigmatismo vertical, trefoil vertical y tetrafoil vertical cambiaron significativamente con la cirugía para ambos diámetros de pupila de 10.0 y 5.0 mm ($P<.0005$) en ambos grupos. El patrón de aberraciones de onda inducido para aberraciones de tercer orden y superior mostraban un lóbulo superior, como consecuencia de una combinación de trefoil vertical positivo (Z_3^{-3}) y tetrafoil negativo (Z_4^4). El astigmatismo vertical promedio se incrementó en 2.47 μm ± 1.49 (SD) y 1.74 ± 1.44 μm, el trefoil vertical se incrementó en 1.81 ± 1.19 μm y 1.20 ± 1.34 μm, y el tetrafoil se incrementó en -1.10 ± 0.78 μm y -0.89 ± 0.68 μm en los grupos Tecnis y AcriSof IQ, respectivamente.

Conclusiones: No se observan diferencias significativas entre las aberraciones corneales post-cirugía en los dos grupos, aunque hubo más términos u órdenes que cambiaron de modo significativo estadísticamente en el grupo de LIO Tecnis, para el que se encontraron que las aberraciones inducidas eran ligeramente mayores.

ABSTRACT

Purpose: To study the effect of cataract surgery (through 3.2-mm superior incisions) on corneal aberrations with 2 types of monofocal intraocular lenses (IOLs) with aspherical designs.

Methods: Corneal topography of 43 eyes was obtained before and after small corneal incision cataract surgery. Twenty-two eyes had implantation of a Tecnis Z9000 silicone IOL (Advanced Medical Optics) and 21 had implantation of an AcrySof IQ SN60WF acrylic IOL (Alcon Research Labs) using the recommended injector for each IOL type. The intended incision size (3.2 mm) was similar in the two groups. Corneal aberrations were estimated using custom-developed algorithms (based on ray tracing) for 10.0 mm and 5.0 mm pupils. Comparisons between preoperative and postoperative measurements and across the groups were made for individual Zernike terms and root-mean-square (RMS) wavefront error.

Results: The RMS (excluding tilt and defocus) did not change in the AcrySof IQ group and increased significantly in the Tecnis group with the 10.0 mm and 5.0 mm pupil diameters. Spherical aberration and coma-like terms did not change significantly; however, vertical astigmatism, vertical trefoil, and vertical tetrafoil changed significantly with surgery with the 10.0 mm and 5.0 mm pupil diameters ($P<.0005$). The induced wave aberration pattern for 3rd-and higher-order aberrations consistently showed a superior lobe, resulting from a combination of positive vertical trefoil (Z_3^{-3}) and negative tetrafoil (Z_4^4). The mean vertical astigmatism increased by 2.47 μm± 1.49 (SD) and 1.74 ± 1.44μm, , vertical trefoil increased by 1.81 ± 1.19μm and 1.20 ± 1.34 μm, and tetrafoil increased by -1.10 ± 0.78 μm and -0.89 ± 0.68 μm in the Tecnis group and AcrySof IQ group, respectively.

Conclusions: There were no significant differences between the corneal aberrations in the 2 postoperative groups, although there was a

tendency toward more terms or orders changing statistically significantly in the Tecnis group, which had slightly higher amounts of induced aberrations.

1. INTRODUCTION

Cataract surgery has advanced considerably in the past few years. Among other advances, foldable intraocular lenses (IOLs) allow implantation through small incisions and more sophisticated optical surfaces give better control of optical outcomes. In particular, monofocal IOLs with aspherical surfaces (resulting in negative spherical aberration) have been introduced with the aim of balancing the positive corneal spherical aberration (Holladay, Piers, Koranyi, van der Mooren & Norrby, 2002). These IOLs reduce the amount of spherical aberration with respect to conventional spherical IOLs (Marcos, Barbero & Jiménez-Alfaro, 2005, Padmanabhan, Rao, Jayasree, Chowdhry & Roy, 2006), and some studies have shown contrast sensitivity improvements over the spherical IOLs (Mester, Dillinger & Anterist, 2003, Packer, Fine, Hoffman & Piers, 2004).

Higher-order aberrations (HOAs) of the cornea (i.e., 3rd and higher order terms), and the geometry and positioning of the IOL, all contribute to final optical quality. The benefit of correcting spherical aberration relies on relative small contribution of other factors that potentially increasing HOAs (Marcos, Burns, Prieto, Navarro & Baraibar, 2001); these include lens tilt and decentration (Rosales & Marcos, 2006), and corneal irregularities.

Several studies (Jacobs, Gaynes & Deutsch, 1999, Rainer, Menapace, Vass, Annen, Findl & Schmetter, 1999) have discussed the potential role of the corneal incision in altering corneal shape. It is well known that the corneal incision modifies corneal astigmatism by about 1.00 diopter (D), and the location of the incision is often created in the steepest meridian with the aim of reducing corneal astigmatism. Hayashi et al (Hayashi, Hayashi, Oshika & Hayashi, 2000) evaluated irregular astigmatism using Fourier analysis of corneal elevation maps from videokeratography preoperatively and after implantation of silicone, acrylic and poly(methyl methacrylate) (PMMA) IOLs through 3.5 mm, 4.1 mm and 6.5 mm incisions in 240 eyes. They found that “high-order irregularities” increased after surgery in all three groups, but this increase persisted 3 months after surgery only in the 6.5 mm group. Guirao (Guirao, Redondo, Geraghty, Piers, Norrby & Artal, 2002) performed one of the first studies reporting corneal aberrations after cataract surgery (extracapsular cataract extraction with a 6.0 mm incision and PMMA IOL implantation). A comparison with corneal aberrations in a healthy age-matched control group (20 eyes in each group) showed no statistically

significant differences for 4.0 mm pupil diameters. Barbero (Barbero, Marcos & Jimenez-Alfaro, 2003) studied total and corneal aberrations in 9 eyes after cataract surgery (phacoemulsification with implantation of acrylic spherical IOLs through a 4.1 mm incision). They found slightly higher (but not statistically significant) corneal aberrations in postoperative eyes than in a young control group (for 5.0 mm); however, all eyes measured preoperatively and postoperatively showed larger amounts of 3rd and higher order corneal aberrations after surgery. One of the most comprehensive studies of changes in corneal aberrations after small-incision cataract surgery is that of Guirao (Guirao, Tejedor & Artal, 2004). They measured corneal aberrations (for 6.0 mm pupils) in the same eyes before and after implantation of monofocal foldable spherical IOLs (silicone and acrylic) through a 3.5 mm superior, nasal or temporal incision. Although a major conclusion was that a small incision does not systematically degrade anterior corneal optical quality, there were changes in some aberrations and a significant increase in astigmatism and trefoil.

The amount and orientation of the aberrations induced depended on the surgical meridian. Pesudovs (Pesudovs, Dietze, Stewart & Cox, 2005) studied the effect of two types of spherical IOLs (PMMA and acrylic) and incision locations (corneal and scleral) on total wave aberrations measured with a Hartmann-Shack wavefront sensor. Aberrations in 20 eyes (PMMA IOL, scleral incision), 21 (acrylic IOL, scleral incision), and 16 (acrylic IOL, corneal incision), were compared with those in an age-matched control group. The authors found that scleral incisions induced fewer aberrations than corneal incisions. The PMMA-scleral group (incision size of 5.2 mm) had fewer aberrations than the acrylic-corneal group (incision size 3.5 mm), and aberrations comparable to those in the control group. They report higher amounts of total tetrafoil in the acrylic-corneal group than in the phakic group.

In this chapter, we report corneal aberrations over 10.0 mm and 5.0 mm diameters in patients who had implantation of recently introduced aspherical IOLs (Tecnis, Z9000, Advanced Medical Optics; Acrysof IQ, SN60WF, Alcon Research Labs). By measuring aberrations over a large pupil diameter, we were able to assess to a greater extent the optical changes produced on the anterior cornea, not limited by the eye´s pupil size. This analysis is relevant in the understanding of corneal biomechanical changes after an incision, and in the assessment of off-axis optical quality. We also present data for 5.0 mm pupils to account for changes potentially more relevant to visual function. The surgical protocol was identical in all eyes, including incision size (3.2 mm) and location

(superior), to avoid confounding factors associated with differences in incision architecture. In this context, the purposes of this work were to assess (1) whether there is a systematic increase in corneal aberrations after small-incision cataract surgery and obtain an average map of induced corneal aberrations with this procedure; (2) whether there are corneal differences associated with the type of IOL implanted. This information will be of great use to simulate surgical outcomes using eye models (in which the average map of induced aberrations can be incorporated), in understanding optical performance in eyes implanted with IOLs, particularly with new designs aiming at reducing the amount of aberrations, and in evaluating which aspects of surgery should be improved. This information will be used in Chapter 8 where the performance of customized model eyes is compared to real measurements of ocular aberrations in pseudophakic eyes with aspheric IOLs.

2. METHODS

2.1 Patients:

Forty-three eyes of twenty-three patients with cataract were studied. Patient were invited to participate in the study and to randomly have bilateral implantation of 1 or 2 types of aspherical IOLs (Tecnis, Z9000, Advanced Medical Optics and Acrysof IQ, SN60WF, Alcon Research Labs). Inclusion criteria included good general health, no ocular pathology, astigmatism less than 2.50 D, younger than 75 years old, and no complications after surgery. All patients recruited before surgery completed the study. All enrolled patients were informed of the nature of the study and signed consent forms. Protocols had been approved by Institutional review boards and ethical committees and adhered to the tenets of the Declaration of Helsinki.

Clinical examination at the hospital (Fundación Jiménez Díaz) included best-spectacle corrected (BSCVA), uncorrected visual acuity (UCVA), refractometry, keratometry, ultrasound biometry, tonometry, biomicroscopy and indirect ophthalmoscopy. Corneal diameters were obtained from infrared front illumination images, using custom algorithms of limbus detection and ellipse fitting. Table 1 shows a profile of the patients.

All procedures were performed by the same surgeon (I.J-A.) on an outpatient basis using topical anaesthesia. The same procedure was used to implant both types of IOLs.

A 3.2 mm superior clear corneal incision (approximately 1 mm from the limbus) and a paracentesis were created with a surgical knife. A 6.0 mm continuous curvilinear capsulorhexis was made under an ophthalmic viscosurgical device (OVD). Phacoemulsicationcation of the lens was performed with the Venturi Millenium system (Bausch & Lomb). After the cortical material was removed, the capsules were cleaned with the automatic irrigation/aspiration straight tip. The Tecnis IOL was implanted using the AMO Silver Series II injector, and the Acrysof IQ using the Monarch II injector. Once the OVD was removed, the incision was closed by hydration, without sutures. Postoperatively, patients were treated with a combination dexamethasone and tobramycin for 4 weeks.

Table 7.1. Profile of patients

	Acrysof group (n=21)	**Tecnis group (n=22)**	**p-value**
Age (yr)	71.1±3.0	68.0±9.5	0.174
Pre-operative spherical error (D)	-1.26 ± 2.6	-1.59±2.85	0.712
Pre-operative astigmatism (D)	0.8 ±0.7	1.5 ± 0.7	0.005*
Corneal diameter @ vertical meridian (mm)**	11.1±0.2	11.05±0.58	0.700
Pre-operative Corneal Astigmatism (D)	0.96±0.68	1.17±0.90	0.397
Pre-operative Mean Corneal Power (D)	44.58±1.30	43.92±1.20	0.095
Post-operative Corneal Astigmatism (D)	0.92±0.53	1.26±0.63	0.072
Post-operative Mean Corneal Power (D)	44.60±1.32	43.92±1.28	0.105
IOL power (D)	20.6±2.0	21.3±3.4	0.428
Time between surgery and post-op measurements (days)	115±106	95±64	0.472

IOL= intraocular lens; SE= spherical equivalent.

* Unpaired t-test, $P<0.05$, significantly different with a confidence interval of 95%

**This parameter includes 10 AcrySof eyes and 19 Tecnis eyes as images from the other eyes were inadequate to estimate vertical corneal diameter.

2.2 Anterior corneal aberrations

Corneal topography was measured by videokeratoscopy (Atlas, Humphrey-Zeiss). Elevation maps measured with respect to a reference plane tangential to the corneal vertex were exported as ASCII files to custom software written in Matlab (Mathworks). Aberrations were obtained using the optical design program Zemax (Focus Software,

Tucson, AZ), launched from a visual interface programmed in Visual Basic. In brief, corneal ray aberrations were obtained by virtual ray tracing on the anterior corneal surface after which wave aberrations were obtained by modal fitting of ray aberrations to the derivatives of Zernike polynomial expansions up to the 7th order. A detailed description of the techniques has been presented previously (Barbero, Marcos, Merayo-Lloves & Moreno-Barriuso, 2002, Barbero, Marcos & Merayo-Lloves, 2002, Marcos, Barbero, Llorente & Merayo-Lloves, 2001). In the present study, corneal aberrations were obtained for 10.0 mm pupil diameters and referred to the corneal reflex. In addition, the corneal Zernike terms, obtained for 10.0 mm, were re-scaled for 5.0 mm pupils

Corneal topography was obtained preoperatively (fewer than 10 days before surgery) and postoperatively (at least 45 days after surgery). Corneal aberrations are expressed as individual Zernike coefficients (i.e. 4^{th}-order spherical aberration, vertical trefoil), as the root mean square (RMS) of a combination of some terms (i.e. coma-like, trefoil) or as the RMS of Zernike orders (i.e 3^{rd}- and higher-order RMS, 3rd-order RMS). Induced aberrations were obtained as the difference between postoperative and preoperative aberrations for each Zernike term.

2.3 Statistical analysis

Corneal aberrations were compared before and after surgery in both groups of patients, and statistical differences were tested using a paired *t* test for 2-sample comparison. Also, preoperative, postoperative, and induced aberrations were compared across groups, and statistical differences were tested using unpaired *t* test for two sample comparison.

3. RESULTS

Figure 7.1 shows typical examples of corneal wave aberration patterns, before and after surgery, as well as the induced wave aberrations (for 3rd and higher orders; that is, excluding tilt, defocus and astigmatism).

The differences between the postoperative and preoperative patterns were consistent across eyes, with a typical superior lobe in the postoperative pattern that was not present in the preoperative pattern. The position of the lobe was consistent with the superior incision. Looking at individual terms, postoperative patterns showed consistently

increased vertical astigmatism Z_2^2, increased vertical trefoil Z_3^{-3} and increased vertical tetrafoil Z_4^4 (toward more negative values). The combination of positive trefoil and negative tetrafoil produces the characteristic superior lobe in the postoperative and induced aberration patterns.

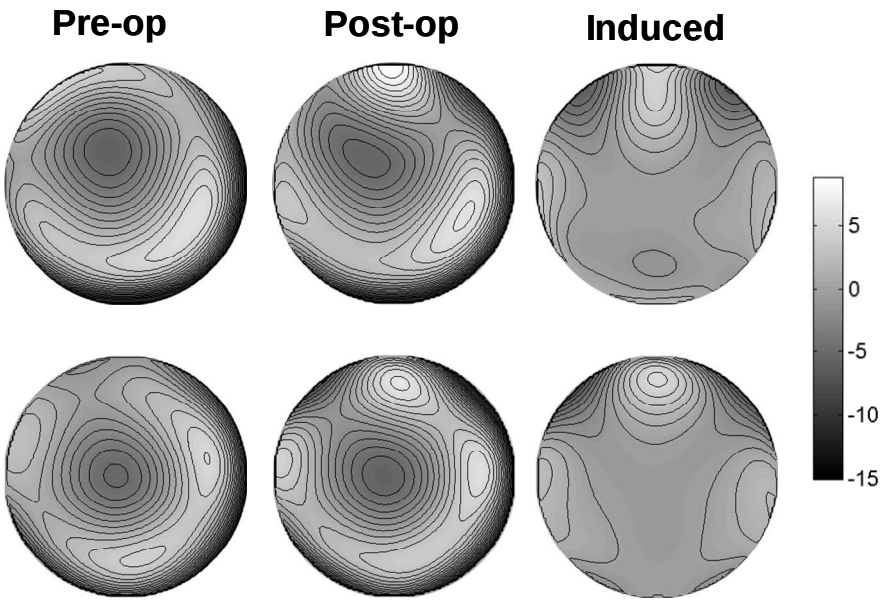

Figure 7.1. Maps of preoperative corneal aberrations, postoperaive corneal aberrations, and induced corneal aberrations (difference between postoperative and preoperative aberrations) in 2 eyes. Top: AcrySof IQ IOL. Bottom: Tecnis IOL. Data are for 3rd-and higher-order aberrations and a 10.0 mm corneal diameter.

Figure 7.2 shows preoperative, postoperative, and induced vertical astigmatism, trefoil, tetrafoil, and spherical aberration in all eyes in each group (10.0 mm). Figure 7.3 shows the RMS, including all terms (except tilt and defocus), in all eyes in each group. Table 2 shows the relevant mean preoperative and postoperative individual Zernike coefficient and RMS (for different orders and terms), for 10.0 and 5.0 mm pupils in the Acrysof IQ group and Tecnis group respectively. Preoperative aberration values, except for vertical coma with a 10.0 mm pupil, were not statistically different between groups. In the Acrysof group, there were statistically significant preoperative and postoperative differences in vertical astigmatism, vertical trefoil and vertical tetrafoil (both for 10 and 5-mm pupils) as well as other 6 and 10 higher order terms respectively (not shown in

the graph). For the Tecnis group there were statistically significant pre/post differences in the vertical astigmatism, vertical trefoil and tetrafoil (for 10.0 mm and 5.0 mm pupils) as well as other 6 and 10 higher-order terms, respectively (not shown in the graphs). In the Tecnis group, there were statistically significant preoperative and postoperative differences in vertical astigmatism, vertical trefoil, and tetrafoil (for 10.0 mm and 5.0 mm pupils) as well as other 8 and 6 higher-order terms (not shown in the graphs). There were not statistically significant differences in spherical aberration or coma-like terms. In terms of RMS, there were statistically significant differences in 3rd and higher-order terms, and 5th- and higher-order terms in the Acrysof IQ group and in 3rd and higher-order, 3rd order alone, 4th- and higher-order, 4th order alone, 5th- and higher-order and trefoil for the Tecnis group, both for 10 and 5-mm pupils. Spherical aberration and coma RMS did not change significantly in either group. Although the Techis group had a significant increase in more terms and orders than the Acrysof IQ group and the postoperative values in the Tecnis group were slightly higher, the differences between postoperative values across groups were not statistically significant.

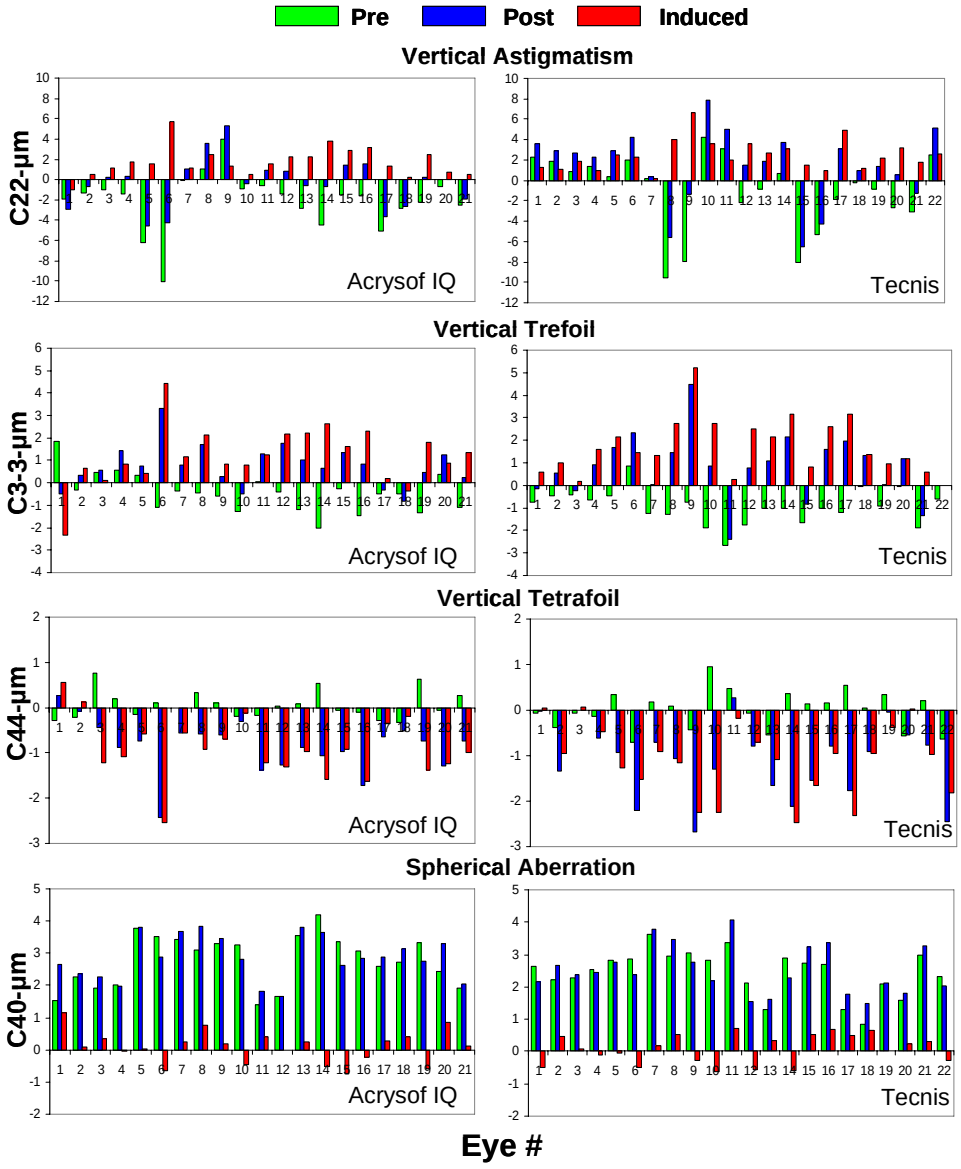

Figure 7.2. Preoperative, postoperative, and induced aberrations in all eyes of the study: 0/90 degree corneal astigmatic term, vertical trefoil,vertical tetrafoil and spherical aberration. Data are for a 10.0 mm corneal diameter.

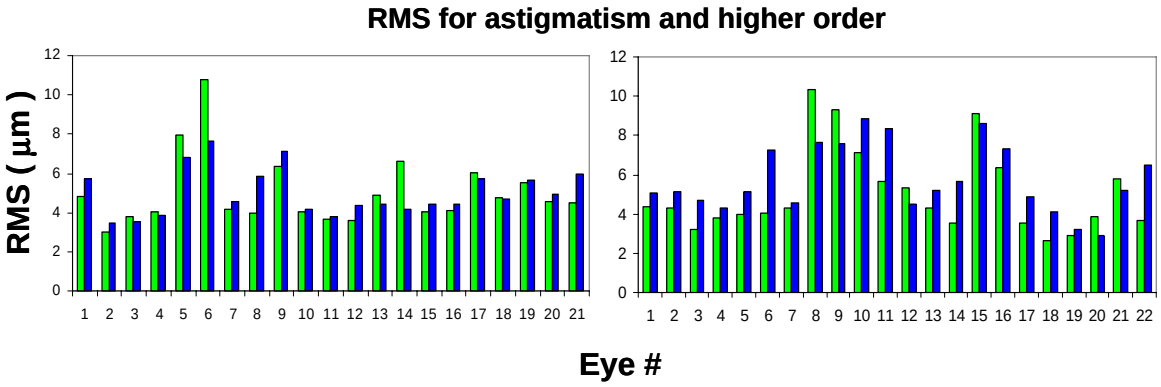

Figure 7.3. Preoperative and postoperative corneal RMS wavefront error in all eyes in the study. Data are for a 10.0 mm corneal diameter.

Table 7.2. Preoperative and postoperative RMS of the corneal wave aberration and relevant Zernike terms for the 2 groups of patients for 10.0 mm and 5.0 mm diameters. Statistical analysis corresponds to comparisons between groups (for preoperative and postoperative measurements) and between preoperative and postoperative measurements (in each group).

	Pre (10.0 mm)			Post (10.0 mm)			Differences pre/post *P*-value+ (10-mm)	
RMS/Zernike terms (μm)	Tecnis	Acrysof IQ	*P* -value§	Tecnis	Acrysof IQ	*P* -value§	Tecnis	Acrysof IQ
RMS all(no defocus or tilt)	5.06±2.10	5.01±1.78	0.93	5.75±1.72	5.01±1.19	0.11	0.0404*	0.98
RMS 3rd & higher	3.54±0.66	3.83±0.53	0.12	4.31±1.17	4.29±0.68	0.95	0.0016*	0.004*
RMS 3rd	2.18±0.80	2.29±0.74	0.65	2.78±1.11	2.57±0.99	0.52	0.015*	0.20
RMS 4th	2.57±0.64	2.86±0.78	0.19	3.01±0.76	3.16±0.60	0.48	0.0006*	0.0095*
RMS 4th & higher	2.69±0.62	2.95±0.75	0.23	3.22±0.80	3.31±0.59	0.66	0.0005*	0.0019*
RMS 5th &higher	0.68±0.34	0.61±0.28	0.47	1.07±0.46	0.96±0.21	0.29	0.005*	<0.0001*
RMS Spherical	2.46±0.69	2.79±0.81	0.16	2.54±0.75	2.88±0.68	0.13	0.43	0.41
RMS trefoil	1.22±0.71	0.99±0.48	0.23	1.85±1.17	1.33±0.72	0.091	0.008*	0.080
RMS coma	1.68±0.75	1.95±0.87	0.28	1.82±0.93	2.10±0.95	0.338	0.43	0.46
Z22	-1.05±3.78	-2.07±2.79	0.32	1.42±3.52	-0.33±2.44	0.066	<0.0001*	<0.0001*
Z3-3	-0.95±0.76	-0.44±0.87	0.0456*	0.86±1.42	0.76±0.94	0.79	<0.0001*	0.0005*
Z40	2.45±0.70	2.78±0.81	0.16	2.53±0.74	2.87±0.68	0.12	0.45	0.42
Z44	0.01±0.43	0.06±0.31	0.66	-1.09±0.82	-0.83±0.58	0.25	<0.0001*	<0.0001*
RMS 3rd & higher	0.29±0.12	0.27±0.06	0.35	0.46±0.18	0.43±0.11	0.53	0.003*	<0.0001*
RMS 3rd	0.24±0.12	0.21±0.07	0.37	0.40±0.19	0.36±0.13	0.44	0.006*	<0.0001*
RMS 4th	0.16±0.05	0.14±0.05	0.41	0.20±0.05	0.21±0.04	0.72	0.002*	0.0001*
RMS 4th & higher	0.16±0.06	0.15±0.05	0.38	0.21±0.05	0.22±0.04	0.63	0.0007*	<0.0001*
RMS 5th &higher	0.03±0.02	0.03±0.01	0.20	0.06±0.02	0.07±0.02	0.28	<0.0001*	<0.0001*
RMS Spherical	0.13±0.05	0.13±0.05	0.67	0.11±0.06	0.12±0.05	0.61	0.065	0.52
RMS trefoil	0.16±0.13	0.10±0.06	0.08	0.35±0.20	0.32±0.13	0.54	0.002*	<0.0001*
RMS coma	0.16±0.07	0.17±0.10	0.88	0.17±0.09	0.16±0.07	0.66	0.76	0.58
C22	-0.05±0.79	-0.36±0.56	0.13	0.57±0.67	0.26±0.62	0.12	<0.0001*	0.002*
C3-3	-0.09±0.15	-0.04±0.08	0.18	0.26±0.22	0.24±0.13	0.74	<0.0001*	<0.0001*
C40	0.13±0.05	0.13±0.05	0.66	0.11±0.06	0.12±0.05	0.57	0.067	0.52
C44	0.00±0.03	0.00±0.03	0.63	-0.12±0.07	-0.10±0.06	0.45	<0.0001*	<0.0001*

Z22, astigmatism at 0/90º; Z3-3, vertical trefoil; Z40, spherical 4th order aberration; Z44 vertical tetrafoil

- p<0.05, significantly different with a confidence interval of 95%

§ unpaired t-test

+ paired t-test

Despite the increase in certain aberrations, in general, corneal aberrations preoperatively correlated well with corneal aberrations post-operatively. In Acrysof IQ eyes, the correlation between all terms (except for tilt) preoperatively and postoperatively was positive and statistically significant in all eyes (P<0.0001). The mean slope across eyes was 0.91±0.21 (SD) and the correlation coefficient (R),

0.88±0.13. When defocus was excluded, the correlation was significant in all eyes except 2, and when defocus and astigmatism were excluded, the correlation was significant in all except 4 eyes. In Tecnis eyes, the correlation between all terms (except tilt) preoperatively and postoperatively was positive and statistically significant in all eyes except eyes 17, 18 and 20 (P<0.0001). The mean slope across eyes (excluding those 3 eyes) was 0.94±0.22 and R, 0.84±0.099. When defocus, astigmatism or both were excluded, the correlation was still significant in all except 5 eyes. Figure 7.4 shows the correlation between preoperative and postoperative Zernike coefficients in two typical eyes. The correlation was preserved primarily because spherical aberration and coma, major contributors to HOAs, do not change significantly with surgery. When analyzing correlations preoperatively and postoperatively (across all eyes), there was no correlation for 21 of the 35 Zernike coefficients for the Acrysof IQ group and 18 of 35 in the Tecnis group (P>0.05). Figure 7.5 shows the correlation between preoperative and postoperative for spherical aberration, vertical trefoil and vertical tetrafoil.

To average individual differences and find the typical changes in corneal aberrations induced by surgery, the mean induced wave aberration patterns were calculated. These are shown in Figure 7.6, and the corresponding coefficients are shown in Table 3, for 10.0 and 5.0 mm pupils. Table 3 shows the Zernike terms that were statistically significantly different from zero (primarily vertical astigmatism, trefoil and tetrafoil). Designers of computer eye models to test the effects of IOLs in optical performance can incorporate these induced aberrations in their models, adding them up to the preoperative corneal aberrations.

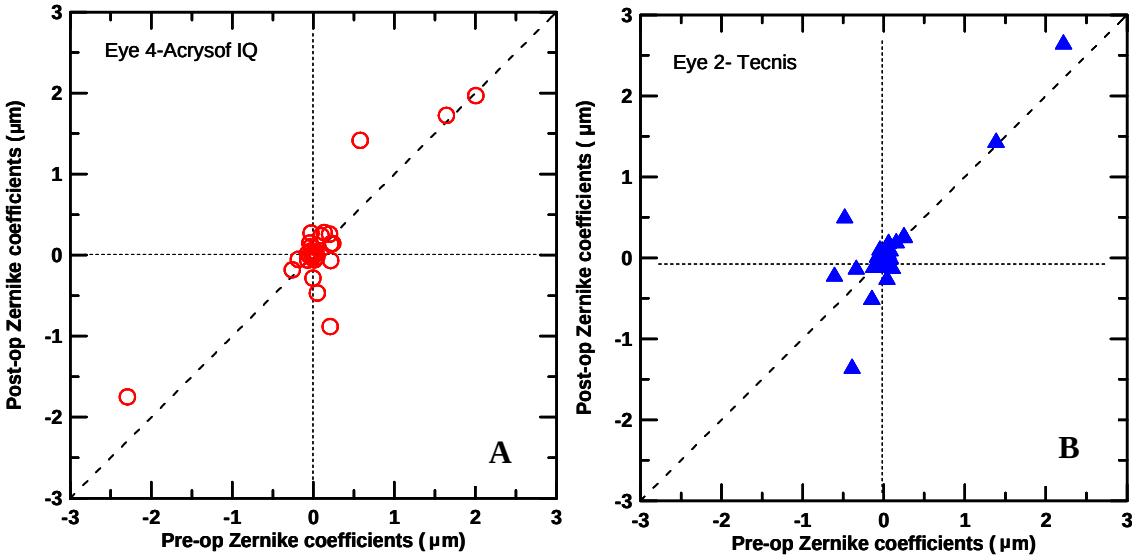

Figure 7.4. Correlation between preoperative and postoperative corneal Zernike coefficients (3 rd order and higher) in 2 eyes. **A**: Eye 4 with an Acrysof IQ IOL. **B**: Eye 2 with a Tecnis IOL. Slopes are 0.1 and 1.08, and correlation coefficients are 0.89 and 0.88 for (**A**) and (**B**), respectively. Dashed lines indicate y = x. Data are for a 10.0 mm corneal diameter.

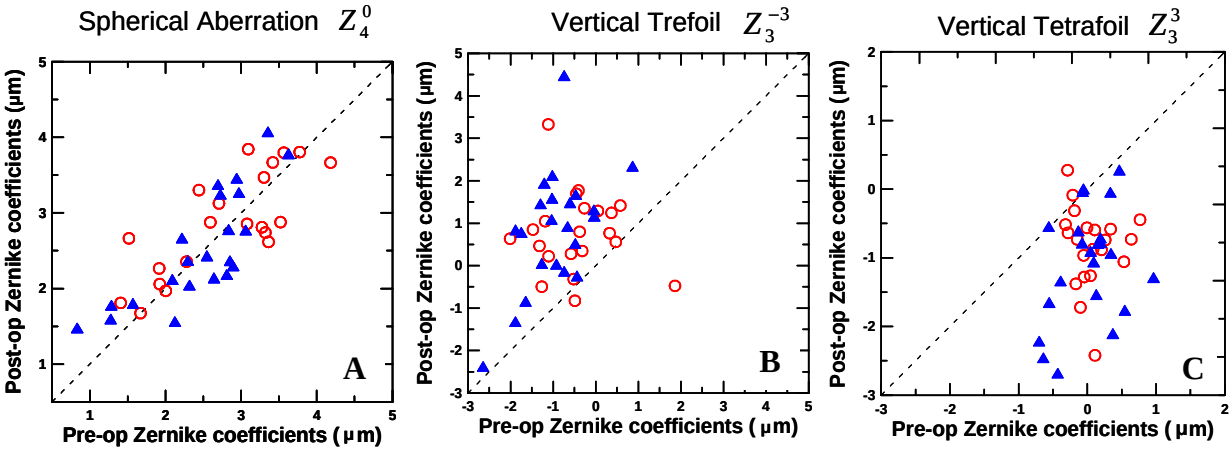

Figure 7.5. Correlations between preoperative and postoperative aberrations for all eyes. **A**: Corneal spherical aberration. **B**: Vertical trefoil. **C**: Vertical tetrafoil. Open circles represent eyes with the Acrysof IQ IOL and solid triangles, eyes with the Tecnis IOL. Dashed line corresponds to y = x. Data are for a 10.0 corneal diameter.

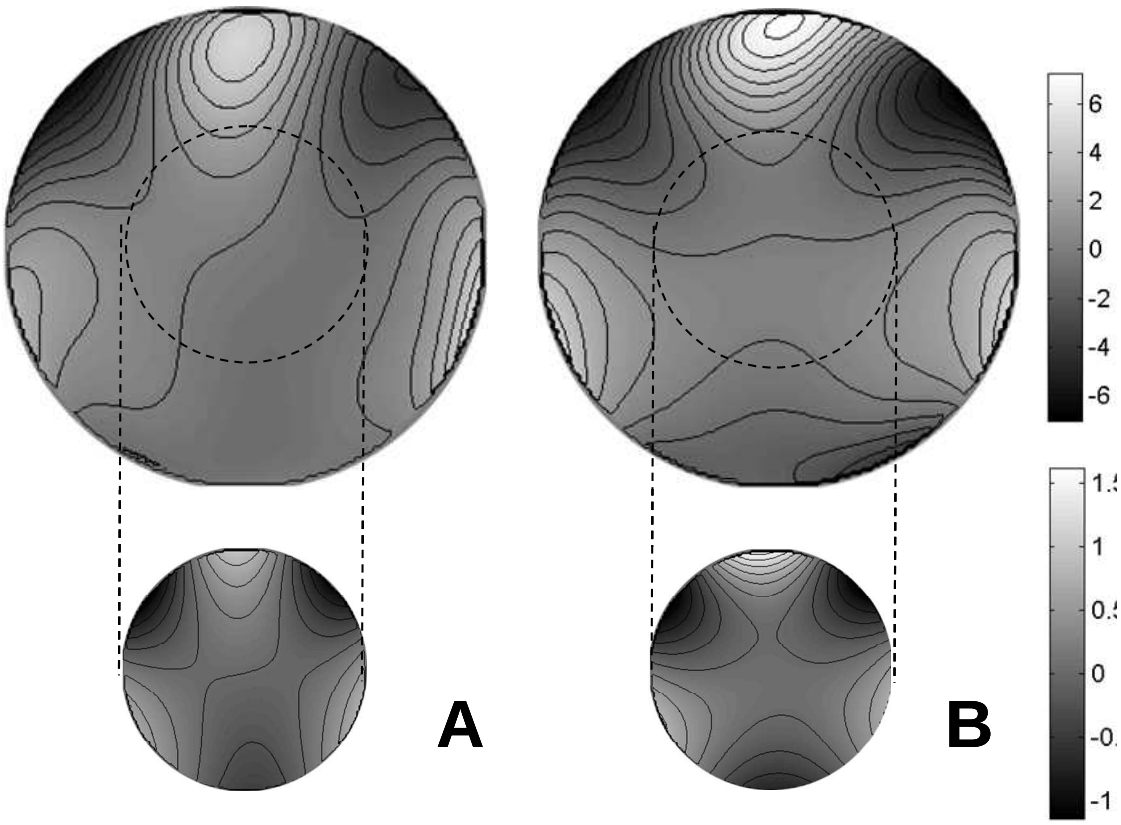

Figure 7.6. Mean induced corneal wave aberration maps for 3rd – and higher-order aberrations. **A**. Eyes with the AcrySof IQ IOL. **B**: Eyes with Tecnis IOL. Top maps are for 10.0 mm diameters, with contour lines every 1.00μm. Bottom maps are for 5.0 mm diameters, with contour lines every 0.25μm. Scale bars are different for each diameter. The 5.0 mm area is highlighted in the 10.0 mm map.

Table 7.3. Induced corneal aberrations (Zernike terms) in each group for 10.0 mm and 5.0 mm diameters and corresponding significance when comparing preoperative and postoperative terms.

	Tecnis (10-mm)		Tecnis (5-mm)		Acrysof (10 mm)		Acrysof (5 mm)	
Zernike coeff.	Average± std (μm)	P value	Average± std (μm)	P value	Average± std (μm)	P value	Average± std (μm)	P value
Z1_1	-0,73±2,25	0,143	-0,079±0,353	0,30	1,21±2,32	0,027*	0,228±0,297	0,002*
Z11	0,06±3,43	0,936	-0,024±0,268	0,68	-0,35±3,40	0,642	0,195±1,372	0,52
Z2_2	-0,12±1,11	0,609	0,035±0,218	0,45	0,00±0,75	0,9892	0,083±0,336	0,27
Z20	-0,11±1,06	0,641	0,019±0,060	0,15	0,11±1,11	0,656	0,003±0,043	0,78
Z22	2,47±1,50	p<0.0001*	0,623±0,390	p<0.0001*	1,74±1,44	p<0.0001*	0,618±0,257	p<0.0001*
Z3_3	1,81±1,19	p<0.0001*	0,344±0,240	p<0.0001*	1,20±1,34	0,0006*	0,277±0,125	p<0.0001*
Z3_1	-0,17±1,13	0,485	-0,036±0,109	0,13	0,37±1,24	0,190	0,068±0,089	0,002*
Z31	0,05±1,66	0,899	-0,003±0,103	0,87	-0,41±1,08	0,095	-0,023±0,083	0,23
Z33	-0,23±1,02	0,302	-0,084±0,174	0,034*	-0,07±0,86	0,696	-0,062±0,208	0,18
Z4_4	0,00±0,52	0,998	-0,054±0,071	0,0018*	-0,08±0,42	0,416	-0,028±0,109	0,26
Z4_2	-0,17±0,31	0,017*	0,004±0,026	0,49	-0,13±0,30	0,064	-0,005±0,030	0,44
Z40	0,07±0,45	0,448	-0,021±0,051	0,067	0,09±0,50	0,417	-0,005±0,034	0,51
Z42	-0,08±0,61	0,567	0,008±0,047	0,44	-0,24±0,65	0,103	-0,017±0,048	0,11
Z44	-1,10±0,79	p<0.0001*	-0,121±0,074	p<0.0001*	-0,89±0,68	p<0.0001*	-0,101±0,058	p<0.0001*
Z5_5	-0,19±0,49	0,092	-0,041±0,022	p<0.0001*	-0,24±0,26	0,0004*	-0,039±0,028	p<0.0001*
Z5_3	-0,20±0,41	0,036*	-0,011±0,020	0,014*	-0,18±0,38	0,049*	-0,014±0,016	0,0005*
Z5_1	0,12±0,39	0,169	-0,004±0,016	0,29	0,04±0,33	0,596	-0,006±0,015	0,07
Z51	-0,02±0,20	0,716	0,003±0,016	0,46	-0,06±0,16	0,104	-0,002±0,011	0,38
Z53	0,14±0,22	0,008*	0,003±0,013	0,33	0,09±0,23	0,077	0,005±0,016	0,18
Z55	-0,06±0,40	0,484	0,011±0,029	0,10	0,05±0,29	0,423	0,013±0,042	0,17
Z6_6	-0,06±0,36	0,472	-0,001±0,006	0,47	-0,01±0,22	0,877	0,000±0,003	0,88
Z6_4	0,19±0,21	0,0003*	0,003±0,003	0,0003*	0,08±0,32	0,252	0,001±0,005	0,25
Z6_2	-0,05±0,12	0,059	-0,001±0,002	0,059	-0,01±0,11	0,627	0,000±0,002	0,63
Z60	0,09±0,20	0,046*	0,001±0,003	0,045*	0,04±0,14	0,237	0,001±0,002	0,24
Z62	-0,05±0,22	0,347	-0,001±0,003	0,34	0,01±0,18	0,844	0,000±0,003	0,84
Z64	0,19±0,29	0,0063*	0,003±0,005	0,006*	0,16±0,17	0,0004*	0,003±0,003	0,0004*
Z66	0,13±0,37	0,118	0,002±0,006	0,12	0,11±0,25	0,051	0,002±0,004	0,051
Z7-7	-0,03±0,16	0,412	0,000±0,001	0,41	0,06±0,10	0,0146*	0,000±0,001	0,015*
Z7_5	0,21±0,13	p<0.0001*	0,002±0,001	p<0.0001*	0,20±0,17	p<0.0001*	0,002±0,001	p<0.0001*
Z7_3	0,03±0,12	0,255	0,000±0,001	0,25	0,05±0,09	0,0155*	0,000±0,001	0,015*
Z7_1	0,05±0,12	0,0815	0,000±0,001	0,08	0,05±0,10	0,043*	0,000±0,001	0,043*
Z71	-0,02±0,07	0,2421	0,000±0,001	0,24	0,00±0,08	0,885	0,000±0,001	0,89
Z73	0,01±0,09	0,599	0,000±0,001	0,5993	-0,01±0,08	0,536	0,000±0,001	0,54
Z75	-0,08±0,15	0,024*	-0,001±0,001	0,0244	-0,07±0,22	0,163	-0,001±0,002	0,16
Z77	0,01±0,17	0,745	0,000±0,001	0,745	0,02±0,15	0,487	0,000±0,001	0,49

4. DISCUSSION

We found that small-incision cataract surgery in patients implanted with two types of aspheric IOLs induced consistent and highly statistically significant changes in astigmatism and tetrafoil. The procedure did not induce significant changes in spherical aberration or coma terms. Interestingly, highly statistically significant differences were found not only in the largest area, but also for pupil diameters (5.0 mm) potentially relevant to vision.

Changes in corneal astigmatism are well known, and changes in corneal trefoil have also been reported. Our conclusions are stronger than those reported by Guirao (Guirao et al., 2004), likely because in our study, all eyes had superior incisions, which allows higher statistical power. While Guirao (Steinert & Deacon, 1996) do not report changes in tetrafoil term, we found that this term was consistently induced in all patients, with similar amounts (and opposite sign) than trefoil. In addition, along with vertical trefoil, it was responsible for the characteristic pattern of induced aberrations. To our knowledge, only Pesudovs (Pesudovs et al., 2005) have reported the presence of ocular tetrafoil in a group with spherical IOL implanted through a corneal incision (not with the same IOL implanted through a scleral incision). Because only total (and not corneal) aberrations were measured, they could not confirm the origin of this aberration. In addition, Guirao et al. used a different phakic group to perform the comparisons, whereas we compute the actual aberrations induced by performing measurements in the same eyes preoperatively and post- operatively.

We confirmed that neither spherical aberration nor coma changed significantly with the procedure. As a result, aspherical IOLs designed to compensate for the mean pre-operative corneal spherical aberration can work under the assumption that spherical aberration remains practically unchanged. Changes in astigmatism, trefoil and tetrafoil are not negligible and should be considered in simulations of optical outcomes of cataract surgery. Along with real corneal topographies and IOL design, corneal aberrations induced by the procedure should be considered when trying to predict the outcomes of cataract surgery, being potentially more important than the presence of moderate amounts of IOL tilt and decentration. The numerical data provided in Table 2 will help to produce more realistic predictions using eye models. Other potential changes, expected to be minor, refer to the posterior corneal surface.

We found slight differences in the change preoperative and postoperative aberrations with the two types of aspherical lenses, with the Tecnis IOLs showing a slightly higher increase in aberrations. Most differences between IOLs were not statistically significant and may not have visual consequences. Corneal diameters (particularly along the meridian of the incision) were not statistically different between groups; therefore, any difference in outcomes cannot be attributed to differences in the effective incision location (relative to the apex). In addition, we did not find a significant correlation between vertical corneal diameter and induced vertical astigmatism, trefoil and tetrafoil.

Although the study was designed to follow identical protocols in the two groups, and the incision size was purposely larger than the minimum values potentially allowed with the two injectors used to implant the two lens types (2.2 mm for the Acrysof HOA and 2.8 mm for the Tecnis), differences may be associated with slight final differences in incision size. The effective incision size after implantation was not measured. However, enlargement of incision at different steps of the procedure (Steinert & Deacon, 1996), and particularly differences between injectors have been reported before (Kohnen & Kasper, 2005), and may play some role in the observed tendencies.

Customized computer models of eyes with intraocular lenses. 8

8. Customized computer models of eyes with intraocular lenses

This chapter is based on the article by Rosales. P et al., *"Customized computer models of eyes with intraocular lenses"* Optics Express, Vol. 15, pp.2204-2218. Coauthors of the study is S. Marcos. The contribution of Patricia Rosales to the study was to measure tilt and decentration and experimental aberrations (together with Lourdes Llorente) in patients with intraocular lenses, to measure simulated aberrations with customized computer model eyes and to analyze the results for the same patients.

RESUMEN

Objetivos: Elaborar un modelo de ojo computacional individualizado con el fin de poder predecir las aberraciones oculares y evaluar la calidad óptica de ojos pseudofáquicos con lentes intraoculares implantadas.

Métodos: A partir de datos individualizados de topografía corneal, el ángulo λ, biometría ocular, geometría de la lente intraocular implantada, inclinación y descentramiento de la lente intraocular medida para cada ojo, se elaboró un modelo de ojo en Zemax con el que se calcularon las aberraciones totales y corneales para cada ojo sin considerar el tilt y el descentramiento de la lente intraocular y teniéndolos en cuenta. Las aberraciones oculares obtenidas de la simulación se compararon con las obtenidas experimentalmente mediante trazado de rayos láser (LRT) en estos ojos de pacientes con lentes intraoculares implantadas.

Resultados: Las aberraciones individuales más relevantes se predicen bien con el modelo de ojo completo. La aberración esférica corneal y el coma horizontal se compensan por efecto de la lente intraocular, y en un 58.3% de los casos, la inclinación y el descentramiento de la lente intraocular contribuyen a la compensación del coma horizontal.

Conclusiones: Los modelos de ojo computacionales individualizados son una buena representación de ojos reales con lentes intraoculares implantadas y permiten comprender la contribución relativa de factores ópticos, geométricos y factores relacionados con la cirugía en la calidad de la imagen. Aunque la aberración esférica corneal se reduce con la lente intraocular esférica, otras aberraciones de alto orden todavía siguen afectando a las aberraciones totales en ojos pseudofáquicos. La inclinación y el descentramiento de las lentes intraoculares tienen poca influencia en la calidad óptica total del ojo.

ABSTRACT

Purpose: To present a customized computational model eye to predict the ocular aberrations and to evaluate the optical quality of pseudophakic eyes with implanted intraocular lenses.

Methods: A model eye was built in Zemax with customized data of each pseudophakic eye obtained from corneal topography, λ angle, ocular biometry, implanted intraocular lens geometry, tilt and decentration of the IOL measured for each eye, to calculate the simulated corneal and total aberrations for each eye without considering IOL's tilt and decentration and taking it into account. Simulated aberrations were compared with those obtained experimentally from laser ray tracing technique measured on the same eyes.

Results: Relevant individual aberrations were well predicted by the complete eye model. Corneal spherical aberration and horizontal coma were compensated by the IOL, and in 58.3% of the cases, IOL tilt and decentration contributed to compensation of horizontal coma.

Conclusions: We conclude that customized computer eye models are a good representation of real eyes with IOLs and allow understanding the relative contribution of optical, geometrical and surgically-related factors to image quality. Corneal spherical aberration is reduced by aspheric IOLs, although other corneal high order aberrations are still a major contributor to total aberrations in pseudophakic eyes. Tilt and decentration of the IOLs represent a relatively minor contribution of the overall optical quality of the eye.

1. INTRODUCTION

Schematic eye models have been used for decades to represent paraxial properties of the ocular optics and, in some cases, to describe general trends for symmetric aberrations. Those schematic eyes are based on average anatomic data of the eye and rely on several simplifications. For example, paraxial schematic eyes of Gullstrand, Le Grand, Emsley or Rabbetts (See Atchison and Smith for a review (Atchison & Smith, 2000)), with spherical surfaces, are unable to predict the amounts of spherical aberrations found in real eyes. More sophisticated eye models are improved by aspherizing one or more surfaces or by including a gradient index distribution in the crystalline lens, such as those of Lotmar, Kooijman, Liou and Brennan (See Atchison and Smith for a review (Atchison & Smith, 2000)). In general, modifications of schematic eye models are proposed for specific purposes. For example, the eye of Liou and Brennan was designed to give a realistic spherical aberration, and off-axis monochromatic aberrations were not considered. In some cases a geometrical property of the ocular components in the model is adjusted to reproduce observed optical performance under different conditions (i.e. change of spherical aberration with accommodation (Navarro, Santamaría & Bescós, 1985), or off-axis aberrations across the visual field (Escudero-Sanz & Navarro, 1999)).

Today, the aberrations of the eye can be reliably measured with ocular aberrometers, and there is a deeper understanding on their change with different conditions (i.e. aging (Mclellan, Marcos & Burns, 2001), accommodation (He, Burns & Marcos, 2000) or surgical interventions (Barbero, Marcos & Jimenez-Alfaro, 2003)). The fact that the amount and spatial distribution of aberrations vary widely in the population (Castejon-Mochon, Lopez-Gil, Benito & Artal, 2002, Thibos, Hong, Bradley & Cheng, 2002) prevents one simple eye model from representing the actual optical performance of real eyes. In addition to the description and measurement of the ocular aberrations, there is an increasing interest in understanding the causes for the optical aberrations of the individual eyes (Marcos, Burns, Prieto, Navarro & Baraibar, 2001). This interest has been paralleled by the development of new instrumentation to measure the geometrical and structural properties of the ocular components (topography of the anterior and posterior corneal surfaces (Dubbelman, Sicam & van der Heijde, 2006) , optical biometry (Drexler, Baumgartner, Findl, Hitzenberger, Sattmann & Fercher,

1997), phakometry (Garner, 1997, Mutti, Zadnik & Adams, 1992), anterior and posterior lens geometry (Dubbelman & van der Heijde, 2001, Dubbelman, van der Heijde & Weeber, 2001, Koretz, Cook & Kaufman, 2001), or lens tilt and decentration (Barry, Dunne & Kirschkamp, 2001, Phillips, Perez-Emmanuelli, Rosskothen & Koester, 1988, Rosales & Marcos, 2006). The combinations of the above measurements allows understanding of phakic ocular development and changes to the ocular condition. Moreover, the new directions for improving the performance of corneal refractive surgery, and intraocular and contact lens design, and particularly the increase of individually customized approaches for correction require more sophisticated eye models, using real individual data of the eye under study.

To model individual eyes is a complex task because it requires accurate biometric eye data, such as the shape of the ocular surfaces, knowledge of the gradient index distribution of the crystalline lens, position of the lens and the position of the fovea. The study of optical performance of pseudophakic eyes, where the natural crystalline lens has been replaced with an intraocular lens (IOL), is particularly interesting. On one hand, the complexity of the eye models can be somewhat reduced, since the intraocular lens has constant index and the shape of the surfaces and optical design is accessible. Identifying the relative contribution of different factors to the optical quality in pseudophakic eyes is helpful to evaluate the real impact of new IOL designs and the potential need of improvement of surgical strategies in cataract surgery. Most studies to date are either based on simple eye models (Atchison, 1989, Atchison, 1990, Holladay, Piers, Koranyi, van der Mooren & Norrby, 2002) or are limited to a global description of optical performance through double-pass (Artal, Marcos, Navarro, Miranda & Ferro, 1995, Guirao, Redondo, Geraghty, Piers, Norrby & Artal, 2002) or aberration measurements (Barbero et al., 2003, Marcos, Barbero & Jiménez-Alfaro, 2005, Mester, Dillinger & Anterist, 2003, Rocha, Soriano, Chalita, Yamada, Bottós, Bottós, Morimoto & Nosé, 2006). Most of the theoretical studies have concentrated on the impact of lens geometry on spherical aberration. The effect of tilt and decentration of the intraocular lens has been discussed by Atchison (Atchison, 1990) and Holladay (Holladay et al., 2002) based on theoretical models. Barbero (Barbero et al., 2003) compared optical aberrations of spherical intraocular lenses measured in vivo with the measurements on same lenses in vitro using laser ray tracing, and estimations from virtual ray tracing using customized computer eye models (incorporating corneal topography, IOL geometry and anterior chamber depth). While the three techniques provided similar

estimates of spherical aberration, third and higher order aberrations were not correctly predicted, since, as shown both in vitro and numerically, they were affected by the actual amounts and combinations of IOL tilt and decentration. Finally, the relevant contribution of corneal optics to overall optical quality, and particularly the systematic induction of high order aberrations (trefoil and tetrafoil) in cataract surgery has also been emphasized as described in Chapter 7 (Guirao, Tejedor & Artal, 2004, Marcos, Rosales, Llorente & Jiménez-Alfaro, 2007, Pesudovs, Dietze, Stewart & Cox, 2005) .

In this Chapter we present a customized model eye in patients with intraocular lenses of known geometry where tilt and decentration values have been measured in vivo. Experimental measurements of ocular aberrations in these eyes are compared with estimates of aberrations from numerical ray tracing using a customized model eye, where individual measurements of post-operative corneal topography, anterior chamber depth, IOL geometry, IOL tilt and decentration and the misalignment of the line of sight are used. This study will allow validation of the accuracy of customized eye models to predict measured aberrations, to investigate the contribution of the different components to overall image quality in eyes with IOLs and to assess the real benefits of new IOL designs.

2. METHODS

2.1 Subjects

The study was performed on 12 eyes of 7 subjects (average age 71.23 ± 3.52 yrs, mean and standard deviation) implanted with aspheric IOLs (Acrysof IQ, Alcon) of known geometry in a standard phacoemulsification surgical procedure with a 3.2-mm superior clear corneal incision. Experimental measurements were performed 81.6±24.43 days after surgery, in a single experimental session. Spherical equivalent ranged pre-operatively from -5.75 to 1.5 D (-1.5 ± 2.4 D, on average) and post-operatively from-0.5 to 0.75 D (-0.125 ± 0.5 D, on average). The mean power of the implanted IOLs was 20.34 D (the power for each eye appears on Table 8.1). Pupils were dilated with Tropicamide 1% for the measurements. The experimental protocols followed the tenets of the Declaration of Helsinki and had been approved by Institutional Review Boards. Subjects were informed on the nature of the experiments and provided written consent.

2.2 Experimental measurements

2.2.1 Total aberrations measurements

Total wave aberrations were measured using a second generation laser ray tracing (LRT), which was developed at the Instituto de Óptica (CSIC) in Madrid, Spain (Llorente, Barbero, Cano, Dorronsoro & Marcos, 2004). This technique has been described and validated in detail in previous publications (Llorente, Diaz-Santana, Lara-Saucedo & Marcos, 2003, Marcos, Díaz-Santana, Llorente & C., 2002, Moreno-Barriuso, Marcos, Navarro & Burns, 2001, Moreno-Barriuso & Navarro, 2000) and was described in Chapter 1. In this technique a scanning system scans a narrow IR laser beam across the pupil. Pupil and retinal images are simultaneously captured by two CCD cameras. Ray aberrations are obtained by estimating the deviations of the centroids of the retinal spots images corresponding to each entry pupil location with respect to the reference (chief ray). These deviations are proportional to the local derivatives of the wave aberrations, which are fitted by a seventh-order Zernike polynomial expansion.

Patients' pupil diameters ranged from 4 to 6 mm, and the sampling pattern (with 37 samples in a hexagonal configuration) was adjusted by software to fit the natural pupil. In order to compare results across subjects, aberrations were scaled to the same pupil diameter (5 mm, except for subjects #4 and #12 with a pupil diameter of 4 mm). Spherical error was corrected by means of a Badal focusing system. High order aberrations are reported in terms of Zernike coefficients, using the convention of the OSA Standards (Applegate, Thibos, Bradley, Marcos, Roorda, Salmin & Atchison, 2000).

2.2.2 Corneal topography.

The anterior corneal elevation was obtained using a Placido disk videokeratoscope (Humphrey-Zeiss MasterVue Atlas Model 990) which uses an arc step reconstruction algorithm (Campbell, 1997). Data were obtained over 10-mm pupils and were referred to the corneal reflex. Corneal heights were fit by a 7^{th} order Zernike polynomial expansion and discrete points were evaluated in a XY equi-space grid, which were introduced in an optical design program (Zemax, Optima Research, 2007 Tucson) for the ray tracing evaluation (Schwiegerling, Greivenkamp & Miller, 1995). Table 1 shows three relevant coefficients (spherical, horizontal coma and trefoil) of the Zernike

polynomial expansion to the corneal height (centered at the corneal reflex and for a 10-mm pupil diameter).

2.2.3 Optical biometry

Anterior chamber depth (ACD) and axial length (AL) were obtained using a commercial optical biometry system (IOL master, Zeiss). This system uses anterior segment slit-lamp images to estimate ACD and low coherence interferometry to estimate AL. Table 1 shows ACD and AL in all eyes of the study.

2.2.4 IOL tilt and decentration.

IOL tilt and decentration were measured with a custom developed Purkinje imaging system described in detail in Chapter 2, 4 and 5 (Rosales & Marcos, 2006, Rosales, Dubbelman, Marcos & van der Heijde, 2006) and IOL tilt and decentration (de Castro, Rosales & Marcos, 2007). In brief, images of PI, PIII and PIV (first, third and fourth Purkinje Images) are obtained with eccentric (14 deg) collimated illumination from LEDs and captured on an IR CCD camera provided with a telecentric lens. The method to obtain tilt and decentration from the relative locations of PI, PIII and PIV with respect to the pupil center has also been described before. IOL tilt (α) is referred to the pupillary axis and the IOL decentration (d) is referred to the pupil center. Sign conventions for tilt (around the horizontal and vertical axes) and decentration (horizontal and vertical) are shown in Table 8.1 and graphically depicted in Figure 2.6 and Figure 8.1.

The Purkinje imaging system was also used to estimate the relative shift of the corneal reflex (first Purkinje image) with respect to the pupil center for foveal fixation. This information was not readily available in the videokeratoscopic images obtained with our corneal topographer due to the superposition of the Placido rings with the pupil edge. For this purpose an additional channel with foveal illumination from a collimated LED was introduced in the Purkinje imaging system. In addition, we have checked that in eyes when only Purkinje images were available for eccentric illumination, similar information was achieved from extrapolations from Purkinje images positions at different fixation angles. Sign conventions for the 1st Purkinje shift (with respect to the pupil center) for foveal fixation are shown in Table 8.1. The off-axis field angle that would produce the measured shift of the first Purkinje image is obtained by virtually rotating using Phillips' linear equations. This angle is referred to the pupillary axis and

can be treated as angle λ (between the line of sight and pupillary axis) under the assumption that pupil decentration is small (Mandell, 1995).

All measurements with the Purkinje imaging system were performed under pupil dilation, so that it was ensured that there were no differences in the relative pupil center across the geometrical measurements obtained with this system and measurements of ocular aberrations with LRT.

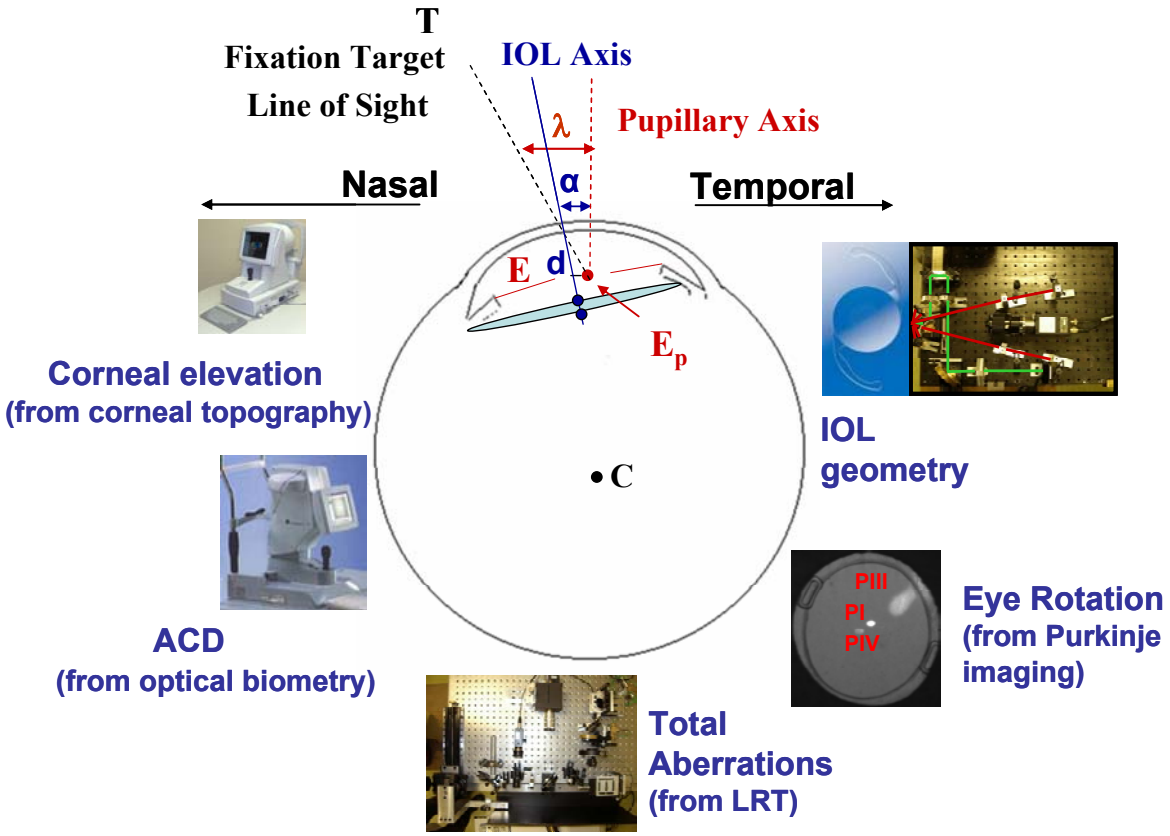

Figure 8.1. Schematic model eye as introduced in Zemax for numerical ray tracing and the different instruments used to obtain individual geometrical data (corneal elevation, anterior chamber depth ACD, IOL tilt and decentration) used in the model, and to measure total aberrations. The reference axes for eye rotation (λ), IOL tilt (α) and decentration (d) are shown. E stands for entrance pupil, E_p for pupil center and C for corneal center of curvature. The eye depicted represents a right eye. The line of sight is rotated nasally so λ_y is positive. The nasal edge of the IOL moves backward, so α_y is positive. The IOL is decentered nasally, so d_x is positive.

Table 8.1. Individual biometrical and geometrical data used in the computer model eye.

Subject	Eye	Cornea[a] C_4^4 µm	Cornea[a] C_3^{-3} µm	Cornea[a] C_4^0 µm	ACD mm	AL mm	IOL Pow (D)	α[b] (deg) x	α[b] (deg) y	d[c] (mm) x	d[c] (mm) y	Purkinje image shift.[d] (mm) x	Purkinje image shift.[d] (mm) y	Eye Rotation[e] (deg) x	Eye Rotation[e] (deg) y
S1	#1 (OD)	-2.4	4.4	-9.2	4.00	23.3	19.5	-1.74	0.98	0.31	0.06	0.53	-0.24	1.82	4.06
	#2 (OS)	-2.1	2.06	-2.2	4.57	23.7	19.5	-1.78	-0.22	-0.28	-0.01	-0.77	-0.19	1.51	-5.92
S2	#3 (OD)	-2.9	1.46	-11	4.11	23.1	20	-1.19	0.98	0.52	-0.12	0.35	-0.11	0.83	2.74
	#4 (OS)	-2.1	0.8	-7.8	3.87	22.8	19.5	-0.90	-0.75	0.19	-0.28	-0.72	0.14	-1.12	-5.71
S3	#5 (OD)	0.12	-4.2	0.6	4.52	23.5	19.5	-0.53	1.78	0.30	-0.02	0.39	0.12	-0.94	2.97
	#6 (OS)	-0.2	-5.5	1.03	2.29	23.1	21.5	2.12	-1.72	-0.23	-0.03	-0.55	0.27	-2.04	-4.19
S4	#7 (OD)	-0.9	-0.8	16.6	4.56	23.9	21	-2.94	1.08	0.27	-0.40	0.32	-0.20	1.55	2.49
S5	#8 (OD)	-1.3	0.5	-14	4.45	22.9	18.5	0.90	1.18	0.51	-0.15	0.27	0.08	-0.61	2.16
	#9 (OS)	-3.0	-1.1	-35	4.40	22.6	21.5	-1.07	-0.07	-0.27	0.26	-0.38	0.06	-0.51	-3.12
S6	#10 (OD)	-2	-2.1	2.9	3.31	24.4	20	-3.39	2.31	0.20	0.53	0.54	0.17	-1.21	3.94
	#11 (OS)	-1.7	-5.8	2.59	4.88	24.4	19	-1.84	-2.60	-0.31	-0.30	-0.36	0.17	-1.27	-2.62
S7	#12 (OD)	-0.6	-2.6	0.64	3.57	21.2	24.5	0.07	1.28	0.38	0.21	0.43	0.27	-2.27	3.48

a.- Corneal heights are fit to a 7th order Zernike polynomial. The table shows three relevant terms as examples.

b.- Tilt x (α_x) stands for tilt around x (or vertical tilt). Sign conventions are: Positive, superior edge of the lens is closer to the cornea than the inferior edge, and vice versa for Negative. Tilt y (α_y) stands for tilt around y (or horizontal tilt). Sign conventions are: Positive, nasal edge of the lens moves backward (for the right eye) or forward (for the left eye), and viceversa for Negative.

c.- Decentration x (d_x) stands for horizontal decentration. Sign conventions are: Positive, the lens is shifted toward the nasal (right eye) or temporal (left eye) direction and viceversa for Negative. Decentration y (d_y) stands for vertical decentration. Sign conventions are: Positive, the lens is shifted upward and viceversa for Negative.

d.-Purkinje image shift x stands for a horizontal shift. Sign conventions are: Positive, the Purkinje image is shifted toward the nasal direction and viceversa for negative. Purkinje image shift in y stands for vertical decentration. Sign conventions are: Positive, the Purkinje image is shifted upward and viceversa for negative.

e.-Eye rotation. Rotation x stands for rotation around x (or vertical rotation). Sign conventions are: Positive, the line of sight is rotated upwards with respect to the pupillary axis, Negative, the line of sight is rotated downwards referred to the pupillary axis. Rotation y stands for rotation around y (or horizontal rotation). Sign conventions are: Positive, the eye rotates to the nasal (right eye) or temporal side (left eye) and viceversa for the Negative. The eye center rotation is considered at 15 mm behind the cornea.

2.2.5 Computer simulations

Customized eye models were built using the Zemax (Focus Software, Tucson, AZ, Zemax, January 2006) optical design program, where an optical system is defined as a sequential group of surfaces separated by refractive index media.

The anterior corneal surface was obtained from videokeratoscopy and modeled with the grid sag surface type within the Zemax program. For the posterior corneal surface, a standard spherical surface with a radius of 6.5 mm was used. Corneal refractive index was taken as 1.376. The IOL anterior and posterior surface geometry was provided by the manufacturer, and introduced in the model eye as standard conic surfaces, with the nominal thickness and refractive index of the lens. Measured values of tilt and decentration of the IOL are introduced with respect to the pupillary axis. Finally, the whole eye is rotated to simulate off-axis measurements obtained due the eccentric location of the fovea.

Figure 8.1 shows the schematic diagram of the model eye introduced in Zemax for the simulations and the different instruments used to measure corneal shape, ocular biometry, lens tilt and decentration and ocular aberrations. We have verified that the relative positions of the ocular surfaces and eye rotation for foveal fixation are correct by simulating in Zemax the locations of PI, PIII and PIV for the model eye and compared them to the real measurements for foveal fixation. Figure 8.2 shows a good agreement between simulated and experimental locations of the Purkinje images for the model eye at foveal fixation.

The simulations of ocular aberrations were performed for a wavelength of 786 nm. The index dependence of the wavelength is introduced fitting experimental longitudinal chromatic aberration with Herzberger formula (Herzberger, 1969). Aberrations were evaluated at best focus (defined as the location where the spot diagram is most compact), since aberrations were measured for best spherical correction. A sampling matrix of 64x64 rays was used to calculate the aberrations.

In order to assess the relative contribution of different factors to ocular wave aberrations, the simulations are performed for the cornea alone, for the cornea and the IOL (assuming no tilt and decentration, i.e. aligned with respect to the pupillary axis), and for the cornea and the IOL with the measured tilt and decentration. All simulations were referred to the pupil center, and accounting for the misalignment of the videokeratoscopic axis and the line of sight (i.e, with a field angle for incoming rays

accounted for by angle λ). Comparisons between simulated (using customized eye models) and measured (with LRT) aberrations were performed in terms of correlations between the sets of simulated and measured Zernike terms (slope and regression coefficient of linear correlations) for each eye, and comparisons of individual Zernike terms for all eyes.

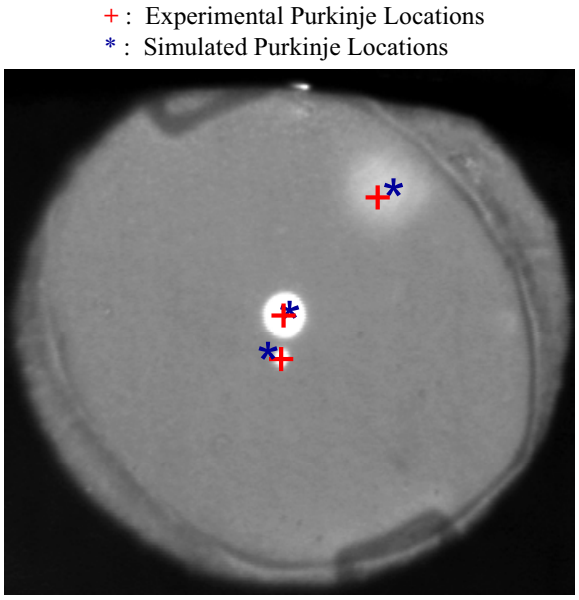

Figure 8.2. Simulated and experimental Purkinje images locations for the eye model depicted in A (for foveal fixation).

2.2.6 Physical eye model and computer simulations

Additional assessment of the accuracy of the virtual eye model to predict wave aberrations was performed using a physical model eye with aspheric and spherical IOLs of several powers (18, 21, 23,5 and 26 D). This model eye had been used in a previous study (chapter 5) for validations of the measurements of IOL tilt and decentration with Purkinje and Scheimpflug imaging system (de Castro et al., 2007). It consists of a PMMA water cell model, with a spherical PMMA contact lens simulating the cornea and IOL lenses on a XYZ micrometer stage and rotational stage. Nominal values of anterior (7.80 mm), posterior corneal radius (6.48 mm) and central thickness (500 μm) were checked with standard contact lens calibration equipment and corneal topography. Decentration was achieved in the horizontal direction, with a precision of 0.1 mm and ranged from 0 to 1 mm. Tilt of the IOL was achieved in the horizontal direction with a precision of 0.01 degrees, and ranged from 1 to 4 deg. Eye rotation was achieved in the

horizontal direction with a precision of 0.1 degree, and was set constant to 5 deg. Anterior chamber depth was variable with a precision of 0.1 mm, and ranged from 3.5 to 5.5 mm. A total of 31 combinations of the former were tested, by measuring total aberrations with the LRT and simulating aberrations by numerical ray tracing in Zemax for each condition.

3. RESULTS

3.1 Individual geometrical data.

Table 8.1 shows the geometrical data measured for each eye and used in Zemax to simulate the optical aberrations. Relevant terms of corneal topography, anterior chamber depth from optical biometry, IOL power from clinical records, IOL tilt and decentration, 1st Purkinje image shift and eye rotation from Purkinje imaging are listed. Measurement error has not been introduced in the Table 1. The average standard deviations of repeated measurements were 0.27±0.21deg (around x-axis) and 0.35±0.22 deg (around y-axis) for IOL tilt, 0.09±0.07mm (x) and 0.05±0.03mm (y) for IOL decentration, and 0.14±0.11deg (around x-axis), 0.07±0.06 deg (around y-axis) for eye rotation and 0.08 mm for ACD.

3.2 Wave aberrations. Simulations vs real measurements.

Figure 8.3 shows examples of measured (first column) and simulated (column 2-4) wave aberrations in four subjects (eyes #2, #3 ,#6, #11) for 3rd and higher order aberrations (i.e, excluding tilt, defocus and astigmatism), and for a pupil diameter of 5 mm. The second column (Cornea) represents a simulation of the wave aberration of the eye without the IOL, (i.e shows the aberrations of the cornea alone), the third column (Cornea +IOL) shows the total wave aberration of the eye with the IOL assuming that the IOL is perfectly aligned with respect to the pupillary axis, and the forth column (Cornea + IOL Tilt and decentration) represents the total wave aberration of the eye with the IOL tilted and decentered according to the measured tilts and decentrations. In the three cases, the eye is rotated according to angle λ in order to incorporate the line-of-sight misalignment. In general, the corneal wave aberration map shows many of the relevant features of the measured wave aberrations. The similarity is slightly improved when the IOL is included, and marginally further improved in some cases when IOL tilts and decentrations are added.

Comparisons of measured and simulated aberrations were performed using linear correlations between total and simulated Zernike terms, eye by eye. The accuracy of the model as well as the relative importance of each factor (corneal topography, IOL geometry and IOL tilt and decentration) is assessed from the slopes and correlation coefficients of these linear regressions (closest to 1 indicated better prediction). Figure 8.4 shows the linear correlations between measured and simulated Zernike terms (excluding tilt and defocus) for the eyes in Figure 8.3 and the corresponding linear regressions. All data are for 5 mm pupil diameters.

The slope values are shown in Table 2. Ideally, a perfect correlation would have a slope of one. Table 3 shows regression coefficients for the fitted linear regressions in each eye, including astigmatism for the Cornea alone model (A), Cornea + IOL (B) and Cornea + IOL with tilt and decentration (C). Except for one eye (#4) there are significant correlations ($p<0.0001$) with high regression coefficients in all cases, even in the cornea-alone model. The slope decreases when the IOL is incorporated (from case A to case B), found in 9 of 12 eyes is indicative of the corrective effect of IOL (with an aspheric design to counteract the positive spherical aberration of the cornea). Predictions are improved (the slope gets closer to one) when real tilt and decentration of the IOL are included in the model in 6 of the eyes. We did not find a significant correlation between the amount of improvement with tilt and decentration and the magnitudes of tilt and decentration.

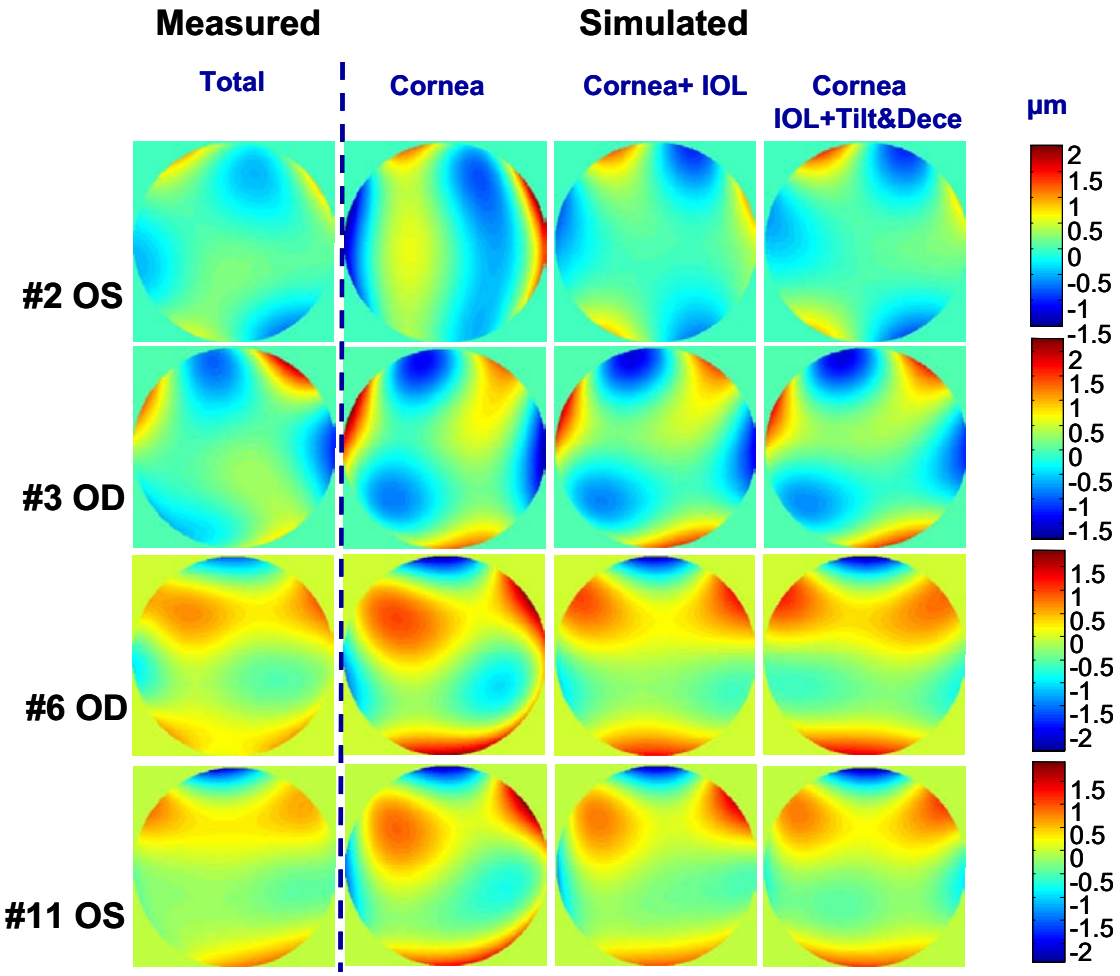

Figure 8.3. Examples of measured and simulated wave aberrations in four eyes for 3rd and higher order aberrations First Column: Measured aberration with Laser ray tracing. Second column: Simulated aberrations with the cornea only (rotated by angle λ), Third column: Simulated aberrations for the model eye with cornea and the corresponding IOL design, Fourth column: Simulated aberrations for the model eye with cornea and IOL introducing the measured tilt and decentration.

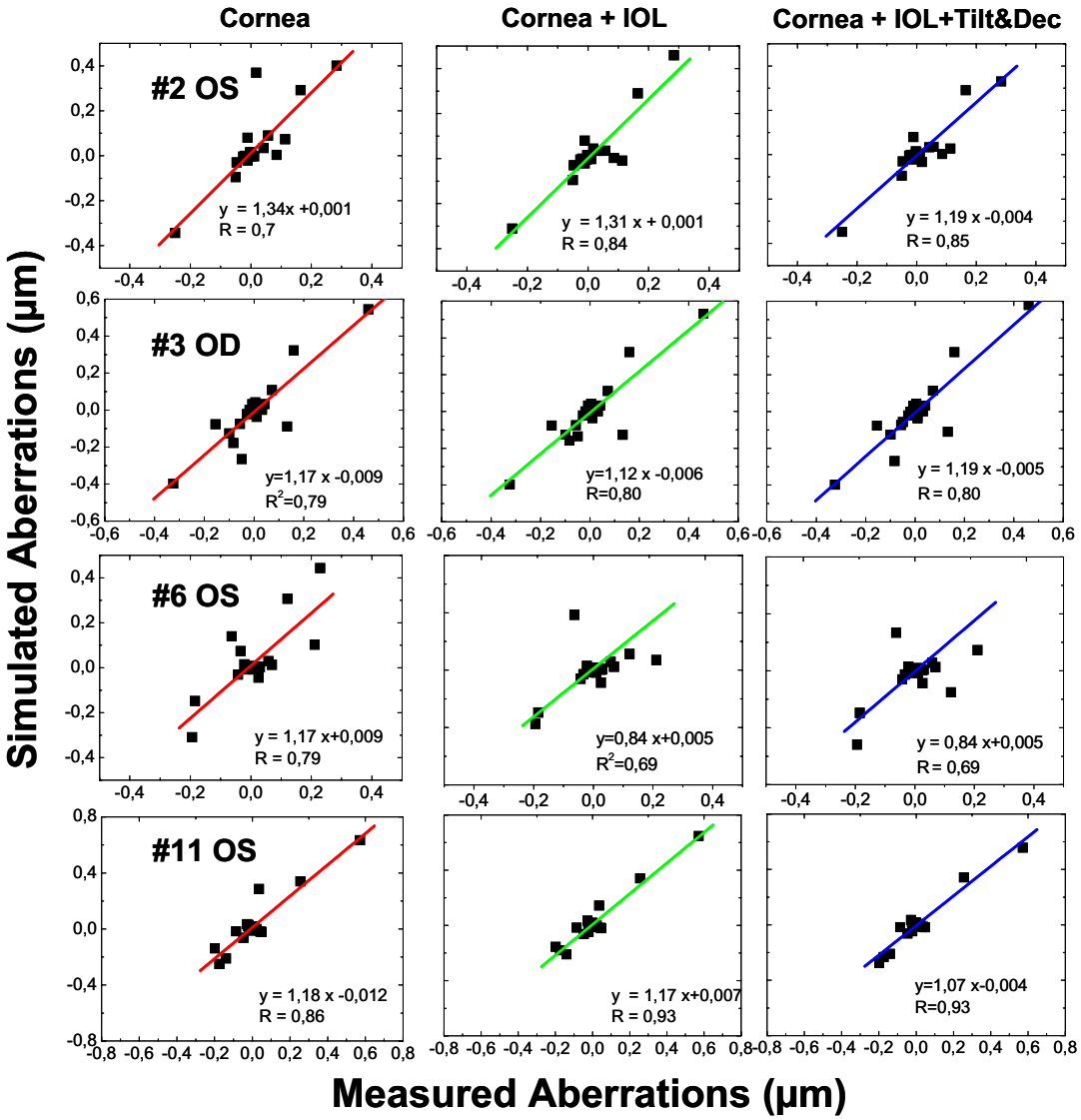

Figure 8.4. Linear correlations between measured and simulated aberrations (only cornea, first column; cornea and IOL, second column; cornea and IOL introducing tilt and decentration, third column), for the examples of Fig. 3. All Zernike terms (except for defocus and tilt) are included. Data are for 5 mm pupil diameters.

Table 8.2. Slopes of the linear correlation between measured and simulated Zernike coefficients, for each eye (including astigmatism)

	SUBJECT/EYES											
	S1		**S2**		**S3**		**S4**	**S5**		**S6**		**S7**
	#1 (OD)	#2 (OS)	#3 (OD)	#4 (OS)	#5 (OD)	#6 (OS)	#7 (OD)	#8 (OD)	#9 (OS)	#10 (OD)	#11 (OS)	#12 (OD)
A[a]	1.28	1.34	1.17	0.67	0.88	1.17	1.34	1.74	2.10	1.48	1.12	2.51
B[b]	0.93	1.31	1.12	0.15	0.85	0.84	1.34	1.72	2.07	1.51	1.11	2.54
C[c]	0.94	1.20	1.19	-0.02	0.81	0.89	1.34	1.88	2.13	1.53	1.07	2.19

a.- Simulated aberrations with only cornea
b.- Simulated aberrations with cornea and IOL
c.- Simulated aberrations with cornea and IOL with tilt and decentration

Table 8.3. Regression coefficients of the linear correlation between measured and simulated Zernike coefficients for each eye (including astigmatism)

	SUBJECT/EYES											
	S1		**S2**		**S3**		**S4**	**S5**		**S6**		**S7**
	#1 (OD)	#2 (OS)	#3 (OD)	#4 (OS)	#5 (OD)	#6 (OS)	#7 (OD)	#8 (OD)	#9 (OS)	#10 (OD)	#11 (OS)	#12 (OD)
A[a]	0.73	0.84	0.89	0.49	0.73	0.79	0.98	0.92	0.93	0.87	0.93	0.78
B[b]	0.76	0.92	0.90	0.14	0.80	0.69	0.99	0.93	0.93	0.90	0.97	0.80
C[c]	0.69	0.92	0.90	-0.02	0.73	0.71	0.98	0.90	0.93	0.92	0.96	0.79

a.- Simulated aberrations with only cornea
b.- Simulated aberrations with cornea and IOL
c.- Simulated aberrations with cornea and IOL with tilt and decentration

The average values for the slopes across the 12 eyes, including astigmatism, were 1.4±0.51 (Cornea), 1.29±0.63 (Cornea + IOL), 1.26±0.62 (Cornea + IOL Tilt and decentration). While the correspondence between simulated and measured aberration coefficients is good in most eyes, there is an overestimation of the simulated coefficients as compared to the measured ones, particularly in eyes #8, #9, #10 and #12. We have repeated the correlation analysis excluding astigmatism and found average values for the slopes of 0.82±0.33 (Cornea), 1.07±0.5 (Cornea + IOL), 1.1±0.45

(Cornea + IOL Tilt and decentration). In general, we found smaller slopes and closer to 1 when astigmatism is not included.

3.3 Individual Zernike coefficients.

We compared measured and simulated individual Zernike coefficients. Correlations between simulated and measured astigmatism are high (r= 0.97± 0,33 for astigmatism at 0/90 deg, Z_2^2, and 0.88 ± 0,2 for oblique astigmatism, Z_2^{-2}). There is a consistent overestimation of the simulated astigmatism by 17.3% for Z_2^2 and by 8.7% for Z_2^{-2}, with respect to the real measurements. The results for the cornea alone are similar to those with the model with the IOL (either lined up or tilted/decentered), indicating that the cornea is the only source of astigmatism in pseudophakic eyes, and IOL tilt and decentration play a negligible role in the post-operative astigmatism. Figure 5 shows 4th order spherical aberration for the simulated and real eyes. Data are for 5 mm pupil diameter, except for subjects #4 and #12 with a pupil diameter of 4 mm. The presence of the aspheric IOL reduces the spherical aberration of the eye, with respect of that of the cornea in all eyes, as previously reported (Barbero et al., 2003). As revealed by both the simulations and real measurements, eyes with the highest amounts of corneal spherical aberration present the highest amount of total spherical aberration (eyes #8 and #9).

However, eyes with similar amounts of corneal spherical aberration (for example #4 and #6) may result in very different total spherical aberration (positive in eye #4 and negative in #6) depending on other anatomical factors, as revealed by both the simulations and real measurements. In general, the eye model predicts the individual variability across eyes and captures the individual trends for spherical aberration found in each eye.

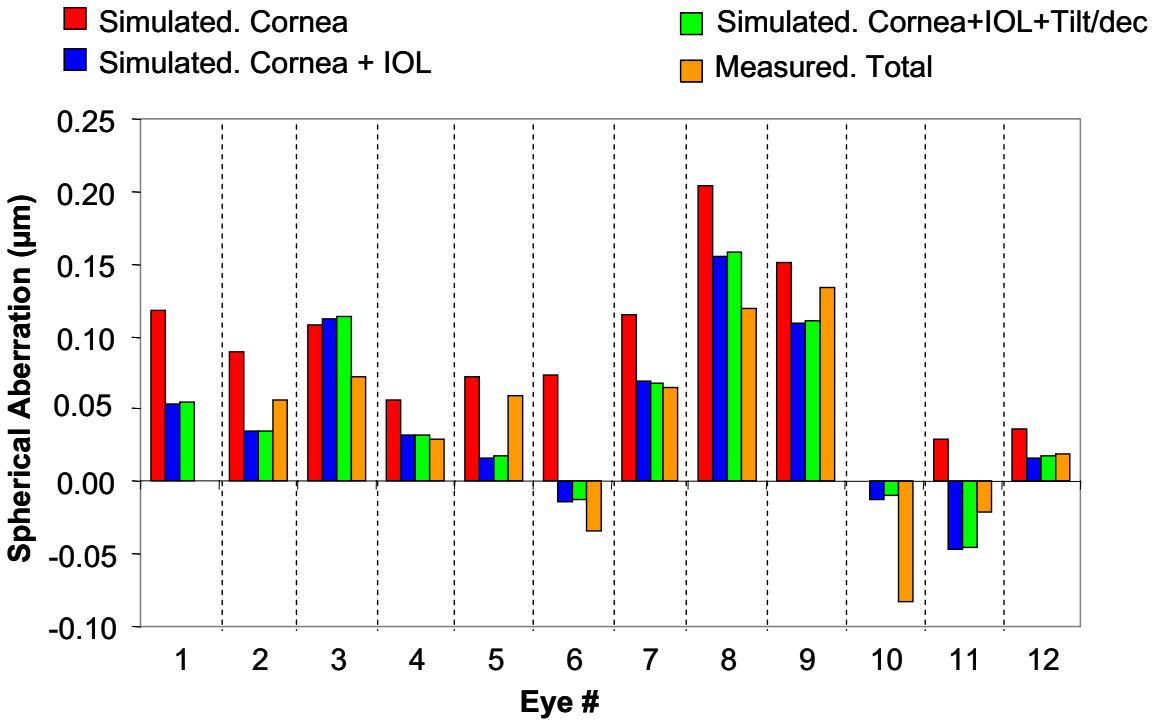

Figure 8.5. 4th order spherical aberration for the simulated and real eyes.

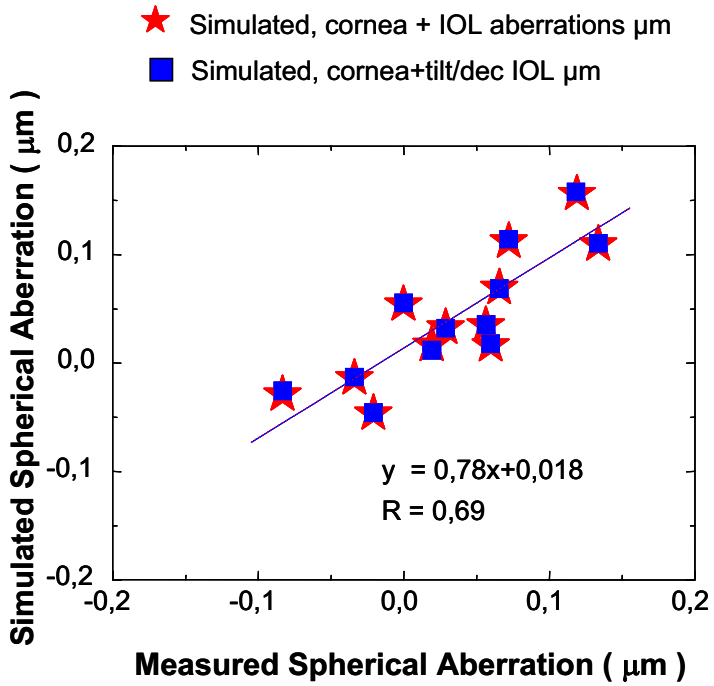

Figure 8.6. Simulated vs measured spherical aberration, for all eyes.

Figure 8.6 demonstrates a high correlation between the simulated spherical aberration of the complete eye model versus the experimental data in Figure 5. The spherical aberration is also close to zero, as expected from the intended design of the aspheric IOL. The simulations also indicate that presence of IOL tilt and decentration does not affect total spherical aberration.

Figure 8.7 shows horizontal coma for the simulated and real eyes. Horizontal coma is reduced in all eyes with respect to corneal values, as shown by both simulated and real data (with a decrease between 5% and 35%). Right/Left eye mirror symmetry is found for the cornea in all pairs of eyes, with negative coma in right eyes and positive in left eyes. This symmetry is found only in three out of the five pairs of eyes for total coma. While the effect of the IOL to reduce the corneal horizontal coma is already captured with the model with centered IOLs, incorporating the actual amounts of IOL tilt and decentration improves the accuracy of the model in 7 out the 12 eyes, and the trends are captured in all eyes except #6 and #9, where the shift of coma when tilt and decentration are incorporated goes in different directions in simulated and real data. Interestingly, in most eyes (1, 2, 3, 5, 10, 11 & 12) the presence of tilt and decentration not only is not associated with larger amounts of horizontal coma, but this is further reduced (10%) with respect to a centered lens.

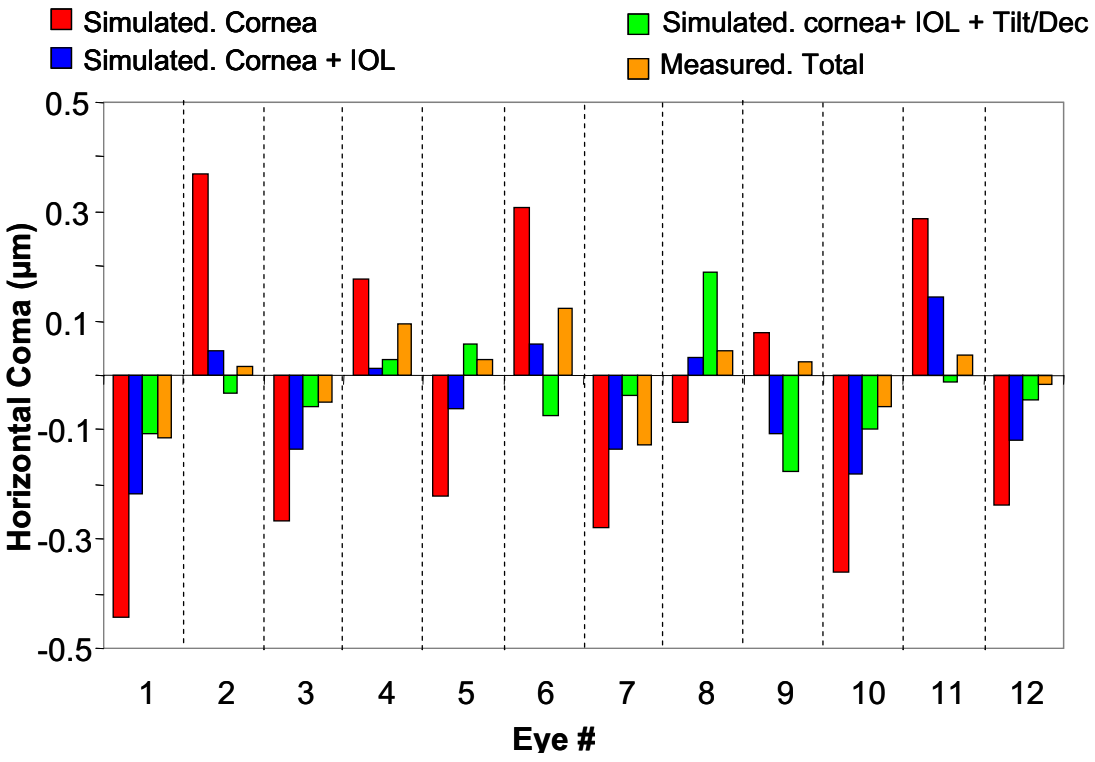

Figure 8.7. Horizontal coma obtained for the simulated and real eyes.

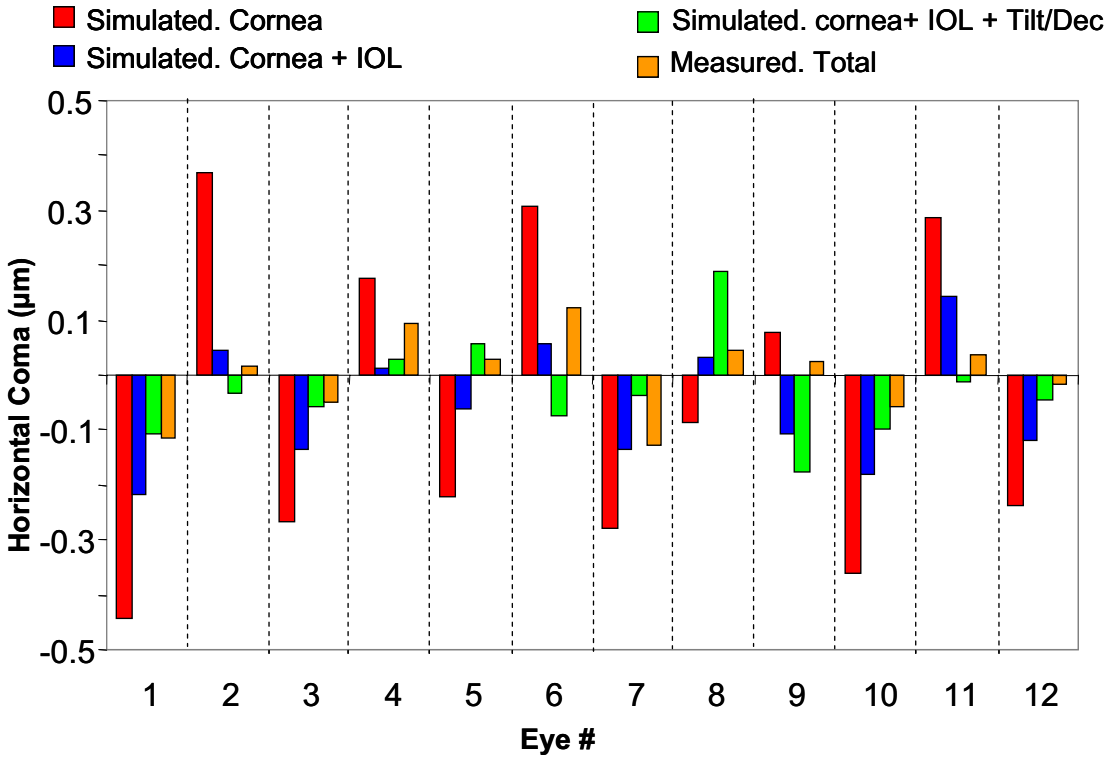

Figure 8.8. Vertical Trefoil obtained for simulated and real eyes.

Figure 8.8 shows vertical trefoil for all eyes. This is a relevant aberration, which has been shown to be induced in the cornea by cataract surgery. The correlation between experimental vs simulated data is significant both for vertical (slope=1 r=0.58±0.15 p=0.05), and horizontal trefoil (slope=1.25 r=0.74±0.15 and p=0.003). The discrepancies are larger for vertical than for horizontal trefoil, although we could not find a systematic over or underestimation from the model with respect to real measurements.

4. DISCUSSION

We have presented a customized computer eye model, using individual geometrical data in eyes with intraocular lenses, which reproduces the wave aberrations measured in the same eyes. We have evaluated the contribution of the different factors (corneal topography, IOL geometry, IOL misalignments, eye rotation) to the wave aberration and demonstrated the interactions between those that result in the measured ocular aberrations. The study of the accuracy and limitations of the model is important to address further applications. The detailed evaluation of the relative contributions of anatomical factors to global optical quality in eyes with IOLs is important for the improvement of IOL design and surgical strategies.

4.1 Validation of the eye model and limitations.

We have found a good correspondence between simulated and measured aberrations. The accuracy of the prediction is in general improved when IOL geometry and actual measurements of IOL tilt and decentration are incorporated. While the correlations are high in all eyes but one (coefficients of correlation of 0.78 on average), the overall predicted aberrations seem to overestimate slightly the measured values, with an average slope (predicted vs measured) of 1.22 across all eyes (see Table 2), particularly when astigmatism is included. This overestimation seems also to occur in a recent study by Tabernero et al. (Tabernero, Piers, Benito, Redondo & Artal, 2006) on eyes with spherical (n=3) and aspheric IOLs (n=4), where a correlation pooling Zernike coefficients (including astigmatism) of all eyes (rather than studying eye by eye) yielded a slope of 0.89 (measured vs predicted). For the spherical aberration term, neither Barbero (Barbero et al., 2003), Tabernero (Tabernero, et al, 2006) or our study show a systematic deviation.

Our model uses a generic posterior corneal spherical surface. Other customized models (Barbero et al., 2003) used one-surface cornea. However, contributions of the posterior corneal shape to corneal astigmatism in particular have been shown. In general it has been found that astigmatism arising from the corneal surface is reduced by astigmatism of the opposite sign arising from the posterior corneal surface (Dubbelman, Sicam & van der Heijde, 2006, Dunne, Royston & Barnes, 1991, Prisant, Hoang-Xuan, Proano, Hernandez, Awad & Azar, 2002). A study by Dunne et al (Dunne, Royston & Barnes, 1991) in a group of 60 young subjects (mean age 22.04±-3.24 years old) showed that the toricity of the posterior corneal surface, if it was purely governed by that of the anterior surface, would produce a reduction of total corneal astigmatism of about 5%, however, if the additional toricity of the posterior cornea was taken into account, total corneal astigmatism would be reduced by approximately 14%. Dubbelman (Dubbelman et al., 2006) using Scheimpflug imaging on 114 subjects, ranging in age from 18 to 65 years, showed that the astigmatism of the posterior corneal surface compensates the astigmatism of the anterior corneal surface by 31%. These results are consistent with our findings comparing total and simulated astigmatism .

Other than the simplified posterior corneal surface, the origin of systematic changes could arise from some assumptions in our model regarding the corneal refractive index (rather than a more complex gradient index of refraction (Barbero, 2006)) or the use of simplified spherical posterior corneal surface (rather than using the actual posterior corneal topography) or deviations associated with the techniques themselves. We verified that simulated aberrations did not deviate systematically from real aberrations in the artificial physical model eye described in Section 2.2.6, for which all geometrical and optical properties (including posterior “corneal” shape and index of refraction) are known. Correlations between simulated and measured Zernike terms yielded a slope of 1.03 on average (averaging across 31 different configurations of the physical model eye). This result suggests that there are not systematic errors associated to the aberration measurement technique neither in the computer eye modeling algorithms. Other sources of discrepancies between simulated and real aberrations can come from errors in the ACD measurement with the IOLmaster, which have been reported to be higher in aphakic eyes (Kriechbaum, Findl, Kiss, Sacu, Petternel & Drexler, 2003), or slight pupil shifts (between the LRT measurement and the Purkinje pupillary image), along with experimental errors of IOL tilt and decentration, corneal topography and aberrometry. We have estimated the standard deviation of the simulated aberrations, based on typical

measurement variability of corneal topography, ACD and geometrical measurements (angle λ, tilt and decentration). We found a standard deviation of 0.0047 μm for the simulated spherical aberration and and 0.005 μm for 3rd and higher order RMS. These values are smaller than the standard deviations of real aberration measurements (0.02 μm and 0.03 μm respectively).

The customized computer eye model relies on the correct location of the optical surfaces of the ocular components with respect to the reference axes of the eye. We have used the location of the 1st Purkinje image for foveal fixation to obtain the angle λ. Tilt and decentration were obtained from Purkinje images obtained with eccentric illumination. Comparisons of the locations of PI, PIII and PIV from real images and simulations using the customized eye models for foveal fixation verified that the relative alignment of ocular surfaces was correct (see Figure 8.2). An assumption in our model is that the shift of the 1st Purkinje image from the pupil center for foveal fixation is solely due to the tilt of the line of sight with respect to the videokeratoscopic axis, while a pupil decentration may also occur. The contributions of each to the shift of 1st Purkinje image cannot be separated in our measurements and therefore cannot be separately introduced in the model. Our previous computer eye model with IOLs (Barbero et al., 2003) did not incorporate angle λ, and the recent study by Tabernero (Tabernero et al., 2006) seems to have attributed all the shift of videokeratoscopic axis to lateral decentration. We repeated the simulations for all 12 eyes assuming just decentration and obtain little differences in terms of the metrics used to assess the accuracy of the model (an average slope of 1.18 and a regression coefficient of 0.77).

4.2 Relative contribution of cornea, IOL geometry and misalignment to eye rotation to ocular aberrations.

The measurement of ocular aberrations in pseudophakic eyes allow assessment of the overall optical performance (Barbero et al., 2003). The use of customized model eyes with individual geometrical data of the eyes, in combination with the actual measurements of ocular aberrations can be used to identify the relative importance of each factor. Our results show that 70% of the variance of ocular aberrations in eyes with aspheric IOLs can be predicted just from the cornea. Given the changes induced by small-incision cataract surgery on corneal aberrations (see Chapter7) the actual post-operative corneal elevation should be used in the model. The use of individual posterior

corneal topography would likely further improve the accuracy of the model particularly for astigmatism and perhaps trefoil. The aspheric geometry of the IOL plays an important role in balancing corneal spherical aberrations. The customized eye model also helps to understand the different amounts of spherical aberration compensation found in different eyes, even for similar amounts of corneal spherical aberration. The eye rotation introduced in the model to compensate the videokerastoscope-line-of sight misalignment appears to be the cause of compensation of off-axis horizontal coma, as previously reported in normal young eyes (Tabernero, Piers, Benito, Redondo & Artal, 2006). Both the simulated and real measurements of our study suggest that this effect also happens in pseudophakic eyes with aspheric IOLs. In addition, the customized eye model has revealed that IOL tilt and decentration play a very limited role in the overall aberrations (predicting less than 2.2% of the variance), at least in this group of eyes. Higher amounts of tilts and decentrations, accounted for separately, are uncorrelated to higher amounts of relevant aberrations such as coma, confirming previous suggestions that the actual combinations of tilt, decentration, and also eye rotation are essential, and simulations using simple eye models are insufficient (Barbero et al., 2003). In fact, we have found that in 7 of the 12 eyes of this study the presence of tilt and decentration of the IOL actually results in further compensation of the off-axis coma.

Balance of corneal horizontal coma by internal optics in eyes with intraocular artificial lenses: Evidence of a passive mechanism.

9

9. Balance of corneal horizontal coma by internal optics in eyes with intraocular artificial lenses: Evidence of a passive mechanism

This chapter is based on the article by Marcos. S et al., *"Balance of corneal horizontal coma by internal optics in eyes with intraocular artificial lenses: Evidence of a passive mechanism"* Vision Research, *In Press*. Coauthors of the study are P. Rosales, L.Llorente, S.Barbero, I. Jiménez-Alfaro. The contribution of Patricia Rosales to the study was to measure tilt and decentration, angle lambda and experimental aberrations (together with Lourdes Llorente) in patients with intraocular lenses and to perform computer simulations using customized computer model eyes.

RESUMEN

Objetivos: Investigar el carácter activo o pasivo de la compensación del coma horizontal empleando ojos pseudofákicos, en los que un mecanismo activo no puede estar presente.

Métodos: Se midieron las aberraciones totales y corneal, inclinación y descentramiento de la lente intraocular en un grupo de 38 ojos implantados con dos tipos de lentes intraoculares diseñadas para compensar la aberración esférica corneal del promedio de la población, tanto a nivel de población como a nivel individual.

Resultados: Encontramos una compensación promedio del 66% para la aberración esférica y del 87% para el coma horizontal. La aberración esférica no aparece compensada a nivel individual, pero sí el coma horizontal (con unos coeficientes de correlación entre la aberración corneal/interna: -0.946, $p<0.0001$). El hecho de que el coma horizontal corneal (no el total) está altamente correlacionado con el ángulo lambda (obtenido a partir del desplazamiento de la primera imagen de Purkinje del centro de la pupila, para fijación foveal, indica que esta compensación procede primordialmente de la configuración geométrica del ojo, que genera coma horizontal de signos opuestos en al cornea y la óptica interna. La cantidad y dirección de inclinación y descentramiento de las lentes son comparables a los encontrados en ojos jóvenes, y en promedio tienden a compensar (mas que incrementar) el coma horizontal. Las simulaciones empleando modelos de ojo con diferentes diseños de lentes intraoculares, muestran que, mientras no todos los diseños producen una compensación del coma horizontal, un amplio rango de diseños asféricos biconvexos pueden producir una compensación comparable a la encontrada en ojos jóvenes con cristalino, sobre un campo de visión relativamente amplio.

Conclusiones: Los resultados obtenidos sugieren que la forma de la lente, el gradiente de índice y la posición de la fóvea no han de estar

sintonizados para conseguir una compensación del coma horizontal. Estos resultados no excluyen una sintonización en la orientación del cristalino, ya que la cirugía de cataratas parece preservar la posición de la cápsula.

ABSTRACT

Purpose: In this study we investigate the active or passive nature of the horizontal coma compensation using eyes with artificial lenses, where no active developmental process can be present.

Methods: We measured total and corneal aberrations, and lens tilt and decentration using the Purkinje imaging system in a group of 38 eyes implanted with two types of intraocular lenses designed to compensate the corneal spherical aberration of the average population, both at the population and individual level.

Results: We found that spherical aberration was compensated by 66%, and horizontal coma by 87% on average. The spherical aberration is not compensated at an individual level, but horizontal coma is compensated individually (coefficients of correlation corneal/internal aberration: -0.946, $p<0.0001$). The fact that corneal (but not total) horizontal coma is highly correlated with angle lamda (computed from the shift of the 1st Purkinje image from the pupil center, for foveal fixation) indicates that the compensation arises primarily from the geometrical configuration of the eye (which generates horizontal coma of opposite signs in the cornea and internal optics). The amount and direction of tilts and misalignments of the lens are comparable to those found in young eyes, and on average tend to compensate (rather than increase) horizontal coma. Computer simulations using customized model eyes and different designs of intraocular lenses show that, while not all designs produce a compensation of horizontal coma, a wide range of aspheric biconvex designs may produce comparable compensation to that found in young eyes with crystalline lenses, over a relatively large field of view.

Conclusions: These findings suggest that the lens shape, gradient index or foveal location do not need to be fine-tuned to achieve a compensation of horizontal coma. Our results cannot exclude a fine-

tuning for the orientation of the crystalline lens, since cataract surgery seems to preserve the position of the capsule.

1. INTRODUCTION

The relative contribution of the cornea and crystalline lens to the overall ocular wave aberration is a relevant question in both the basic study of human eye optical quality and clinical ophthalmic applications. As presented in Section 4 of the Introduction, it is known that there are differences in the aberrations of the ocular components and their interactions between different refractive groups (myopic, emmetropic and hyperopic eyes) due to the different geometrical properties of these eyes (Artal, Benito & Tabernero, 2006, Coletta, Han & Moskowitz, 2006, Llorente, Barbero, Cano, Dorronsoro & Marcos, 2004) as well as the fact that the structural properties of the crystalline lens (Dubbelman & Heijde, 2001, Glasser & Campbell, 1998), and the cornea to a lesser extent (Dubbelman, Sicarn & Van der Heijde, 2006) change over time, leading to a significant increase of the aberrations with age (Applegate, Donnely, Marsack, Koenig & Pesudovs, 2007, Artal, Berrio, Guirao & Piers, 2002, Calver, Cox & Elliott, 1999, Mclellan, Marcos & Burns, 2001). On the other hand, refractive and intraocular corrections change the natural structure of the ocular components: corrections with contact lenses (particularly rigid gas permeable) alter the relative contribution of the ocular components to retinal image quality and individual interactions of aberrations play a role on their optical performance (Dorronsoro, Barbero, Llorente & Marcos, 2003); corneal refractive surgery modifies corneal shape and therefore corneal aberrations (Applegate & Howland, 1997, Marcos, Barbero, Llorente & Merayo-Lloves, 2001); and in cataract surgery the crystalline lens is replaced by intraocular lenses which specific design (spherical or aspheric), in combination with the optics of the other components of the eye (cornea), determines the final optical quality of the eye (Barbero, 2003, Marcos, Barbero & Jiménez-Alfaro, 2005).

Although the magnitude and distribution of ocular aberrations differ substantially across subjects, a balance of corneal aberrations by internal optics, resulting in smaller ocular aberrations than those of the individual ocular components appears to be a common trend in young eyes. Several studies have shown that the spherical aberration of the cornea is generally positive, while that of the crystalline lens is negative, reducing the total spherical aberration of the eye (Artal & Guirao, 1998, Barbero, Marcos & Merayo-Lloves, 2002, El Hage & Berny, 1973, Glasser & Campbell, 1999, Sivak & Kreuzer, 1983, Smith, Cox, Calver & Garner, 2001, Tomlinson, Hemenger & Garriott,

1993). More recent studies have also shown a reduction of corneal third-order coma by internal optics in young eyes (Artal et al., 2001, Coletta et al., 2006, Kelly, Mihashi & Howland, 2004). The contribution of the posterior surface of the cornea to this compensation seems to be practically negligible (Dubbelman, Sicam & van der Heijde, 2007) and therefore the crystalline lens appears to be the major responsible of the effect. This corneal/internal balance of spherical aberration and coma has been shown to get disrupted in older eyes (Artal et al., 2002), presumably because of structural changes in the crystalline lens, producing the reported increase of aberrations with age.

The question whether the corneal/internal compensation arises from a passive mechanism or through an active developmental feedback process has been debated. Similarly to the emmetropization process that leads ocular growth to emmetropia by actively adjusting eye length to the optical power of the cornea and crystalline lens, it has been suggested that high order aberrations may equally "emmetropize", by tuning the geometry of the ocular surfaces, gradient index distribution or position to achieve optimal image quality. A cross-sectional study in humans from age 5 (Brunette, Bueno, Parent, Hamam & Simonet, 2003) and longitudinal studies in animal models (García de la Cera, Rodriguez & Marcos, 2006, Kisilak, Campbell, Hunter, Irving & Huang, 2006) show a decrease of aberrations during development. While it has been suggested that visual feedback cannot be excluded from playing a role in an active compensation of aberrations (Kisilak et al., 2006), a decrease of aberrations (coma in particular) occurs in chicks during the first two weeks post-hatching, even in eyes occluded with diffusers, and therefore with no visual feedback (García de la Cera et al., 2006), suggesting a passive mechanism. In fact, a simple geometrical model of the growing eye can predict an improvement of optical quality with age, for a constant pupil size (Howland, 2005).

Kelly et al (Kelly et al., 2004) in a study involving 30 normal young human eyes, found a significant average corneal/internal compensation of horizontal/vertical astigmatism, spherical aberration and horizontal coma. Individually, they did not find a significant correlation between corneal and internal spherical aberration, what led them to suggest that the average compensation of spherical aberration observed was inherent to the geometrical properties of the cornea and the lens and was probably determined over the course of evolution (i.e. due to a passive mechanism). For horizontal coma, however, they found that the compensation occurred individually and suggested an active fine-tuning between the cornea and crystalline lens (i.e. by subtle tilting or decentering of the lens) that would reduce horizontal coma during development.

Artal and collegues (Artal et al., 2006) investigated specifically the compensation of horizontal coma in a group of 73 myopic and hyperopic young eyes. They found that, while corneal horizontal coma typically was larger in hyperopic eyes (showing larger displacements of the pupil center with respect to the corneal reflex), compensation occurred equally in both groups, resulting in similar amounts of ocular horizontal coma. They concluded that compensation resulted from the geometrical structure of the eye, and was primarily a passive mechanism.

The active or passive nature of the compensation mechanism can be investigated using eyes with artificial lenses, which cannot be subject to an active developmental process. We investigated the compensation of horizontal coma in a group of patients that had undergone cataract surgery, with replacement of the crystalline lens by intraocular lenses (IOLs). The IOLs were of two different types, with aspheric anterior and posterior surfaces, respectively, producing negative internal spherical aberration, aiming at compensating the average spherical aberration of the cornea. The comparison of the compensation of horizontal coma in these eyes with that reported in previous studies in normal eyes will shed light into the nature of the compensation mechanism.

2. METHODS

2.1 Subjects

A total of 38 eyes from 21 patients participated in the study. All patients had undergone uneventful cataract surgery (phacoemulsification with 3.2-mm superior clear corneal incision) at least two months before the measurements. In all cases, the implanted IOLs had an aspheric design producing negative internal spherical aberration. The IOLs were either Tecnis (Advanced Medical Optics), with aspheric anterior surface (Group 1, n=18) or Acrysof IQ (Alcon Research Laboratories), with aspheric posterior surface (Group 2, n=20). Table 1 summarizes the profile of the eyes of the study. The experimental protocols were approved by Institutional Review Boards and met the Declaration of Helsinki. All subjects signed an Informed Consent Form after the nature of the study and potential consequences had been explained.

Table 9.1. Eyes' profile

	Group 1 (n=18) Tecnis	**Group 2 (n=20) Acrysof IQ**
Age (yr)	63.77±15.20	72.07±3.27
# males / # females	13/7	12/6
# patients / # eyes	11/20	10/18
# OD / # OS	11/9	9/9
Pre-operative spherical error (D)	-1.75±3.21	-1.41± 2.66
Axial length	23.28 ± 0.89	23.20±0.87
IOL power (D)	21.15±3.75	20.60±2.02

2.2 Corneal aberrations

The anterior corneal elevation was obtained using a Placido disk videokeratoscope (Humphrey-Zeiss MasterVue Atlas), for a 10-mm area centered at the corneal reflex. Corneal elevations were exported as a grid sag surface to a computer eye model programmed in an optical design software (Zemax). Corneal aberrations were computed assuming a spherical posterior corneal surface of 6.5 mm radius, a corneal refractive index of 1.376, and a wavelength of 786 nm. Computations were done referred to the pupil center, and accounting for the misalignment between the videokeratoscopic axis and the line of sight, i.e, with a field angle for incoming rays accounted for by the displacement of the 1st Purkinje image with respect to the pupil center, assuming a center of rotation 15 mm behind the cornea. As a control, corneal aberrations were also computed assuming a lateral shift of the reference, rather than a rotation. Corneal wave aberrations were obtained for the maximum pupil diameter available in total wave aberrations in the same patients. Corneal wave aberrations were fit to 7th order Zernike polynomials, and the OSA standards for reporting aberrations were followed. Third order horizontal coma (Z_3^1) and 4th order spherical aberration (Z_4^0) were reported.

Pre- and post-operative anterior corneal aberrations had already been reported on this group of eyes (part of a larger sample of 43 eyes), that had participated in the study on incision-induced corneal aberrations presented in Chapter 7 (Marcos, Rosales, Llorente & Jimenez-Alfaro, 2007). The corneal aberrations previously reported differ on those reported here in several aspects: they had been calculated using the corneal reflex as a

reference and they referred to anterior corneal aberrations assuming no posterior corneal surface, and a refractive index of 1.3367.

2.3 Total aberrations measurements

Total wave aberrations were measured using a second generation laser ray tracing (LRT), which was developed at the Instituto de Óptica (CSIC) in Madrid, Spain (Llorente et al., 2004). The technique has been described in Chapter 1 and Chapter 8, and validated in several publications of the Visual Optics and Biophotonics Lab (Llorente, Diaz-Santana, Lara-Saucedo & Marcos, 2003, Marcos, Díaz-Santana, Llorente & C., 2002, Moreno-Barriuso, Marcos, Navarro & Burns, 2001).

In this study, measurements were done under mydriasis (1 drop 1% tropicamide). Pupil diameters ranged from 4 to 6 mm, and the sampling pattern (with 37 samples in a hexagonal configuration) was adjusted by software to fit the natural pupil. Spherical error was corrected by means of a Badal focusing system. Total wave aberrations were fit to 7^{th} order Zernike polynomials, and the OSA standards for reporting aberrations (Applegate, Thibos, Bradley, Marcos, Roorda, Salmin & Atchison, 2000) were followed. Third order horizontal coma $Z_3^{\ 1}$ and 4^{th} order spherical aberration $Z_4^{\ 0}$ were reported.

Internal aberrations were obtained by subtraction of total minus corneal aberrations.

2.4 Angle λ, IOL tilt and decentration

IOL tilt and decentration were measured with a custom developed Purkinje imaging system described and experimentally validated elsewhere (de Castro, Rosales & Marcos, 2007, Rosales & Marcos, 2006, Rosales & Marcos, 2007). (See Chapter 2 for a comprehensive description of the method and page 56 and Figures 2.6 and Table 8.1 for a detailed description of the sign convention).

The Purkinje imaging system was also used to estimate the relative shift of the corneal reflex (first Purkinje image) with respect to the pupil center for foveal fixation, and angle λ was calculated as described elsewhere (Rosales & Marcos, 2007). Additionally, the Purkinje imaging system has channel for phakometry measurements (Rosales, Dubbelman, Marcos & Van der Heijde, 2006, Rosales & Marcos, 2006).

Measurements of lens tilt and decentration were obtained in dilated eyes, in the same session as total and ocular aberrations. This guaranteed that measurements were not

affected by potential changes of pupil center with pupil size. Optical biometry (with the IOLMaster, Zeiss) was obtained in all eyes, and phakometry (with the phakometry mode of the Purkinje imaging apparatus) was performed when the radii of curvature of the IOL were not known, since those parameters are required to process the data.

Lens tilt and decentrations had already been reported in a subset of 21 eyes (12 patients) who participated in a study comparing IOL tilt and decentration from Scheimpflug and Purkinje imaging (de Castro, Rosales & Marcos, 2007).

2.5 Computer eye modelling

Customized computer eye models in Zemax were used to compare predictions of horizontal coma (with and without IOL lens tilt and decentration) with real measurements. Simulations were performed for 15 eyes from Group 2, for which a full geometrical description was available. A full description of the customized computer eye has been presented elsewhere (Rosales & Marcos, 2007).

2.6 Data analysis

Right and left eyes were included in the study, to test for mirror symmetry, and in view of the fact that surgeries were carried out independently. For average calculations, the sign of horizontal coma was reversed in right eyes (Kelly et al., 2004, Marcos & Burns, 2000, Smolek, Klyce & Sarver, 2002) to account for the enantiomorphism of the right and left eyes. Otherwise, data from left and right eyes are presented without changing signs. The individual compensation of corneal by internal aberrations (spherical aberration and horizontal coma) was tested by means of correlations. Relationships between total and corneal horizontal coma and angle λ, and between angle λ and IOL tilt and decentration (horizontal components) were tested using linear regressions.

Statistical analysis was performed using Matlab: unpaired two-tailed t-tests were used to test the statistical significance of mean differences across Groups 1 and 2; a Wilcoxon signed rank test was used to test the statistical significance of differences across mean total and corneal aberrations (to assess the compensatory role of the internal optics); and a z-test was used to test the statistical significance of correlations. Statistical significance was set to the $p<0.01$ level for all tests.

Finally, both for averages and correlation analysis, corneal and total aberration data were scaled from the maximum pupil size down to 5-mm. Therefore 6 patients from Group 1 and 5 patients from Group 2 with pupil sizes smaller than 5 mm were excluded for this analysis. Angle λ was available from all eyes, whereas IOL tilt and decentration was missing in 3 eyes from Group 1 and 5 eyes from Group 2 (where the third Purkinje image was vignetted by the pupil).

3. RESULTS

3.1 Average compensation

We investigated the compensation of spherical aberration and horizontal coma on the entire sample, and Groups 1 and 2 separately. The mean coefficient values are shown in Table 9.2, for 5-mm pupils (i.e. eyes with pupils smaller than 5-mm pupils were not included).

These results are indicative of a high compensation of the corneal spherical aberration of the average population, in keeping with the intended performance of the aspheric IOL designs. The compensation of the corneal horizontal coma is also highly statistically significant, with average reduction close to 90%. Compensation is slightly higher for Group 1 than 2, although the resulting total aberration is not statistically significantly different across groups.

Table 9.2. Average values of spherical aberration and horizontal coma, for 5-mm pupils

Spherical aberration, Z_4^0 (µm)	**Total**	**Corneal**	**% compensation**	**P value[a]**
Group 1	0.035± 0.07	0.13 ±0.06	73.6	<0.0001*
Group 2	0.041± 0.06	0.096±0.06	57.0	<0.0001*
All eyes	0.038 ± 0.06	0.11±0.06	66.2	<0.0001*
p value[b]	0.79	0.13		
Horizontal coma Z_3^1 (µm)				
Group 1	0.005 ± 0.10	0.11±0.12	94.8	0.0068*
Group 2	0.038± 0.05	0.24±0.19	84.3	<0.0001*
All eyes	0.023±0.08	0.18±0.17	87.3	<0.0001*
p value[b]	0.30	0.033*		

Group 1, n=12; Group 2, n=15; All eyes, n=27.

A p-value, indicating significant compensation (*), for Wilcoxon signed rank test.

B p-value, indicating significant differences across groups (*), for unpaired two-tailed t-test.

3.2 Individual compensation

Individually, 16 eyes from 18 in Group 1 and 18 eyes from 20 in Group 2 showed a reduction of corneal spherical aberration. In two eyes, with almost zero or negative corneal spherical aberration there was a shift of the spherical aberration toward negative values (with a larger absolute total than corneal aberration). In 11 eyes from 18 in Group 1 and 20 eyes from 20 in Group 2 there is a reduction of the absolute value of horizontal coma. In 4 eyes from Group 1 there is an overcompensation of horizontal coma, which resulted in larger absolute total than corneal aberration.

Quantitative analysis of compensation of spherical aberration and horizontal coma on an individual basis was performed by testing for linear correlations between internal and corneal values for these aberrations. Figure 9.1 shows internal versus corneal spherical aberration, for 5-mm pupils (only eyes with pupil diameters of 5-mm and larger are therefore included). In most eyes, internal spherical aberration is negative. Although the IOLs are nominally designed to exhibit a constant negative spherical aberration (for a specific model eye), there is a significant scattering in the internal spherical aberration . These differences arise from the fact that estimates of internal aberrations incorporate the effect of ray convergence from the cornea, and therefore they are affected by corneal curvature and anterior chamber depth, which differ across subjects. There is no significant correlation between corneal and internal spherical aberration values, confirming that compensation is not provided at an individual level. Figure 9.2 shows a significant linear negative correlation ($p=0.0035$) between corneal and internal horizontal coma, for 5-mm pupils. The sign of horizontal coma has not been reversed for right eyes (closed symbols). Table 9.3 shows correlation coefficients, p values and slopes for each group and all eyes together for spherical aberration and horizontal coma

A perfect compensation occurs for a slope of –1. No significant correlations were found for spherical aberration, but we found significant correlations for horizontal coma, with slopes of –0.82.

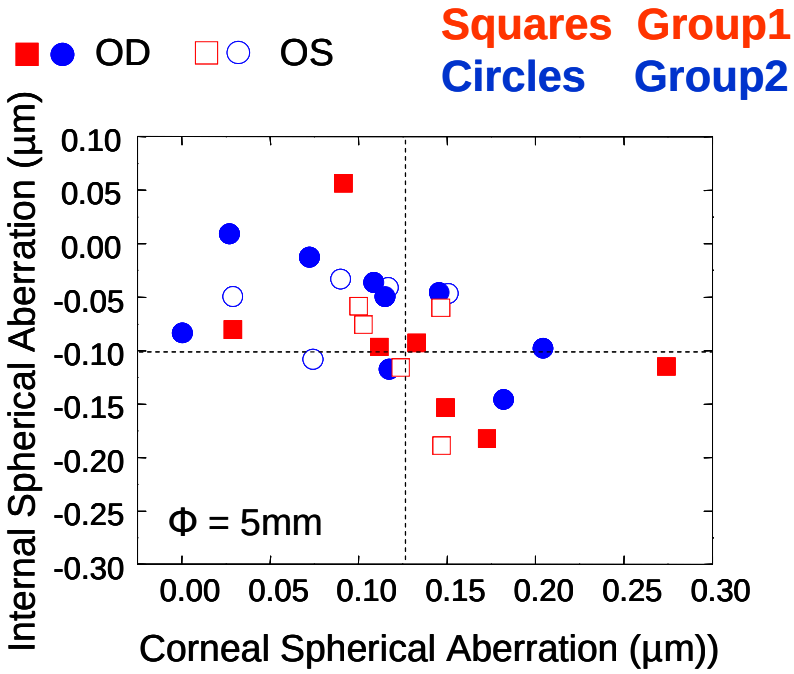

Figure 9.1. Corneal spherical aberration versus internal spherical aberration. Closed symbols stand for right eyes, and open symbols for left eyes. Circles stand for eyes from Group 1 (anterior surface asphericity IOLs) and squares for eyes from Group 2 (posterior surface asphericity IOLs). Data are for 5-mm pupil diameters.

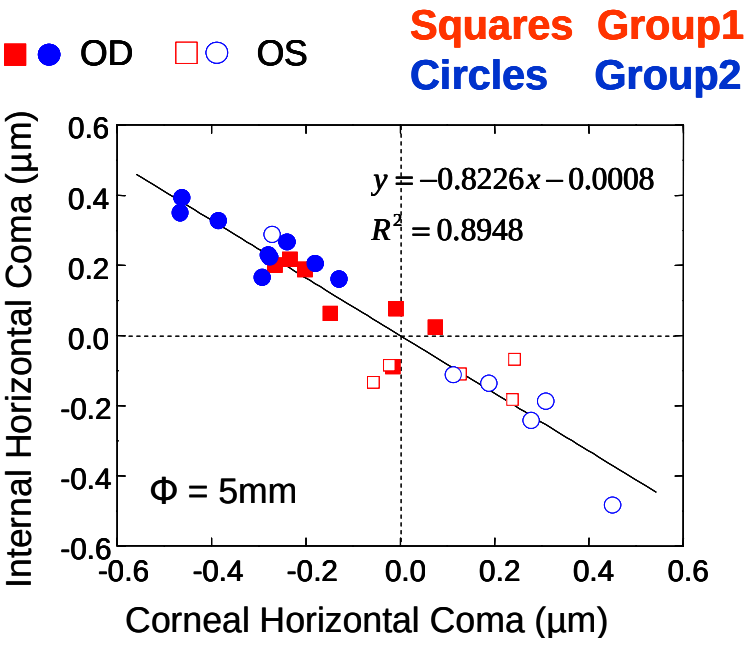

Figure 9.2. Corneal horizontal coma versus internal horizontal coma, showing a significant linear correlation (r=-0.946, p<0.0001). Closed symbols stand for right eyes, and open symbols for left eyes. Circles stand for eyes from Group 1 (anterior surface asphericity IOLs) and squares for eyes from Group 2 (posterior surface asphericity IOLs). Data are for 5-mm pupil diameters.

Table 9.3. Correlations, significance and slopes of the linear regression of corneal and internal coefficients, for spherical aberration and horizontal coma.

Corneal vs Internal Spherical aberration Z_4^0 (μm)	**Coefficient of correlation R**	**p**	**slope**
Group 1	-0.418	0.176	-0.418
Group 2	-0.258	0.395	-0.169
All eyes	-0.423	0.035	-0.347
Corneal vs Internal Horizontal coma Z_3^1 (μm)			
Group 1	-0.799	0.001*	-0.662
Group 2	-0.979	<0.0001*	-0.852
All eyes	-0.946	<0.0001*	-0.819

Group 1, n=12; Group 2, n=15; All eyes, n=27.

3.3 Effect of angle λ

Figure 9.3 shows the shift of the Purkinje image (horizontal and vertical coordinates) with respect to the pupil center measured in all eyes of the study (circles and squares). On the same plot we have superimposed (broken symbols and squares) the estimated angle of rotation of the model eye (customized to each patient) needed to achieve the measured 1st Purkinje image shift (related to angle λ). As expected, there is mirror left/right eye symmetry in the horizontal coordinates of Purkinje shift and angle λ. There are significant differences ($p<0.0001$, unpaired t-test) in the mean horizontal 1st Purkinje shift (or angle λ) between Groups 1 and 2 (0.17 mm or 1.34 deg, and 0.43 mm or 3.52 deg, on average, respectively), which explains the significant difference in corneal horizontal coma (Table 2).

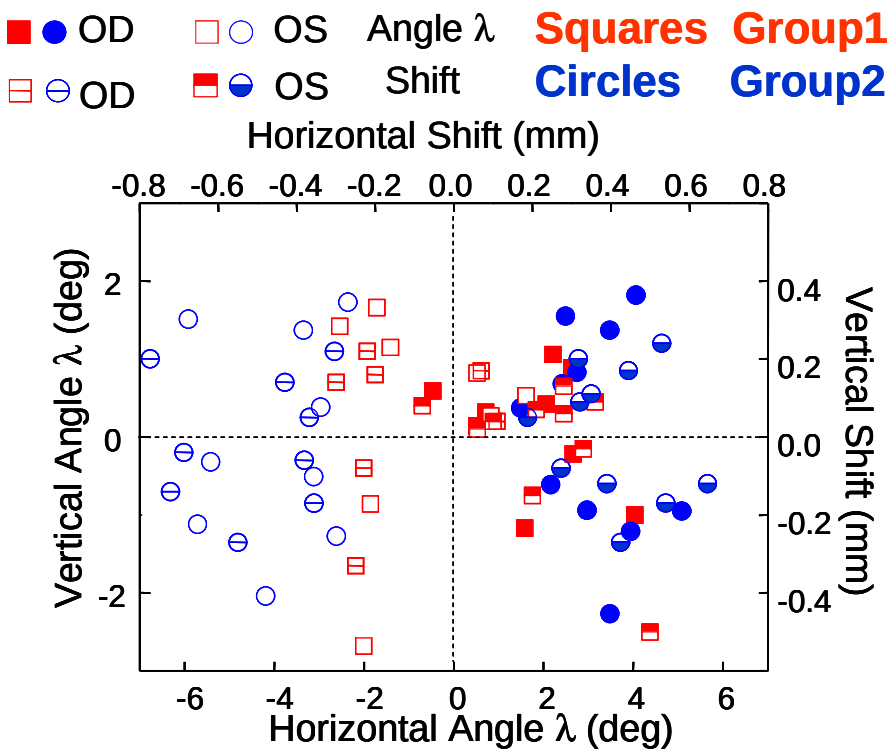

Figure 9.3. Horizontal and vertical shift of the 1st Purkinje image with respect to the pupil center (top horizontal and right vertical axes, respectively), and the equivalent horizontal and vertical coordinates of angle λ (bottom horizontal and left vertical axes, respectively, and broken symbols), for the eyes of the study. Closed symbols stand for right eyes, and open symbols for left eyes. Circles stand for eyes from Group 1 (anterior surface asphericity IOLs) and squares for eyes from Group 2 (posterior surface asphericity IOLs). Sign conventions for the 1st Purkinje image shift with respect of the pupil center are as follows. For horizontal shift x: Positive, the Purkinje image is shifted toward the nasal direction and viceversa for negative. For vertical shift: Sign conventions are: Positive, the Purkinje image is shifted upward and viceversa for negative. Sign conventions for angle λ are as follows. For the horizontal coordinate: Positive, the line of sight is rotated upwards with respect to the pupillary axis, Negative, the line of sight is rotating downwards referred to the pupillary axis. For the vertical coordinate: Positive, the line of sight is rotated to the nasal (right eye) or temporal side (left eye) and viceversa for the Negative.

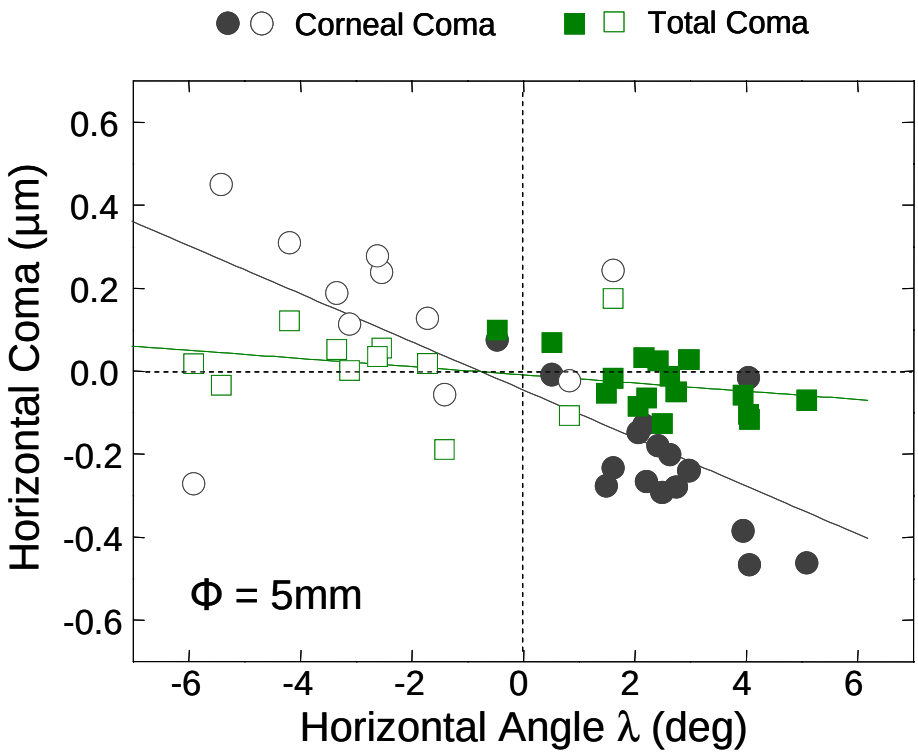

Figure 9.4. Horizontal coma as a function of angle λ (see Figure 9.3). Data from Groups 1 and 2 have been combined. Circles stand for corneal coma and squares for total coma. Closed symbols represent right eyes and open symbols left eyes. Solid lines represent linear correlations to the data (r=-0.71, p<0.0001, for corneal, and r=-0.36, p=0.058 for total). Data are for 5-mm pupil diameters.

Individually, there are highly significant correlations between corneal horizontal coma and the horizontal component of angle λ (Figure 9.4, open and filled circles), indicating that corneal horizontal coma arises primarily from the misalignment of the pupillary axis and the line of sight. For total horizontal coma there is a slight dependency with λ in the same direction that corneal coma (Figure 9.4, open and filled squares), although the correlation is only significant for Group 2. Table 9.4 shows coefficients of correlation coefficients, p values and slopes for each group and all eyes together, for the linear regressions of corneal and total horizontal coma as a function of angle λ.

Table 9.4. Correlations, significance and slopes of the linear regression of corneal and total horizontal coma as a function of angle λ

Corneal horizontal coma vs angle λ	**Coefficient of correlation R**	**p**	**Slope (μm/deg)**
Group 1 (n=12)	-0,5464	0,0534	-0,0504
Group 2 (n=15)	-0,7965	0,0004*	-0,0843
All eyes (n=27)	-0,7105	<0.0001*	-0,0833
Total horizontal coma vs angle λ			
Group 1 (n=12)	-0,1716	0,5751	-0,0159
Group 2 (n=15)	-0,5699	0,0266*	-0,0099
All eyes (n=27)	-0,3618	0,0585	-0,0108

3.4 Effect of IOL tilt and decentration

IOL tilt (measured with respect of the pupillary axis) and IOL decentration (with respect to the pupil center) also exhibit left/right eye midline symmetry, as shown in Figure 9.5 A (horizontal vs vertical coordinates of IOL tilt) and 9.5 B (horizontal vs vertical coordinates of decentration of IOL decentration), as had been reported previously for the crystalline lens. On average, IOLs are tilted by +1.86±1.29 deg for Group 1 and +1.35±0.74 deg for Group 2, with no statistically significant differences between the two groups (p=0.20) and decentered nasally by 0.25 mm for Group 1 and 0.29 mm for Group 2, with no statistically significant differences between the two groups (p=0.20).

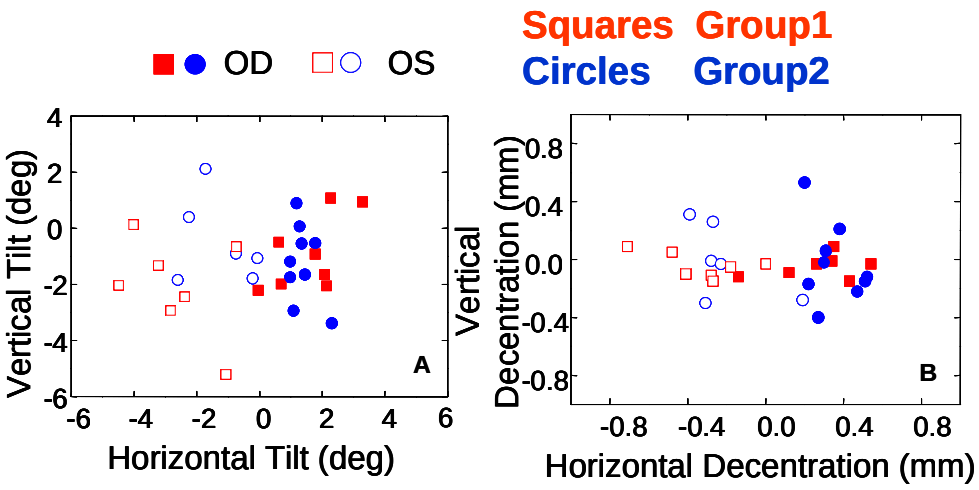

Figure 9.5. Horizontal and vertical coordinates of **(A)** IOL tilt and **(B)** IOL decentration. Closed symbols stand for right eyes, and open symbols for left eyes. Circles stand for eyes from Group 1 and squares for eyes from Group 2. Signs convention for horizontal tilt (around the vertical axis) are: Positive, superior edge of the lens is closer to the cornea than the inferior edge, and vice versa for Negative. For vertical tilt (around the horizontal axis): Positive, nasal edge of the lens moves backward (for the right eye) or forward (for the left eye), and viceversa for Negative. Signs conventions for horizontal decentration are;. For horizontal decentration: Positive, the lens is shifted toward the nasal (right eye) or temporal (left eye) direction and viceversa for Negative. For vertical decentration: Positive, the lens is shifted upward and viceversa for Negative.

We made use of a customized model eye see Chapter 8, (Rosales & Marcos, 2007) to test whether IOL tilt and decentration induced additional coma, or on the contrary played a compensatory role. Wave aberrations were estimated, assuming no tilt and decentration of the IOL, i.e. collinear with the pupillary axis, and also introducing the measured amounts of tilt and decentration. Internal aberrations were computed for each condition, subtracting total minus corneal aberrations. Figure 9.6 presents linear correlations of internal vs corneal horizontal coma, with data from the simulations assuming a centered lens in circles, with the actual tilt and decentration in triangles, and the experimental data in squares. Results are for 15 eyes from Group 2. The slope of the correlation of corneal versus simulated internal horizontal coma increases from –0.62 to –0.96 (gets closer to 1) when IOL tilt and decentration are incorporated, revealing that IOL tilt and decentration contribute to the compensation of horizontal coma. Predicted values are close to the experimental values of horizontal coma (particularly for right eyes shown in the left side of the graph). The slope of the corneal vs real total horizontal coma in this group of eyes is –0.81. In all three cases, the coefficient of correlation is higher than -0.958 and $p<0.0001$.

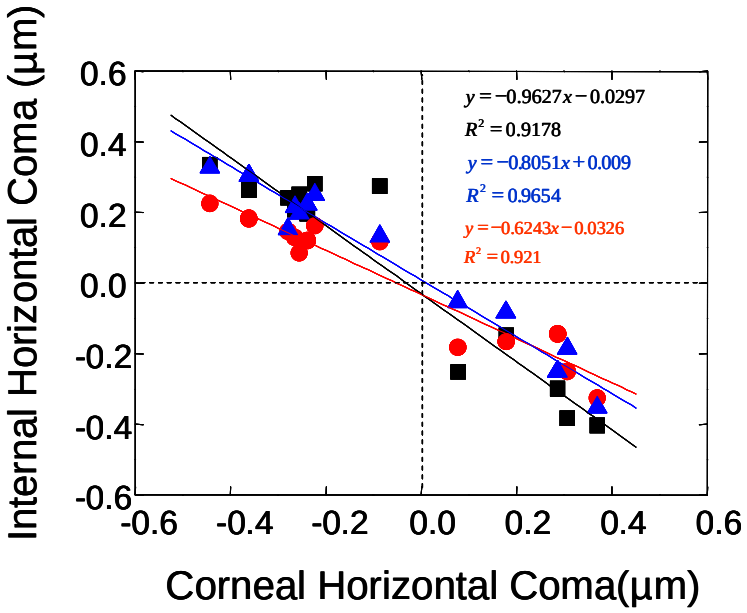

Figure 9.6. Corneal versus internal horizontal coma for customized model eyes with IOLs (squares) aligned to the pupillary axis, misaligned according to the measured amounts of IOL tilt and decentration (diamonds) and for real aberration measurements (triangles). Linear correlations are highly statistical significant (coefficients of correlations are 0.96, 0.96 and 0.98 respectively, $p<0.0001$). The lower slope (further from –1, indicative of lower compensation) correspond to eyes with centered IOLs (-0.62, as opposed to the eyes simulated with misaligned IOLs or real eyes, -0.96 and –0.80 respectively). Data correspond to eyes from Group 2.

4. DISCUSSION

We found a systematic compensation of corneal horizontal coma in eyes implanted with artificial lenses, designed to correct for the corneal spherical aberration of the average population. The compensation of spherical aberration over a sample-wide population (66.2 %) is of the same order or even larger than that found in young eyes with natural crystalline lenses. For example, previous studies found an average compensation of spherical aberration of 52% (n=7, (Artal et al., 2001)), or 36% (n=30, (Kelly et al., 2004).). An individual compensation of corneal spherical aberration was not found, as expected from the generic design of the intraocular lenses. Remarkably, an individual compensation (i.e. a significant correlation between internal and corneal spherical coefficients) had neither been found in young individuals. Furthermore, as previously reported in young eyes, we found a large compensation of horizontal coma in eyes with aspheric IOLs (87% as opposed to 51% in (Kelly et al., 2004).), both on average an in the individual eye correlations. It should be noted that our study, as well as previous studies did not include posterior corneal asphericity in the estimations of

corneal aberrations. Dubbelman (Dubbelman et al., 2007) showed a minor compensation of coma arising from the posterior cornea. Kelly (Kelly et al. 2004) attributed part of the horizontal coma compensation to the eccentricity of the fovea, but they also hypothesized an active mechanism during development that would fine-tune the internal horizontal coma to match in magnitude (with opposite sign) that of the cornea. Our results do not favor this hypothesis, and rather support a passive mechanism, since we have found an even higher compensation with artificial generic IOLs of aspheric design. Simple computations using general eye models in a previous study Kelly (Kelly et al., 2004) seemed to suggest that the presence of a gradient index distribution in the lens would play a role in the compensation of horizontal coma. While certainly the gradient of index (GRIN) of the crystalline lens may have a major contribution to the spherical aberration of the eye (and intraocular lens designs could incorporate this property), our data in patients with artificial lenses of constant refractive index demonstrate that compensation of horizontal coma is not determined by the presence of GRIN. Several authors (Artal et al., 2001, Kelly et al., 2004) have argued that compensation of horizontal coma may be achieved by fine-tuning of the crystalline lens position. While tilt and decentration of the lens do not appear to be major contributor to the compensation of horizontal coma, our data however support a compensatory role of lens misalignments, rather than an additional source of aberration. It is interesting that tilt and decentration appear to have a systematic bilateral symmetry and in the same direction than angle λ, in most eyes, even those implanted with intraocular lenses. We do not have preoperative data of crystalline lens tilt and decentration in these eyes, but a comparison with data in a young population from a previous study (see Chapter 8) suggests that surgery does not induce a significant increase in the magnitude of lens tilt and decentration and does not appear to change its orientation (perhaps preserved by the capsule). Whether this "beneficial" orientation of the lens was the result of an active process or a geometrical feature cannot be determined by our study, but in any case the role of tilt and decentration of the lens in horizontal coma is small compared to that of foveal misalignment and surface geometry. Our study supports the hypothesis of a passive, geometry-driven mechanism for compensation of horizontal coma. In agreement with previous studies (Artal et al., 2006, Coletta et al., 2006), we found high correlation of corneal horizontal coma with the shift of the 1st Purkinje image from the pupil center (or angle λ). Unlike suggested by a previous model (Kelly et al., 2004), our customized eye model with IOLs shows

similar results whether the 1st Purkinje shift is fully attributed to the eccentric fixation of the fovea or to a displacement of the pupil. Previous studies (Artal et al., 2006) conclude that the eye is a robust optical system, in the sense that eyes with different geometrical structure (such as hyperopes and myopes) exhibit similar optical performance (by compensation of spherical aberration and coma). We have not attempted to use refractive error as a variable in our study (although we have observed that longer eyes tended to have lower angle λ). However, our study also supports the robustness of the optical layout of the eye, in the sense that generic intraocular lenses with negative spherical aberration (but very different optical and geometrical structure than that of the crystalline lens) still are capable to produce an almost complete compensation of horizontal coma. This confirms the idea that the oblique incidence of rays that produces corneal horizontal coma, also generates coma in the lens, which for several designs (such as those of the IOLs of this study, designed to produce negative spherical aberration) has opposite sign to that of the cornea. We have compared the amounts of absolute total horizontal coma in the eyes (n=27) of this study (0.067± 0.049 μm, for 5-mm pupil diameter) with a group of eyes (n=9) of a previous study (Barbero, 2003), implanted with spherical IOLs (Acrysof, Alcon) using identical surgical technique, which showed significantly higher values of horizontal coma (0.28 ± 1.78 μm). To our knowledge, no experimental study comparing optical performance of eyes with spherical and aspheric IOLs (Bellucci, Morselli & Pucci, 2007, Marcos et al., 2005, Mester, Dillinger & Anterist, 2003) have been able to find larger amounts of coma in eyes with aspheric IOLs compared to those with spherical IOLs, despite early predictions indicating that aspheric designs would be more susceptible to induce asymmetric aberrations in the presence of random tilt and decentrations (Atchison, 1989).

Our study also has implications for the design of aspheric IOL designs, which try to mimic the performance of the young crystalline lens, and particularly to compensate for off-axis coma (Tabernero, Piers, Benito, Redondo & Artal, 2006). We have found that two different designs (one with the asphericity in the anterior and the other with asphericity in the posterior surface of the lens) both produce similar compensation of horizontal coma for foveal fixation.

In order to investigate to which extent different designs could achieve a compensation of corneal horizontal coma, we evaluated computationally the optical

performance of three different lenses minimizing defocus and spherical aberration (a meniscus, a biconvex lens with aspheric anterior surface and a biconvex lens with posterior aspheric surfaces) generated using analytical tools (Barbero & Marcos, 2007). Tests were performed on a customized pseudophakic eye model (Rosales & Marcos, 2007) for Eye #1 from Group 2. We found a compensation of spherical aberration with all three designs. However, horizontal coma increased 20% for the meniscus lens, it decreased by 46% for the biconvex lens with aspheric anterior surface, and by 58% for the biconvex lens with aspheric posterior surface. This indicates that while not all, quite different designs can produce significant amounts of compensation. Also, we evaluated the behavior of a spherical and an aspheric IOL of the same optical power in the same model eye and found that simulated total horizontal coma was twice with the spherical than with the aspheric lens, in keeping with the experimental results. Finally, we simulated the off-axis optical performance using the customized model eye for Eye #1 from Group 2, with its actual IOL. We found that, while significant compensation of horizontal coma occurred over a few degrees of retinal eccentricities, there was a given angle (-2 deg for this eye) for which compensation was optimal (as opposed to 4 deg, which was the measured eccentricity for this eye). While maximum optical quality would be achieved if the fovea was located in the optimal position, compensation of horizontal coma in the eyes of the study is similar or even better than in normal young eyes, indicating that significant compensations can be obtained with generic lenses not necessarily fine tuned to the foveal location.

As conclusion the findings suggest that the lens shape, gradient index or foveal location follow a passive mechanism for compensation of horizontal coma, although our results cannot exclude an active mechanism for the orientation of the crystalline lens, since cataract surgery seems to preserve the position of the capsule.

Conclusions 10

This thesis addresses the measurement of geometrical properties (surface geometry, tilt and decentration) of the crystalline lens in normal eyes, and their changes with accommodation. In addition, it addresses the impact of intraocular lens geometry, tilt, decentration and corneal aberrations on optical quality in pseudophakic eyes. We have demonstrated that knowledge of these structural properties allow us a deeper understanding of the optical quality of the normal eye (unaccommodated and accommodated) and the factors contributing to optical degradation in eyes with intraocular lenses.

1) We have developed a compact and reliable Purkinje-imaging based instrument to measure radii of curvature, tilt and decentration of the crystalline lens in normal eyes and of intraocular lenses in pseudophakic eyes. Equivalent mirror and Merit Function methods have been developed for phakometry, and linearity between Purkinje images locations and lens tilt, decentration and eye rotation were assumed. The system has been validated computationally (using computer eye models of various degrees of complexity) and experimentally (using physical model eyes, and in real eyes also measured with Scheimpflug imaging). Average reproducibility of the data is 0.308 mm for the anterior lens radius of curvature, 0.352 mm for the posterior lens radius of curvature, 0.39 deg for horizontal tilt, 0.45 deg for vertical tilt, 0.05 for horizontal and 0.04 for vertical lens decentration. We present in vivo measurements of lens tilt and decentration using this method on a total of 58 normal eyes, 43 eyes with intraocular lenses (spherical and aspheric monofocal lenses) and in 4 monkey eyes. **(Goal 1)**

2) We have developed processing algorithms to correct for geometrical distortion and optical distortion of a new Scheimpflug imaging system (Pentacam, Oculus). Those algorithms include an optimization routine to obtain the Scheimpflug camera lens nodal point. Those algorithms have been tested on normal crystalline lens and physical model eyes. **(Goal 2)**

3) Purkinje imaging and Scheimpflug imaging have been cross-validated for phakometry in normal young subjects and for tilt and decentration measurements in pseudophakic eyes. For the anterior lens radius of curvature, Scheimpflug and Purkinje data show highly statistically significant correlations.

On average, measurements from each technique are not statistically significantly different to each other. Individually, there are no significant differences across techniques in the anterior radius of curvature, while there are significant differences in half of the eyes in the posterior radius of curvature. Discrepancies can arise from the aspheric geometry of the lens. **(Goal 3)**

4) Validations of the Purkinje and Scheimpflug methods to measure lens tilt and decentration perfomed on physical model eye with set nominal values of tilt and decentration show absolute discrepancies between nominal and measured values of 0.279 deg (Purkinje) and 0.243 deg (Scheimpflug) for tilt and 0.094 mm (Purkinje) and 0.228 mm (Scheimpflug) for decentration. Scheimpflug and Purkinje imaging measurements of lens tilt around the vertical axis and lens horizontal decentration in pseudophakic eyes show highly statistically signifincant correlations across both techniques. **(Goal 3)**

5) Lens radii of curvature vary significantly in the population. In 58 young human eyes the anterior lens radius of curvature of the unaccommodated human lens ranged from 7.23 ± 0.04 mm to 13.45±0.59 mm (average 10.77±0.32 mm) and the posterior lens radius of curvature ranged between -4.73 ±0.43 mm to -9.49±0.18 mm for the posterior lens radius (average: -6.54±0.35) Average anterior and posterior lens radii of curvature in unaccommodated iridectomized monkey eyes were 11.11±1.58 mm and -6.64±0.62 mm respectively. **(Goals 4 and 5)**

6) Anterior and posterior lens radii changed systematically with accommodation. In young human eyes, the anterior lens radius of curvature decreased at a rate of 0.57±0.03 mm/D and the posterior lens radius of curvature at 0.29±0.05 mm/D, for static accommodation and as a function of accommodative demand. In iridectomised anaesthetized monkeys, the anterior lens radius of curvature decreased at a rate of 0.48±0.14 mm/D and the posterior lens radius of curvature at 0.17±0.03 mm/D, for dynamic accommodation and as a function of accommodative response. **(Goals 4 and 5)**

7) In normal young eyes, crystalline lens tilt ranged from 2.8±0.4 to -2.87±0.34 deg horizontally (average 1.31±0.76 deg) and from 2.58±0.27 to –1.00±0.31 deg vertically (average 1.21±0.81 deg), with respect to the pupillary axis. Crystalline lens decentration ranged from 0.09±0.031 to 0.45±0.02 mm horizontally (average 0.28±0.12 mm) and from -0.22±0.82 to 0.39±0.03 mm vertically (average 0.11±0.08 mm), with respect to the pupil center. Lens tilt and decentration tend to be mirror symmetric across right and left eyes. **(Goal 4).**

8) Lens tilt and decentration of the crystalline lens did not change significantly with dynamic accommodation in Rhesus Monkeys. However vertical tilt changed systematically with accommodation in some eyes, in agreement with reported increased vertical coma with accommodation in some monkey eyes. **(Goal 5)**

9) In pseudophakic eyes (after phakoemulsification and intracapsular lens implantation) lens tilt ranged from -0.72±0.52 to 3.6±0.58 deg horizontally (average 1.63±0.87 deg) and –3.39±0.4 to 5.97±0.82 deg vertically (average 1.77±1.30 deg), with respect to the pupillary axis. Lens decentration ranged from -0.53±0.06 to 0.54±0.03 mm horizontally (average 0.31±0.15 mm) and -0.4±0.06 to 0.54±0.03 vertically (average 0.14±0.13 mm), with respect to the pupil center. Lens tilt and decentration tend to be mirror symmetric across right and left eyes, suggesting that lens misalignment is determined by the capsule position, rather than being induced during the surgical procedure. **(Goal 6)**

10) Some corneal high order aberrations (trefoil and tetrafoil) increase significantly with cataract surgery, both for large and small pupil sizes. For vertical incision locations (3.2 mm) the changes occur in the vertical Zernike terms. No significant change occurs for spherical aberration. Slight differences in the amount and significance of the change appear to be associated to the design of intraocular lens implanted. **(Goal 7)**

11) Customized computer eye models of pseudophakic eyes (with individual data of corneal topography, lens geometry, lens tilt and decentration and fovea

misalignment) predict the high order aberrations of pseudophakic eyes. Measured and simulated aberrations agree 66% on average. These individual models have allowed to evaluate the effect of corneal aberrations, lens geometry, lens misalignment and angle lambda on the optical quality of eyes with implanted aspheric IOLs. Aspheric IOLs are able to correct the spherical aberration on average (although the exact amount of correction depends on the amount of corneal spherical aberration and several other biometric factors). Corneal aberrations play a major role in optical degradation is pseudophakic patients. The contribution of lens tilt and decentration to optical quality degradation is relatively minor. In 60% of the cases, the presence of lens tilt and decentration contributed favourably to high order aberrations prediction (with respect to the centered case). **(Goals 8 and 9)**

12) The active or passive nature compensation of horizontal coma has been tested using pseudophakic eyes with aspheric IOLs (with negative spherical aberration). While the spherical aberration is compensated on average, but not individually in these eyes, coma appears to be compensated individually (there is significant correlation between corneal and internal aberration). This compensation does not occur in eyes with spherical IOLs, but occurs in eyes with different aspheric designs. This indicates that lens shape, gradient index or foveal position do not need to be fine-tuned to achieve a compensation of horizontal coma (so it would be a passive mechanism) although, because the cataract surgery seems to preserve the position of the capsule a fine-tuning for the orientation of the crystalline lens cannot be completely excluded. **(Goal 10)**

The results can establish the basis for future research line directions:

1) The study of dynamic changes of lens geometry and misalignment with accommodation, in relationship with the dynamic changes of ocular aberrations, which would shed mechanism into the mechanism of lenticular accommodation and presbyopia.

2) The study of the contribution of gradient index distribution in the lens to the optical aberrations of the eye, expanding the customized model eyes developed

in this thesis for pseudophakic eyes to phakic eyes. This development involves the development of new regression techniques to retrieve the gradient index profile in vivo, and further developments of the optical distortion correction algorithms for Scheimpflug imaging (considering more complicated surfaces in the crystalline lens and the effects of a gradient index structure).

3) The development of new intraocular lens designs, and cataract surgery directions, considering realistic ocular component misalignments and the effect of corneal incision.

Conclusiones 10

Esta tesis se centra en al medida de las propiedades geométricas (geometría de la superficie, inclinación y descentramiento) del cristalino en ojos normales, y sus cambios con la acomodación. También se ha enfocado en el impacto de la geometría de la lente intraocular, su inclinación y descentramiento y las aberraciones corneales en la calidad óptica en ojos pseudofáquicos. Se ha demostrado que el conocimiento de estas propiedades estructurales nos permite un conocimiento más profundo de la calidad óptica del ojo normal (desacomodado y acomodado) y de los factores que contribuyen a la degradación óptica en ojos con lentes intraoculares.

1) Se ha desarrollado un instrumento compacto basado en imágenes de Purkinje, para medir los radios de curvatura, inclinación y descentramiento del cristalino en ojos normales y en lentes intraoculares en ojos pseudofáquicos. Para las medidas de facometría se han desarrollado los métodos del Espejo Equivalente y una Función de Mérito. Para las medidas de inclinación y descentramiento, se ha asumido una relación lineal entre las posiciones de las imágenes de Purkinje, inclinación y descentramiento de la lente y rotación del ojo. El sistema se ha validado computacionalmente (empleando modelos de ojo computacionales con varios grados de complejidad) y experimentalmente (empleando modelos físicos de ojos, y también en ojos reales también medidos con imágenes de Scheimpflug). La reproducibilidad promedio de los datos son 0.308 mm para el radio de la cara anterior del cristalino, 0.352 mm para el radio posterior, 0.39 deg para la inclinación horizontal, 0.45 deg para la inclinación vertical, 0.05mm y 0.004 mm para el descentramiento horizontal y vertical respectivamente. En esta tesis se presentan medidas en-vivo en un total de 58 ojos normales, 43 ojos con lentes intraoculares (lentes intraoculares monofocales esféricas y esféricas) y en 4 ojos de mono. **(Objetivo 1)**

2) Se han desarrollado algoritmos de procesado para corregir la distorsión geométrica y óptica de una cámara de Scheimpflug comercial (Pentacam, Oculus). Estos algoritmos incluyen una rutina de optimización para obtener los puntos nodales de la cámara. Estos algoritmos se han probado en sujetos con ojos normales y en modelos físicos de ojos. **(Objetivo 2)**

3) Las medidas empleando imágenes de Purkinje e imágenes de Scheimpflug se han validado mutuamente con medidas en ojos normales de sujetos jóvenes, mientras que la validación de medidas de inclinación y descentramiento se ha realizado en ojos pseudofáquicos. Las medidas del radio de curvatura de la cara anterior del cristalino muestran una alta correlación estadísticamente significativa para todos los ojos del estudio, las medidas realizadas con cada técnica no son estadísticamente diferentes. Los radios de curvatura de la cara anterior son muy similares en todos los ojos. Para las medidas de los radios de curvatura de la cara posterior de la lente, los datos obtenidos con imágenes de Scheimpflug y de Purkinje, muestran correlaciones estadísticamente significativas, y para la mitad de los ojos, las medidas obtenidas con cada una de las técnicas, muestran diferencias estadísticamente significativas. Las discrepancias pueden deberse a que en las imágenes de Scheimpflug se considera la asfericidad de las superficies oculares, mientras que en las imágenes de Purkinje se consideran superficies esféricas. **(Objetivo 3)**

4) Las medidas de inclinación alrededor del eje vertical y descentramiento horizontal obtenidas a partir de imágenes de Purkinje y Scheimpflug en ojos pseudofáquicos muestran también altas correlaciones estadísticamente significativas. En un modelo físico de ojo con un conjunto de valores nominales de inclinación (0-4 deg, cada 2 deg) y descentramiento (0-2 mm, cada 1 mm), la discrepancia entre valores nominales y medidos fue de 0.279 deg (Purkinje) y 0.243 deg (Scheimpflug) para inclinación y 0.094 mm (Purkinje) y 0.228 mm (Scheimpflug) para descentramiento**. (Objetivo 3)**

5) El radio de curvatura del cristalino varía significativamente entre sujetos. En los 58 ojos jóvenes del estudio, el radio de curvatura de la cara anterior del cristalino en el ojo humano desacomodado, variaba desde 7.23 ± 0.04 mm hasta 13.45±0.59 mm para el radio de la cara anterior del cristalino (promedio 10.77±0.32 mm) y para la cara posterior del cristalino, el radio variaba desde -4.73 ±0.43 mm hasta -9.49±0.18 mm (promedio: 6.54±0.35mm). En promedio, el radio de curvatura obtenido para las caras anterior y posterior del cristalino, en

ojos de mono iridectomizados en estado desacomodados fue de 11.11±1.58 mm y -6.64±0.62 mm respectivamente. **(Objetivos 4 y 5)**

6) Los radios de curvatura de las caras anterior y posterior del cristalino cambiansistemáticamente con la acomodación. En ojos humanos jóvenes, los radios de las caras anterior y posterior del cristalino decrecían a razón de 0.57±0.03 mm/D y 0.29±0.05 mm/D respectivamente, para acomodación estática y en función de la demanda acomodativa. En ojos iridectomizados de monos anestesiados, los radios de las caras anterior y posterior del cristalino decrecían a razón de 0.48±0.14 mm/D y 0.17±0.03 mm/D respectivamente, para acomodación dinámica y en función de la respuesta acomodativa. **(Objetivos 4 y 5)**

7) En ojos normales jóvenes, la inclinación del cristalino se encuentra entre 2.8±0.4 y -2.87±0.34 deg (promedio 1.31±0.76 deg) y entre 2.58±0.27 y -1±0.31 deg alrededor del eje y y del eje x respectivamente, referidos al eje pupilar. El descentramiento del cristalino se encuentra entre 0.09±0.031 y 0.45±0.02 mm (promedio: 0.28±0.12 mm) y entre -0.22±0.82 y 0.39±0.03 mm (promedio: 0.11±0.08 mm), en las direcciones horizontal y vertical respectivamente, ambas medidas referidas al centro de la pupila. La inclinación y el descentramiento del cristalino tiende a tener simetría especular entre los ojos derecho e izquierdo. **(Objetivo 4)**

8) La inclinación y el descentramiento del cristalino no cambia significativamente con la acomodación dinámica en el Rhesus Monkey. Sin embargo, la inclinación vertical cambiaba con la acomodación en algunos ojos. Este resultado concuerda con resultados previos que encuentran un incremento en el coma vertical con la acomodación en algunos ojos de mono. **(Objetivo 5)**

9) En ojos pseudofáquicos, tras facoemulsificación e implantación intracapsular de la lente, la inclinación de la lente intraocular se encontraba entre -0.72±0.52 y 3.6±0.58 deg (promedio: 1.63±0.87 deg) y entre –3.39±0.4 y 5.97±0.82 deg (promedio 1.77±1.30 deg), en las direcciones horizontal y vertical,

respectivamente, con respecto al eje pupilar. El descentramiento de la lente se encuentra entre -0.53±0.06 y 0.54±0.03 mm (promedio: 0.31±0.15 mm) y -0.4±0.06 y 0.54±0.03 mm (promedio: 0.14±0.13 mm), en las direcciones horizontal y vertical respectivamente, con respecto al eje pupilar. La inclinación y el descentramiento de la lente intraocular tiende a tener simetría especular entre los ojos derecho e izquierdo, sugiriendo que el desalineamiento de la lente intraocular está determinada por la posición de la cápsula, más que inducida durante la cirugía. **(Objetivo 6)**

10) Algunas aberraciones corneales de alto orden (trefoil y tetrafoil) aumentan significativamente con la cirugía de cataratas, tanto para 10 mm como para 5 mm. Para posiciones verticales de la incisión (3.2mm) los cambios se producen en los términos verticales de Zernike. No se producen cambios significativos para la aberración esférica. Las pequeñas diferencias que se producen en la cantidad e importancia del cambio, parecen estar asociados al diseño de la lente intraocular implantada. **(Objetivo 7)**

11) Los modelos de ojo computacionales de ojos pseudofáquicos (con datos individualizados de la topografía corneal, geometría de la lente, inclinación y descentramiento de la lente y posición de la fóvea) predicen las aberraciones de alto orden en ojos pseudofáquicos. Las aberraciones medidas y simuladas se corresponden en un 66% en promedio. Estos modelos individualizados han permitido evaluar el efecto de las aberraciones corneales, geometría de la lente, desalineamiento de la lente y del ángulo lambda en la calidad óptica de ojos con lentes intraoculares asféricas implantadas. Las lentes intraoculares asféricas están diseñadas para corregir la aberración esférica en promedio (aunque la cantidad exacta corregida depende de la cantidad de aberración esférica y muchos otros factores biométricos). La contribución de la inclinación y descentramiento a la degradación de la calidad óptica es una contribución menor. En el 60% de los casos, la existencia de inclinación y descentramiento contribuyen favorablemente a la predicción de aberraciones de alto orden (comparados con las predicciones obtenidas en el caso centrado). **(Objetivos 8 y 9)**

12) La naturaleza activa o pasiva de la compensación del coma horizontal se ha probado empleando ojos pseudofáquicos con lentes intraoculares esféricas (con aberración esférica negativa). Mientras que la aberración asférica se compensa en promedio, pero no individualmente en estos ojos, el coma parece que se compensa individualmente (ya que se produce una correlación significativa entre aberraciones corneales e internas). Esta compensación no se produce en ojos con lentes intraoculares esféricas, pero sí que se produce en ojos con diferentes diseños asféricos. Esto indica que la forma de la lente, el gradiente de índice o la posición de la fóvea no necesitan sintonizarse para conseguir una compensación del coma horizontal (mecanismo pasivo) aunque, debido a que la cirugía de cataratas parece conservar la posición de la cápsula, una sintonización en la orientación del cristalino no puede excluirse completamente. **(Objetivo 10)**

Estos resultados pueden establecer las bases para futuras líneas de investigación:

1) El estudio de cambios dinámicos en la geometría del cristalino y el desalineamiento con la acomodación, en relación con los cambios dinámicos de aberraciones oculares, pueden ayudar a comprender con mayor profundidad el mecanismo de la acomodación y el desarrollo de la presbicia.

2) El estudio de la contribución del gradiente de índice en el cristalino en las aberraciones ópticas del ojo, expandiendo el modelo de ojo personalizado desarrollado en esta tesis para ojos pseudofáquicos a ojos fáquicos. Este desarrollo requiere la elaboración de nuevas técnicas de regresión para obtener el perfil del gradiente de índice en vivo, y desarrollos mas avanzados de algoritmos de corrección de distorsión óptica para imágenes de Scheimpflug (considerando superficies del cristalino más complicadas y el efecto de la estructura del gradiente de índice).

3) El desarrollo de nuevos diseños de lentes intraoculares, y procedimientos en la cirugía de cataratas, considerando desalineamientos realistas de los componentes oculares y el efecto de la incisión corneal.

Bibliography 11

Agarwal, A. (2002). The human crystalline lens, ciliary body, and zonules. Their relevance to Presbyopia. (Chapter two). In: N.S. Thorofare, cop.2002 (Ed.) *Presbyopia: a surgical textbook* .

Altmann, G.E. (2005). Aspheric lenses and lens family. United States Patent: 20050203619, *Application Number*: 057278

Altmann, G.E., Nichamin, L.D., Lane, S.S., & Pepose, J.S. (2005). Optical performance of 3 intraocular lens designs in the presence of decentration. *J. Cataract Refractive Surg., 31*, 574-585.

Allemann, N., Silverman, R.H., Reinstein, D.Z., & Coleman, D.J. (1993). High-frequency ultrasound imaging and spectral analysis in traumatic hyphema. *Ophthalmology, 100*, 1351-1357.

Applegate, R., Thibos, L., Bradley, A., Marcos, S., Roorda, A., Salmin, T., & Atchison, D. (2000). Reference axis selection: subcommittee Report of the OSA working group to establish standards for measurement and reporting of optical aberrations of the eye. *J. Refractive Surg., 16*, 656-658.

Applegate, R.A., Donnely, W.J., Marsack, J.D., Koenig, D.E., & Pesudovs, K. (2007). Three-dimenional relationship between high-order root-mean-square wavefront error, pupil diameter, and aging. *J. Opt. Soc. Am. A., 24(3)*, 578-587.

Applegate, R.A., & Howland, H.C. (1997). Refractive surgery, optical aberrations, and visual perfomance. *J. Refractive Surg., 13*, 295-299.

Artal, P., Benito, A., & Tabenero, J. (2006). The human eye is an example of robust optical design. *J. Vision, 6*, 1-7.

Artal, P., Berrio, E., Guirao, A., & Piers, P. (2002). Contribution of the cornea and internal surfaces to the change of ocular aberrations with age. *J. Opt. Soc. Am. A., 19*, 137-143.

Artal, P., & Guirao, A. (1998). Contributions of the cornea and the lens to the aberrations of the human eye. *Optics Letters, 23* (21), 1713-1715.

Artal, P., Guirao, A., Berrio, E., & Williams, D.R. (2001). Compensation of corneal aberrations by the internal optics in the human eye. *J. Vision, 1*, 1-8.

Artal, P., Marcos, S., Iglesias, I., & Green, D.G. (1996). Optical modulation transfer function and contrast sensitivity with decentered small pupils. *Vision Res., 6*, 3575-3586.

Artal, P., Marcos, S., Navarro, R., Miranda, I., & Ferro, M. (1995). Through-focus image quality of eyes implanted with monofocal and multifocal intraocular lenses. *Opt. Engineering, 34*, 772-779.

Artal, P.F.M., Miranda I, Navarro R. (1993). Effects of aging in retinal image quality.

J. Opt. Soc. Am. A., 10, 1656-1662.

Atchison, D.A. (1989). Optical design of intraocular lenses .1. On-axis performance. *Optom. Vis. Sci., 66* (8), 492-506.

Atchison, D.A. (1990). Design of aspheric intraocular lenses. *Ophthalmic. Physiol. Opt., 11(2)*, 137-146.

Atchison, D.A., & Smith, G. (1995). Continuous gradient index and shell models of the human lens. *J. Opt. Soc. Am. A., 14*, 1684-1695.

Atchison, D.A., & Smith, G. (2000a). Monochromatic aberrations of schematic eyes. In: *Optics of the human eye* (Oxford: Butterworth-Heinemann).

Atchison, D.A., & Smith, G. (2000b). Optics of the Human Eye. (Oxford: Butterworth-Heinemann).

Augusteyn, R.C., Rosen, A.M., Borja, D., Ziebarth, N.M., & Parel, J.M. (2006). Biometry of primate lenses during immersion in preservation media. *Molecular Vision, 12*, 740-747.

Babcock, H.W. (1953). The possibility of compensating astronomical seeing. *Publications of the Astronomical Society of the Pacific, 65*, 229 (Abstract).

Barbero, S. (2003). Calidad óptica se la córnea y el cristalino: Desarrollo de métodos objetivos de medida y aplicaciones técnicas. *Instituto de Óptica "Daza de Valdés",* Tesis Doctoral, (pages: 195). Madrid: Consejo Superior de Investigaciones Científicas.

Barbero, S. (2006). Refractive power of a multilayer rotationally symmetric model of the human cornea and tear film. *J. Opt. Soc. Am. A., 23*, 1578-1585.

Barbero, S., & Marcos, S. (2007). Analytical tools for customized design of monofocal intraocular lenses. *Opt. Express, 15*, 8576-8591.

Barbero, S., Marcos, S., & Jimenez-Alfaro, I. (2003). Optical aberrations of intraocular lenses measured in vivo and in vitro. *J. Opt. Soc. Am. A., 20*, 1841-1851.

Barbero, S., Marcos, S., Merayo-Lloves, J., & Moreno-Barriuso, E. (2002). Validation of the estimation of corneal aberrations from videokeratography in keratoconus. *J. Cataract Refractive Surg., 18*, 263-270.

Barry, J.C., Branmann, K., & Dunne, M. (1997). Catoptric properties of eyes with misaligned surfaces studied by exact ray tracing. *Invest. Ophthalmol. Visual Sci., 38* (8), 1476-1484.

Barry, J.C., Dunne, M., & Kirschkamp, T. (2001). Phakometric measurement of ocular surface radius of curvature and alignment: evaluation of method with physical model eyes. *Ophthalmic Physiol. Opt., 21* (6), 450-460.

Baumeister, M., Neidhardt, B., Strobel, J., & Kohnen, T. (2005). Tilt and Decentration of Three-Piece Foldable High-Refractive Silicone and Hidrophobic Acrylic Intraocular Lenses With 6-mm Optics in an Intraindividual Comparison. *Am. J. Ophthalmol., 140*, 1051-1058.

Beers, A., & van der Heijde, G.L. (1994a). In vivo determination of the biomechanical properties of the component elements of the accommodation mechanism. *Vision Res., 34*, 2897-2905.

Beers, A.P.A., & van der Heijde, G.L. (1994b). Presbyopia and velocity of sound in the lens. *Optom. Vision Sci., 71*, 250-253.

Bellucci, R., Morselli, S., & Pucci, V. (2007). Spherical aberration and coma with an aspherical and a spherical intraocular lens in normal age-matched eyes. *J. Cataract Refractive Surg., 33* (2), 203-209.

Bennett, A.G., & Rabbetts, R.B. (1984). Clinical Visual Optics. (pp. 306-309). London, UK: Butterworths.

Bolz, M., Prinz, A., Drexler, W., & Findl, O. (2007). Linear relationship of refractive and biometric lenticular changes during accommodation in emmetropic and myopic eyes. *Br. J. Ophthalmol., 91*, 360-365.

Bradley, A., Thibos, L., Zhang, X.X., & Ye, M. (1991). The effects of ocular chromatic aberration on visual performance for displayed achromatic and chromatic information. *Society for Information Display International Symposium* (pp. 304-307). Anaheim, CA: Society for Information Display.

Brown, N. (1973). Slit-image photography and measurement of the eye. *Med Biol Illus, 23*, 192-203.

Brown, N. (1974). The change in lens curvature with age. *Exp. Eye Res., 19*, 175-183.

Brunette, I., Bueno, J.M., Parent, M., Hamam, H., & Simonet, P. (2003). Monochromatic aberrations as a function of age, from childhood to advanced age. *Invest. Ophthalmol. Vis. Sci., 44* (12), 5438-5446.

Burd, H.J., Judge, S.J., & Flavell, M.J. (1999). Mechanics of accommodation of the human eye. *Vision Res., 39*, 1591-1595.

Busin, M., Wilmanns, I., & Spitznas, M. (1989). Automated corneal topography: computerized analysis of photokeratoscope images. *Graefes. Arch. Clin. Exp. Ophtalmol., 227*, 230-236.

Calver, R., Cox, M., & Elliott, D. (1999). Effect of aging on the monochromatic aberrations of the human eye. *J. Opt. Soc. Am. A., 16*, 2069-2078.

Campbell, C. (1997). Reconstruction of the corneal shape with the MasterVue Corneal Topography System. *Optom. Vision Sci., 74*, 899-905.

Castejon-Mochon, F.J., Lopez-Gil, N., Benito, A., & Artal, P. (2002). Ocular wave-front aberration statistics in a normal young population. *Vision Res., 42*, 1611-1617.

Cline, D., Hofstetter, H.W., & Griffin, J.R. (1989). Dictionary of Visual Science. (ChiltonTrade Book Publishing).

Cobb, M.J., Liu, X.M., & Li, X.D. (2005). Continuous focus tracking for real-time optical coherence tomography. *Opt. Lett., 30*, 1680-1682.

Coleman, D.J., Woods, S., Rondeau, M.J., & Silverman, R.H. (1992). Ophthalmic ultrasonography. *Radiol. Clin. North. Am., 30*, 1105-1114.

Coletta, N., Han, H., & Moskowitz, A. (2006). Internal compensation of lateral coma aberration: relationship to refractive error: ARVO E-Abstract 1504. *Invest. Ophthalmol. Vis. Sci., 48*

Cook, C., & Koretz, J.F. (1998). Methods to obtain quantitative parametric descripions of the optical surfaces of the human crystalline lens from scheimpflug slit-lamp images I. image processing methods. *J. Opt. Soc. Am. A., 15* (6), 1473-1485.

Coopens, J.E., Van den Berg, T.J., & Budo, D.J. (2005). Biometry of phakic intraocular lens using Scheimpflug photography. *J. Cataract Refractive Surg., 31*, 1904-1914.

Crawford, K., Kaufman, P.L., & Bito, L.Z. (1990). The role of the iris in accommodation of rhesus monkeys. *Invest. Ophthalmol. Visual Sci., 31*, 2185-2190.

Croft, M., Glasser, A., Heatley, G., McDonald, J., Ebbert, T., Nadkarni, N., & Kaufman, P. (2006). The zonula, lens, and circumlental space in the normal iridectomized rhesus monkey eye. *Invest. Ophthalmol. Vis. Sci., 47*, 1087-1095.

Croft, M.A., Glasser, A., & Kaufman, P.L. (2001). Accommodation and presbyopia. *Int. Ophthalmol. Clin., 41*, 33-46.

Cusumano, A., Coleman, D.J., Silverman, R.H., Reinstein, D.Z., Rondeau, M.J., Ursea, R., Daly, S.M., & Lloyd, H.O. (1998). Three-dimensional ultrasound imaging. Clinical applications. *Ophthalmology, 105*, 300-306.

Chen, B., & Makous, W. (1989). Light capture by human cones. *J. Physiol., 414*, 89-109.

Chen, L., Kruger, P., Hofer, H., Singer, B., & Williams, D. (2006). Accommodation with higher-order monochromatic aberrations corrected with adaptive optics. *J. Opt. Soc. Am. A., 23*, 1-8.

Cheng, H., Barnett, J., Vilupuru, A., Marsack, J., Kasthurirangan, S., Applegate, R., & Roorda, A. (2004). A population study on changes in wave aberrations with accommodation. *J.Vision, 4*, 272-280.

Chinn, S.R., Swanson, E.A., & Fujimoto, J.G. (1997). Optical coherence tomography using a frequency-tunable optical source. *Opt. Lett., 22*, 340-342.

Choma, M.A., Hsu, K., & Izatt, J.A. (2005). Swept source optical coherence tomography using an all-fiber 1300-nm ring laser source. *J. Biomed. Opt., 10*

Choma, M.A., Sarunic, M.V., Yang, C., & Izatt, J.A. (2003). Sensitivity advantage of swept source and Fourier domain optical coherence tomography. *Opt. Express, 11*, 2183-2189.

Chung, S.H., Lee, S.J., Lee, H.K., Seo, K.Y., & Kim, E.K. (2007). Changes in higher order aberrations and contrast sensitivity after implantation of a phakic artisan intraocular lens. *Ophthalmologica., 221*, 167-172.

de Boer, J.F., Cense, B., Park, B.H., Pierce, M.C., Tearney, B.E., & Bouma, B.E. (2003). Improved signal-to-noise ratio in spectral-domain compared with time-domain optical coherence tomography. *Opt. Lett., 28*, 2067-2069.

de Castro, A., Rosales, P., & Marcos, S. (2007). Tilt and decentration of intraocular lenses in vivo from Purkinje and Scheimpflug imaging - Validation study. *J. Cataract Refractive Surg., 33* (3), 418-429.

de Guzman, M.H.P., Thiagalingam, S., Ong, P.Y., & Goldberg, I. (2005). Bilateral acute angle closure caused by supraciliary effusions associated with venlafaxine intake. *Medical J. Australia., 182*, 121-123.

Dick, G. (1994). Optical method for estimating the equivalent refractive index of the crystaline lens in vivo. *Ophthalmic Physiol. Opt., 14* (2), 177-183.

Doan, K.T., Olson, R.J., & Mamalis, N. (2002). Survey of intraocular lens material and design. *Current Opinion in Ophthalmology, 13*, 24-29.

Dorronsoro, C., Barbero, S., Llorente, L., & Marcos, S. (2003). On-eye measurement of optical performance of Rigid Gas Permeable contact lenses based on ocular and corneal aberrometry. *Optom. Vis. Sci., 80*, 115-125.

Downey, D.B., Nicolle, D.A., Levin, M.F., & Fenster, A. (1996). 3-D ultrasound imaging of the eye. *Eye, 10*, 75-81.

Drexler, W., Baumgartner, A., Findl, O., Hitzenberger, C., Sattmann, H., & Fercher, A. (1997). Submicrometer precision biometry of the anterior segment of the human eye. *Invest. Ophtalmol. Vis. Science, 38* (7), 1304-1313.

Drexler, W., Findl, O., Menapace, R., Rainer, G., Vass, C., Hitzenberger, C., & Fercher, A. (1998). Partial coherence interferometry: a novel approach to biometry in cataract surgery. *Am. J. Ophthalmol., 126* (4), 524-534.

Drexler, W., Hitzenberger, C.K., Sattmann, H., & Fercher, A.F. (1995). Measurement of the thickness of fundus layers by partial coherence tomography. *Opt. Engineering, 34*, 701-710.

Drexler, W., Morgner, U., Kartner, F.X., Pitris, C., Boppart, S.A., Li, X.D., Ippen, E.P., & Fujimoto, J.G. (1999). In vivo ultrahigh-resolution optical coherence tomography. *Opt. Lett., 24*, 1221-1223.

Dubbelman M, Sicam VA, & van der Heijde G. L (2006). The shape of the anterior and posterior surface of the aging human cornea. *Vision Res., 46(6-7)*, 993-1001.

Dubbelman M, van der Heijde G.L, & HA., W. (2001). The thickness of the aging human lens obtained from corrected Scheimpflug images. *Optom Vis Sci, 78*, 411-416.

Dubbelman, M., & Heijde, V. (2001). The shape of the aging human lens: curvature, equivalent refractive index and the lens paradox. *Vision Res., 41*, 1867-1877.

Dubbelman, M., Sicam, A., & van der Heijde, G.L. (2007). The contribution of the posterior surface to the coma aberration of the human cornea. *J. Vision, 7*, 1-8.

Dubbelman, M., Sicam, V.A., & van der Heijde, G.L. (2006). The shape of the anterior and posterior surface of the aging human cornea. *Vision Res., 46(6-7)*, 993-1001.

Dubbelman, M., van der Heijde, G.L., & Weeber, H.A. (2001b). The thickness of the aging human lens: curvature equivalent refractive index and the lens paradox. *Vision Res., 41*, 1867-1877.

Dubbelman, M., van der Heijde, G.L., & Weeber, H.A. (2005). Change in shape of the aging human crystalline lens with accommodation. *Vision Res., 45*, 117-132.

Dubbelman, M., Weeber, H.A., van der Heijde, G.L., & Volker-Dieben, H.J. (2002). Radius and asphericity of the posterior corneal surface determined by corrected Scheimpflug photography. *Acta Ophthalmol. Scand., 80*, 379-383.

Dunne, M., Davies, L.N., Mallen, E.A.H., Kirschkamp, T., & Barry, J.C. (2005). Non-invasive phakometric measurement of corneal and crystalline lens alignment in human eyes. *Ophthalmic Physiol. Opt., 25*, 143-152.

Dunne, M., Royston, J., & Barnes, D. (1991). Posterior corneal surface toricity and total corneal astigmatism. *Optom. Vision Sci.*, 68, 708-710.

El Hage, S.G., & Berny, F. (1973). Contribution of the crystalline lens to the spherical aberration of the eye. *J. Opt. Soc. Am. A., 63*, 205-211.

Ellis, M. (2001). Sharp-edged intraocular lens design as a cause of permanent glare. *J. Cataract Refractive Surg., 27*, 1061-1064.

Escudero-Sanz, I., & Navarro, R. (1999). Off-axis aberrations of a wide-angle schematic eye model. *J. Opt. Soc. Am. A., 16*, 1-11.

Farbowitz, M.A., Zabriskie, N., & Crandall, A.S. (2000). Visual complaints associated with the Acrysof Acrylic intraocular lens. *J. Cataract Refractive Surg., 26*, 1339-1345.

Faucher, A., & Rootman, D.S. (2001). Dislocation of a plate-haptic silicone intraocular lens into the anterior chamber. *J. Cataract Refractive Surg., 27*, 169-171.

Fercher, A.F., Hitzenberger, C.K., Drexler, W., Kamp, G., & Sattmann, H. (1993). In vivo optical coherence tomography. *Am. J. Ophthalmol., 116*, 113-114.

Fercher, A.F., Hitzenberger, C.K., Kamp, G., & Elzaiat, S.Y. (1995). Measurement of intraocular distances by backscattering spectral interferometry. *Opt. Commun., 117*, 43-48.

Fernandez, E.J., & Artal, P. (2005). Study on the effects of monochromatic aberrations in the accommodation response by using adaptive optics. *J. Opt. Soc. Am. A., 22*, 1732-1738.

Fincham, E.F. (1925). The changes in the form of the crystalline lens in accommodation. *Trans. Opthal. Soc, 26*, 239-269.

Findl, O., Drexler, W., Menapace, R., Heinzl, H., Hitzenberger, C.K., & Fercher, A.F. (2001). Improved prediction of intraocular lens power using partial coherence interferometry. *J. Cataract Refractive Surg., 27*, 861-867.

Fisher, R.F. (1971). The elastic constant of the human lens. *J. Physiol., 1971*, 147-212.

Fisher, R.F. (1977). The force of contracion of the human ciliary muscle during accomodation. *J. Physiol.*, 270:251.

García de la Cera, E., Rodriguez, G., & Marcos, S. (2006). Longitudinal changes of optical aberrations in normal and form-deprived myopic chick eyes. *Vision Research, 46*, 579-589.

Garner, L.F. (1983). Mechanisms of Accommodation and Refractive Error. *Ophthalmic Physiol. Opt., 3*, 287-293.

Garner, L.F. (1997). Calculation of the radii of curvature of the crystalline lens surfaces. *Ophthalmic Physiol. Opt., 17*, 75-80.

Garner, L.F., Ooi, C., & Smith, G. (1998). Refractive index of the crystalline lens in young and aged eyes. *Clin. Exp. Optom., 81*, 145-150.

Garner, L.F., & Smith, G. (1997). Changes in equivalent and gradient refractive index of the crystalline lens with accommodation. *Optom. Vision Sci., 74*, 114-119.

Garner, L.F., & Yap, M.K.H. (1997). Changes in ocular dimensions and refraction with accommodation. *Ophthalmic Physiol. Opt., 17*, 12-17.

Glasser, A., & Campbell, M. (1998). Presbyopia and the optical changes in the human crystalline lens with age. *Vision Res., 38*, 209-229.

Glasser, A., & Campbell, M. (1999). Biometric, optical and physical changes in the isolated human crystalline lens with age in relation to presbyopia. *Vision Res., 39*, 1991-2015.

Glasser, A., Croft, M.A., & Kaufman, P. (2001). Aging of the human lens and presbyopia. *Int Ophthalmol Clin., 41*, 1-15.

Glasser, A., & Kaufman, P.L. (1999). The mechanism of accommodation in primates. *Ophthalmology, 106*, 863-872.

Glasser, A., Wendt, M., & Ostrin, L.A. (2006). Accommodative changes in lens diameter in rhesus monkeys. *Invest. Ophthalmol. Vis. Science, 47*, 278-286.

Goldsmith, J.A., Li, Y., Chalita, M.R., Westphal, V., Patil, C.A., Rollins, A.M., Izatt, J.A., & Huang, D. (2005). Anterior chamber width measurement by high-speed optical coherence tomography. *Ophthalmology, 112*, 238-244.

Guirao, A., Gonzalez, C., Redondo, M., Geraghty, E., Norrby , S., & Artal, P. (1999). Average optical performance of the human eye as a function of age in a normal population. *Invest. Ophthalmol. Vis. Sci., 40*, 203-213.

Guirao, A., Redondo, M., & Artal, P. (2000). Optical aberrations of the human cornea as a function of age. *J. Opt. Soc. Am. A., 17*, 1697-1702.

Guirao, A., Redondo, M., Geraghty, E., Piers, P., Norrby, S., & Artal, P. (2002). Corneal optical aberrations and retinal image quality in patients in whom monofocal intraocular lenses were implanted. *Archives of Ophthalmology, 120*, 1143-1151.

Guirao, A., Tejedor, J., & Artal, P. (2004). Corneal aberrations before and after small-incision cataract surgery. *Invest. Ophtalmol. Vis. Science, 45*, 4312-4319.

Gullstrand, A. (1909). appendix in H. von Helmholtz. In: *Handbuch der Physiologischen Opitik* (pp. Bd. 1, p.299). Hamburg: Voss.

Gullstrand, A. (1911). Demonstration der Nernstpaltlampe. Edit: Heidelberger Bericht

Guyton, D., Uozato, H., & Wisnick, H. (1990). Rapid determination of intraocular lens tilt and decentration through the undilated pupil. *Opthalmology, 97*, 1259-1264.

Hartmann, J. (1900). Bemerkungen über den Bau und die Justierung von Spektrographen. *Zeitschrift für Instrumentenkunde, 20*, 47.

Häusler, G., & Lindner, M.W. (1998). "Coherence radar" and "spectral radar"- new tools for dermatological diagnosis. *J. Biomed. Opt., 3*, 21-31.

Hayashi, K., Hayashi, H., & Hayashi, F. (1995). Topographic analysis of the changes in corneal shape due to aging. *Cornea, 14*, 527-532.

Hayashi, K., Hayashi, H., & Nakao, F. (1998). Quantitavive comparison of posterior capsule opacification after polymethylmethacrylate, silicone, and soft acrylic intraocular lens implantation. *Arch. Ophthalmol., 116*, 1579-1582.

Hayashi, K., Hayashi, H., Nakao, F., & Hayashi, F. (1998). Comparison of decentration and tilt between one piece and three piece polimethyl methacrylate intraocular lenses. *Br. J. Ophtalmol., 82*, 419-422.

Hayashi, K., Hayashi, H., Nakao, F., & Hayashi, F. (2000). Influence of astigmatism on multifocal and monofocal intraocular lenses. *Am. J. Ophthalmol., 130*, 477-482.

Hayashi, K., Hayashi, H., Oshika, T., & Hayashi, F. (2000). Fourier analysis of irregular astigmatism after implantation of 3 types of intraocular lenses. *J. Cataract Refractive Surg., 26,* 1510-1506.

He, J.C., Burns, S.A., & Marcos, S. (2000). Monochromatic aberrations in the accommodated human eye. *Vision Res., 40*, 41-48.

He, J.C., Marcos, S., Webb, R.H., & Burns, S.A. (1998). Measurement of the wave-front aberration of the eye by a fast psychophysical procedure. *J. Opt. Soc. Am. A., 15*, 2449-2456.

Hemenger, R.P., Garner, L.F., & Ooi, C. (1995). Change with age of the refractive index gradient of the human ocular lens. *Invest. Ophthalmol. Vis. Science, 36*, 703-707.

Hermans, E.A., Dubbelman, M., van der Heijde, G.L., & Heethaar, R.M. (2006). Estimating the external force acting on the human eye lens during accommodation by finite element modelling. *Vision Res., 46*, 3642-3650.

Herzberger, M. (1969). Colour Correction in Optical Systems and a New Dispersion Formula. *Opt. Acta, 5*, 197-215.

Hitzenberger, C.K. (1991). Optical measurement of the axial eye length by laser Doppler interferometry. *Invest. Ophthalmol. Vis. Sci., 32*, 616-624.

Ho, A., Erickson, P., Manns, F., & Parel, J.M. (2006). Supplementary endo-capsular lens and method of implantation*.,* (*United States Patent:* 7060095, *Application Number:* 7060095).

Hofer, H., Artal, P., Singer, B., Aragon, J., & Williams, D. (2001). Dynamics of the eye´s wave aberration. *J. Opt. Soc. Am. A., 18* (3), 497-506.

Holladay, J., Piers, P., Koranyi, G., van der Mooren, M., & Norrby, N. (2002). A new intraocular lens design to reduce spherical aberration of pseudophakic eyes. *J. Refractive Surg., 18*, 683-691.

Howland, B. (1960). Use of crossed cylinder lens in photographic lens evaluation. *Applied Optics, 7*, 1587-1588.

Howland, B., & Howland, H.C. (1976). Subjective measurement of high-order aberrations of the eye. *Science, 193*, 580-582.

Howland, H.C. (2005). Allometry and scaling of wave aberration of eyes. *Vision Res., 45*, 1091-1093.

Howland, H.C., & Howland, B. (1977). A subjective method for the measurement of the monochromatic aberrations of the eye. *J. Opt. Soc. Am. A., 67*, 1508-1518.

Huang, D., Swanson, E., Lin, C.P., Schuman, J.S., Stinson, W.G., Chang, W., Hee, M.R., Flotte, T., Gregory, K., & Pulifito, C.A. (1991). Optical coherence tomography. *Science, 254*, 1178-1181.

Ismet, D. (2000). Tilt and decentration after primary and secondary transsclerally sutured posterior chamber intraocular lens implantation. *J Cataract Refract Surg., 27*, 227:232.

Israel, H.M. (2003). Accommodating intraocular lens assembly*.,* (*United States Patent*: 6524340, *Application Number*: 862426) .

Izatt, J.A., Hee, M.R., Swanson, E.A., Lin, C.P., Huang, D., Schuman, J.S., Puliafito, C.A., & Fujimoto, J.G. (1994). Micrometer-scale resolution imaging of the anterior eye in vivo with optical coherence tomography. *Arch. Ophthalmol., 112*, 1584-1589.

Jacobs, B., Gaynes, B.L., & Deutsch, T.A. (1999). Refractive astigmatism after oblique clear corneal phacoemulsification cataract incision. *J. Cataract Refractive Surg., 25*, 949-952.

Jae Soon Kim, & Shyn, K.H. (2001). Biometry of 3 types of intraocular lenses using Scheimpflug photography. *J. Cataract Refractive Surg., 27*, 533-536.

Jensen, P.K., & Hansen, M.K. (1991). Ultrasonographic, three-dimensional scanning for determination of intraocular tumor volume. *Acta Ophthalmol.*, 178-186.

Jezzi, R., Rosen, R.B., & Tello, C. (1996). Personal computer-based 3-dimensional ultrasound biomicroscopy of the anterior segment. *Arch. Ophthalmol., 114*, 520-524.

Judge, S.J., & Burd, H.J. (2002). Modelling the mechanics of accommodation and presbyopia. *Ophthalmic Physiol. Opt., 22*, 397-400.

Jung, C.K., Chung, S.K., & Baek, N.H. (2000). Decentration and tilt: silicone multifocal versus acrylic soft intraocular lenses. *J. Cataract Refractive Surg., 26*, 582-585.

Kasthurirangan, S., Markwell, E., Atchison, D.A., Pope, J.M., & Smith, G. (2007). Magnetic resonance imaging study of crystalline lens shape with accommodation and age. *Invest. Ophtalmol. Vis. Science, 48:E-Abstract 6008*

Kaufman, P.L., & Lütjen-Drecoll, E. (1975). Total iridectomy in the primate in vivo: surgical technique and postoperative anatomy. *Invest. Ophthalmol. , 14*, 766-771.

Kelly, J.E., Mihashi, T., & Howland, H.C. (2004). Compensation of corneal horizontal/vertical astigmatism, lateral coma, and spherical aberration by internal optics of the eye. *J. Vision, 4*, 262-271.

Kim, J., S., & Shyn, K.H. (2001). Biometry of 3 types of intraocular lenses using scheimpflug photography. *J. Cataract Refractive Surg., 27*, 533-536.

Kirschkamp, T., Dunne, M., & Barry, J.C. (2004). Phakometric measurement of ocular surface radii of curvature, axial separations and alignment in relaxed and accommodated human eyes. *Ophthalmic Physiol. Opt., 24*, 65-73.

Kisilak, M.L., Campbell, M.C.W., Hunter, J.J., Irving, E.L., & Huang, L. (2006). Aberrations of chick eyes during normal growth and lens induction of myopia. *Journal of Comparative Physiology A -Neuroethology Sensory Neural and Behavioral Physiology, 192* (8), 845-855.

Kohnen, T., & Kasper, T. (2005). Incision sizes before and after implantation of 6-mm optic foldable intraocular lneses using Monarch and Unfolder injector systems. *Ophthalmology, 112*, 58-66.

Koopmans, S.A., Terwee, T., Glasser, A., Wendt, M., Vilupuru, A.S., van Kooten, T.G., & et al (2006). Accommodative lens refilling in rhesus monkeys. *Invest. Ophthalmol. Vis. Science, 47*, 2976-2984.

Koretz, J.F., Bertasso, A., Neider, M., & Kaufman PL (1988). Slit-lamp studies of the rhesus monkey eye: III. The zones of discontinuity. *Exp. Eye Res, 46*, 871-880.

Koretz, J.F., Bertasso, A.M., Neider, M.W., True-Galbelt, B.A., & Kaufman, P.L. (1987). Slit-lamp studies of the rhesus monkey eye:II. Changes in crystalline lens shape, thickness and position during accommodation and aging. *Exp. Eye Res., 45*, 317-326.

Koretz, J.F., Cook, C., & Kaufman, P. (1997). Accommodation and presbyopia in the human eye. Changes in the anterior segment and crystalline lens with focus. *Invest. Ophthalmol. Vis. Sci., 38*, 569-578.

Koretz, J.F., Cook, C., & Kaufman, P. (2001). Aging of the human lens: changes in lens shape at zero-diopter accommodation. *J. Opt. Soc. Am. A., 18*, 265-272.

Koretz, J.F., Cook, C., & Kaufman, P. (2002). Aging of the human lens: changes in lens shape upon accommodation and with accommodative loss. *J Opt Soc Am A, 19*, 144-151.

Koretz, J.F., Cook, C.A., & Kuszak, J.R. (1994). The zones of discontinuity in the human lens: development and distribution with age. *Vision Res., 34*, 2955-2962.

Koretz, J.F., & Handelman, G. (1986). The lens paradox and image formation in accommodating human lenses. *Top. Aging. Res. Eur, 6*, 57-64.

Koretz, J.F., & Handelman, G.H. (1988). How the human eye focuses. *Sci. Am, 92*

Koretz, J.F., Handelman, G.H., & Brown, N. (1984). Analysis of human crystalline lens shape, thickness and position during accommodation and aging. *Exp. Eye. Res., 45*, 317-326.

Koretz, J.F., Kaufman, P.L., Neider, M.W., & Goeckner, P.A. (1989). Accommodation and presbyopia in the human eye, aging of the anterior segment. *Vision Res., 1989*, 1685-1692.

Koretz, J.F., Neider, M.W., Kaufman, P.L., Bertasso, A.M., DeRousseau, C.J., & Bito, L.Z. (1987). Slit-lamp studies of the rhesus monkey eye. I. Survey of the anterior segment. *Exp. Eye Res., 44*, 307-318.

Koretz, J.F., Strenk, S.A., Strenk, L.M., & Semmlow, J.L. (2004). Scheimpflug and high-resolution magnetic resonance imaging of the anterior segment: a comparative study. *J. Opt. Soc. Am. A., 21*, 346-354.

Krag, S., Olsen, T., & Andreassen, T. (1997). Biomechanical characteristics of the human anterior lens capsule in relation to age. *Invest. Ophtalmol. Vis. Science, 38*, 357-363.

Kriechbaum, K., Findl, O., Kiss, B., Sacu, S., Petternel, V., & Drexler, W. (2003a). Comparison of anterior chamber depth measurement methods in phakic and pseudophakic eyes. *J Cataract Refractive Surg., 29*, 89-94.

Kriechbaum, K., Findl, O., Preussner, P.R., Koppl, C., Wahl, J., & Drexler, W. (2003). Determining postoperative anterior chamber depth. *J. Cataract Refractive Surg., 29*, 2122-2126.

Krueger, R., Seiler, T., Gruchman, T., Mrochen, M., & Berlin, M. (2001). Stress wave amplitudes during laser surgery of the cornea. *Ophtalmology, 108*, 1070-1074.

Küchle, M., Seitz, B., Langenbucher, A., & et al (2004). Comparison of 6-month results of implantation of the 1CU accommodative intraocular lens with conventional intraocular lenses. *Ophthalmology, 111*, 318-124.

Kuszak, J.R. (2004). Development of lens sutures. *Int. J Dev Biol., 48*, 889-902.

Kuszak, J.R., Peterson, K.L., Sivak, J.G., & Herbert, K.L. (1994). The interrelationship of lens anatomy and optical quality. II. Primate lens. *Exp. Eye Res, 59*, 521-535.

Lapuerta, P., & Schein, J. (1995). A four-surface schematic eye of macaque monkey obtained by an optical method. *Vision Res., 35*, 2245-2254.

Le Grand, Y., & El Hage, S.G. (1980). Physiological Optics (Vol. 1). *Springer Series in Optical Sciences* (Berlin-Heidelberg: Springer Verlag.

Lee, C.S., & Simpson, M.J. (1997). Diffractive multifocal ophthalmic lens. *Patent Number:* 5699142, *Application Number*: 655346) (Alcon Laboratiories, Inc.)

Lewis, R. (1983). The Conquest of Presbyopia. (p. 111).Sydney, Austr.: R. & M. Lewis.

Lexer, F., Hitzenberger, C.K., Drexler, W., Molebny, S., Sattmann, H., Sticker, M., & Fercher, A.F. (1999). Dynamic coherent focus OCT with depthindependent transversal resolution. *J. Md. Opt., 46*, 541-553.

Li, Y., Shekhar, R., & Huang, D. (2006). Corneal pachimetry mapping with high-speed optical coherence tomography. *Ophthalmology, 113*, 792-799.

Liang, J., Grimm, B., Goelz, S., & Bille, J.F. (1994). Objective measurement of wave aberrations of the human eye with the use of a Hartmann-Shack wave-front sensor. *J. Opt. Soc. Am., 11*, 1949-1957.

Llorente, L., Barbero, S., Cano, D., Dorronsoro, C., & Marcos, S. (2004). Myopic versus hyperopic eyes: axial length, corneal shape and optical aberrations. *J. Vision, 4*, 288.

Llorente, L., Diaz-Santana, L., Lara-Saucedo, D., & Marcos, S. (2003). Aberrations of the human eye in visible and near infrared illumination. *Optom. Vision Sci., 80*, 26-35.

Maldonado, M.J., Nieto, J.C., Díez-Cuenca, M., & Piñero, D.P. (2006). Repeatability and reproducibility of posterior corneal curvature measurements by combined scanning-slit and placido-disc topography after LASIK. *Ophthalmology, 113*, 1918-1926.

Mandell, R. (1995). Locating the corneal sighting center from videokeratography. *J. Cataract Refractive Surg., 11*, 253-258.

Marcos, S. (2005). Calidad de imagen retiniana. *Investigación y Ciencia, 34*, 6674.

Marcos, S., Barbero, B., Llorente, L., & Merayo-Lloves, J. (2001a). Optical response to LASIK for myopia from total and corneal aberrations. *Invest. Ophtalmol. Vis. Science, 42*, 3349-3356.

Marcos, S., Barbero, S., & Jiménez-Alfaro, I. (2005). Optical quality and depth-of-field of eyes implanted with spherical and aspheric intraocular lenses. *J. Refractive Surg., 21*, 223-235.

Marcos, S., Barbero, S., McLellan, J.S., & Burns, S.A. (2003). Optical quality of the eye and aging. In: S.I. (2004) (Ed.) *Wavefront customized visual correction: The quest for supervision II.* (p. 416).

Marcos, S., & Burns, S.A. (2000). On the symmetry between eyes of wavefront aberration and cone directionality. *Vision Res., 40*, 2437-2447.

Marcos, S., Burns, S.A., Moreno-Barriuso, E., & Navarro, R. (1999). A new approach to the study of ocular chromatic aberrations. *Vision Res., 39*, 4309-4323.

Marcos, S., Burns, S.A., Prieto, P.M., Navarro, R., & Baraibar, B. (2001b). Investigating sources of variability of monochromatic and transverse chromatic aberrations across eyes. *Vision Res., 41*, 3861-3871.

Marcos, S., Díaz-Santana, L., Llorente, L., & C., D. (2002). Ocular aberrations with ray tracing and Shack-Hartmann wavefront sensors: does polarization play a role? *J. Opt. Soc. Am. A., 19*, 1063-1072.

Marcos, S., Rosales, P., Llorente, L., & Jimenez-Alfaro, I. (2007). Change in corneal aberrations after cataract surgery with 2 types of aspherical intraocular lenses. *J. Cataract Refractive Surg., 33* (2), 217-226.

McDonald, M.B. (2003). Intraocular multifocal lenses. Nashville, TN, United Stated *Patent Number*: 20060293747, *Application Number*:20060293747.

McGinty, S.J., & Truscott, R.J. (2006). Presbyopia: the first stage of nuclear cataract? *Ophthalmic Res., 38*, 137-148.

Mclellan, J., Marcos, S., & Burns, S. (2001). Age-related changes in monochromatic wave aberrations in the human eye. *Invest. Ophthalmol. Visual Sci.*, *42*, 1390-1395.

McLellan, J.S., Marcos, S., Prieto, P.M., & Burns, S.A. (2002). Imperfect optics may be the eye's defense against chromatic blur. *Nature, 417*, 174-176.

McWhae, J.A., & Reimer, J. (2000). The mechanism of accommodation in primates. *Ophthalmology, 107*, 627-628.

Mester, U., Dillinger, P., & Anterist, N. (2003). Impact of a modified optic design on visual function: clinical comparative study. *J. Cataract Refractive Surg., 29*, 653-660.

Millodot, M., & Sivak, J. (1979). Contribution of the cornea and lens to the spherical aberration of the eye. *Vision Res., 19*, 685-687.

Moffat, B., Atchison, D., & Pope, J. (2002a). Age-related changes in refractive index distribution and power of the human lens as measured by magnetic resonance micro-imaging in vitro. *Vision Res.*, 1683-1693.

Moffat, B.A., Atchison, D.A., & Pope, J.M. (2002b). Explanation of the Lens Paradox. *Optom. Vision Sci., 79*, 147-149.

Moreno-Barriuso, E., Marcos, S., Navarro, R., & Burns, S.A. (2001a). Comparing Laser Ray Tracing, Spatially Resolved Refractometer and Hartmann-Shack sensor to measure the ocular wavefront aberration. *Optom. Vision Sci., 78*, 152 - 156.

Moreno-Barriuso, E., Merayo-Lloves, J., Marcos, S., Navarro, R., Llorente, L., & Barbero, S. (2001b). Ocular aberrations before and after myopic corneal refractive surgery: LASIK-induced changes measured with Laser Ray Tracing. *Invest. Ophthalmol. Vis. Science, 42*, 1396-1403.

Moreno-Barriuso, E., & Navarro, R. (2000). Laser Ray Tracing versus Hartmann-Shack Sensor for Measuring Optical Aberrations in the Human Eye. *J. Opt. Soc. Am. A., 17*, 974-985.

Mundt, G.H., & Hughes, W.F. (1956). Ultrasonics in ocular diagnosis. *Am. J. Ophthalmol., 41*, 488-498.

Mutti, D., Zadnik, K., & Adams, A. (1992). A video technique for phakometry of the human crystalline lens. *Invest Ophthalmol Vis Sci., 33*, 1771-1782.

Mutti, D., Zadnik, K., Fusaro, R., Friedman, N., Sholtz, R., & Adams, A. (1998). Optical and structural development of the crystalline lens in childhood. *Invest Ophthalmol Vis Sci., 39* :120-133.

Myers, R.I., & Krueger, R.R. (1998). Novel approaches to correction of presbyopia with laser modification of the crystalline lens. *J. Refractive Surg., 14*, 136-139.

Navarro, R., & Losada, M.A. (1997). Shape of stars and optical quality of the human eye. *J. Opt. Soc. Am. A., 14*, 353-359.

Navarro, R., & Moreno-Barriuso, E. (1999). Laser ray-tracing method for optical testing. *Opt. Letters, 24*, 1-3.

Navarro, R., Santamaría, J., & Bescós, J. (1985). Accommodation-dependent model of the human eye with aspherics. *J. Opt. Soc. Am. A., 2*, 1273-1281.

Neider, M.W., Crawford, K., Kaufman, P.L., & Bito, L.Z. (1990). In vivo videography of the rhesus monkey accommodative apparatus. Age-related loss of ciliary muscle response to central stimulation. *Arch. Ophthalmol., 108*, 69-74.

Nejima, R., Miyata, K., Honbou, M., Tokunaga, T., Tanabe, T., Sato, M., & Oshika, T. (2004). A prospective, randomised comparison of single and three piece acrylic foldable intraocular lenses. *Br. J. Ophtalmol., 88*, 746-749.

Niessen, A.G.J.E., De Jong, L.B., & van der Heijde, G.L. (1992). Pseudo-accommodation in psedophakia. *Eur. J. Implant. Refr. Surg, 4*, 91-94.

Nishi, O., Nishi, K., & Akura, J. (2001). Effect of round-edged acrylic intraocular lenses on preventing posterior capsule opacification. *J. Cataract Refractive Surg., 27*, 608-613.

Norrby, S., Koopmans, S., & Terwee, T. (2006). Artificial crystalline lens. *Ophthal. Clin. North. Am., 19*, 143-146.

Ooi, C., & Grosvenor, T. (1995). Mechanisms of emmetropization in the aging eye. *Optom. Vision Sci., 72*, 60-66.

Oshika, T., Kawana, K., Hiraoka, T., Kaji, Y., & Kiuchi, T. (2005). Ocular higher-order wavefront aberration caused by mayor tilting of intraocular lens. *Am. J. Ophthalmol.,*
Oshika, T., Klyce, S.D., Applegate, R.A., & Howland, H.C. (1999). Changes in corneal wavefront aberrations with aging. *Invest. Ophthalmol. Vis. Sci., 40*, 1351-1355.

Ostrin, L.A., & Glasser, A. (2007). Edinger-Westphal and pharmacologically stimulated accommodative refractive changes and lens ciliary process movements in rhesus monkeys. *Exp. Eye Res, 84*, 302-313.

Ostrin, L.A., Kasthurirangan, S., Win-Hall, D., & Glasser, A. (2006). Simultaneous measurements of refraction and A-scan biometry during accommodation in humans. *Optom. Vision Sci., 83*, 657-665.

Packer, M., Fine, I.H., Hoffman, R.S., & Piers, P.A. (2004). Improved functional vision with a modified prolate intraocular lens. *J. Cataract Refractive Surg., 30, 986-992.*

Padmanabhan, P., Rao, S.K., Jayasree, R., Chowdhry, M., & Roy, J. (2006). Monochromatic aberrations in eyes with different intraocular lens optic designs. *J. Refractive Surg., 22,*172-177.

Pandey, S.K., Thakur, J., Werner, L., Wilson, M.E., Werner, L.P., Izak, A.M., & Apple, D.J. (2002). The human crystalline lens, ciliary body and zonules. Their relevance to presbyopia. In: N.S. Thorofare, cop.2002 (Ed.) *Presbyopia: A Surgical Textbook.*

Pandey, S.K., Wilson, M.E., & Trivedi, R.H. (2001). Pediatric cataract surgery and intraocular lens implantation:current techniques, complications and management. *Int. Ophthalmol. Clin., 41*, 175-196.

Park, B.H., Pierce, M.C., Cense, B., Yun, S.H., Mujat, G.J., Tearney, B.E., Bouma, B.E., & de Boer, J.F. (2005). Real-time fiber-based multi-functional spectral-domain coherence tomography at 1.3 μm. *Opt. Expess, 13*, 3931-3344.

Pavlin, C.J., Harasiewicz, K., Sherar, M.D., & Foster, F.S. (1991). Clinical use of ultrasound biomicroscopy. *Ophthalmology, 98*, 287-295.

Pavlin, C.J., Sherar, M.D., & Foster, F.S. (1990). Subsurface ultrasound microscopi imaging of the intact eye. *Ophthalmology, 98*, 287-295.

Peng, Q., Yang, Y., & Zhang, X. (2005). Accommodative intraocular lens. *United States Patent Number*: 6926736, *Application Number*: 453994, (Alcon, Inc.).

Pesudovs, K., Dietze, H., Stewart, N.B., & Cox, M. (2005). Effect of cataract surgery incision location and intraocular lens type on ocular aberrations. *J. Cataract Refractive Surg.*, 725-734.

Petersen, A.M., Bluth, L.L., & Campion, M. (2000). Delayed posterior dislocation of silicone plate-haptic lenses after nodymium:yag capsulotomy. *J. Cataract Refractive Surg., 26*, 1827-1829.

Phillips, P., Perez-Emmanuelli, J., Rosskothen, H.D., & Koester, C.J. (1988). Measurement of intraocular lens decentration and tilt in vivo. *J. Cataract Refractive Surg., 14*, 129-135.

Pierscionek, B. (1997). Refractive index contours in the human lens. *Exp. Eye Res, 64*, 887-893.

Plainis, S., Ginis, H.S., & Pallikaris, A. (2005). The effect of ocular aberrations on steady-state errors of accommodative response. *J.Vision, 23*, 466-477.

Porter, J., Guirao , A., Cox , I., & Williams, D. (2001). Monochromatic aberrations of the human eye in a large population. *J. Opt. Soc. Am. A., 18* (8), 1793-1803.

Prisant, O., Hoang-Xuan, Proano, C., Hernandez, E., Awad, S., & Azar, D.T. (2002). Vector summation of anterior and posterior corneal topographical astigmatism. *J. Cataract Refractive Surg.*, 1578-1585.

Qazi, M.A., Pepose, J.S., & Shuster, J.J. (2002). Implantation of scleral expansion band segments for the treatment of presbyopia. *Am. J. Ophthalmol., 134*, 808-815.

Quisling, S., Sjoberg, S., Zimmerman, B., Goins, K., & Sutphin, J. (2006). Comparison of Pentacam and Orbscan II on posterior curvature topography measurements in keratoconus eyes. *Ophthalmology, 113*, 1629-1632.

Radhakrishnan, H., & Charman, W.N. (2007). Changes in astigmatism with accommodation *Ophthalmic Physiol. Opt., 27*, 275-280.

Rainer, G., Menapace, R., Vass, C., Annen, D., Findl, O., & Schmetter, K. (1999). Corneal shape changes after temporal and suprolateral 3.0 clear corneal incisions. *J. Cataract Refractive Surg., 25*, 1121-1126.

Rainer, G., Petternel, V., Findl, O., Schmetterer, L., Skorpik, C., Luksch, A., & Drexler, W. (2002). Comparison of ultrasound pachymetry and partial coherence interferometry in the measurement of central corneal thickness. *J. Cataract Refractive Surg., 28*, 2065-2066.

Rajan, M.S., Keilhorn, I., & Bell, J.A. (2002). Partial coherence laser interferometry vs conventional ultrasound biometry in intraocular lens power calculations. *Eye, 16*, 552-556.

Ramamirtham, R., Kee, C.S., Hung, L.F., Qiao-Grider, Y., Roorda, A., & Smith, E.r. (2006). Monochromatic ocular wave aberrations in young monkeys. *Vision Res., 46*, 3616-3633.

Reinstein, D.Z., Silverman, R.H., Trokel, S.L., & Coleman, D.J. (1994). Corneal phachymetric topography. *Ophthalmology, 101*, 432-438.

Reynolds, A. (1980). Introduction: History of corneal measurement. In : Corneal tophography; measuring and modifying the cornea. *New York, Springer Verlag*, 8-10.

Rocha, K.M., Soriano, E.S., Chalita, M.R., Yamada, A.C., Bottós, J., Bottós, J., Morimoto, L., & Nosé, W. (2006). Wavefront analysis and contrast sensivity of aspheric and spherical intraocular lenses: a randomized prospective study. *Am. J. Ophthal., 142*, 750-756.

Roorda, A., & Glasser, A. (2004). Wave aberrations of the isolated crystalline lens. *J. Vision, 4* (4), 250-261.

Rosales, P., Dubbelman, M., Marcos, S., & Van der Heijde, G.L. (2006). Crystalline lens radii of curvature from Purkinje and Scheimpflug imaging. *J. Vision, 6*, 1057-1067.

Rosales, P., & Marcos, S. (2006). Phakometry and lens tilt and decentration using a custom-developed Purkinje imaging apparatus: validation and measurements. *J. Opt. Soc. Am. A., 23*, 509-520.

Rosales, P., & Marcos, S. (2007). Customized computer models of eyes with intraocular lenses. *Opt. Express, 15*, 2204-2218.

Rosales, P., Wendt, M., Marcos, S., & Glasser, A. (2007). Changes in the crystalline radii of curvature and lens tilt and decentration during dynamic accommodation in Rhesus Monkeys. *Journal of Vision (accepted for publication).*

Salmon, T.O., & van de Pol, C. (2006). Normal-eye Zernike coefficients and root-mean-square wavefronts errors. *J. Cataract Refractive Surg., 32*, 2064-2074.

Sasaki, K., Sakamoto, Y., Shibata, T., Nakaizumi, H., & Emori, Y. (1989). Measurement of postoperative intraocular lens tilting and decentration using Scheimpflug images. *J. Cataract Refract. Surg., 15* (454-457)

Schachar, R.A. (1994). Zonular function: a new hypothesis with clinical implications. *Ann. Opthalmo.l, 26*, 36-38.

Schachar, R.A., Cudmore, D.P., & Black, T.D. (1993). Experimental support for Schachar's hypothesis of accommodation. *Ann. Opthalmol., 25*, 404-409.

Schaeffel, F., Farkas, L., & Howland, H.C. (1987). Infrared photoretinoscope. *App. Opt., 26*, 1505-1509.

Schaeffel, F., Howland, H.C., & Farkas, L. (1986). Natural accommodation in the growing chicken. *Vision Res., 26*, 1977-1993.

Scheiner, C. (1619). Oculus, sive fundamentum opticum. *Innspruk*, 113.

Schmack, W.H., & Gerstmeyer, K. (2000). Long-term results of the foldable CeeOn Edge intraocular lens. *J. Cataract Refractive Surg., 26*, 566-570.

Schwiegerling, J., Greivenkamp, J., & Miller, J. (1995). Representation of videokeratoscopic height data with Zernike polynomials. *J. Opt. Soc. Am. A., 12* (10), 2105-2113.

Shack, R.V., & Platt, B.C. (1971). Production and use of a lenticular Hartmann screen. *J. Opt. Soc. Am., 61*, 656.

Sicam, V.A., Dubbelman, M., & van der Heijde , G.L. (2006). The spherical aberration of the anterior and posterior surface of the human cornea. *J. Opt. Soc. Am. A., 23(3)*, 1300-1306.

Sicam, V.A., & van der Heijde, G.L. (2006). Topographer reconstruction of the nonrotation-simmetric anterior corneal surface features. *Optom. Vision Sci., 83*, 910-918.

Silverman, R.H., Rondeau, M.J., Lizzi, F.L., & Coleman, D.J. (1995). Three dimensional high frequency ultrasonic parameter imaging of anterior segment pathology. *Ophthalmology, 102*, 837-843.

Simonet, P., & Campbell, M.C.W. (1990). The optical transverse chromatic aberration on the fovea of the human eye. *Vision Res., 30*, 187-206.

Sivak, J.G., & Kreuzer, R.O. (1983). Spherical aberration of the crystalline lens. *Vision Res., 23*, 59-70.

Smirnov, M.S. (1961). Measurement of the wave aberration of the human eye. *Biofizika, 6*, 687-703.

Smith, G., & Atchison, D. (2001). The gradient index and spherical aberration of the lens of the human eye. *Ophthalmic Physiol. Opt., 21* (4), 317-326.

Smith, G., Atchison, D., & Pierscionek, B. (1992). Modeling the power of the aging human eye. *J. Opt. Soc. Am. A., 9*, 2111-2117.

Smith, G., Cox, M., Calver, R., & Garner, L.F. (2001). The spherical aberration of the crystalline lens of the human eye. *Vision Res., 41* (2), 235-243.

Smith, G., & Garner, L.F. (1996). Determination of the radius of curvature of the anterior lens surface from the Purkinje images. *Ophthalmic Physiol. Opt., 16* (2), 135-143.

Smith, P. (1883). Diseases of crystalline lens and capsule. *Trans. Ophthalmol. Soc. UK., 3*, 79-99.

Smolek, M.K., Klyce, S.D., & Sarver, E.J. (2002). Inattention to nonsuperimposable midline symmetry causes wavefront analysis error. *Archives of Ophthalmology, 120* (4), 439-447.

Sorsby A, Benjamin B, & Sheridan M (1961). Refraction and its components during the growth of the eye from the age of three. (London: Medical Research Council Special Report Series.

Spierer, A., & Shalev, B. (2003). Presbyopia among normal individuals. *Graefes Arch Clin Exp Ophthalmol., 241*, 101-105.

Stachs, O., Schneider, H., Stave, J., & Guthoff, R. (2005). Potentially accommodating intraocular lenses- an in vitro and in vivo study using three-dimensional high-frequency ultrasound. *J. Refractive Surg., 21*, 321-323.

Steinert, R., & Deacon, J. (1996). Enalargement of incision width during phacoemulsification and folded intaocular lens implant surgery. *Ophthalmology, 103*, 220-225.

Strenk, S., Strenk, L., & Koretz, J.F. (2005). The mechanism of presbyopia. *Prog Retin Eye Res., 24*, 379-393.

Strenk, S., Strenk, L., Semmlow, J., & DeMarco, J. (2004). Magnetic resonance imaging study the effects of age and accommodation on the human lens cross-sectional area. *Invest. Ophthalmol. Vis. Science, 45*, 539-545.

Strenk, S.A., Semmlow, J.L., & Strenk, L.M. (1999). Age-related changes in human ciliary muscle and the lens: a magnetic resonance imaging study. *Invest. Ophtalmol. Vis. Science, 40*, 1162:1169.

Strenk, S.A., & Strenk, L.M. (2006). Magnetic resonance imaging of aging, accommodating, phakic, and pseudophakic ciliary muscle diameter. *J. Cataract Refractive Surg., 32*, 1792-1798.

Sverker, N., Artal, P., Ann Piers, P., & Van Der Mooren, Z. (2003). Methods of obtaining ophthalmic lenses providing the eye with reduced aberrations. (United States Patent Number: 7137702 , Application Number: 10768755)

Swanson, E.a., Huang, D., Hee, M.R., Fujimoto, J.G., Lin, C.P., & Puliafito, C.A. (1992). High-Speed optical coherence domain reflectometry. *Opt. Lett., 17*, 151-153.

Tabenero, J., Piers, P.A., & Artal, P. (2007). Intraocular lens to correct corneal coma. *Opt. Lett., 32*, 406-408.

Tabernero, J., Piers, P., Benito, A., Redondo, M., & Artal, P. (2006). Predicting the optical performance of eyes implanted with IOLs to correct spherical aberration. *Invest. Ophthalmol. Vis. Science, 47*, 4651-4658.

Tamm, S., Tamm, E., & Rohe, J.W. (1992). Age-related changes of the human ciliary muscle. A quantitative morphometric study. *Mech. Aging Dev., 62*, 209-221.

Thibos, L., Hong, X., Bradley, A., & Cheng, X. (2002). Statistical variation of aberration structure and image quality in a normal population of healthy eyes. *J. Opt. Soc. Am. A., 19*, 2329-2348.

Thibos, L.N. (1987). Calculation of the influence of lateral chromatic aberration on image quality across the visual field. *J. Opt. Soc. Am. A., 4*, 1673-1680.

Thibos, L.N., Applegate, R.A., Schwiegerling, J.T., Webb, R.H., & Members, V.S.T. (2000). Standards for reporting the optical aberrations of eyes. *Vision Science and its Applications, OSA Trends in Optics & Photonics, 35*, 110-130.

Thibos, L.N., Bradley, A., Still, D.L., Zhang, X., & Howarth, P.A. (1990). Theory and measurement of ocular chromatic aberration. *Vision Res., 30*, 33-49.

Tomlinson, A., Hemenger, R.P., & Garriott, R. (1993). Method for estimating the spheric aberration of the human crystalline lens in vivo. *Invest. Ophthalmol. Vis. Science, 34* (3), 621-629.

Tran, S.T., & van Noy, S.J. (2003). Anterior chamber phakic lens. *United States Patent Number:* 6562070, *Application Number*: 44763, (United Stated: Alcon, Inc.)

Tscherning, M. (1894). Die monochromatischen Aberrationen des menschlichen Auges. *Z. Physiol. Sinne, 6*, 456-471.

Tscherning, M. (1904). Physiologic Optics. *Philadelphia PA: The Keystone*, 160-189.

Tyson, R.K. (1997). Principles of adaptive optics. (San Dieg, CA, USA: Academic Press, 2nd edn.)

van der Heijde, G.L., Beers, A.P.A., & Dubbelman, M. (1996). Microfluctuations during steady state accommodation measured with echography. *Ophthalmic Physiol. Opt., 16*, 216-221.

van der Heijde, G.L., Dubbelman, M., & Beers, A.P.A. (1999). Continuous ultrasonographic biometry (CUB) used to measure thickening and translation of the aging lens. *Optical Society of America Technical Digest*, 110-113.

van der Heijde, G.L., & Weber, J. (1989). Accommodation used to determine ultrasound velocity in the human lens. *Optom. Vis. Sci., 66*, 830-833.

van Meeteren, A. (1974). Calculations on the optical modulation transfer function of the human eye for white light. *Optica Acta, 21*, 395-412.

van Meeteren, A., & Dunnewold, C.J. (1983). Image quality of the human eye for eccentric entrance pupils. *Vision Res., 23*, 573-579.

Van Veen HG, G.D. (1988). Simplified system of Purkinje image photography for phakometry. *Am. J. Optom. Physiol. Opt., 65*, 905.

Vilupuru, A., & Glasser, A. (2002). Dynamic accommodation in rhesus monkeys. *Vision. Res., 42*, 125-141.

Vilupuru, A., & Glasser, A. (2003). Dynamic accommodative changes in rhesus monkey eyes assessed with A-scan ultrasound biometry. *Optom. Vis. Sci, 80*, 383-394.
Vilupuru, A., & Glasser, A. (2005). The relationship between refractive and biometric changes during Edinger-Westphal stimulated accommodation in rhesus monkeys. *Exp. Eye Res., 80*, 349-360.

Vilupuru, A., Roorda, A., & Glasser, A. (2004). Spatially variant changes in lens power during ocular accommodation in a rhesus monkey eye. *J. Vision, 22*, 299-309.

Von Helmholtz, H. (1855). Über die akkommodation des auges. *Albrecht von Graefe's Arch. Ophthalmol., 1*, 1-74.

Walsh, G., & Charman, W.N. (1985). Measurement of the axial wavefront aberration of the human eye. *Ophthalmic Physiol. Opt., 5*, 23-31.

Walsh, G., & Charman, W.N. (1988). The effect of pupil centration and diameter on ocular performance. *Vision Res., 28*, 659 - 665.

Walsh, G., Charman, W.N., & Howland, H.C. (1984). Objective technique for the determination of monochromatic aberrations of the human eye. *J. Opt. Soc. Am. A., 1*, 987-992.

Wang, L., Dai, E., Koch, D., & Nathoo, A. (2003). Optical aberrations of the human anterior cornea. *J. Cataract Refractive Surg., 29*, 1514-1521.

Wang, L., & Koch, D. (2003). Ocular higher-order aberrations in individuals screened for refractive surgery. *J. Cataract Refractive Surg., 29*, 1896-1903.

Wang Meng-Chi, Woung Lin-Chung, Hu Chao-Yu, & Han-Chin., K. (1998). Position of poly(methyl methacrylate) and silicone intraocular lenses after phacoemulsification. *J. Cataract Refractive Surg., 24*, 1652-1657.

Webb, R.H., Penney, C.M., & Thompson, K.P. (1992). Measurement of ocular wavefront distortion with a spatially resolved refractometer. *Appl. Opt., 31*, 3678-3686.

Weeber, H.A., & van der Heijde , G.L. (2007). On the relationship between lens stiffness and accommodative amplitude. *Exp. Eye Res (Accepted for publication).*

Wilson, S.E. (2000). Cautions regarding measurements of the posterior corneal curvature. *Ophthalmology, 107*, 1223.

Willekens, B., Kappelhof, J.P., & Vrensen, G.F.J.M. (1987). Morphology of the aging human lens. *Lens. Res., 4*, 207-230.

Wulfeck, J. (1955). Infrared Photography of the So-Called Third Purkinje Image. *J. Opt. Soc. Am., 45*, 928-931.

Y Bron, A.J., Vrensen, G.F.J.M., Koretz, J.F., Maraini, G., & Harding, J.J. (2000). The ageing lens. *Ophthalmologica., 214*, 86-104.

Yabo, Y., Thompson, K., & Burns, S.A. (2002). Pupil location under mesopic, photopic and pharmacologically dilated conditions. *Invest. Ophthalmol. Vis. Sci., 43*, 2508-2512.
Yun, S.H., Tearney, B.E., De Boer, J.F., Iftimia, N., & Bourna, B.E. (2003). High-speed optical frequency-domain imaging. *Opt. Express, 11*, 2953-2963.

Zadnik, K., Mutti, D., & Adams, A. (1992). The repeatibility of measurement of the ocular components. *Invest Ophthalmol Vis Sci, 33*, 2325-2333.

Zadnik, K., Mutti, D.O., Fusaro, R.E., & Adams, A.J. (1995). Longitudinal evidence of crystalline lens thinning in children. *Invest. Ophthalmol. Vis. Sci., 36*, 1581-1587.

Zadnik, K., Mutti, D.O., Mitchell, G.L., Jones, L.A., Burr, D., & Moeschberger, M.L. (2004). Normal eye growth in emmetropic schoolchildren. *Optom. Vision Sci., 81*, 819-828.

Zernike, F. (1934). Physica. 1:689.

This thesis has resulted in the following peer-reviewed publications:

P.Rosales, S. Marcos
"Phakometry and lens tilt and decentration using a custom-developed Purkinje imaging apparatus: validation and measurements."
Journal of the Optical Society of America A, Vol 23, Pg 509-520 (2006).

P. Rosales, M.Dubbleman, S.Marcos and G.L. Van der Heijde.
"**Crystalline radii of curvature from Purkinje and Scheimpflug imaging "**
Journal of Vision, Vol 6, Pg 1057-1067.

Susana Marcos, P. Rosales, Llorente Lourdes, Jiménez-Alfaro, I
"**Change of corneal aberrations after cataract surgery with two types of aspheric intraocular lenses"**
Journal of Cataract Refractive Surgery, Vol 33, Pg 217-226 (2007).

A. de Castro, P. Rosales, and S. Marcos
"**Tilt and decentration of intraocular lenses in vivo from Purkinje and Scheimpflug imaging: A validation study"**
Journal of Cataract Refactive Surgery, Vol 33, Pg 418-429, (2007).

P.Rosales, S. Marcos
"Customized models of eyes with intraocular lenses"
Optics Express, Vol 15, Pg 2204-2218, (2007).

P.Rosales, M.Wendt, S.Marcos, and A. Glasser
"**Phakometric Measurement of Crystalline Lens Curvature, Tilt and Decentration During Edinger-Weshphal Stimulated Accommodation in Rhesus Monkeys"**
Journal of Vision, Vol 8, Pg 1-12, (2008).

S. Marcos, P. Rosales, L. Llorente, and I. Jiménez-Alafaro
"**Corneal/Internal Compensation of Aberrations: Evidence for a Passive Mechanism"**
Vision Research, Vol 48, Pg 70-79, (2008).